

TOBIAS BASSE
PH.D. DISSERTATION

Aspects of
DARK ENERGY

Supervision by Prof. Steen Hannestad
Department of Physics and Astronomy
Faculty of Science and Technology
Aarhus University
Denmark
August 2014



ASPECTS OF DARK ENERGY

A DISSERTATION PRESENTED TO THE FACULTY OF SCIENCE AND
TECHNOLOGY OF AARHUS UNIVERSITY IN PARTIAL FULFILMENT OF THE
REQUIREMENTS FOR THE PH.D. DEGREE

BY
TOBIAS BASSE
AUGUST 2014

CONTENTS

Contents	i
Acknowledgements	v
List of publications	vii
Dansk resumé	ix
Summary in English	xi
I Introduction and motivation	1
1 Introduction	3
2 Motivation	5
2.1 Cosmic timeline	5
2.2 Cosmology and the expanding universe	6
2.3 Observations	10
2.3.1 Supernovae type Ia	10
2.3.2 Cosmic microwave background	11
2.3.3 Baryon acoustic oscillations	12
3 Models of dark energy	15
3.1 Cosmological constant – Λ CDM	15
3.1.1 Λ and observations	16
3.2 Quintessence models	17
3.2.1 A model inspired by particle physics	18
3.3 Modified gravity	19
3.3.1 $f(R)$ gravity	19
3.4 A fluid model	20
4 Dark matter	23

Contents

4.1	Neutrinos	25
4.1.1	Neutrinos and cosmology	25
II	Theoretical framework	29
5	Cosmological perturbation theory	31
5.1	Evolution equations	31
5.2	Statistical properties of the density fluctuations	33
5.3	Angular power spectra	35
6	Structure formation and the cluster mass function	41
6.1	Press-Schechter theory	41
6.2	Excursion set theory	42
6.3	The spherical collapse model	45
6.3.1	Virialization of the system	47
6.4	Comparing to N-body simulations	47
7	Gravitational lensing	51
8	Bayesian statistics and parameter inference	55
8.1	Bayesian statistics	55
8.1.1	Parameter inference	56
8.2	Markov chain Monte Carlo analysis	57
8.2.1	Metropolis-Hastings algorithm	58
8.2.2	Parameter inference II	58
8.3	Fisher information matrix	59
8.4	Two simple examples	61
III	My work	67
9	Spherical collapse of dark energy with an arbitrary sound speed	69
10	Confronting the sound speed of dark energy with future cluster surveys	97
11	Dark energy properties from large future galaxy surveys	123
11.1	Angular power spectra	124
11.2	Results	126
12	Non-linear approaches	155
12.1	Non-linear dark energy and spherical collapse	155
12.1.1	State of the project	157

Contents

12.2 Dark energy N-body simulations	157
12.2.1 Halofit	158
12.2.2 State of the project	159
IV Outlook	161
13 Conclusions and perspectives	163
V Back matter	165
Appendix	167
A Details of excursion set theory	167
Bibliography	171

ACKNOWLEDGEMENTS

First, I would like to thank my supervisor Steen Hannestad for granting me the opportunity to study the field of cosmology in an informal yet adept environment. Current as well as former members of the cosmology group also deserve appreciation: Rasmus Sloth-Hansen, Io Odderskov, Maria Archidiacono, Thomas Tram, and Jan Hamann. A special thanks to Ole Bjælde for joining ventures into new scientific grounds and, through his teaching, inspiring me to study cosmology, and to Christian Schultz for sharing many offices with me, especially during the heat of the writing process and for comments to this manuscript. I acknowledge computing resources from the Danish Center for Scientific Computing.

I thank Yvonne Wong for hosting my exchange at the University of New South Wales in Sydney, and for letting me experience that science transcends borders and that European winter is a good time to visit Australia. My fellow students at the University of New South Wales, especially Vincent Dumont and the Wednesday soccer group, made my stay unforgettable. Also, thanks to the Australian Institute of Physics for the chance to present my research.

During my Ph.D. years, I have enjoyed many lunch breaks with Søren Andersen, Kasper Laursen, and Kristian Høvinghoff. These breaks, as well as other occasions, have been the scenes of discussions about pretty much everything – both inside and outside the walls of the university. Penultimately, a special thanks to my brother, Kristoffer Basse, for proofreading this dissertation and for comments improving the coherence of the manuscript. Finally, to my girlfriend, Sanne Lundsgaard, I am grateful for her support through the ups and downs, and for her constant ability to put a smile on my face.

LIST OF PUBLICATIONS

Published papers

Tobias Basse, Ole E. Bjaelde, Yvonne Y. Y. Wong.

Spherical collapse of dark energy with an arbitrary sound speed.

JCAP, 1110, 038.

Tobias Basse, Ole E. Bjaelde, Jan Hamann, Steen Hannestad, Yvonne Y. Y. Wong.

Dark energy properties from large future galaxy surveys.

JCAP, 1405, 021.

Unpublished papers

Tobias Basse, Ole E. Bjaelde, Steen Hannestad, Yvonne Y. Y. Wong.

Confronting the sound speed of dark energy with future cluster surveys.

arXiv:1205.0548.

In preparation

Tobias Basse, Jan Hamann, Steen Hannestad, Yvonne Y. Y. Wong.

Getting leverage on inflation.

In preparation.

Maria Archidiacono, Tobias Basse, Jan Hamann, Steen Hannestad, Georg Raffelt, Yvonne Y. Y. Wong.

Future cosmological sensitivity for hot dark matter axions.

In preparation.

DANSK RESUMÉ

I årtusinder har vi studeret nattehimmelen; først med det blotte øje og senere med mere og mere avancerede instrumenter. Selvom moderne kosmologi er en relativ ung disciplin, relaterer den til spørgsmål om den virkelighed, vi lever i og sanser – spørgsmål der er ligeså gamle som menneskeheden. På trods af den store mængde information, vi har samlet om universet, er en af de mere bemærkelsesværdige indsigter, vi er blevet ført til, at vores viden om størstedelen af universets indhold er overraskende lille. Vi ved i dag, at partikelfysikkens standardmodel kun succesfuldt beskriver ca. fem procent af indholdet. Det resterende indhold i universet er blevet døbt mørkt stof og mørk energi. Det sidstnævnte er fokus for denne afhandling.

Det videnskabelige felt mørk energi er i en rivende udvikling, og der findes utallige forskellige modeller, hvorfor der er behov for observationelle metoder til at skelne imellem dem. Forskningen i denne afhandling præsenterer en generel model, hvor mørk energi er en væske med en tilstandsparameter, som kan være konstant eller variere i tid. Yderligere indeholder modellen – gennem en konstant lydhastighed – mulighed for at mørk energi er inhomogent. Vi diskuterer de kosmologiske implikationer samt manglerne ved denne model.

Vi udvikler numeriske redskaber til udregning af observable, som eksperimenter over de næste ti år vil kunne måle. Disse redskaber kan ligeledes anvendes på modeller for mørkt stof og til at analysere effekten af inflationsparametre. Ved brug af Markov kæde Monte Carlo simulering og Bayesianske metoder til parameter estimering analyserer vi, hvor meget fremtidige galakse observationer vil afsløre om mørk energis natur.

Vores undersøgelser viser, at tilstandsparameteren for mørk energi kan bestemmes med hidtil uset præcision af næste generation af eksperimenter. Der er behov for yderligere teoretiske landvindinger med hensyn til perturbationer i fordeling af mørk energi, før vi kan udnytte det fulde potentiale i fremtidige data. Vi konkluderer, at kosmologi vil bevare momentum over de næste ti år, og at fremtiden syner lys nok til at afsløre nogle af mysterierne om mørk energi.

SUMMARY IN ENGLISH

For millennia, we have studied the night sky. At first with the naked eye and later with increasingly advanced instruments. While the modern field of cosmology is a relatively young discipline, it relates to ancient philosophical questions concerning the origin of the reality we inhabit and experience. Although the information about the universe gathered through time is impressive, one of the most noticeable insights that we have been led to is that we know surprisingly little about most of the contents of the universe. To be specific, we now know that the standard model of particle physics only succeeds in explaining five percent of the contents. The remaining content of the universe has been dubbed dark matter and dark energy, the latter of which is the focus of this dissertation.

The field of dark energy is in rapid development and the different models are countless. Therefore, there is a call for observational ways to distinguish these. The scientific research in this dissertation presents a generic model, where dark energy is a fluid with an equation of state that is either constant in time or shows a simple evolution with the scale factor of the universe. Furthermore, the model accommodates dark energy inhomogeneities through an arbitrary sound speed. We discuss the cosmological implications and the flaws of this models.

We develop numerical tools capable of computing observables, which will be accessible to surveys over the next decade. These tools can also be applied to models describing dark matter as well as be used to analyse the effect of inflationary parameters. Using Markov chain Monte Carlo simulations and Bayesian parameter inference techniques, we investigate the ability of future galaxy surveys to reveal information about the nature of dark energy.

We find that the dark energy equation of state will be constrained with unprecedented precision by the next generation of surveys. Regarding dark energy perturbations, our studies show that theoretical advancements are needed in order to fully appreciate the future data. In conclusion, cosmology is going to keep up the momentum over the next decade and the future looks bright enough to shed light on the some of the mysteries of dark energy.

Part I

**INTRODUCTION AND
MOTIVATION**

1

INTRODUCTION

Current observational evidence for the accelerated expansion of the universe is compelling, see, e.g., Komatsu et al. (2011); Kowalski et al. (2008); Wood-Vasey et al. (2007). This accelerated expansion is generally attributed to the presence of a dark energy component in the universe's energy budget – a component with a strong negative pressure, which dominates gravitational physics on large scales. The nature of this dark energy is, however, still a secret, which the universe keeps to itself – at least for now – and much effort is being invested in measuring the properties of this dark energy in order for us to reveal its secret one day. In the standard cosmological model, dark energy is constant in space and time, yet a dynamical nature of dark energy has not been ruled out. The overall goal of this project is to investigate and quantify the effects of generic dynamical dark energy on the formation of structures in the universe. This dissertation will answer questions like: Does dynamical dark energy carry a unique signature and in that case is it significant enough for near future experiments to detect it? Along the way, we will touch upon other interesting topics of cosmology, e.g., the impact of neutrino physics on the universe.

The work in this dissertation is done in natural units where $c = \hbar = 1$. This means that mass and energy have the same units, while length and time have units of inverse energy. Furthermore, we shall at times make use of Einstein summation notation, where repeated indices are summed over. Greek indices run from zero to three, while Roman indices run from one to three. By convention, zero refers to the temporal coordinate, while one to three refer to the spatial coordinates. Subscript α is reserved to refer to different particle species or different redshift bins. A tilde will denote Fourier quantities in the sense that $\tilde{\delta}$ is the Fourier transform of δ , etc.. It has been the aim to use a notation that is consistent across the dissertation and papers included in III, however, deviations may occur.

The main body of this dissertation is divided into four parts. You are now reading part one, which serves to set the scene by introducing cosmology and the observations hinting at the existence of dark energy. Part two puts the technical details into play describing the theoretical framework of my Ph.D. project. Next, part three presents my work in various forms: Finished works that have resulted in papers are presented as these papers, in their most recent arXiv form, accompanied by extra introductions

1. Introduction

summarizing the paper and my contributions, some unfinished works have also been granted a chapter describing the details and the state of the project. Finally, the forth part sums up the course of my Ph.D. and looks to the future. The back matter contains one appendix and the bibliography of the dissertation.

2

MOTIVATION

As stated in the introduction, the observational evidence for the existence of dark energy is extensive. This chapter gives an overview of the key observations supporting dark energy, see Davis (2014) for a recent review of these observations. Before digging into the details and equations, however, we will begin by establishing a cosmic timeline.

2.1 Cosmic timeline

The age of the universe has most recently been measured by the ESA Planck mission, Ade et al. (2013), to be approximately 13.8 billion years. Although the universe has existed for such a long period of time, some of the important epochs in the cosmic timeline last only a tiny fraction of a second. It all starts with a Big Bang, and without a philosophical discussion of the phenomenon time, this Big Bang represents a point from which time can be measured. In the first minuscule fraction of a second, the universe undergoes a period of very rapid expansion called inflation. During the inflation epoch, the size of the universe increases by ~ 50 orders of magnitude. Among others, inflation solves the *flatness problem* and the *horizon problem*, by explaining why the universe is flat and how the universe can be homogeneous and isotropic and large scales, respectively. The BICEP2 experiment, Ade et al. (2014), on the south pole recently claimed detection of significant B-mode polarization in the cosmic microwave background, which is a signature of gravitational waves produced during inflation. As the universe expands, it also cools, and because the universe has been expanding since the Big Bang, temperature can also be used as a measure of time, with a lower temperature corresponding to a later time in general. Note that the universe is reheated by, e.g., annihilation processes, as we shall see during the discussion of neutrinos.

In the hot early universe, no bound neutral atoms or bound nuclei exist, as those created are destroyed immediately by numerous high energy photons present at the time. Neutrons and protons are kept in thermal equilibrium by reactions with lighter electrons and neutrinos. At a temperature of $T \sim \text{MeV}$, less than a second after Big Bang, the rates of these reactions drop below the expansion rate of the universe and thermal equilibrium can no longer be maintained. Now, unstable neutrons decay into protons, an electron and an anti electron-neutrino, and the neutrons will continue to decay until

they can be bound in stable nuclei. A few seconds after Big Bang, the universe has cooled enough for Big Bang nucleosynthesis to commence. This is the epoch where light nuclei ranging from deuterium to lithium and beryllium are created through nuclear fusion. At this time, protons outnumber neutrons roughly seven to one, and almost all neutrons are bound in helium-4, which has the highest binding energy per nucleon of the lightest elements. After Big Bang nucleosynthesis, the baryonic matter in the universe is distributed by mass in approximately 75 percent protons or hydrogen, 25 percent helium-4 and small, but not negligible, amounts of other nuclei. This procedure is completed within the first minutes of the existence of the universe.

For another 380.000 years, the high energy photons keep neutral atoms from forming. Thompson scattering of photons on free electrons keeps the mean free path of the photons very short and they are essentially trapped in the electron gas. Around year 380.000, the recombination process helps initiate the decoupling of the photons from the electron gas. Recombination is the combination of the free electrons with nuclei to form neutral atoms and it happens because the fraction of photons with energies high enough to destroy the atoms becomes lower as the temperature drops. Recombination results in a sudden decrease in the number density of free electrons and hence the Thompson scattering rate. Shortly after, the expansion of the universe drives this number density so low that the mean free path of the photons exceeds the size of the universe and they decouple from the electron gas. The now free photons propagate undisturbed through the universe until they by chance hit something, e.g., a telescope on earth or the Planck satellite at the present time. As they propagate, the continuing expansion of the universe causes their energy to decrease so much that it is in the microwave range today – these photons make up what we call the cosmic microwave background. As will be discussed later in this chapter, much information about the universe is contained in these photons and their statistical distribution.

Some hundreds of millions of years pass before the formation of stars, galaxies and even larger structures begins, and nine billion years after the Big Bang our solar system is formed. On the cosmic timeline, dark energy starts to dominate the energy budget on cosmological scale just around the time of the formation of the solar system depending on the particular model of dark energy. To fully understand how this works, we have to dig into the equations governing the evolution the universe.

2.2 Cosmology and the expanding universe

The framework of standard cosmology relies on the Cosmological or Copernican principle, which states that we are not special observers of the universe. Essentially, this means that there exists no preferred location or direction in the universe. Clearly, on Earth one can define a preferred direction to be towards the center of the Earth, due to the gravitational attraction of the Earth – and similarly, a preferred direction exists in

the Solar System and our galaxy. To specify, the Cosmological principle states that the universe is homogeneous and isotropic on large scales. The deviation of the principle on intermediate scales is assumed to be tiny, such that deviations from homogeneity and isotropy can be treated using perturbation theory. The concepts of cosmological perturbation theory are discussed in chapter 5. To understand the evolution on small scales, we typically rely on N-body simulations.

The only time evolutions of the universe that preserve homogeneity and isotropy are overall expansion or contraction – or a static universe with no time evolution. This overall expansion or contraction can be captured by the scale factor, $a(t)$. The line element in general relativity is given by $ds^2 = g_{\mu\nu}dx^\mu dx^\nu$, where $g_{\mu\nu}$ is the metric tensor and x^μ and x^ν are coordinate vectors in some arbitrary coordinate system. The spatial part of the metric tensor describing the universe is conveniently expressed in terms of co-moving coordinates, since this isolates the spatial time evolution in the scale factor. In co-moving spherical coordinates, the large scale homogeneous and isotropic universe is described by the Friedmann-Robertson-Walker metric,

$$ds^2 = -dt^2 + a(t)^2 \left[d\chi^2 + S_\kappa(\chi)^2 \left(d\theta^2 + \sin^2 \theta d\phi^2 \right) \right], \quad (2.1)$$

where χ is co-moving distance and $S_\kappa(\chi)$ encapsulates the possibility that space is curved. S_κ depends solely on χ , since large scale homogeneity and isotropy permits only uniform curvature, i.e., the universe is either uniformly negatively curved, flat, or uniformly positively curved – corresponding to $\kappa = -1, 0, 1$, and

$$S_\kappa = \begin{cases} \sinh \chi & , \quad \kappa = -1 \\ \chi & , \quad \kappa = 0 \\ \sin \chi & , \quad \kappa = 1 \end{cases} . \quad (2.2)$$

When the scale factor is a monotone function of time, as it is the case in the standard model of cosmology, a can be used as the time coordinate. Furthermore, we sometimes use the redshift, $z = a^{-1} - 1$, which measures the red- or blueshift of light due to the expansion or contraction of the metric as the time coordinate. Henceforth, we will omit writing the time dependence of variables explicitly.

Before turning to cosmological distance measures, let us devote some attention to the time evolution of the universe. On large scales, the evolution is governed by gravity, and thus general relativity, in form of the Einstein equations,

$$G_{\mu\nu} \equiv R_{\mu\nu} - \frac{1}{2}Rg_{\mu\nu} = 8\pi GT_{\mu\nu}, \quad (2.3)$$

where the left hand side describes the curvature of space and time through the metric and derivatives thereof, while the right hand side describes the contents of the universe through the energy-momentum tensor. $R_{\mu\nu}$ and R are the Ricci tensor and Ricci scalar, respectively. They are related to the metric through the Riemann curvature tensor and the Christoffel symbols. For a perfect fluid, i.e., a fluid with no shear stress, viscosity

or heat conduction, the energy-momentum tensor in the fluid rest frame is diagonal and given by $T_{\mu}^{\nu} = \text{diag}(-\rho, P, P, P)$, where ρ is the energy density and P the pressure of the fluid. Covariant energy conservation leads to the fluid equation,

$$\frac{d\rho}{dt} + 3H(\rho + P), \quad (2.4)$$

where $H \equiv a^{-1}da/dt$ is the Hubble parameter.

The Einstein equations lead us to the Friedmann equations, the first of which, in a Newtonian approximation, is a statement of energy conservation in the expansion of the universe,

$$H^2 = \frac{8\pi G}{3} \sum_{\alpha} \rho_{\alpha} - \frac{\kappa}{R_0^2 a^2}, \quad (2.5)$$

where R_0 is the present day radius of curvature of the universe – the latter term disappears in a flat universe with $\kappa = 0$. The second Friedmann equation is also known as the acceleration equation,

$$\frac{1}{a} \frac{d^2 a}{dt^2} = -\frac{4\pi G}{3} \sum_{\alpha} (\rho_{\alpha} + 3P_{\alpha}). \quad (2.6)$$

Often, one introduces the density parameter $\Omega_{\alpha} = \rho_{\alpha}/\rho_{\text{cr}}$, where $\rho_{\text{cr}} \equiv 3H^2/8\pi G$, and the equation of state $w_{\alpha} = P_{\alpha}/\rho_{\alpha}$, where $w = 0$ for matter and $w = 1/3$ for radiation. As hinted in the beginning of this chapter, the purpose of dark energy is to explain the acceleration of the expansion of the universe. Equation (2.6) tells us that in a universe containing only dark energy the equation of state must be $w_{\text{de}} < -1/3$ to cause positive acceleration. When dark energy is mixed with significant amounts of matter or radiation, the requirements for w_{de} are more strict. In the standard model of cosmology, dark energy is a cosmological constant with $w_{\Lambda} = -1$. This model will be discussed later in chapter 3.

Figure 2.1 shows the distribution of the contents of the universe in the species, baryons, dark matter, radiation, and dark energy – the figure is based on cosmological parameters from Ade et al. (2013) assuming a flat universe with a cosmological constant and without the neutrinos discussed in chapter 4. From the figure, we see how the universe has gone through a radiation dominated period, followed by a matter (baryons and dark matter) dominated period, before recently becoming dark energy dominated.

When constraining the evolution history of the universe, cosmologists often rely on standard rulers or standard candles, i.e., objects of known extension or luminosity, respectively. To clarify how these objects are useful, a discussion of distances in cosmology is needed. To identify the co-moving distance, we consider a radial light ray moving on a null geodesic, i.e., $ds^2 = d\theta^2 = d\phi^2 = 0$. We thus find $dt = ad\chi$. As such the co-moving distance between an observer receiving light at $t = t_0$ and the source emitting light at

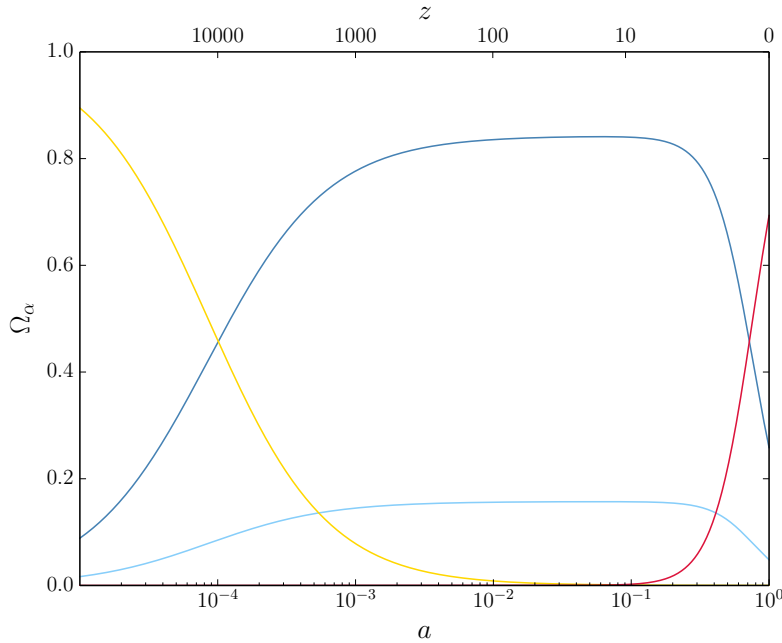


Figure 2.1: Density parameter of the species baryons (lightblue), dark matter (blue), radiation (yellow), and dark energy (red) as a function of the scale factor and redshift.

$t = t_e$ is

$$\chi = \int_{t_e}^{t_0} \frac{dt}{a} = \int_{a_e}^{a_0} \frac{da}{a^2 H} = \int_0^{z_e} \frac{dz}{H}. \quad (2.7)$$

The co-moving distance between two objects is not changed by the overall expansion of the universe.

When dealing with standard candles, the important distance measure is the luminosity distance, d_L . As light propagates through space-time, it is affected by the expansion or contraction of the universe such that the frequency of the light observed is $f_0 = (1 + z_e)^{-1} f_e$. Assuming that the light from an object with luminosity L is distributed uniformly, we can use the metric to calculate the area of the sphere over which the light is distributed and thus the flux from the source. The redshifting of the light's frequency gives an effective luminosity of the source, $(1 + z_e)^{-2} L$, since the energy per photon and the number of photons per time are both affected by a factor of $(1 + z_e)^{-1}$,

$$F = \frac{L}{4\pi S_\kappa(\chi)^2 (1 + z_e)^2} \equiv \frac{L}{4\pi d_L^2}. \quad (2.8)$$

In dealing with standard rulers, the angular diameter distance is of importance. If the transverse length of some object is known to be ℓ , then the angular diameter distance

is defined as $d_A \equiv \ell/\delta\theta$, where $\delta\theta$ is the angular extension of the object on the sky. Using the metric to describe the object, we find $\ell = a(t_e) S_\kappa(\chi) \delta\theta$, and thus

$$d_A = a(t_e) S_\kappa(\chi) = \frac{S_\kappa(\chi)}{1+z_e}. \quad (2.9)$$

The luminosity and angular diameter distances, both being functions of χ , probe the expansion history of the universe.

2.3 Observations

Since the late 1920's, where Edwin Hubble related the recession velocity of galaxies to their distance from us through Hubble's law, it has been known that we live in an expanding universe. However, more recent observations suggest that not only is the universe expanding, the expansion is also accelerating. This section deals briefly with these observations as they form the foundation of the field of dark energy, since the acceleration cannot be accommodated in a universe consisting of radiation and matter. In the standard model of cosmology, the universe consists of radiation, baryons, dark matter and dark energy. For reviews on the cosmic expansion see, e.g., Frieman (2008); Frieman et al. (2008); Silvestri & Trodden (2009); Bean (2010); Padmanabhan (2003).

2.3.1 Supernovae type Ia

Supernovae type Ia (SNIa) are thermonuclear explosions of white dwarves in binary systems with red giants. As the red giant evolves through stellar stages, it expands and at some point it will extend beyond its Roche lobe, which defines the region where matter stays bound to the red giant. When this occurs, matter starts flowing from the red giant onto the white dwarf. Matter continues to accrete until the white dwarf reaches the Chandrasekhar mass of approximately 1.4 solar masses. At this point, it becomes unstable and undergoes a thermonuclear explosion. Since SNIa are characterized by the explosion of a 1.4 solar mass white dwarf, one would expect these supernovae to be standard candles. The light curve of SNIa is determined by decays of radioactive iron peak elements. The amount of iron peak elements produced in the explosions differ and thus SNIa are not perfect standard candles. However, an empirical relation between the SNIa peak brightness and the rate at which light curves decay after peaking has been found. In this Phillips relation, intrinsically brighter supernovae decay more slowly. Utilizing this relation, SNIa can be used as standard candles.

If the luminosity of SNIa is measured using nearby supernovae, the observations of distant SNIa can be used to measure the luminosity distance as a function of redshift and thus probe the evolutionary history of the universe. The SNIa observations essentially

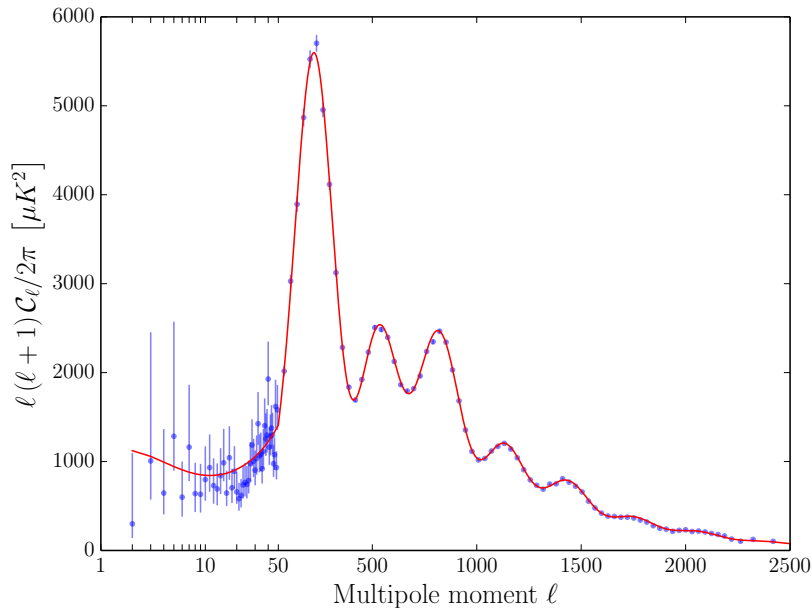


Figure 2.2: Angular power spectrum of the CMB anisotropies measured by Planck. The scale is logarithmic from $\ell = 1$ to $\ell = 50$ and linear onwards (the logarithmic part has been scaled for better presentation). The data points beyond $\ell = 50$ are binned with a bin width of 31 multipoles. The red line shows a theoretical calculation of the spectrum using CAMB and the best-fit parameters from Planck for a Λ CDM model (see table 5 of Ade et al. (2013)).

constrain the contents of the universe by pinning down the combination,

$$q_0 \equiv -\frac{1}{aH^2} \frac{d^2 a}{dt^2} \Big|_{t_0} = \frac{1}{2} \sum_{\alpha} \Omega_{\alpha,0} (1 + 3w_{\alpha,0}). \quad (2.10)$$

This is known as the deceleration parameter and SNIa observations suggest that q_0 is negative, corresponding to accelerated expansion. When constraining q_0 , SNIa observations leave a degeneracy in the parameter space of the contents in the universe. This degeneracy can be broken by including other observations.

2.3.2 Cosmic microwave background

The cosmic microwave background (CMB) was briefly discussed as part of the cosmic timeline, but important points will be recapped here. The CMB consists of relic photons released around the time of recombination. Prior to recombination, photons, electrons, and baryons form an ionised plasma. The highly energetic photons are responsible for

ionising the plasma. The photons, electrons, and protons are tightly bound due to Thomson scattering between photons and electrons and the electrostatic attraction between electrons and protons. At recombination, the plasma has cooled enough for neutral hydrogen to form. While photons readily scatter off free electrons through Thomson scattering, they interact negligibly with neutral hydrogen, so after recombination, photons propagate with minimal interaction until they are detected.

The CMB photons are remarkably homogeneous in temperature following a Planck distribution in frequency, with present fluctuations at a level of 10^{-5} . This homogeneity is one of the observations favouring a period of inflation in the early universe, since the entire visible universe was not causally connected at the time of recombination and prior to that. The small fluctuations in the CMB can be used to constrain the contents of the universe, since the size of the correlations in the fluctuations acts as a standard ruler. Investigating the behaviour of the photons in the ionized plasma prior to recombination gives the expected intrinsic size of these correlations.

In the epoch prior to recombination, the universe is dominated by dark matter, and thus the evolution of the photon-baryon plasma is governed by the gravitational potential of the dark matter. After inflation, adiabatic conditions rule in the universe such that perturbations in the density field are correlated in position, i.e., over-densities in the plasma are located the same place as over-densities in the dark matter density. An over-density in the plasma located in a dark matter potential well falls towards the center hereof and contracts – at the same time under-densities expand. The contraction leads to an increased photon pressure in the plasma and at some point this pressure forces the plasma to expand again – now under-densities contract.

These acoustic oscillations set a scale in the CMB, which depends on the speed of the photons in the plasma. In the plasma, the photons propagate with an effective sound speed depending on the ratio between baryon and photon energy densities in the early universe – this is inferred from Big Bang Nucleosynthesis. The first peak in the CMB power spectrum corresponds to regions that are fully contracted or expanded for the first time at the time of recombination. Measuring the angular size of this scale is a probe of the angular diameter distance and thus the curvature of the universe. Adding dark energy is degenerate with the universe having a curvature. This degeneracy can, however, be broken by measuring the present day Hubble parameter, H_0 . To conclude, CMB constrains the curvature of the universe, i.e., Ω_{tot} , and suggests we live in a spatially flat universe.

2.3.3 Baryon acoustic oscillations

The acoustic oscillations discussed above also leave an imprint on the large scale distribution of matter. The pressure of the photons causes the over-densities in the plasma to be dislocated from the over-densities in the dark matter. At the time of recombination, this dislocation is roughly 150 Mpc. After recombination, the baryons no longer

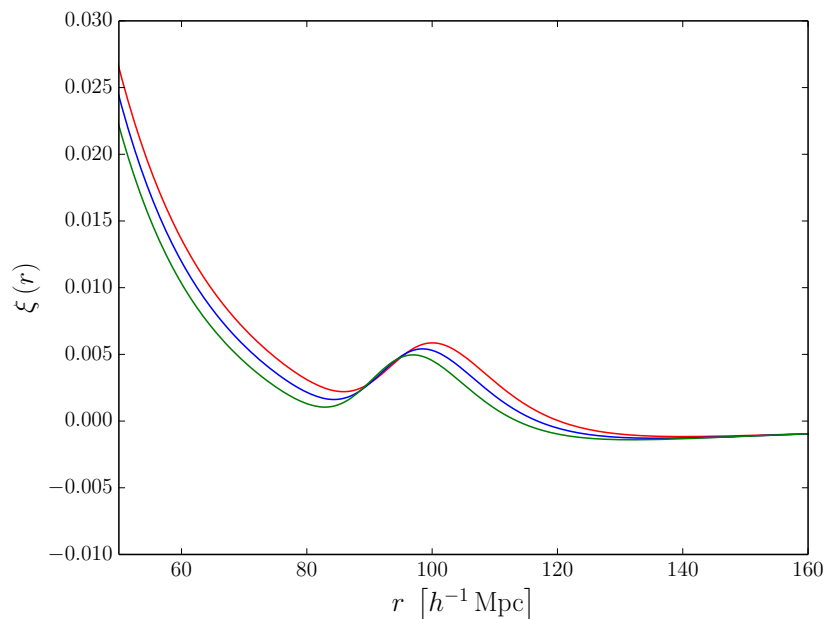


Figure 2.3: Real space correlation function of the matter distribution in the universe. The red curve corresponds to the Λ CDM model of Ade et al. (2013). The blue and green curves are made by changing Ω_m to 0.13 and 0.14, respectively.

follow the photons and baryons start flowing towards the dark matter potential wells. However, dark matter also starts flowing towards the baryon potential wells separated from the center of the dark matter over-density by roughly 150 Mpc. As a result, it is more likely for galaxies to be separated by 150 Mpc than for instance 120 or 180 Mpc, see figure 2.3 for the spatial correlation function of the matter distribution. As seen on figure 2.3, this shows up as a single acoustic peak in the correlation function. In the power spectrum of the distribution of matter perturbations, it shows up as a sequence of acoustic oscillations. The Baryon Acoustic Oscillations primarily constrain the amount of matter in the universe, i.e., Ω_m .

3

MODELS OF DARK ENERGY

The landscape of dark energy models is vast, so the aim of this chapter is to introduce some of the most general models with their strengths and weaknesses. Although the amount of information about the universe gathered by astronomers and cosmologists through time may seem overwhelming, it still leaves significant uncertainties on even standard parameters, e.g., the contents of the universe. The existing observations, simplifying approximations in analysis, and conclusions drawn thereof are subject to constant scrutiny, e.g., abandoning the assumption of large scale homogeneity and isotropy could open up for different interpretations of the observations discussed in the previous chapter. Overall, the assumption of large scale homogeneity and isotropy appears to be valid and will be kept in this work.

3.1 Cosmological constant – Λ CDM

The observations discussed in the previous chapter and others indicate that we find ourselves in a spatially flat universe, presently consisting of negligible amounts of radiation, roughly one quarter of matter and three quarters of some dark energy component – the latter causing late time acceleration of the expansion of the universe. In the consensus cosmological model, which fits observational data very well within the errorbars, dark energy is a cosmological constant, Λ . The cosmological constant was originally introduced by Einstein as a property of the space-time to create a static universe, but it was later realized that Λ could be the source of the late time acceleration of the expansion. For detailed reviews of the cosmological constant see Peebles & Ratra (2003); Carroll (2001); Padmanabhan (2003).

Today, the theoretical foundation of the cosmological constant is that it is the contribution to the energy-momentum tensor from quantum fluctuations of vacuum. The energy-momentum tensor of vacuum must be proportional to the metric tensor to ensure Lorentz invariance and the constant of proportionality is by definition minus the energy density. As a result we find,

$$P_{\Lambda} = \frac{1}{3}T_{i,\Lambda}^i = \frac{1}{3}g^{ij}T_{ij,\Lambda} = -\frac{1}{3}\rho_{\Lambda}g^{ij}g_{ij} = -\rho_{\Lambda}. \quad (3.1)$$

Thus, the equation of state of the cosmological constant is $w_\Lambda = -1$, which means that the energy density is constant in time according to equation (2.4). This seems reasonable as Λ is a property of vacuum. ρ_Λ can be inferred from observations requiring that the total energy density matches the critical energy density, i.e., the universe is flat.

The energy density of vacuum can be estimated from a simple calculation. The contribution from a single free quantum field can be calculated as,

$$\rho_\alpha = \frac{g_\alpha}{2} \int_0^{k_{\max}} \frac{d^3k}{(2\pi)^3} \sqrt{k^2 - m^2} \simeq \frac{g_\alpha k_{\max}^4}{16\pi^2}, \quad (3.2)$$

where g_α is a spin factor of the field α and k_{\max} is some reasonable cut-off scale. For any reasonable cut-off scale, the contribution from a single quantum field is more than fifty orders of magnitude higher than ρ_Λ inferred from observations. For fermions, g_α is negative, while it is positive for bosons. Thus, for vacuum fluctuations to be the origin of Λ , the contributions from fermions and bosons must cancel to very high accuracy. In exact super symmetry, these contributions exactly cancel, but if the cut-off scale is taken to be the scale where super symmetry is broken, the contribution from a single quantum field is still more than fifty orders of magnitude larger than ρ_Λ . See Martin (2012) for a calculation including the different particles in the standard model of particle physics.

This required cancellation is perhaps the most severe theoretical obstacle for the cosmological constant, which encourages cosmologists to search for alternative explanations to the accelerated expansion of the universe. Another challenge is the *coincidence problem* asking why ρ_m and ρ_Λ are the same order of magnitude today. This problem is often met with the anthropic principle. The dark energy alternatives have a dynamical nature that allows for solutions to these problems. All other alternatives essentially face the problem of explaining why there is no cosmological constant – perhaps a slightly less daunting task than explaining why it is tiny.

3.1.1 Λ and observations

The compatibility between theoretical predictions in the framework of Λ CDM and observations of the cosmic microwave background is impressive – as shown in figure 3.1. It no longer surprises when new data from better experiments show compatibility with Λ CDM. The real surprise would be evidence not supporting this model. However, a number of considerations encourage the investigation of alternative models. First, alternatives are very important to avoid bias in the data analysis, which could arise because we know what we expect to find. Second, the cosmological constant has been on the table decades now, and the theoretical challenges persist. Most importantly, as previously mentioned, the allowed ranges of some cosmological parameters are still fairly wide, especially for parameters in the dark energy sector beyond Λ CDM.

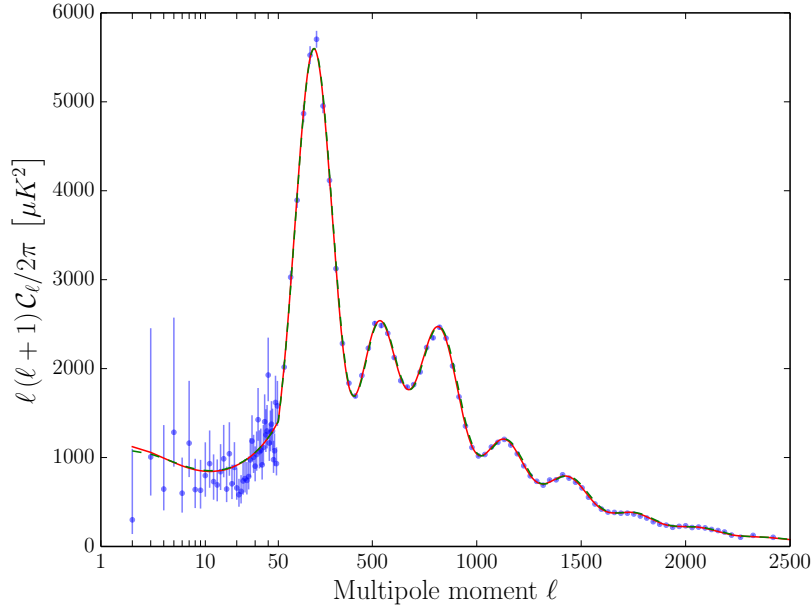


Figure 3.1: This figure is similar to figure 2.2. The red line shows a theoretical calculation of the spectrum using CAMB and the best-fit parameters from Planck for a Λ CDM model (see table 5 of Ade et al. (2013)). The green dashed line shows the theoretical calculations if the present day hubble parameter is changed to 60km/s/Mpc and the dark energy equation of state to $w_{de} = -0.8$.

3.2 Quintessence models

Quintessence models are canonical scalar field models. These models get their name because they often result in an extra long-range force mediated by the associated scalar particle – a fifth force. Quintessence is inspired by the most basic models of inflation, where a slow-rolling scalar field drives the rapid (and accelerated) expansion of the early universe. We will get back to the meaning of the term slow-rolling. Both standard inflation and quintessence models gain credibility from the discovery of the Higgs boson at the Large Hadron Collider at CERN, since the Higgs boson is the only fundamental scalar particle known to exist. See Copeland et al. (2006) for a review of Quintessence and other dark energy models.

In quintessence, some unknown mechanism ensures that the vacuum energy is zero and the scalar particle associated with quintessence is sufficiently light such that the universe has not settled at the vacuum state yet. As a result, the scalar field dominates the energy density on large scales. Starting from a canonical Lagrangian for a scalar field, i.e., kinetic minus potential energy, and the variation principle, one can derive the

stress-energy tensor for the scalar field,

$$T_{\mu\nu} = g_{\mu\nu} \left[-\frac{1}{2} (\nabla\phi)^2 - V(\phi) \right] + \partial_\mu\phi\partial_\nu\phi. \quad (3.3)$$

Continuing to take the temporal part and the trace of the spatial part of the stress-energy tensor, we find the leading terms in the energy and pressure density of the scalar field,

$$\rho_\phi = \frac{1}{2}\dot{\phi}^2 + V(\phi), \quad P_\phi = \frac{1}{2}\dot{\phi}^2 - V(\phi), \quad w_\phi \equiv \frac{P_\phi}{\rho_\phi} = \frac{\frac{1}{2}\dot{\phi}^2 - V(\phi)}{\frac{1}{2}\dot{\phi}^2 + V(\phi)}. \quad (3.4)$$

From the previous chapter, we know that for the scalar field to act as dark energy, the equation of state must be sufficiently negative. Thus it is clear, from equation (3.4), that the potential energy must dominate the kinetic energy of the quintessence field. In the limit where the potential energy completely dominates the kinetic, the background evolution mimics that of a Λ CDM model. Note, however, that the equation of state is time dependent in these models – unlike for the cosmological constant. The equation of motion for the field can be found by inserting the energy and pressure density into the continuity equation. The resulting equation is called the Klein-Gordon equation,

$$\ddot{\phi} + \frac{\partial V(\phi)}{\partial\phi} + 3H\dot{\phi} = 0. \quad (3.5)$$

This second order differential equation involves a Hubble friction term and a driving term that is the derivative of the potential, i.e., to keep the kinetic energy low, the potential needs to be a very flat function of the field. The low kinetic energy is why the quintessence field is said to be slow-rolling.

Further analysis shows that the mass of the particle associated with the scalar field is given by the curvature of the potential, i.e., $m_\phi \equiv \partial^2 V(\phi)/\partial\phi^2$. The flat potential is equivalent to a very low mass of the scalar particle, i.e., $m_\phi \sim H \sim 10^{-31}$ eV. This gives rise to two issues. First, any coupling to other sectors of the standard model would lead to a long range fifth force mediated by the light scalar particle. A fifth force like this is heavily constrained by, e.g., tests of the dynamics in the solar system. Second, it is very difficult to protect the low mass from quantum corrections.

Some quintessence models show appealing properties, but they all suffer from a need of finetuning to fix the problems discussed above or to get the correct present energy density of dark energy. A model inspired by particle physics deal with the problems through a symmetry in the potential that protects the mass of the scalar particle.

3.2.1 A model inspired by particle physics

From the point of view of quantum field theory, the only natural way to have an ultra-low mass scalar particle is a pseudo-Nambu-Goldstone boson – this model is discussed

in details in Frieman et al. (1995) and Kaloper & Sorbo (2006). The particle mass is kept low by an approximately global symmetry in the Lagrangian. The theory involves a spontaneous symmetry-breaking scale, f , and an explicit symmetry-breaking scale, μ . Below the energy scale f , found to be of the order of the Planck scale (10^{18} GeV), ϕ is the phase of a complex field Φ in a Mexican hat potential,

$$V_{\Phi} = \lambda \left(|\Phi|^2 - \frac{f^2}{2} \right)^2. \quad (3.6)$$

Below the scale $\mu \sim 10^{-3}$ eV, the $U(1)$ rotational symmetry of this potential is broken. This corresponds to a small tilt of the potential, leading to a unique minimum of the potential. After the symmetry has been explicitly broken the potential has the form

$$V(\phi) = \mu \left[1 + \cos\left(\frac{\phi}{f}\right) \right]. \quad (3.7)$$

Cosmological considerations lead to the energy scales quoted above, which also seem reasonable from a particle physics point of view. The mass of the pseudo scalar particle is tiny, $m_{\phi} = \mu^2/f \sim 10^{-33}$ eV. In addition to the protection of the particle mass, the symmetry provides a natural way to keep couplings to the standard model low, explaining why they have not yet been detected – if present.

3.3 Modified gravity

The explanations of the accelerated expansion discussed so far have modified the right hand side of the Einstein equations (2.3), i.e., the stress-energy tensor, by adding new content to the universe. In truth, the Λ -term of the cosmological constant can appear on both sides of the Einstein equations and thus be thought of as either additional content or a property of space-time. A different approach is to say that general relativity is not the correct large-scale description of gravity – this approach is commonly referred to as modified gravity. General relativity is very well tested on astrophysical scales, solar system scale, as well as laboratory scale, so any modified gravity model must reproduce general relativity on these scales. Changing the metric part of the Einstein equations does not resolve the problem with the large vacuum energy, so modified gravity models also need to explain why there is essentially no vacuum energy. Most models assume that this is the case due to some unknown mechanism – as with the scalar field models.

3.3.1 $f(R)$ gravity

An example of a family of modified gravity models is the $f(R)$ -models. In these models the standard Einstein-Hilbert action of general relativity is modified by adding a function of the Ricci scalar, i.e.,

$$\mathcal{S} = \frac{1}{16\pi G} \int d^4x \sqrt{-g} R \quad \rightarrow \quad \mathcal{S} = \frac{1}{16\pi G} \int d^4x \sqrt{-g} [R + f(R)], \quad (3.8)$$

where g is the determinant of the metric tensor $g_{\mu\nu}$. A contribution with the Lagrangian describing the contents of the universe minimally coupled to metric should be added to this action. Varying the action with respect to the metric and using the Friedmann-Robertson-Walker metric ultimately leads to new versions of the Friedmann equations. In a flat universe with $f(R)$ gravity, the Friedmann equations take the form,

$$H^2 + \frac{f(R)}{6} - \frac{1}{a} \frac{d^2 a}{dt^2} f_R(R) + H \frac{df_R(R)}{dt} = \frac{8\pi G}{3} \sum_{\alpha} \rho_{\alpha}, \quad (3.9)$$

$$\frac{1}{a} \frac{d^2 a}{dt^2} - f_R(R) H^2 + \frac{f(R)}{6} + \frac{1}{2} \frac{d^2 f_R(R)}{dt^2} = -\frac{4\pi G}{3} \sum_{\alpha} (\rho_{\alpha} + 3P_{\alpha}), \quad (3.10)$$

where $f_R(R)$ is the derivative of $f(R)$ with respect to R . With an appropriate choice of $f(R)$, late time cosmic acceleration can occur. Note, general relativity is recovered in the limit $f(R) = f_R(R) = 0$ as required.

With a conformal transformation of the metric, the gravitational part of the action can be converted to the Einstein-Hilbert action. The price of this transformation is a non-minimal coupling between the contents of the universe and the metric and the introduction of a new scalar degree of freedom acting as dark energy in a manner analogous to that seen in the scalar field models, see, e.g., Silvestri & Trodden (2009). In fact, it is true for most modified gravity models that they essentially corresponds to adding a new scalar degree of freedom, see Carroll et al. (2004), and they, therefore, suffer the same issues as scalar field models. Different mechanisms, such as screening, can be used avoid the effects of the force mediated by the new light scalar degree, see, e.g., Hu & Sawicki (2007). The bottomline is that modified gravity models, as the scalar field models, required a large degree of fine tuning to coincide with observations.

3.4 A fluid model

The sections above comprise an exhausting but by no means exhaustive list of dark energy models. The growing length of this list is one of the motivations behind the main focus of my Ph.D. – it calls for tools to tell the models apart. The ultimate goal is to find observable quantities, where the expectations of the different models differ as much as possible, because that makes it easier to distinguish them based on real observations of the universe. Instead of analysing the different models in detail, we adopt an effective model of dark energy that covers a large range of models with respect to the observables of our interest.

In our effective model, dark energy is a generic fluid with no anisotropic stress. Thus, the dark energy fluid is completely described by an equation of state, w_{de} , and a sound speed, $\hat{c}_{s,\text{de}}$, in the rest frame of the fluid. In a physical fluid model, the equation of state and the sound speed are typically tied together, but we choose to view them as independent parameters to cover a larger range of models. This constitutes a problem

that will be discussed in chapter 12, since some combinations of w_{de} and $\hat{c}_{s,\text{de}}$ result in the breaking of energy conditions of general relativity. In some of the work presented in part III, the equation of state is taken to be constant in time, while in the more recent work it is taken to be a linear function of the scale factor. The sound speed is always taken to be constant in time. See, e.g., Bean & Dore (2004); Ballesteros & Lesgourgues (2010); Anselmi et al. (2011); Creminelli et al. (2010) for discussions of similar or related models.

Many quintessence models can effectively be described by this model, with a time-varying equation of state determined by the potential, i.e., through equation (3.4), and a sound speed matching the speed of light. Some modified gravity models are also covered by our model in a similar fashion.

This model allows for dark energy to have over- and under-densities at different spatial locations in universe. The over- and under-densities in dark energy could potentially imprint a unique signature in the distribution of ordinary and dark matter in the universe. Quantifying this unique signature is one of the main goals of this dissertation.

4

DARK MATTER

Although the main focus of this dissertation is on the properties of dark energy, some of the analysis tools developed during the project can be and have been used to gain information about dark matter. Dark matter is characterised by no electromagnetic interactions and, can as such not be directly detected by our conventional observational techniques, i.e., detecting light from an emitting source. A detailed discussion of dark matter detection is beyond the scope of this chapter. We just note that the existence of dark matter is established through the gravitational interaction, e.g., rotation curves of spiral galaxies, structure formation, gravitational lensing. We will discuss the details and cosmological implications of one dark matter candidate – neutrinos. However, two other models deserve mention as well: The weakly interacting massive particles or WIMPs for short, and Axions.

WIMPs interact only via the weak interaction and gravity. In the early universe, WIMPs are abundant and kept in thermal equilibrium by pair production and annihilation. When the temperature of the universe drops below the mass of the WIMP, pair production stops and annihilation drives the abundance of WIMPs down until the annihilation rate drops below the expansion rate of the universe. At this point, the interactions freeze out just as we see in the processes leading to Big Bang nucleosynthesis. The WIMPs are thought to be non-relativistic at the time of freeze out, so they are a cold dark matter candidate. From matching the annihilation rate with the expansion rate, we can estimate the number density of WIMPs at freeze out, which can then be translated into an estimate of the present energy density of WIMPs. Adopting a particle mass corresponding to the electroweak scale, i.e., a few GeV to a few TeV, and a typical electroweak cross section for the annihilation process, the estimated energy density of WIMPs, Ω_X , is of order unity today – strikingly close to the observed dark matter density in the universe. If WIMPs exist, they can potentially be detected through their weak interaction – either directly or indirectly. Direct dark matter detection experiments search for rare scattering events between dark matter particles and a target nucleus in the detector, while indirect detection experiments search for the products of dark matter annihilation in, e.g., the galactic halo.

Axions are related to the strong CP (charge+parity) problem – a fine-tuning problem of Quantum Chromodynamics (QCD). The true vacuum of QCD is a superposition

4. Dark matter

of a number of degenerate states, and as a consequence, the neutron is expected to have an electric dipole moment unless parameters are fine-tuned. This problem can be solved by imposing the Peccei-Quinn symmetry on the QCD Lagrangian, see Peccei & Quinn (1977). The axion is the pseudo-Nambu-Goldstone boson associated with the spontaneous breaking of the Peccei-Quinn symmetry – quite similar to the dark energy model in section 3.2.1.

Axions can be produced in multiple ways – for the purpose of this dissertation, two different production mechanisms are worth mentioning. First, we have thermal production, where the axions decouple from the primordial plasma when the interaction rate keeping them in thermal equilibrium drops below the Hubble rate. The axions that are left will act as hot dark matter today. Second, we have misalignment production. Here, we shall focus on the scenario, where the Peccei-Quinn symmetry is broken before inflation, i.e., the axion field is homogeneous over the visible universe after inflation. Axions produced via misalignment act as cold dark matter today.

The axion potential is given by

$$V_a = f_a^2 m_a^2 (T) \left[1 - \cos \left(\frac{\theta_a}{f_a} \right) \right], \quad (4.1)$$

where θ_a is the axion field, m_a is the axion mass, and f_a is related to the energy scale at which the Peccei-Quinn symmetry is broken. The axion is a scalar particle, so the evolution of the field is governed by the Klein-Gordon equation,

$$\frac{d^2 \theta_a}{dt^2} + 3H \frac{d\theta}{dt} + \frac{dV_a}{d\theta_a} = 0. \quad (4.2)$$

The dynamics of the axion field can be divided into three regimes. As long as the Compton wavelength of the axion is outside the horizon, the axion is effectively massless and the Hubble friction term in equation (4.2) forces the axion field to remain constant. Once the axion mass becomes of the order of the Hubble expansion rate, $m_a \sim 3H$, the axion mass becomes relevant, and the axion field begins to roll down the potential. Because of the kinetic energy of the axion rolling down the potential, it will overshoot the minimum and eventually begin to oscillate. Expanding the potential around the minimum shows that it is harmonic, so the oscillations will after a few oscillations become harmonic and the axion will behave as non-relativistic matter and the axion number density per comoving volume is conserved.

If the results of BICEP2 holds with regard to the scale of inflation, then the scenario where the Peccei-Quinn symmetry is broken before inflation is ruled out, see, e.g., Visinelli & Gondolo (2014). For further reading on axions, see Sikivie (2008). The numerical tools presented in this dissertation can be applied to axion models as well as dark energy models, we are currently working on a paper that is very close to completion on this topic, Archidiacono et al. (2014).

4.1 Neutrinos

Neutrinos stand out among the dark matter candidates, since laboratory experiments let us know that they actually exist. For now we still refer to them as a *candidate*, because we have yet to see if they can make up all the dark matter observed in the universe. In the next section, we will learn why all the dark matter cannot be neutrinos. The existence of neutrinos was proposed in order for beta decays to conserve energy and momentum, and they were indirectly detected as missing energy in beta decay processes. As the WIMPs, neutrinos interact only via the weak interaction and gravitation, i.e., they are by definition dark matter. Three different flavours of neutrinos are known to exist, one for each of the charged leptons in the standard model of particle physics: Electron, muon, and tau neutrinos - each with a corresponding anti-neutrino.

Neutrinos have interesting particle physical properties and one worth mentioning is the neutrino oscillations. This phenomenon arises because the neutrino flavour eigenstates of the weak interaction are different from the neutrino mass eigenstates. Neutrinos are produced via the weak interaction in a flavour eigenstate and their presence is indirectly detected via the weak interaction. When neutrinos propagate, they do so as mass eigenstates, and these are linear combinations of the flavour eigenstates. This opens the possibility that, e.g., a neutrino created as an electron neutrino can be detected as a muon neutrino after propagating through space. The probability of this occurring depends on the squared mass difference between the different mass eigenstates. Thus, neutrino oscillation experiments probe the squared mass differences in the neutrino mass hierarchy. Current data allow two different mass hierarchies: The normal hierarchy with two light neutrinos and one heavier neutrino, or the inverted hierarchy with one light neutrino and two heavier neutrinos. The absolute mass scale of the neutrinos has yet to be measured, but assuming that the lightest neutrino is massless, a lower bound on the sum of the neutrinos masses can be inferred. This lower bound is $\sum m_\nu \simeq 0.06$ (0.10) eV in the normal (inverted) hierarchy.

4.1.1 Neutrinos and cosmology

Cosmology puts the strongest upper bound on the sum of neutrino masses through measurements of the CMB and the baryon acoustic oscillations. The current upper bound is $\sum m_\nu < 0.230$ eV at 2σ in a standard Λ CDM model extended only with massive neutrinos, see Ade et al. (2013). It is remarkable how studying the large scales of the universe can tell us about the small scales of particle physics. Note, that the bounds can weaken if the analysis includes additional parameters, e.g., the equation of state of dark energy, which is degenerate with the sum of neutrino masses as we will see in chapter 11.

We will now investigate how cosmology is sensitive to massive neutrinos. The main effect of massive neutrinos on the background evolution is to change the transition be-

tween radiation and matter domination, and on the level of perturbations the main effect is suppression of growth. Just as the cosmic microwave background, it is predicted that the universe contains a cosmic neutrino background that has yet to be observed. The neutrinos decouple from the plasma in the early universe before the photons, because neutrinos only interact weakly. As seen before, the neutrinos decouple when the rate of the interaction that keeps them in thermal equilibrium with the plasma drops below the Hubble expansion rate. A simple estimate shows that this decoupling happens around a temperature of 1 MeV, so neutrinos with a mass in the eV range are highly relativistic at this time. Both before and after decoupling, the temperature of neutrinos scale in the same way as the temperature of photons. Shortly after decoupling, however, the temperature drops below the electron mass and annihilation of electron-positron pairs reheats the photons that are still coupled to the plasma. If the neutrinos are completely decoupled and the entropy of the plasma is conserved, then the temperature of the cosmic neutrino background is related to that of the cosmic microwave background after reheating by

$$T_\nu = \left(\frac{4}{11}\right)^{1/3} T_\gamma. \quad (4.3)$$

So the present temperature of the neutrino background is $T_{\nu,0} \simeq 1.95$ K. In reality, the neutrinos are not completely decoupled, which gives a small correction to the relation above.

As long as the neutrino are relativistic, they contribute to the energy density of radiation. For relativistic species, the energy density is proportional to T^4 , i.e., the total radiation energy density is

$$\rho_r = \rho_\gamma + \rho_\nu = \left(1 + \frac{7}{8} \left(\frac{4}{11}\right)^{4/3} N_{\text{eff}}\right) \rho_\gamma, \quad (4.4)$$

where the factor of $7/8$ comes from the fact that neutrinos are fermions, and N_{eff} is the effective number of neutrinos. With three standard neutrinos, we have $N_{\text{eff}} = 3.046$, where the deviation from three comes from the non-instantaneous neutrino decoupling. This energy density fixes the expansion rate during radiation domination and the time of transition to matter domination. The effect of changes in N_{eff} on the CMB is seen on the left panel of figure 4.1. N_{eff} different from the standard value can be realized in a range of models, e.g., models with sterile neutrinos or low reheating temperature, for larger and smaller values of N_{eff} , respectively.

After decoupling, the neutrinos act as a collisionless fluid. The neutrinos free-stream with an average thermal velocity, v_{th} – we define the free-streaming length as,

$$\lambda_{\text{fs}} = 2\pi \sqrt{\frac{2}{3}} \frac{v_{\text{th}}}{H}. \quad (4.5)$$

The effect of free-streaming is to damp neutrino density fluctuations on small scales, because neutrinos cannot be confined by the gravitational potential on scales smaller

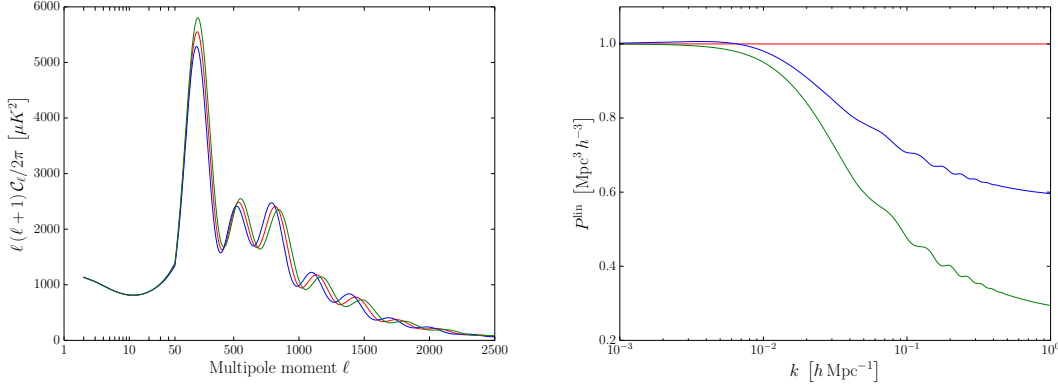


Figure 4.1: The left panel shows the effect of changing N_{eff} on the CMB angular temperature spectrum. The blue, red and green lines correspond to $N_{\text{eff}} = 2.046$, $N_{\text{eff}} = 3.046$, and $N_{\text{eff}} = 4.046$, respectively. The right panel shows the effect of changing $\sum m_\nu$ on the linear matter power spectrum at $z = 0$. The total amount of dark matter, $\Omega_{\text{cdm}} + \Omega_\nu$, is kept constant. The red, blue and green lines correspond to $\sum m_\nu = 0$ eV, $\sum m_\nu = 0.6$ eV, and $\sum m_\nu = 1.2$ eV. In both panels, all other cosmological parameters are kept to the values of Ade et al. (2013).

than the free-streaming length. The reason is that the average thermal velocity of the neutrinos is larger than the escape velocity in the gravitational potential wells. On scales larger than the free-streaming length, the neutrinos essentially behave as cold dark matter, when they become non-relativistic.

The effect of massive neutrinos on the present linear matter power spectrum for models with different sums of neutrinos masses, can be seen on the right panel of figure 4.1. The models in the figure all have the same present dark matter density. Most of the effect is due to a slower growth rate of cold dark matter perturbations on small scales, because of the absence of gravitational attraction from the neutrinos on scales below the free-streaming scale.

The relative suppression of the linear power spectrum is $\Delta P(k)/P(k) \simeq -8f_\nu$, where $f_\nu \equiv \Omega_\nu/\Omega_m$ is the fraction of non-relativistic matter in the form of neutrinos. The density fraction of massive neutrinos is given by,

$$\Omega_\nu h^2 = \frac{\sum m_\nu}{94.1 \text{ eV}}. \quad (4.6)$$

The potential sensitivities of future observational probes toward the neutrino parameters discussed in this section are estimated in chapter 11.

Part II

THEORETICAL FRAMEWORK

5

COSMOLOGICAL PERTURBATION THEORY

The purpose of this chapter is to determine how the obvious deviations from complete homogeneity and isotropy evolve in the universe. The deviations from homogeneity are, for now, assumed to be small in the sense that they can be described by linear perturbation theory – an assumption that clearly breaks down at some point, e.g., the Earth cannot be considered a perturbation to the average density in the solar system and so on. As established in the previous chapter, we find ourselves in a flat universe. On that account, the discussion in this chapter will focus on perturbations in such a universe. We introduce a new time coordinate referred to as conformal time, $d\tau = dt/a$, and a dot will denote derivatives with respect to τ , i.e., $\dot{a} = da/d\tau$.

The most general perturbations can be divided into three categories: Scalar, vector, and tensor perturbations. Scalar perturbations are of interest as they source the structure formation in the universe. Vector perturbations decay in the early universe and are, as a result, of little interest. Finally, tensor perturbations correspond to gravity waves and can be of great importance. To this project, however, they are not. In linear perturbation theory, the three types of perturbations evolve independently, so it makes sense to consider only scalar perturbations. The next section deals with scalar perturbations on a flat Friedmann-Robertson-Walker background and follows discussions in Ma & Bertschinger (1995) closely.

5.1 Evolution equations

The first consideration in cosmological perturbation theory is the choice of a gauge to describe the perturbations. The two most common choices are the conformal Newtonian gauge and the synchronous gauge. The latter is the gauge chosen by most numerical codes, as it tends to be more well-behaved, numerically. Here, the conformal Newtonian gauge is chosen, since it is simple when considering scalar perturbations. In this gauge, the perturbed metric gives the line element,

$$ds^2 = a^2 \left[- (1 + 2\psi) d\tau^2 + (1 - 2\phi) dx^i dx_i \right], \quad (5.1)$$

where x_i are co-moving spatial, Cartesian coordinates, and ψ corresponds to the Newtonian gravitational potential satisfying the Poisson equation.

In addition to perturbing the metric, the energy-momentum tensor describing the contents in the universe should also be perturbed. Henceforth, barred quantities such as $\bar{\rho}_\alpha$ refer to background quantities. The energy density, ρ_α , and pressure, P_α , of a perturbed species are given by $\rho_\alpha = \bar{\rho}_\alpha + \delta\rho_\alpha$ and $P_\alpha = \bar{P}_\alpha + \delta P_\alpha$, respectively. Furthermore, we define the density contrast as $\delta_\alpha \equiv \delta\rho_\alpha/\bar{\rho}_\alpha$. To linear order, the contents can also have a peculiar velocity relative to that of the background, $v^i \equiv dx^i/d\tau$. With this, the energy-momentum tensor perturbed to linear order is given by

$$\begin{aligned} T_{0,\alpha}^0 &= -\rho_\alpha, \\ T_{i,\alpha}^0 &= (\bar{\rho}_\alpha + \bar{P}_\alpha) v_{i,\alpha} = -T_{0,\alpha}^i, \\ T_{j,\alpha}^i &= P_\alpha \delta_j^i + \Sigma_{j,\alpha}^i, \quad \Sigma_{i,\alpha}^i = 0, \end{aligned} \tag{5.2}$$

where δ_j^i is a Kronecker delta and Σ_j^i is an anisotropic shear perturbation to T_j^i . As previously stated, the Einstein equations dictate energy conservation in a covariant form, which leads to Euler equations for each separate fluid. We will return to these equations in the context of the spherical collapse model in the next chapter.

In the conformal Newtonian gauge, the linear Einstein equations in Fourier space are

$$\begin{aligned} 4\pi G a^2 \delta \tilde{T}_0^0 &= k^2 \tilde{\phi} + 3 \frac{\dot{a}}{a} \left(\dot{\tilde{\phi}} + \frac{\dot{a}}{a} \tilde{\psi} \right), \\ 4\pi G a^2 i k^j \delta \tilde{T}_j^0 &= k^2 \left(\dot{\tilde{\phi}} + \frac{\dot{a}}{a} \tilde{\psi} \right), \\ \frac{4\pi}{3} G a^2 \delta \tilde{T}_i^i &= \ddot{\tilde{\phi}} + \frac{\dot{a}}{a} \left(\dot{\tilde{\psi}} + 2\dot{\tilde{\phi}} \right) + \left(2 \frac{\ddot{a}}{a} - \frac{\dot{a}^2}{a^2} \right) \tilde{\psi} + \frac{k^2}{3} (\tilde{\phi} - \tilde{\psi}), \\ -12\pi G a^2 \left(\hat{k}_i \hat{k}^j - \delta_i^j / 3 \right) \tilde{\Sigma}_j^i &= k^2 (\tilde{\phi} - \tilde{\psi}), \end{aligned} \tag{5.3}$$

where $T_j^i = \sum_\alpha T_{j,\alpha}^i$. From the last equation, it is evident that if the universe contains only perfect fluids such that $\Sigma_j^i = 0$, then $\phi = \psi$. The above equations govern the evolution of the metric and energy-momentum perturbations through general relativity, i.e., when the only interaction is gravity. For later use, we introduce the parameters θ and σ as the divergence of the peculiar velocity and the anisotropic stress,

$$\begin{aligned} \tilde{\theta} &\equiv i k^j \tilde{v}_j = i k^j \delta \tilde{T}_j^0 / (\bar{\rho} + \bar{P}) \\ \tilde{\sigma} &\equiv - \left(\hat{k}_i \hat{k}^j - \delta_i^j / 3 \right) \tilde{\Sigma}_j^i / (\bar{\rho} + \bar{P}) \end{aligned} \tag{5.4}$$

If the contents of the universe interact by other means than gravity, e.g., tight-coupling in the photon-baryon plasma prior to recombination, we need a phase space description of the energy-momentum tensor. Let P_i denote the conjugate momenta for x^i , i.e., the spatial part of the four-momentum, P_μ . For the remainder of this section, P refers to momentum. The evolution of x^i and P_i is, in general, determined by Hamilton's equations. In the absence of metric perturbations, Hamilton's equations imply that

the P_i 's are constant indicating that proper momenta redshift as a^{-1} . The energy-momentum tensor depends on the integral over the distribution function, $f(x^i, P_j, \tau)$,

$$T_{\mu\nu} = \int dP_1 dP_2 dP_3 (-g)^{-1/2} \frac{P_\mu P_\nu}{P^0} f(x^i, P_j, \tau). \quad (5.5)$$

The phase space distribution is conveniently written as a zeroth order distribution plus a perturbation,

$$f(x^i, P_j, \tau) = f_0(x^i, P_j, \tau) [1 + \Psi(x^i, P_j, \tau)], \quad (5.6)$$

where f_0 is the Fermi-Dirac or Bose-Einstein distribution for fermions and bosons, respectively. Furthermore, f_0 only depends on the norm of the momentum vector. The evolution of the distribution function can be determined through the Boltzmann equation,

$$\mathbf{L}[f] = \mathbf{C}[f], \quad (5.7)$$

where \mathbf{L} is the Liouville operator describing the evolution of the phase space volume, while \mathbf{C} is the collision operator describing the non-gravitational interactions with other particle species. In the case of neutrinos for instance, the Boltzmann equation leads to an infinite Boltzmann hierarchy of equations, which is typically truncated in some approximation scheme.

For a given cosmological model, one can use Boltzmann codes such as CLASS¹ (Blas et al. (2011)) or CAMB² (Lewis et al. (2000)) to solve the linearized Einstein and Boltzmann equations for the relevant particle species. The outputs of these Boltzmann codes are typically the power spectrum of the CMB temperature and polarization anisotropies and the power spectrum of the distribution of the density fluctuations. The next section is devoted to a discussion of the statistical properties of these density fluctuations. We will return to the CMB anisotropies later.

5.2 Statistical properties of the density fluctuations

When considering the statistical properties of the density field, a useful quantity is the Fourier transform of the density contrast,

$$\tilde{\delta}(\mathbf{k}) = \frac{1}{(2\pi)^{3/2}} \int d^3x \delta(\mathbf{x}) e^{i\mathbf{k}\cdot\mathbf{x}}, \quad (5.8)$$

where some cut-off scale, set to the largest significant scale, is introduced to make the integral over d^3x finite – typically this would be the size of the horizon or larger depending on the context. The inverse Fourier transform is

$$\delta(\mathbf{x}) = \frac{1}{(2\pi)^{3/2}} \int d^3k \tilde{\delta}(\mathbf{k}) e^{-i\mathbf{k}\cdot\mathbf{x}}. \quad (5.9)$$

¹<http://class-code.net>

²<http://camb.info>

The physical observable, and therefore the quantity of interest, is actually the density field smoothed on some resolution scale, R ,

$$\delta(\mathbf{x}, R) \equiv \int d^3x' W(|\mathbf{x}' - \mathbf{x}|, R) \delta(\mathbf{x}'), \quad (5.10)$$

where $W(|\mathbf{x}' - \mathbf{x}|, R)$ is called the window function and by dimensional analysis has the dimension of inverse volume. Normalizing the window function such that,

$$\int d^3x W(x, R) = 1, \quad (5.11)$$

determines the volume, V , associated with the window function. Roughly speaking, the smoothing process returns the average density fluctuation within a region of volume V . The smoothing scale corresponds to a mass given by the mean density times the volume, i.e., $M = \bar{\rho}V$. The Fourier transform of the smoothed density field is

$$\tilde{\delta}(\mathbf{k}, R) \equiv \tilde{W}(\mathbf{k}, R) \tilde{\delta}(\mathbf{k}), \quad (5.12)$$

where $\tilde{W}(\mathbf{k}, R)$ is the Fourier transform of the window function. The most important window functions are those which are top-hat functions in either real space or Fourier space. For a real-space top-hat, the window function and its, Fourier transform are

$$W(x, R) = \begin{cases} \frac{3}{4\pi R^3} & \text{for } x \leq R \\ 0 & \text{for } x > R \end{cases}, \quad (5.13)$$

$$\tilde{W}(k, R) = \frac{3[\sin(kR) - kR \cos(kR)]}{(kR)^3},$$

while a Fourier space top-hat is described by,

$$W(x, R) = \frac{3}{4\pi R^3} \frac{3[\sin(xR^{-1}) - xR^{-1} \cos(xR^{-1})]}{(xR^{-1})^3},$$

$$\tilde{W}(k, R) = \begin{cases} 1 & \text{for } k \leq 2\pi R^{-1} \\ 0 & \text{for } k > 2\pi R^{-1} \end{cases}. \quad (5.14)$$

For a real-space top-hat, the associated volume is clearly $4\pi R^3/3$. This window function suffers from the fact that it leads to power on all scales in Fourier space, as seen when combining equations (5.12) and (5.13). This is obviously not an issue with the Fourier-space top-hat, but this window function has no well-defined volume. When using a Fourier-space top-hat, the volume is taken to be the volume of a real-space top-hat with radius R , i.e., $4\pi R^3/3$.

The initial conditions or primordial density fluctuations are assumed to be well described by a statistically homogeneous and isotropic Gaussian random field, and in linear perturbation theory, the fluctuations will remain a Gaussian random field. These two statistical properties of the density fluctuations dictate certain properties of the two-point correlation function, $\xi(\mathbf{x}_1, \mathbf{x}_2)$, of the perturbations. Homogeneity renders the

two-point correlation function invariant under translations and ξ is therefore a function of the separation vector of \mathbf{x}_1 and \mathbf{x}_2 , i.e., $\mathbf{x}_1 - \mathbf{x}_2$, only. Isotropy dictates that ξ is invariant under rotations and hence a function solely of the distance between the two points, i.e., $r \equiv |\mathbf{x}_1 - \mathbf{x}_2|$.

Since the density fluctuation field is a Gaussian random field, the smoothed density field, which then represents a sum of Gaussian random variables, will also be a Gaussian random field. This permits calculation of the variance of the smoothed density field,

$$\begin{aligned} S \equiv \sigma^2(R) &= \langle \delta^2(\mathbf{x}, R) \rangle = \frac{1}{2\pi^2} \int d \ln k k^3 V^{-1} |\tilde{\delta}(k, R)|^2 \\ &= \int d \ln k \Delta^2(k) |\tilde{W}(k, R)|^2, \end{aligned} \quad (5.15)$$

where $\Delta^2(k)$ is the dimensionless matter power spectrum defined by,

$$\Delta^2(k) \equiv \frac{k^3}{2\pi^2} P^{\text{lin}}(k) \equiv \frac{k^3}{2\pi^2} V^{-1} \langle |\tilde{\delta}(k)|^2 \rangle. \quad (5.16)$$

$P^{\text{lin}}(k)$ is the power spectrum of the linear density fluctuations obtained with Boltzmann codes like CLASS and CAMB. The power spectrum is often written as the product of the primordial power spectrum, $\Delta_{\mathcal{R}}(k)$, and a transfer function, $T(k, \tau_1, \tau_2)$, squared. The variance of the density field smoothed on the 8 Mpc/ h scale, σ_8 , is often used as a measure of the fluctuations on cluster scales. When including more than one particle species in the power spectrum, the additive quantities are densities and not density contrasts, i.e.,

$$\delta_{\text{tot}} \equiv \frac{\sum_{\alpha} \rho_{\alpha} - \sum_{\alpha} \bar{\rho}_{\alpha}}{\sum_{\alpha} \bar{\rho}_{\alpha}} = \frac{\sum_{\alpha} (\rho_{\alpha} - \bar{\rho}_{\alpha})}{\sum_{\alpha} \bar{\rho}_{\alpha}} = \frac{\sum_{\alpha} \delta \rho_{\alpha}}{\sum_{\alpha} \bar{\rho}_{\alpha}}. \quad (5.17)$$

As established, the smoothed density field is a Gaussian random field with mean zero and variance given by equation (5.15), so the probability of $\delta(\mathbf{x}, R)$ lying between δ and $\delta + d\delta$ is

$$p(\delta, R) d\delta = \frac{1}{\sqrt{2\pi S}} e^{-\frac{\delta^2}{2S}} d\delta. \quad (5.18)$$

5.3 Angular power spectra

Since cosmologists observe the sky and sometimes lack precise information about the longitudinal direction, it is convenient to transform the Fourier power spectrum into the power spectrum of the angular correlation function. This section discusses this procedure working with the CMB as an example. We have already seen an angular power spectrum of the CMB on figures 2.2 and 3.1. A multipole expansion of the relative temperature anisotropies of the CMB takes the form,

$$\frac{\delta T(\theta, \phi)}{T_{\text{CMB}}} = \frac{T(\theta, \phi) - T_{\text{CMB}}}{T_{\text{CMB}}} = \sum_{\ell=0}^{\infty} \sum_{m=-\ell}^{\ell} a_{\ell m} Y_{\ell m}(\theta, \phi), \quad (5.19)$$

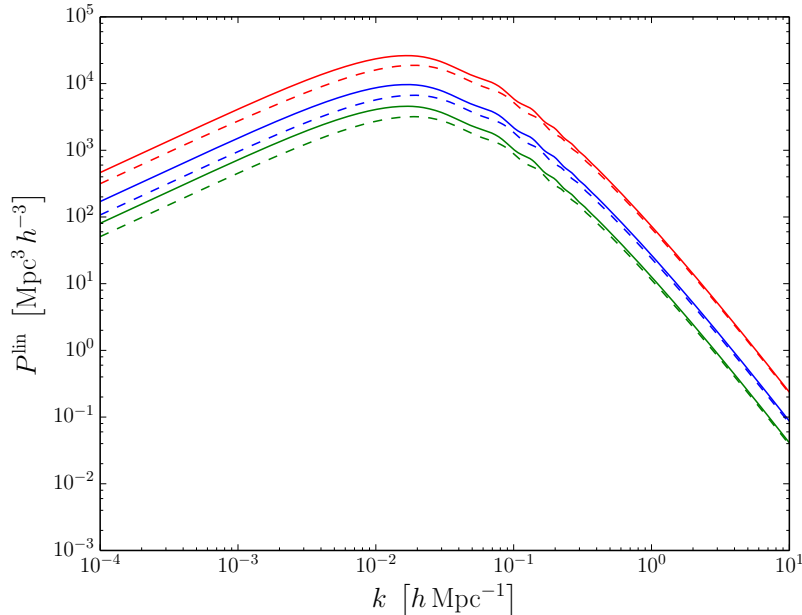


Figure 5.1: The linear matter power spectrum at redshifts $z = 0$ (red), $z = 1$ (blue), and $z = 2$ (green) calculated with CAMB (Lewis et al. (2000)). The solid lines show power spectra for the best-fit parameters from Planck for a Λ CDM model, see table 5 of Ade et al. (2013). The dashed lines show the calculations if the present day hubble parameter is changed to 60km/s/Mpc and the dark energy equation of state to $w_{\text{de}} = -0.8$. The point of the dashed lines is to show that two models which cannot be distinguished by one observational probe, can look completely different to another, see figure 3.1. An important feature in order to break degeneracies between parameters.

where the $Y_{\ell m}$'s are the spherical harmonics, which are orthonormal functions on a sphere. The coefficients $a_{\ell m}$ can thus be calculated as

$$a_{\ell m} = \int d\Omega Y_{\ell m}^*(\theta, \phi) \frac{\delta T(\theta, \phi)}{T_{\text{CMB}}}, \quad (5.20)$$

where $Y_{\ell m}^*$ denotes the complex conjugate of $Y_{\ell m}$. Y_{00} is constant, so a_{00} is proportional to the average of $\delta T(\theta, \phi)$ across the sky and, therefore, zero by definition. The dipole coefficients, $\ell = 1$, are contaminated by the Doppler effect of our motion relative to the surface of last scattering. Hence, we are only interested in $\ell \geq 2$. Note that the spherical harmonics are defined such that $a_{\ell m}^* = a_{\ell -m}$.

The temperature anisotropies, and therefore $a_{\ell m}$, are approximately Gaussian random variables (a discussion of non-Gaussianities will not be a part of this thesis), so we expect $\langle a_{\ell m} \rangle = 0$. Thus, the variance, $\langle |a_{\ell m}|^2 \rangle$, holds all the statistical information

about the coefficients. Since the $Y_{\ell m}$ s make an orthonormal set, the $a_{\ell m}$ are independent, i.e., $\langle a_{\ell' m'}^* a_{\ell m} \rangle = \delta_{\ell' \ell} \delta_{m' m} \langle |a_{\ell m}|^2 \rangle$, where $\delta_{\ell' \ell}$ and $\delta_{m' m}$ are Kronecker deltas. The index ℓ relates to the angular size of the anisotropies, while m relates to the orientation, so the isotropy of the universe tells us that the variance depends only on ℓ and not m . The angular power spectrum is defined as

$$\mathcal{C}_\ell = \langle |a_{\ell m}|^2 \rangle = \frac{1}{2\ell + 1} \sum_m \langle |a_{\ell m}|^2 \rangle. \quad (5.21)$$

The angular power spectrum relates to the variance of the temperature anisotropies via the equation

$$\begin{aligned} \left\langle \left(\frac{\delta T(\theta, \phi)}{T_{\text{CMB}}} \right)^2 \right\rangle &= \left\langle \sum_{\ell m} a_{\ell m} Y_{\ell m}(\theta, \phi) \sum_{\ell' m'} a_{\ell' m'}^* Y_{\ell' m'}^*(\theta, \phi) \right\rangle \\ &= \sum_{\ell m} \sum_{\ell' m'} Y_{\ell m}(\theta, \phi) Y_{\ell' m'}^*(\theta, \phi) \langle a_{\ell m} a_{\ell' m'}^* \rangle \\ &= \sum_{\ell} \mathcal{C}_\ell \sum_m |Y_{\ell m}(\theta, \phi)|^2 = \sum_{\ell} \frac{2\ell + 1}{4\pi} \mathcal{C}_\ell, \end{aligned} \quad (5.22)$$

where we have used the closure relation of the spherical harmonics. The average here is over an ensemble of realizations of the universe with the statistics of the angular power spectrum.

Obviously, we can only observe *one* realization of the universe. The observed angular power spectrum is

$$\mathcal{C}_{\ell, \text{obs}} = \frac{1}{2\ell + 1} \sum_m |a_{\ell m, \text{obs}}|^2. \quad (5.23)$$

Our expectation is that the observed spectrum matches the theoretical, i.e., $\langle \mathcal{C}_{\ell, \text{obs}} - \mathcal{C}_\ell \rangle = 0$. The variance of the difference between the two spectra, however, is not zero. We find,

$$\begin{aligned} \langle (\mathcal{C}_{\ell, \text{obs}} - \mathcal{C}_\ell)^2 \rangle &= \langle \mathcal{C}_{\ell, \text{obs}}^2 + \mathcal{C}_\ell^2 - 2\mathcal{C}_{\ell, \text{obs}} \mathcal{C}_\ell \rangle = \langle \mathcal{C}_{\ell, \text{obs}}^2 \rangle + \mathcal{C}_\ell^2 - 2\langle \mathcal{C}_{\ell, \text{obs}} \rangle \mathcal{C}_\ell \\ &= \frac{1}{(2\ell + 1)^2} \sum_{mm'} \langle a_{\ell m, \text{obs}} a_{\ell m, \text{obs}}^* a_{\ell m', \text{obs}} a_{\ell m', \text{obs}}^* \rangle - \mathcal{C}_\ell^2 \\ &= \frac{1}{(2\ell + 1)^2} \sum_{mm'} \left(\langle a_{\ell m, \text{obs}} a_{\ell m, \text{obs}}^* \rangle \langle a_{\ell m', \text{obs}} a_{\ell m', \text{obs}}^* \rangle \right. \\ &\quad + \langle a_{\ell m, \text{obs}} a_{\ell m', \text{obs}} \rangle \langle a_{\ell m, \text{obs}}^* a_{\ell m', \text{obs}}^* \rangle \\ &\quad \left. + \langle a_{\ell m, \text{obs}} a_{\ell m', \text{obs}}^* \rangle \langle a_{\ell m, \text{obs}}^* a_{\ell m', \text{obs}} \rangle \right) - \mathcal{C}_\ell^2 \\ &= \frac{\mathcal{C}_\ell^2}{(2\ell + 1)^2} \sum_{mm'} (1 + \delta_{m-m'} \delta_{m'-m} + \delta_{mm'} \delta_{m'm}) - \mathcal{C}_\ell^2 \\ &= \frac{2}{2\ell + 1} \mathcal{C}_\ell^2, \end{aligned} \quad (5.24)$$

where we have employed a relation for the average of products of even numbers of the $a_{\ell m}$ s, see Weinberg (2008). The cosmic variance reflects the fact that the sky *only* allows $2\ell + 1$ measurements of $a_{\ell m}$. This results in an inherent uncertainty in the comparison of observed and theoretical angular power spectra known as cosmic variance. Cosmic variance is important at low ℓ or large scales, where only a few values of $a_{\ell m}$ are accessible.

For theoretical calculations, the equations of perturbation theory are solved in Fourier space. Therefore, to compute a theoretical angular power spectrum, we need to relate the coefficients, $a_{\ell m}$, to the different Fourier modes of the perturbations. In a flat universe, we can take the Fourier transform of functions on a time slice, e.g., the time at which the CMB was released. For some function $f(\mathbf{x})$, we have the Fourier relation

$$f(\mathbf{x}) = \frac{1}{(2\pi)^{3/2}} \int d^3k \tilde{f}(\mathbf{k}) e^{-i\mathbf{k}\cdot\mathbf{x}}. \quad (5.25)$$

To proceed, we need the expansion of the plane wave in terms of the spherical harmonics,

$$e^{-i\mathbf{k}\cdot\mathbf{x}} = 4\pi \sum_{\ell m} (-i)^\ell j_\ell(kx) Y_{\ell m}(\hat{\mathbf{x}}) Y_{\ell m}^*(\hat{\mathbf{k}}), \quad (5.26)$$

where j_ℓ is the spherical Bessel function. We want the multipole expansion of f on a sphere, i.e., constant x .

$$\begin{aligned} a_{\ell m} &= \int d\Omega Y_{\ell m}^*(\hat{\mathbf{x}}) f(\mathbf{x}) = \frac{1}{(2\pi)^{3/2}} \int d^3k \int d\Omega Y_{\ell m}^*(\hat{\mathbf{x}}) \tilde{f}(\mathbf{k}) e^{i\mathbf{k}\cdot\mathbf{x}} \\ &= \sqrt{\frac{2}{\pi}} \int d^3k \sum_{\ell' m'} \int d\Omega Y_{\ell m}^*(\hat{\mathbf{x}}) \tilde{f}(\mathbf{k}) i^{\ell'} j_{\ell'}(kx) Y_{\ell' m'}(\hat{\mathbf{x}}) Y_{\ell' m'}^*(\hat{\mathbf{k}}) \\ &= \sqrt{\frac{2}{\pi}} (-i)^\ell \int d^3k \tilde{f}(\mathbf{k}) j_\ell(kx) Y_{\ell m}^*(\hat{\mathbf{k}}), \end{aligned} \quad (5.27)$$

where the orthonormality of the spherical harmonics has been utilized. The spherical Bessel functions, j_ℓ , are oscillating with decreasing amplitude as a function of the argument and have the first and largest peak around an argument of ℓ . Therefore, the $a_{\ell m}$ s get the largest contribution from Fourier modes, where $kx \sim \ell$. If $\tilde{f}(\mathbf{k})$ is a random variable, such as $\tilde{\delta}(\mathbf{k})$, then we have

$$\begin{aligned} \langle |a_{\ell m}|^2 \rangle &= \frac{2}{\pi} \int d^3k \int d^3k' \langle \tilde{f}(\mathbf{k}) j_\ell(kx) Y_{\ell m}^*(\hat{\mathbf{k}}) \tilde{f}^*(\mathbf{k}') j_\ell(k'x) Y_{\ell m}(\hat{\mathbf{k}}') \rangle \\ &= \frac{2}{\pi} \int d^3k \langle |\tilde{f}(\mathbf{k})|^2 \rangle j_\ell^2(kx) |Y_{\ell m}(\hat{\mathbf{k}})|^2. \end{aligned} \quad (5.28)$$

To get the angular power spectrum, we use equation (5.21),

$$\begin{aligned} C_\ell &= \frac{1}{2\ell + 1} \frac{2}{\pi} \sum_m \int d^3k \langle |\tilde{f}(\mathbf{k})|^2 \rangle j_\ell^2(kx) |Y_{\ell m}(\hat{\mathbf{k}})|^2 \\ &= \frac{1}{2\pi^2} \int d^3k V^{-1} \langle |\tilde{f}(\mathbf{k})|^2 \rangle j_\ell^2(kx). \end{aligned} \quad (5.29)$$

Inserting the Fourier transformation of the density perturbations and using the definition of the spatial power spectrum, we find

$$\mathcal{C}_\ell = 4\pi \int d \ln k \Delta^2(k) j_\ell^2(kx), \quad (5.30)$$

relating the spatial power spectrum to the angular power spectrum.

6

STRUCTURE FORMATION AND THE CLUSTER MASS FUNCTION

The aim of this chapter is to establish a way to quantify the effect of dynamical dark energy on structure formation in the universe. In the standard, hierarchical, cold dark matter paradigm of cosmological structure formation, structures form on all scales and galaxy formation occurs subsequently to the gravitational collapse of over-dense regions into virialized clusters or halos of dark matter. The baryons are bound in the potential wells of the dark matter halos and condense to form galaxies. In order to understand the formation and properties of galaxies, a detailed understanding of the properties and abundances of the dark matter halos is key. The abundances of dark matter halos can be quantified by the cluster mass function – also referred to as the halo mass function in literature. The cluster mass function is the number density of virialized objects per mass interval, i.e., the number of objects with mass between M and $M + dM$. The first two sections in this chapter are based on semi-analytical calculations of the cluster mass function, originally introduced by Press & Schechter (1974) and reviewed by Zentner (2007). These semi-analytic models fare remarkably well when comparing to N-body simulations.

6.1 Press-Schechter theory

The Press-Schechter theory uses the statistical properties of the density fluctuations to return a mass spectrum of virialised objects in the universe. As noted above, structures form on all scales in the hierarchical model. Furthermore, the variance, S , of the density fluctuations approaches infinity as the smoothing scale, R, M , approaches zero. The principal assumption in Press-Schechter theory is that over-dense regions will collapse and form a virialized object of mass M if the density contrast smoothed on the scale R , corresponding to M , exceeds some critical value, δ_c . Furthermore, it is assumed that the non-linearities introduced by the virialized objects do not affect the collapse of over-dense regions on larger scales.

The mass contained in a region, where the smoothed density contrast corresponds to the critical density contrast, δ_c , at a given redshift, represents an object of mass $M(R)$ that has virialized. The relationship between mass and smoothing scale is determined by the volume of the window function, see section 5.2. Smoothing the density contrast

on the scale of the size of the universe returns zero by definition, since δ is fluctuations around the mean density in the universe. From this, it follows that if $\delta(x, R) > \delta_c$ there exists some $R' > R$ such that $\delta(x, R') < \delta_c$. The cumulative probability for a region to have $\delta(x, R) > \delta_c$ corresponds to the fractional volume occupied by virialised object heavier than $M(R)$, $F(M)$. Integrating the probability in equation (5.18), with respect to the density contrast, from the critical density contrast to infinity yields,

$$\begin{aligned} F(M) &= \int_{\delta_c}^{\infty} p(\delta, R) d\delta = \frac{1}{\sqrt{2\pi S}} \int_{\delta_c}^{\infty} e^{-\frac{\delta^2}{2S}} d\delta \\ &= \frac{1}{\sqrt{\pi}} \int_{\delta_c/\sqrt{2S}}^{\infty} e^{-\mathcal{T}^2} d\mathcal{T} = \frac{1}{2} \operatorname{erfc}\left(\frac{\delta_c}{\sqrt{2S}}\right), \end{aligned} \quad (6.1)$$

where the substitution $\mathcal{T} = \delta/\sqrt{2S}$ has been applied and $\operatorname{erfc}(x)$ is the complementary error function. $F(M)$ gives the fraction of mass contained in virialised objects heavier than M , so as M decreases, more and more objects are included and in the limit of M going to zero, all the mass in the universe is included. Again, in the hierarchical model, S approaches infinity as M goes to zero. Thus, $F(M=0) = \operatorname{erfc}(0)/2 = 1/2$ and only half of the mass in the universe is contained in virialised objects. Press & Schechter (1974) noted the flaw in the theory and corrected it by multiplying with an ad hoc factor of 2. The flaw is closely connected to what is referred to as the cloud-in-cloud problem.

The cloud-in-cloud problem relates to the fact that if the smoothed density contrast of a given region is below the critical density contrast on smoothing scale R , there may exist an even larger smoothing scale, $R' > R$, at which $\delta(x, R') > \delta_c$. One would expect the larger volume to collapse upon the less dense region inside, forming a virialised object of mass $M(R')$. In order to solve the cloud-in-cloud problem, one must locate the largest smoothing scale at which the critical density contrast is exceeded. The excursion set theory that deals with this will be discussed in the next section.

6.2 Excursion set theory

The objective of the excursion set theory is to solve the cloud-in-cloud problem by determining the first up-crossing of the critical density when smoothing the density field on successively smaller scales, i.e., the largest scale at which the barrier is breached, see, e.g., Bond et al. (1991) or Peacock & Heavens (1990).

In the excursion set theory, we consider the perturbed density field computed in linear theory. Since the density contrast is a linear extrapolation of the initial density contrast, it is not restricted by $\delta \geq -1$. As in the approach of Press and Schechter, the density contrast field is smoothed on the scale R with some filter. The probability distribution in equation (5.18) is still valid, so for large R , the variance, $S \equiv \sigma^2(R)$, of the smoothed density field is well below the critical density contrast. Thus, the probability of $\delta(R)$ lying above δ_c is negligible. Due to the properties of the dimensionless linear matter power spectrum, S is a monotonically decreasing function of R and thus an injective

function. Since the mapping between R and S is an injection, it is common to refer to S as the smoothing scale. Now, the key is to compute the probability for the first up-crossing to occur at the smoothing scale R or equivalently S .

Starting the smoothing at small S (large R), where $\delta(S) \equiv \delta < \delta_c$, there is some probability distribution for arriving at smoothed density contrast $\delta + \Delta\delta$ after changing the smoothing scale by $\Delta S > 0$. In a general scenario, the determination of this probability distribution is non-trivial, since the probability may depend on both the step size, ΔS , and the value of the smoothed density field on other scales. For now, the special case of a Fourier space top-hat window function will be considered, since it is greatly simplified and leads to the familiar result of Press & Schechter (1974) without having to introduce the factor of 2 ad hoc.

For the sharp Fourier space filter, increasing S corresponds to including a set of independent Fourier modes in $\delta(S)$. These new modes are uncorrelated with previous modes and $\delta(S)$ is independent of the density field smoothed on larger scales. As a consequence, the probability of a change $\Delta\delta$ in response to the change in scale, ΔS , is Gaussian with zero mean and variance, $\langle (\Delta\delta)^2 \rangle = \Delta S$. The sequence $\delta(S_i)$ resulting from successive increments of S by ΔS_i , is referred to as a trajectory for $\delta(S)$. In this case, each trajectory will perform Brownian motion. The probability of a transition from δ to $\delta + \Delta\delta$ when increasing S to $S + \Delta S$ is given by,

$$\Pi(\delta + \Delta\delta, S + \Delta S) d(\delta + \Delta\delta) = \Psi(\Delta\delta, \Delta S) d(\Delta\delta), \quad (6.2)$$

where,

$$\Psi(\Delta\delta, \Delta S) d(\Delta\delta) = \frac{1}{\sqrt{2\pi\Delta S}} e^{-\frac{(\Delta\delta)^2}{2\Delta S}} d(\Delta\delta), \quad (6.3)$$

is the Gaussian transition probability. The possibility of crossing δ_c from below at scale S and subsequently crossing δ_c from above at scale $S' > S$, i.e., the cloud-in-cloud problem, has not been accounted for so far.

The probability distributions of δ for two successive steps are related by

$$\Pi(\delta, S + \Delta S) = \int \Psi(\Delta\delta, \Delta S) \Pi(\delta - \Delta\delta, S) d(\Delta\delta). \quad (6.4)$$

In the limit of taking small steps, the left hand side can be Taylor expanded around S and the distribution in the integrand around δ . Since $\langle (\Delta\delta)^2 \rangle = \Delta S$, an expansion to first order in ΔS requires an expansion to second order in $\Delta\delta$. The left hand side gives,

$$\Pi(\delta, S + \Delta S) \simeq \Pi(\delta, S) + \Delta S \frac{\partial \Pi(\delta, S)}{\partial S}, \quad (6.5)$$

while the distribution in the integrand gives,

$$\Pi(\delta - \Delta\delta, S) \simeq \Pi(\delta, S) - \Delta\delta \frac{\partial \Pi(\delta, S)}{\partial \delta} + \frac{1}{2} (\Delta\delta)^2 \frac{\partial^2 \Pi(\delta, S)}{\partial \delta^2}. \quad (6.6)$$

When inserting the latter into equation (6.4), the first term, being the integral over the entire transition probability, is of course unity. For the second term, the integral is over the transition probability multiplied by the change in δ , i.e. the average of $\Delta\delta$, $\langle\Delta\delta\rangle$. The third term gives an integral over the transition probability multiplied the change in δ squared, i.e., $\langle(\Delta\delta)^2\rangle$. The resulting equation is,

$$\Pi(\delta, S) + \Delta S \frac{\partial \Pi(\delta, S)}{\partial S} = \Pi(\delta, S) - \langle\Delta\delta\rangle \frac{\partial \Pi(\delta, S)}{\partial \delta} + \frac{1}{2} \langle(\Delta\delta)^2\rangle \frac{\partial^2 \Pi(\delta, S)}{\partial \delta^2}. \quad (6.7)$$

Remembering the statistical properties, $\langle\Delta\delta\rangle = 0$ and $\langle(\Delta\delta)^2\rangle = \Delta S$, this reduces to a diffusion or Fokker-Planck equation with no drift term,

$$\frac{\partial \Pi(\delta, S)}{\partial S} = \frac{1}{2} \frac{\partial^2 \Pi(\delta, S)}{\partial \delta^2}. \quad (6.8)$$

Solving this equation with appropriate boundary conditions returns the probability distribution for trajectories that do not exceed δ_c prior to smoothing scale S . The first boundary condition is that $\Pi(\delta, S)$ is finite as $\delta \rightarrow -\infty$ and the second is that $\Pi(\delta_c, S) = 0$, corresponding to removing the trajectory from the set, as it crosses the barrier. The initial conditions are chosen such that all trajectories start at $\delta(S_0) \equiv \delta_0$, i.e., $\Pi(\delta, S_0) = \delta_D(\delta - \delta_0)$ where $\delta_D(x)$ is the Dirac delta function.

Equation (6.8) is solved by applying a Fourier transform. The complete process is left for the reader, but, detailed hints can be found in appendix A. The solution is,

$$\Pi(\delta, S) = \frac{1}{\sqrt{2\pi(S-S_0)}} \left[e^{-\frac{(\delta-\delta_0)^2}{2(S-S_0)}} - e^{-\frac{(2\delta_c-\delta_0-\delta)^2}{2(S-S_0)}} \right]. \quad (6.9)$$

The first term accounts for the points above the barrier, while the second term accounts for the trajectories that have been removed after crossing the barrier at $S' < S$ but would have crossed below again. Choosing $S_0 = 0$ and $\delta_0 = 0$ corresponds to smoothing at the size of the ensemble. The fraction of trajectories that have crossed the barrier at or prior to the scale S is,

$$F(S) = 1 - \int_{-\infty}^{\delta_c} \Pi(\delta, S) d\delta = \operatorname{erfc}\left(\frac{\delta_c}{\sqrt{2S}}\right). \quad (6.10)$$

Again details are in appendix A. This result is similar to that of Press & Schechter (1974) with a natural introduction of the factor of 2. To arrive at the cluster mass function, we make the following considerations: The potential number of objects of mass M per volume is $\bar{\rho}/M$, while the fractional number of objects per mass interval is $|dF(M)/dM| dM$, so,

$$\frac{dn}{dM} dM = \frac{\bar{\rho}}{M} \left| \frac{dF(M)}{dM} \right| dM. \quad (6.11)$$

Inserting equation (6.10) yields,

$$\frac{dn}{dM} dM = \frac{\bar{\rho}}{M} \left| \frac{1}{\sqrt{\pi}} \frac{d}{d\mathcal{T}} \int_{\delta_c/\sqrt{2S}}^{\infty} e^{-t^2} d\mathcal{T} \right| \left| \frac{d\mathcal{T}}{dM} \right| dM = \frac{1}{\sqrt{\pi}} \frac{\bar{\rho}}{M} e^{-\frac{\delta_c^2}{2S}} \left| \frac{dt}{dM} \right| dM. \quad (6.12)$$

In the literature, it is common to introduce the critical density contrast in units of the standard deviation, $\sigma(R)$, $\nu = \delta_c/\sigma(R)$. The cluster mass function then takes the form

$$\frac{dn}{dM}dM = \sqrt{\frac{2}{\pi}} \frac{\bar{\rho}}{M^2} \nu \left| \frac{d \ln \nu}{d \ln M} \right| e^{-\frac{\nu^2}{2}} dM. \quad (6.13)$$

The excursion set has other applications than computing the cluster mass function, see Zentner (2007) for an overview. See Bond et al. (1991) and Maggiore & Riotto (2010) for two different approaches with a more realistic filter than a sharp Fourier space filter. A different filter introduces correlations between the different scales. Numerically, one can account for the this by the method of coloured noise, see Bond et al. (1991).

6.3 The spherical collapse model

This section presents the details of calculating the critical density contrast. One theoretical framework for calculating δ_c is the so called spherical collapse model. Starting with a spherically symmetric over-dense region of space in a flat background, we seek to track the evolution of size and density of this region. Qualitatively, what happens is that the region expands along with the background expansion of the universe at first, then it gradually decouples from the expansion and eventually re-collapses. In this simple model, the collapse results in a point of infinite density, but more on that later. We are interested in the spherical collapse with inhomogeneous dark energy, but as an introduction we analyse the collapse in an Einstein-de Sitter universe containing only matter. Including dark energy is one of the topics of chapters 9, 10, and 11.

Using Birkhoff's theorem, the spherically symmetric over-dense region can be treated as an isolated system, where the evolution is governed by the Friedmann equations and the continuity equation presented in chapter 2. Of the three equations, only two are independent, so we can use (2.4) and either the Friedmann equation (2.5) or the acceleration equation (2.6). We use the latter combination in chapters 9, 10, and 11, so for completeness the first combination is presented in this chapter.

The over-dense region is analogous to a positively curved universe containing only matter (Peebles (1980)). The evolution of the size of the region, i.e., the scale factor in the analogous universe, follows a parametric form similar to that of a fixed point on a generalized cycloid produced by rolling an ellipse along a straight line (Ryden (2003)),

$$R(\eta) = A(1 - \cos \eta), \quad t(\eta) = B(\eta - \sin \eta), \quad (6.14)$$

with $A^2 = GMB^3$, where M is the mass of the system. The collapse to a single point is complete when $\eta = 2\pi$ or at time $t_c = 2\pi B$. The maximum size of the region is $2A$ at the time $t = \pi B$. The mass of this isolated system is preserved throughout the evolution, so at t_c , this idealized system is obviously highly non-linear, as the density of the system, $\rho_m = 3M/4\pi R(\eta)^3$, approaches infinity.

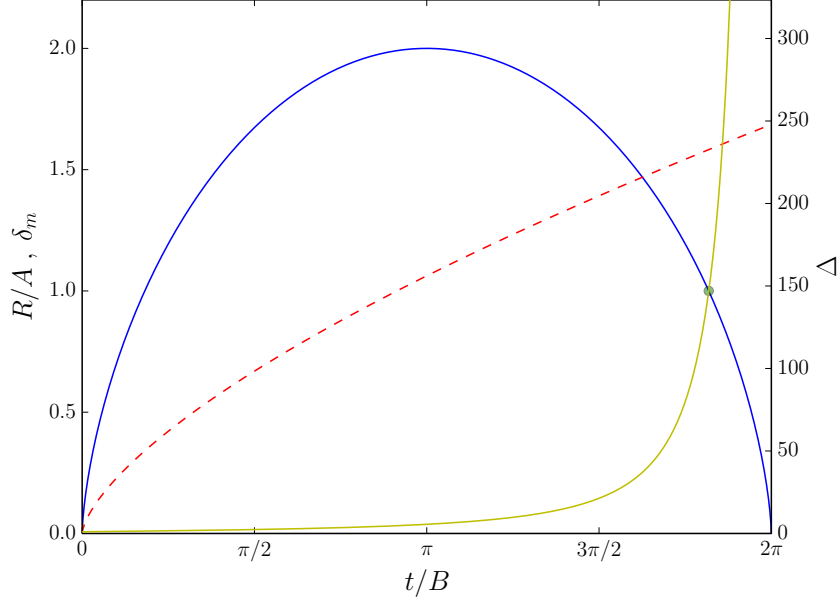


Figure 6.1: Evolution of a spherical over-dense region on a flat Einstein-de Sitter background in the spherical collapse model as a function of time. The blue curve shows radius, R , the red dashed curve shows the density contrast evolved with linear perturbation theory, δ_m , the yellow curve shows the density relative to the density of the background universe, Δ , and the green dot denotes the time of virialization.

The critical density contrast is defined as the density contrast evolved with linear perturbation theory until the time t_c . This can be recovered by expanding the expression in equation (6.14) to lowest order in η . To lowest order in η , we have $t \simeq B\eta^3/6 = t_c\eta^3/12\pi$. The background density of the universe surrounding the region is by the flat Einstein-de Sitter solution, $H = 2/3t$ and $\bar{\rho}_m = 3H^2/8\pi G = (6\pi Gt^2)^{-1}$. This allows us to calculate the linearly evolved density contrast,

$$\delta_m = \frac{\rho_m}{\bar{\rho}_m} - 1 \simeq \frac{3\eta^2}{20} = \frac{3}{20} \left(\frac{12\pi t}{t_c} \right)^{2/3}. \quad (6.15)$$

At the time of collapse, we find $\delta_c = 3(12\pi)^{2/3}/20 = 1.686$, regardless of the mass of the system or the actual time of collapse – this is a consequence of the simple Einstein-de Sitter universe and it no longer holds when we include homogeneous or inhomogeneous dark energy, as we shall see in chapter 9. In linear perturbation theory, the density contrast evolves as $\delta \propto (1+z)^{-1}$, so an over-density of $\delta = \delta_c/(1+z)$ at redshift z would collapse today.

6.3.1 Virialization of the system

As we saw above, the over-density collapses to a single point of infinite density in the spherical collapse model. This is, of course, unphysical and not the way the system actually evolves. In reality, some mechanism causes the system to stabilize and stop the collapse in what is called a virialization process. The density of the system relative to the background at the time of virialization is another important quantity when trying to understand the dark matter halos surrounding galaxy clusters. The simple spherical collapse model holds the power to estimate the ratio of these densities by estimating the time of virialization.

The time of virialization is taken to be the time, when the virial theorem is fulfilled, i.e., when two times the kinetic energy minus the potential energy of the system equals zero, or when the second derivative of the moment of inertia of the system equals zero. The moment of inertia of a sphere is given by $I = 2MR^2/5$, and for collapsing matter M is constant in time, i.e.,

$$\frac{d^2 I}{dt^2} = \frac{4M}{5} \left[\left(\frac{dR}{dt} \right)^2 + R \frac{d^2 R}{dt^2} \right] = 0 \quad \Rightarrow \quad \left(\frac{dR}{dt} \right)^2 + R \frac{d^2 R}{dt^2} = 0. \quad (6.16)$$

Inserting equation (6.14) into the above, we find $\cos \eta = 0$, and $\eta = \pi/2$ with $t = \pi/2 - 1$ or $\eta = 3\pi/2$ with $t = 3\pi/2 + 1$. The first solution is not the virialization that we seek, since the region is expanding and still coupled to the background at this point. So in the spherical collapse model virialization sets in at $\eta = 3\pi/2$, i.e., when the size of the region is $R = A$ – exactly half of the maximum size during the collapse.

From this we can proceed to find the ratio of the density in the region to the background density,

$$\Delta_{\text{vir}} = \left. \frac{\rho_m}{\bar{\rho}_m} \right|_{\eta=3\pi/2} = \frac{9}{2} \left(\frac{3\pi}{2} + 1 \right)^2 = 147. \quad (6.17)$$

Thus, a virialized dark matter halo is expected to have density of 147 times the background density at the time it virializes. After virialization, ρ_m does not evolve, but the background density continues to decrease as the universe expands, i.e., the density of the halo relative to the present background density is $\Delta = \Delta_{\text{vir}} (1 + z_{\text{vir}})^3$, where z_{vir} is the redshift at which the halo virialized. At the time of collapse, the ratio is $\Delta = \Delta_{\text{vir}} (1 + z_{\text{vir}})^3 / (1 + z_c)^3$, where z_c is the redshift at collapse. As we shall see in chapter 10, the picture of virialization also changes when dark energy is included.

6.4 Comparing to N-body simulations

The opening of this chapter stated that the semi-analytic models of cluster mass functions fare well when compared to N-body simulations. This section puts that statement to

the test and highlights some of the improvements that has been made to the Excursion Set result.

Two of the commonly used mass functions are the Sheth-Tormen (Sheth & Tormen (1999)) and Tinker (Tinker et al. (2008)) mass functions – both build on the Excursion Set result. The Tinker mass function has been fitted to Λ CDM N-body simulations. The functional form is

$$\nu f(\nu) = A [(\nu b)^a + 1] e^{-c\nu^2} \quad (6.18)$$

where the fitted constants A , a , b , and c are found in Tinker et al. (2008). Note that for the scaling parameters b and c , the values from Tinker et al. (2008) should be adjusted from the value of $\delta_c = 1.69$ to match the δ_c calculated with the spherical collapse model, see chapter 9 for δ_c different from this value. The Sheth-Tormen mass function has the form,

$$\nu f(\nu) = A \left(1 + \frac{1}{\nu'^{2p}}\right) \left(\frac{\nu'^2}{2}\right)^{1/2} \frac{e^{-\nu'^2/2}}{\sqrt{\pi}}, \quad (6.19)$$

where $\nu'^2 = a\nu^2$. Again the parameters a , A and p have been fitted to a number of N-body simulation, see Sheth & Tormen (1999). For the Sheth-Tormen mass function, the parameters are $a = 0.707$, $p = 0.3$, and A is determined by the requirement that the integral of $f(\nu)$ over all ν is unity. Comparing equation (6.19) to the Excursion Set mass function, the latter is recovered with $a = 1$, $p = 0$, and $A = 1/2$. The Sheth-Tormen mass function will be used in chapter 11.

Figure 6.2 shows a comparison of the mass functions discussed above. The green curve is the Excursion Set mass function, the red curve is the Tinker mass function, the blue curve is the Sheth-Tormen mass function, and the yellow curve is the Jenkins mass function (Jenkins et al. (2001)) with the functional form

$$\nu f(\nu) = A e^{-|\ln \sigma^{-1+b}|^c}. \quad (6.20)$$

As with the Tinker mass function, the Jenkins function has been fitted to Λ CDM N-body simulations, and the parameters are $A = 0.315$, $b = 0.61$, and $c = 3.8$. The mass functions are presented as functions of the inverse of the square root of the variance of the matter density field, and the underlying cosmological model comes into play through the relation between σ and the halo or cluster mass, M . For typical cosmological models the range plotted corresponds to a mass range from $M \sim 10^{11}M_\odot$ to $M \sim 10^{16}M_\odot$ with the highest mass to the right. The mass functions are all characterized by the exponential decrease in the number of halos at high masses.

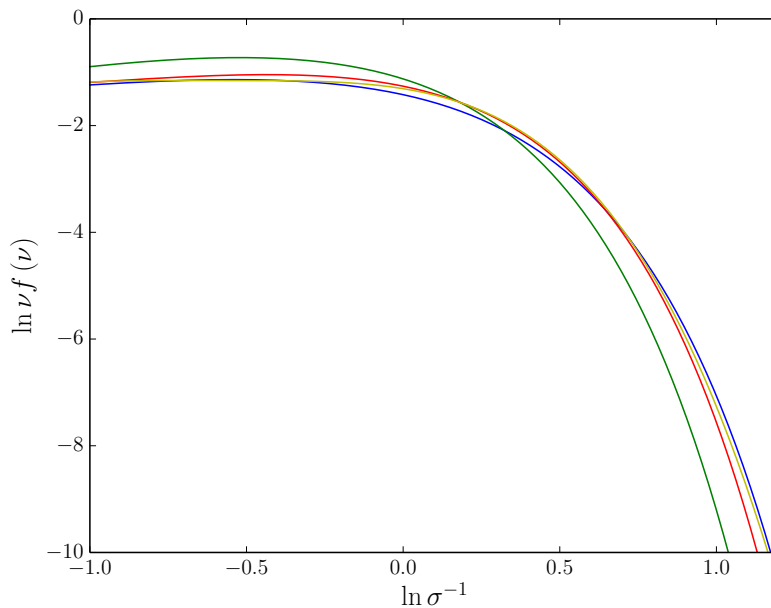


Figure 6.2: This figure compares four different mass functions: Green is Press-Schechter (Press & Schechter (1974)), red is Tinker (Tinker et al. (2008)), blue is Sheth-Tormen (Sheth & Tormen (1999)), and yellow is Jenkins (Jenkins et al. (2001)).

The Tinker, Sheth-Tormen, and Jenkins mass functions fit the N-body simulations quite well, see the respective references, and from figure 6.2, it is clear that the Excursion Set theory holds the same characteristics. The Sheth-Tormen mass function has been tested against simulations with massive neutrinos with good performance, see Brandbyge et al. (2010). This is the reason we opt to use this mass function in chapter 11.

7

GRAVITATIONAL LENSING

We know that gravity bends the path of light – even in a combination of Newtonian gravity and special relativity. This gives rise to the phenomenon of gravitational lensing, where light from distant sources is deflected on the path towards us by the gravitational potential along the path. In this chapter, we focus on weak lensing, which is a statistical phenomenon. In addition to the deflection of a light beam, gravitational lensing also distorts the light beam due to differential deflection of different parts of the beam. This distortion is manifested through changes in the size and shape of the image of a galaxy, and through the change in size, the apparent magnitude is altered. The luminosity of the galaxy is of course not changed, but a change in the size of the image will change the measured outgoing flux.

In the case of weak lensing, the distortion of a source galaxy image is too weak to be detected in an individual image. This is due to the intrinsic ellipticity of the galaxies, i.e., the fact that galaxies are not circular objects. The observed image is a superposition of the intrinsic shape and the lensing effect. The distortion of adjacent galaxies should, however, be similar, since the light from these galaxies experience similar gravitational potentials. Averaging over a large number of source galaxies allows us to measure the distortion, since the intrinsic shapes and orientations of the source galaxies are expected to be completely random. The obtained distortion enables us to determine the average convergence within some filter, stemming from the local gravitational field of a galaxy cluster for instance.

Weak gravitational lensing has multiple applications in cosmology, e.g., the search for galaxy clusters. The large concentrations of matter generate a tangential shear field in the vicinity of a galaxy cluster. Observationally, one searches for this kind of tangential shear field, which cannot be attributed to any concentration of visible galaxies along the line of sight. The advantage is of course, sensitivity to the total matter distribution, rather than only luminous matter, through gravity. Now, we will go through the details of weak lensing by a galaxy cluster.

The basic approximation is that the lens cluster acts as a thin lens, i.e., the spatial extent of the cluster along the line of sight is negligible compared to other distances in the configuration, and that all incoming light rays are parallel to the line of sight. The cluster can effectively be treated as a continuous distribution of point masses. Figure 7.1

7. Gravitational lensing

displays the configuration of the lensing system. Distances along the line of sight are angular diameter distances.

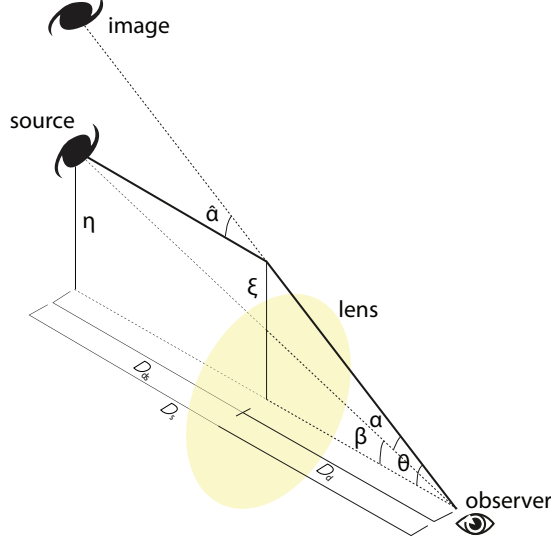


Figure 7.1: Sketch of the lens configuration.

For small deflection angles, $\hat{\alpha} \ll 1$, general relativity predicts that a light beam passing a point mass m_i at a distance ξ is deflected by the angle,

$$\hat{\alpha} = \frac{4Gm_i}{\xi}. \quad (7.1)$$

From figure 7.1, we have the following geometric relations: $\beta = \eta/D_s$, $\theta = \xi/D_d$ and $\eta = D_s\xi/D_d - D_{ds}\hat{\alpha}(\xi)$. Using all three relations, we find,

$$\beta = \theta - \frac{D_{ds}}{D_s} \hat{\alpha}(D_d\theta). \quad (7.2)$$

Defining the reduced deflection angle $\alpha(\theta) \equiv D_{ds}\hat{\alpha}(D_d\theta)/D_s$, equation (7.1) gives us,

$$\alpha(\theta) = 4Gm_i \frac{D_{ds}}{D_s D_d} \frac{\theta}{|\theta|^2}. \quad (7.3)$$

If the gravitational field is weak, the gravitational effects can be linearized. Hence, the effect of several mass elements can be calculated by linear superposition. Proceeding to a cluster defined as a collection of point masses, we find,

$$\hat{\alpha}(\xi) = \sum_i \hat{\alpha}_i(\xi) = \sum_i 4Gm_i \frac{\xi - \xi_i}{|\xi - \xi_i|^2}, \quad (7.4)$$

where ξ_i is the projected position vector of mass element m_i . For a continuous mass distribution, we can divide the lens into mass elements $dm = \Sigma(\xi) d^2\xi$, where $\Sigma(\xi)$ is

7. Gravitational lensing

the surface mass density of the lens at $\boldsymbol{\xi}$. Σ is calculated by projecting the spatial mass density along the line of sight to the position of the lens. Now, the deflection angle is transformed into an integral,

$$\hat{\boldsymbol{\alpha}}(\boldsymbol{\xi}) = 4G \int d^2\xi' \Sigma(\boldsymbol{\xi}') \frac{\boldsymbol{\xi} - \boldsymbol{\xi}'}{|\boldsymbol{\xi} - \boldsymbol{\xi}'|^2}. \quad (7.5)$$

Recasting equation (7.5) in terms of the reduced deflection angle, we find,

$$\boldsymbol{\alpha}(\boldsymbol{\theta}) = \frac{1}{\pi} \int d^2\theta' \kappa(\boldsymbol{\theta}') \frac{\boldsymbol{\theta} - \boldsymbol{\theta}'}{|\boldsymbol{\theta} - \boldsymbol{\theta}'|^2}, \quad (7.6)$$

where,

$$\kappa(\boldsymbol{\theta}) \equiv \frac{\Sigma(D_d\boldsymbol{\theta})}{\Sigma_{\text{cr}}}, \quad (7.7)$$

is the dimensionless surface mass density or convergence, which is a measurable quantity, and

$$\Sigma_{\text{cr}} \equiv \frac{D_s}{4\pi G D_d D_{\text{ds}}} \quad (7.8)$$

is the critical surface mass density depending only on the geometry of the configuration. In the case of multiple source galaxies, one must integrate over the distribution of these. To find the average from a physical cluster and a distribution of source galaxies, we must integrate equation (7.7) over all values of the impact parameter $D_d\boldsymbol{\theta}$ and the redshift distribution of the source galaxies. The numerator in equation (7.7) depends only on the impact parameter and not the redshift of the source since all incoming light rays are parallel to the line of sight. The denominator depends solely on the redshift of the source through the ratio D_s/D_{ds} . In part III, we will work with a theoretical mass distribution of the cluster to do the integral over the impact parameter. Regarding the redshift integration, we note here that in a flat universe, where comoving distance and angular diameter distance are related by equation (2.9), we find the redshift averaged inverse critical surface mass density as,

$$\begin{aligned} \Sigma_{\text{cr}}^{-1} &= 4\pi G \int_0^\infty \frac{dn}{dz}(z) \frac{D_d(z_l) D_{\text{ds}}(z_l, z)}{D_s(z)} \theta(z - z_l) dz \\ &= 4\pi G \frac{\chi(z_l)}{1 + z_l} \int_{z_l}^\infty \frac{dn}{dz}(z) \left(1 - \frac{\chi(z_l)}{\chi(z)}\right) dz, \end{aligned} \quad (7.9)$$

where z_l is the redshift of the cluster, dn/dz is the normalized redshift distribution of galaxies, and $\theta(z - z_l)$ is the Heaviside step function ensuring that only the fraction of galaxies behind the cluster contributes.

8

BAYSIAN STATISTICS AND PARAMETER INFERENCE

This chapter deals with the task of inferring parameters of cosmological models and some of the issues related thereto. First, we will familiarize ourselves with the cornerstone of parameter inference: Bayesian statistics and Bayes' theorem. Second, we discuss ways of inferring parameters and uncertainties thereon in practise, i.e., the Monte Carlo method and the Fisher matrix approach.

8.1 Bayesian statistics

Within the field of statistics, we have two fundamentally different schools: The frequentist and the Bayesian approach. In the frequentist school, the probability of an event is defined as the ratio of the number of occurrences and the number of trials in the limit of infinite *equiprobable* repetitions – arguably a circular definition. One of the shortcomings of the frequentist view is the incapability of dealing with unreproducible events, e.g., the probability of rain or sunshine on a certain date. In the Bayesian school, probability can be thought of as the degree of belief in a proposition. This clearly allows dealing with probabilities in unreproducible events. For reviews of Bayesian statistics in the context of cosmology and some comparison to frequentist statistics see Trotta (2008); Liddle (2009).

Bayes' theorem is a consequence of a few simple rules regarding probabilities. It is an intuitive requirement that the sum of probabilities of some proposition A and its negation \bar{A} should be unity, i.e., the proposition is either true or its negation must be true. Another rule is the product rule stating that the joint probability of two propositions, A and B , being true (or two events occurring) is the product of the probability of one being true and the probability of the other being true under the condition that the first is true. Note that A and B need not be related and the probability of A can be completely independent of the nature of B . Mathematically we have,

$$p(A|I) + p(\bar{A}|I) = 1, \quad p(A, B|I) = p(A|B, I) p(B|I), \quad (8.1)$$

where the vertical bar denotes that the probability is conditional on the information given on the right, and I represents any relevant information assumed to be true. When

forecasting weather, I would include, e.g., the past weather. Together the two rules of equation (8.1) imply that,

$$p(B|I) = \sum_A p(A|B, I) p(B|I) = \sum_A p(A, B|I), \quad (8.2)$$

where the sum runs over all possible outcomes of A and $p(B|I)$ is the marginal probability of B .

Bayes' theorem follows after realizing that $p(A, B|I) = p(B, A|I)$. Before writing the theorem we will exchange A with the observed data D and the B with our hypothesis or cosmological model represented by a vector of parameters θ . Bayes' theorem then reads,

$$p(\theta|D, I) = \frac{p(D|\theta, I) p(\theta|I)}{p(D|I)}. \quad (8.3)$$

The left hand side, $p(\theta|D, I)$, is the posterior probability of the hypothesis or the parameters when taking the data into account – this is what we ultimately seek. In the numerator on the right hand side, we have the sampling distribution or the likelihood of the data as a function of the parameters, $p(D|\theta, I)$, also denoted $\mathcal{L}(\theta)$, and the prior probability of the parameters, $p(\theta|I)$. The likelihood is not a probability distribution and the denominator in equation (8.3) serves to normalise the posterior probability. $p(D|I)$ is the marginal likelihood or Bayesian evidence given by

$$p(D|I) \equiv \sum_{\theta} p(D|\theta, I) p(\theta|I), \quad (8.4)$$

where the sums runs over all possible values of θ . In cosmology, we mostly deal with continuous parameters and thus replace the sum with an integral over the entire volume of the allowed parameter space, i.e., the space where $p(\theta|I)$ is non-zero.

A source of criticism toward the Bayesian school is the dependence of the posterior probability on the *subjective* prior probability, $p(\theta|I)$. Arguably, the posterior probability depends on the choice of the prior probability. As more data is gathered, however, the effect of the prior is gradually erased, see, e.g., Trotta (2008). The choice of prior is of greater importance to the discipline of model selection than to parameter inference. Here, it will suffice to say that in cosmology, flat priors are often used, reflecting no prior knowledge of the parameters other than the most basic, e.g., masses and amplitudes should be positive.

8.1.1 Parameter inference

In parameter inference, we choose a model, M , described by the parameters θ . The model is taken to be true, i.e., it takes the place of I in the above. The parameters can be divided into two categories. First, we have parameters of our interest, e.g., Ω_m and Ω_{de} . Second, there are nuisance parameters that influence the data, but are otherwise

uninteresting, e.g., unknown parameters related to the measurement or survey. Nuisance parameters will be denoted θ_{nuis} and parameters of interest θ . The posterior probability of θ can be found by marginalizing over the nuisance parameters,

$$p(\theta|D, M) \propto \int \mathcal{L}(\theta, \theta_{\text{nuis}}) p(\theta, \theta_{\text{nuis}}|M) d\theta_{\text{nuis}}. \quad (8.5)$$

With a flat prior and an estimator of the likelihood of the data given the parameters θ , we can calculate the posterior for any set of values of θ . As the volume of the parameter space increases, it quickly becomes intractable to map out the posterior on a sufficiently fine grid or similar. Thus, there is a need for a method of efficient sampling of the posterior. Some of the obstacles involved in this process are sharply peaked likelihood, high dimensionality of the parameter space (six to ten or more), and parameter degeneracies resulting in directions in the parameter space, where changes in the likelihood are small. Also, the computational demand for evaluating the likelihood can be very high, so the fewer evaluations the better. The next section describes the Markov chain Monte Carlo (MCMC) method for sampling the likelihood.

Finally, the parameters inferred from the posterior are presented by statistics, e.g., the mean and the standard deviation of the distribution, or by plotting one or two dimensional subsets of θ after marginalizing over the remaining parameters. We shall encounter examples hereof in multiple chapters of part III.

8.2 Markov chain Monte Carlo analysis

The goal is to visit points, θ , in the parameter space with a probability described by the posterior, $p(\theta|D, M)$, or at least a distribution proportional thereto. This ensures that the computational power is used where the posterior is large and our interest lies. Consequently the number of samples needed to sample the posterior sufficiently is lowered by orders of magnitude. A Markov chain, i.e., a series of locally correlated points $\theta_0, \theta_1, \theta_2, \dots$, with the right properties accomplishes the task. Markov refers to the fact that each point θ_i is drawn from a distribution that only depends on the preceding point θ_{i-1} , so the chain is completely defined by a starting point θ_0 and the transition probability function $p(\theta_i|\theta_{i-1})$.

If the transition probability satisfies the requirement of detailed balance,

$$\pi(\theta_i) p(\theta_j|\theta_i) = \pi(\theta_j) p(\theta_i|\theta_j), \quad (8.6)$$

then the chain will sample the distribution, $\pi(\theta)$, ergodically, which is exactly what we want. Here, the distribution, $\pi(\theta) = p(D|\theta, I) p(\theta|I)$, is proportional to the posterior probability. Integrating equation (8.6) over θ_i ,

$$\int \pi(\theta_i) p(\theta_j|\theta_i) d\theta_i = \pi(\theta_j) \int p(\theta_i|\theta_j) d\theta_i = \pi(\theta_j), \quad (8.7)$$

we see that if θ_i is drawn from π then so is θ_j . Obviously, we do not a priori know π , but rather we want to map it out, so how is the transition probability constructed in a fashion that ensures fulfillment of equation (8.6)? The Metropolis-Hastings algorithm provides a way of doing this.

8.2.1 Metropolis-Hastings algorithm

First off, we pick a proposal distribution $q(\theta_j|\theta_i)$. Often this is a multivariate Gaussian centred on θ_i , but we are not limited to this choice. With the chain standing in θ_i , we draw θ'_j from this distribution as a proposal for the next point in the chain. This point is then accepted with a probability,

$$\alpha(\theta_i, \theta'_j) = \min\left(1, \frac{\pi(\theta'_j) q(\theta_i|\theta'_j)}{\pi(\theta_i) q(\theta'_j|\theta_i)}\right). \quad (8.8)$$

If the point is accepted, we have $\theta_j = \theta'_j$. Otherwise, we duplicate θ_i in the chain setting $\theta_j = \theta_i$. The resulting transition probability is

$$p(\theta_j|\theta_i) = q(\theta_j|\theta_i) \alpha(\theta_i, \theta_j), \quad (8.9)$$

for $\theta_j \neq \theta_i$. To see how this is in agreement with the detailed balance, we multiply equation 8.8 by $\pi(\theta_i) q(\theta_j|\theta_i)$,

$$\begin{aligned} \pi(\theta_i) q(\theta_j|\theta_i) \alpha(\theta_i, \theta_j) &= \min(\pi(\theta_i) q(\theta_j|\theta_i), \pi(\theta_j) q(\theta_i|\theta_j)) \\ &= \min(\pi(\theta_j) q(\theta_i|\theta_j), \pi(\theta_i) q(\theta_j|\theta_i)) \\ &= \pi(\theta_j) q(\theta_i|\theta_j) \alpha(\theta_j, \theta_i). \end{aligned} \quad (8.10)$$

This is exactly the detailed balance requirement. Equation (8.8) is simplified when the proposal distribution is a function only of the distance between the two points in the parameter space, since $q(\theta_i|\theta_j)/q(\theta_j|\theta_i) = 1$. Ergo, using the Metropolis-Hastings algorithm we can sample the distribution $\pi(\theta)$ ergodically and map the posterior probability of θ up to the normalization, which is all we need to do parameter inference.

8.2.2 Parameter inference II

Some key elements of parameter inference have to be covered. First, how do we know when to stop sampling the posterior distribution? Second, how are the desired quantities inferred from the chains? There are several methods for estimating the convergence of Markov chains toward the target distribution $\pi(\theta)$, see Cowles & Carlin (1996) for a review. We will restrict ourselves to the Gelman-Rubin diagnostics of Gelman & Rubin (1992) and Brooks & Gelman (1998).

Based on $m \geq 2$ chains with $2n$ samples each, the diagnostics follow a sequence of steps for each parameter in the parameter space. First, discard the first n samples in

each chain, and then calculate the mean of the variance of the parameter within the chains, W , and the variance of the mean of the parameter between the chains, B/n .

$$W = \frac{1}{m(n-1)} \sum_{j=1}^m \sum_{i=1}^n (\theta_{ij} - \bar{\theta}_j)^2, \quad \frac{B}{n} = \frac{1}{m-1} \sum_{j=1}^m \left(\bar{\theta}_j - \frac{1}{m} \sum_{k=1}^m \bar{\theta}_k \right)^2, \quad (8.11)$$

where θ_{ij} is the i th sample of the j th chain and $\bar{\theta}_j$ is the mean of θ of the j th chain. W is likely to underestimate the true variance of $\pi(\theta)$ since the chains are unlikely to have sampled all points of the distribution.

Second, the variance of $\pi(\theta)$ is estimated as a weighted average of W and B ,

$$W' = \left(1 - \frac{1}{n}\right) W + \frac{B}{n}. \quad (8.12)$$

Third, the potential scale reduction factor, R , is calculated as

$$R = \sqrt{\frac{W'}{W}}. \quad (8.13)$$

If R is closer to unity than some set criterion, for all parameters, the chains are said to have converged to $\pi(\theta)$.

After convergence has been achieved, the chains can be combined into one chain of length mn . The means of the parameters, θ , with respect to the posterior can be estimated as

$$\theta_{\text{inf}} \simeq \int p(\theta|D, M) \theta d\theta = \frac{1}{mn} \sum_{i=1}^{mn} \theta_i, \quad (8.14)$$

where θ_i is the i th sample of the combined chain. The last equality in equation (8.14) follows from the fact that θ_i has been sampled from a distribution proportional to the posterior. The expectation value of any function of the parameters, $f(\theta)$, can be calculated as

$$f_{\text{inf}}(\theta) \simeq \frac{1}{mn} \sum_{i=1}^{mn} f(\theta_i). \quad (8.15)$$

8.3 Fisher information matrix

The Fisher matrix formalism provides a quick way to compute the expected sensitivity of an experiment to cosmological parameters, although Monte Carlo methods are arguably more robust, see, e.g., Perotto et al. (2006). See, e.g., Tegmark et al. (1997) for a discussion of the Fisher matrix in the context of cosmology. The Fisher matrix approach has some advantages over MCMC in terms of time consumption. First, the parameter space is only analyzed in the vicinity of the maximum likelihood, which for the purpose of a

forecast is easy to locate – it is just the fiducial model. Second, the Fisher matrix has the property that, once computed, individual Fisher matrices for different observational probes can be combined as a simple sum. Third, prior knowledge can simply be added to the diagonal elements of the matrix.

As noted, we are interested in the behaviour of the likelihood close to the maximum likelihood, $\hat{\theta}$, i.e., the point where the first derivatives of the likelihood with respect to the parameters vanish. Here, we ignore that the likelihood could have multiple maxima, since the Fisher matrix approach is not applicable in such scenarios. A Taylor expansion of $\ln \mathcal{L}$ around the maximum likelihood takes the form

$$\ln \mathcal{L}(\theta) = \ln \mathcal{L}|_{\hat{\theta}} + \sum_i \left. \frac{\partial \ln \mathcal{L}}{\partial \theta_i} \right|_{\hat{\theta}} \delta\theta_i + \frac{1}{2} \sum_{i,j} \left. \frac{\partial^2 \ln \mathcal{L}}{\partial \theta_i \partial \theta_j} \right|_{\hat{\theta}} \delta\theta_i \delta\theta_j + \dots, \quad (8.16)$$

where $\theta = \hat{\theta} + \delta\theta$. The first order term is zero and the local behaviour is dominated by the quadratic term, i.e., the likelihood itself behaves as a Gaussian. In other words, the Taylor expansion to second order is a good approximation of $\ln \mathcal{L}$, when the likelihood is Gaussian. Note, the constant term, $\ln \mathcal{L}|_{\hat{\theta}}$, acts as a scaling of the likelihood which is not relevant for parameter inference.

The Fisher information matrix is defined symmetrically as,

$$F_{ij} \equiv \left\langle -\frac{\partial^2 \ln \mathcal{L}}{\partial \theta_i \partial \theta_j} \right\rangle. \quad (8.17)$$

The inverse Fisher matrix provides the best attainable covariance matrix, regardless of the specific method used to estimate the parameters from the data, see Tegmark et al. (1997). As a consequence, $(F^{-1})_{ii}^{1/2}$ is the optimal statistical uncertainty achievable on the parameter θ_i after marginalization over all other parameters.

The Fisher matrix formalism can also be used to investigate parameter subspaces and correlation between different parameters. To analyze a subspace without accounting for the posterior of the remaining parameter, we just remove the rows and columns corresponding to the parameters of no interest from the Fisher matrix. To analyse a subspace with marginalization over the remaining parameters, we first invert the Fisher matrix and then single out the sub-matrix corresponding to the parameters of interest. Let's pretend that we are interested in the subspace (θ_j, θ_k) . The covariance matrix of this subspace can be written,

$$\mathcal{C} = \begin{pmatrix} \sigma_j^2 & \rho\sigma_j\sigma_k \\ \rho\sigma_j\sigma_k & \sigma_k^2 \end{pmatrix}, \quad (8.18)$$

where $\sigma_j = (F^{-1})_{jj}^{1/2}$ and ρ is known as the correlation coefficient, ranging from zero to one, i.e., θ_j and θ_k being either independent or completely correlated.

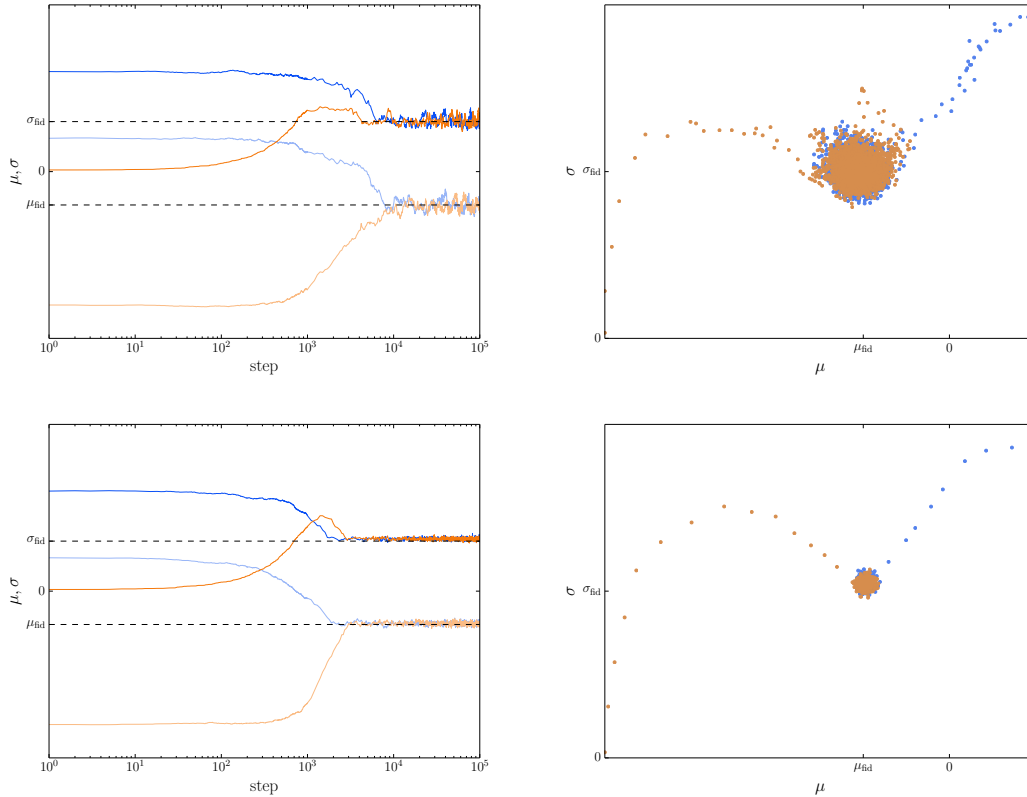


Figure 8.1: The left panes show the evolution of two different chains (μ, σ) in blue and orange colours, respectively. The upper panes have $n = 100$ and the lower panes have $n = 1000$. After the first thousand steps the chains have been thinned for the purpose of plotting, so only every one hundredth step is shown. The right panes show every one hundredth sample in the (μ, σ) parameter space.

8.4 Two simple examples

First, consider a data set of y_1, y_2, \dots, y_n that is drawn from a normal distribution with mean μ_{fid} and standard deviation σ_{fid} . We wish to estimate the mean and the standard deviation of this distribution based on the data points. The likelihood for a set of parameters $\theta = (\mu, \sigma)$ is

$$\mathcal{L}(\theta) = \prod_{i=1}^n \frac{1}{\sqrt{2\pi}\sigma} e^{-\frac{(y_i - \mu)^2}{2\sigma^2}}, \quad \ln \mathcal{L} = -n \ln \sigma - \sum_{i=1}^n \frac{(y_i - \mu)^2}{2\sigma^2} - \frac{n}{2} \ln 2\pi. \quad (8.19)$$

Adopting a flat prior, this likelihood is exactly the distribution, π , from which we want to sample with the Metropolis-Hastings algorithm. The proposal distribution is

Table 8.1: This table summarizes the parameter inference example with n random numbers drawn from a normal distribution with mean μ_{fid} and standard deviation σ_{fid} . The actual mean and standard deviation of the data are $\hat{\mu}$ and $\hat{\sigma}$, respectively. According to equation (8.21), these are also our maximum likelihood estimates of the parameters. The parameters inferred from the MCMC are μ_{inf} and σ_{inf} with an estimated uncertainty of $\sigma_{\text{inf}}(\mu)$ and $\sigma_{\text{inf}}(\sigma)$. The last column holds the uncertainty estimates $\sigma(\hat{\mu})$ and $\sigma(\hat{\sigma})$ from a Fisher matrix analysis.

n	steps	$R - 1$	μ_{fid}	$\hat{\mu}$	μ_{inf}	$\sigma_{\text{inf}}(\mu)$	$\sigma(\hat{\mu})$
10	10^6	0.15	-2	-1.64	-2.13	1.11	0.55
100	5×10^5	0.034	-2	-1.91	-1.92	0.32	0.31
1000	10^5	0.021	-2	-2.26	-2.26	0.10	0.10
n	steps	$R - 1$	σ_{fid}	$\hat{\sigma}$	σ_{inf}	$\sigma_{\text{inf}}(\sigma)$	$\sigma(\hat{\sigma})$
10	10^6	0.15	3	1.73	2.34	0.89	0.39
100	5×10^5	0.034	3	3.07	3.10	0.23	0.22
1000	10^5	0.021	3	3.13	3.14	0.07	0.07

taken to be a multivariate Gaussian with the same variance in both the μ and σ direction. Figure 8.1 shows the evolution of two Markov chains starting at different locations in parameter space for different values of n . It is apparent that higher n , i.e., more data, leads to better inference of the parameter values and faster convergence. The different fiducial values, inferred parameters, and the uncertainty on the parameter inference are summarised in table 8.1. From the table, it is again clear that higher n reduces the number steps needed and leads to a smaller uncertainty on the inferred parameter values. The $n = 10$ chains have not fully converged after 10^6 steps, which is reflected by the relatively large deviation between the actual mean and variance of the data and the inferred parameters. The values still match within the estimated one standard deviation error.

To calculate the Fisher information matrix, we first derive $\ln \mathcal{L}$ with respect to the two parameters,

$$\frac{\partial \ln \mathcal{L}}{\partial \mu} = \sum_{i=1}^n \frac{y_i - \mu}{\sigma^2}, \quad \frac{\partial \ln \mathcal{L}}{\partial \sigma} = -\frac{n}{\sigma} + \sum_{i=1}^n \frac{(y_i - \mu)^2}{\sigma^3}. \quad (8.20)$$

Setting these derivatives to zero, we find the unsurprising maximum likelihood estimation $\hat{\theta} = (\hat{\mu}, \hat{\sigma})$,

$$\hat{\mu} = \frac{1}{n} \sum_{i=1}^n y_i, \quad \hat{\sigma} = \sqrt{\sum_{i=1}^n \frac{(y_i - \hat{\mu})^2}{n-1}}. \quad (8.21)$$

Upon further derivation again with respect to the parameters, we find the elements of the Hessian,

$$\begin{aligned}\frac{\partial^2 \ln \mathcal{L}}{\partial \mu^2} &= -\frac{n}{\sigma^2}, & \frac{\partial^2 \ln \mathcal{L}}{\partial \mu \partial \sigma} &= \frac{\partial^2 \ln \mathcal{L}}{\partial \sigma \partial \mu} = -2 \sum_{i=1}^n \frac{y_i - \mu}{\sigma}, \\ \frac{\partial^2 \ln \mathcal{L}}{\partial \sigma^2} &= \frac{n}{\sigma^2} - 3 \sum_{i=1}^n \frac{(y_i - \mu)^2}{\sigma^4}.\end{aligned}\quad (8.22)$$

Averaging over an infinite number of realizations of the data set y_1, y_2, \dots, y_n , we find the Fisher information matrix. On average, the sum in the cross terms gives zero, when μ estimates the mean of the distribution, while the sum in the last term above average to n/σ^2 . So the Fisher matrix and its inverse read,

$$F = \begin{pmatrix} \frac{n}{\hat{\sigma}^2} & 0 \\ 0 & \frac{2n}{\hat{\sigma}^2} \end{pmatrix}, \quad F^{-1} = \begin{pmatrix} \frac{\hat{\sigma}^2}{n} & 0 \\ 0 & \frac{\hat{\sigma}^2}{2n} \end{pmatrix}, \quad (8.23)$$

i.e., the uncertainties associated with the estimates $\hat{\mu}$ and $\hat{\sigma}$ are $\hat{\sigma}/\sqrt{n}$ and $\hat{\sigma}/\sqrt{2n}$, respectively. In addition, we note that the off-diagonal terms are zero, so the parameters are uncorrelated. The Fisher matrix uncertainty estimates are compared to those of MCMC in table 8.1. For $n = 100$ and $n = 1000$, the error estimates from MCMC and the Fisher matrix approach match very well, reflecting that the posterior is Gaussian and hence well described by the Fisher matrix, and that the chains are converged. For $n = 10$, the estimated error from MCMC is twice that of the Fisher matrix, so expectedly a better uncertainty can be obtained by running the chains longer.

Another, even simpler, example, relevant to counting observations such as a survey counting galaxy clusters, is where the integer data points y_1, y_2, \dots, y_n are drawn from a Poisson distribution completely specified by the mean, λ_{fid} . In this case, the likelihood of the parameter λ , is

$$\mathcal{L}(\theta) = \prod_{i=1}^n \frac{\lambda^{y_i}}{y_i!} e^{-\lambda}, \quad \ln \mathcal{L} = \sum_{i=1}^n y_i \ln \lambda - n\lambda - \sum_{i=1}^n \ln y_i!. \quad (8.24)$$

To calculate the Fisher matrix, we go through the same exercise as before. For illustrative purposes we take λ to be a function of a vector of parameters, θ . We find

$$\frac{\partial \ln \mathcal{L}}{\partial \theta_j} = \left(\sum_{i=1}^n \frac{y_i}{\lambda} - n \right) \frac{\partial \lambda}{\partial \theta_j}, \quad (8.25)$$

$$\frac{\partial^2 \ln \mathcal{L}}{\partial \theta_k \partial \theta_j} = \left(\sum_{i=1}^n \frac{y_i}{\lambda} - n \right) \frac{\partial^2 \lambda}{\partial \theta_k \partial \theta_j} - \sum_{i=1}^n \frac{y_i}{\lambda^2} \frac{\partial \lambda}{\partial \theta_k} \frac{\partial \lambda}{\partial \theta_j}. \quad (8.26)$$

Equation (8.25) tells us that $\hat{\lambda}$ is the mean of the data points. Averaging over infinitely many realizations of the data, we expect $y_i = \hat{\lambda}$, so the Fisher matrix becomes,

$$F_{kj} = \frac{n}{\hat{\lambda}} \left. \frac{\partial \lambda}{\partial \theta_k} \right|_{\hat{\theta}} \left. \frac{\partial \lambda}{\partial \theta_j} \right|_{\hat{\theta}}. \quad (8.27)$$

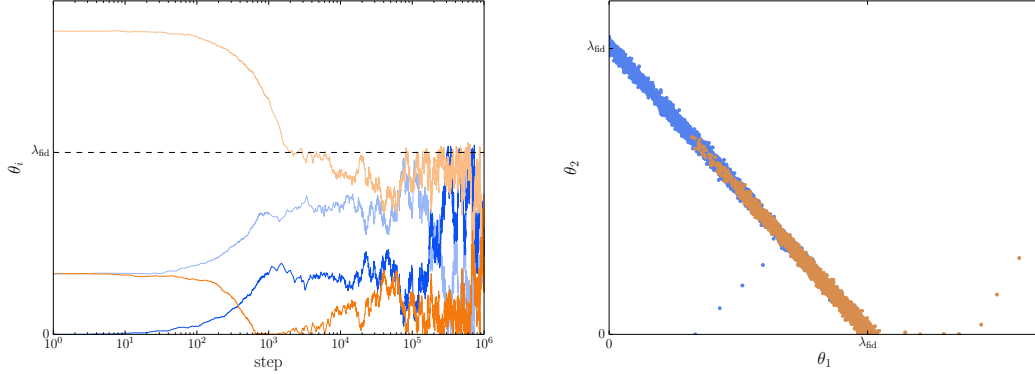


Figure 8.2: The left pane shows the evolution of two different chains (θ_1, θ_2) in blue and orange colours, respectively. After the first thousand steps the chains have been thinned for the purpose of plotting, so only every one hundredth step is shown. The right pane shows every one hundredth sample in the (θ_1, θ_2) parameter space.

To highlight the effects of a correlation between parameters, we construct the mean of the Poisson distribution as $\lambda = \theta_1 + \theta_2$ and use MCMC to determine θ_1 and θ_2 . We restrict θ_1 and θ_2 to be positive, but it is clear what would happen without this restriction. Figure 8.2 shows the evolution of two chains trying to estimate the parameters. It is apparent that the parameters are correlated, i.e., lower θ_1 can be compensated by higher θ_2 and vice versa. From the scatter plot of the samples, it is clear that the samples lie along the line $\theta_1 + \theta_2 \simeq \lambda_{\text{fid}}$.

The Fisher matrix for the parameters θ_1 and θ_2 is singular and the system of equations for determining the maximum likelihood estimate is under-determined. Hence, the Fisher matrix approach is not applicable in this case. The Fisher matrix approach can, however, be used to estimate λ and the uncertainty on this estimate – the latter agrees with the uncertainty inferred from the chains. So for both the examples put forward in this section, there is a good agreement between MCMC and Fisher estimates of the errors on the inferred parameters, when the latter is applicable. This will not always be the case, however. When, for instance, the posterior probability deviates significantly from a Gaussian, Fisher matrix results become more unreliable. Chapter 11 contains a short discussion of this.

As mentioned, the Poisson example is relevant to cluster counts and we will see the Poisson statistics utilised in part III. In this case, the n data points, y_i , are drawn from n different Poisson distributions with means λ_i . In chapter 10, i will refer to different mass and redshift bins, in which the number of clusters has been measured. The Fisher

matrix for this kind of data takes the form,

$$F_{jk} = \sum_{i=1}^n \frac{1}{\hat{\lambda}_i} \left. \frac{\partial \lambda_i}{\partial \theta_k} \right|_{\hat{\theta}} \left. \frac{\partial \lambda_i}{\partial \theta_j} \right|_{\hat{\theta}}. \quad (8.28)$$

Part III

MY WORK

9

SPHERICAL COLLAPSE OF DARK ENERGY WITH AN ARBITRARY SOUND SPEED

These investigations were already ongoing, when my Ph.D. commenced. Besides discussion of the results and their implications, my main contribution to this paper was on the numerical side. Specifically writing the code for the spherical collapse and the testing of different aspects of the code.

The paper (Basse et al. (2011)) investigates the spherical collapse model discussed in section 6.3 with the inclusion of clustering dark energy. Our dark energy component is a model with constant equation of state and sound speed, the latter of which can range from zero and unity, i.e., the speed of light. These two limits of the sound speed allow exact treatment of the system as a homogeneous sphere. In the limit, where the sound speed approaches the speed of light, dark energy is effectively homogeneous throughout the universe. Thus, the effect of the dark energy fluid is solely on the background expansion of the universe. In the case of exactly zero speed of sound, the Euler equation of the dark energy fluid is similar to that of non-relativistic matter. This allows an exact modeling of the dark energy density inside the sphere. See Creminelli et al. (2010) for a treatment of the two limits within a quintessence framework.

For sound speeds between these two values, sound waves will arise and disturb the homogeneous spherical configuration. However, we assume that the effect of the dark energy perturbation on the Poisson equation can be modeled with the average perturbation inside a sphere. Even under spherical symmetry the fluid equations of the dark energy are non-trivial to solve, so we resort to what we call the "quasi-linear" approach. Here, the dark matter component is treated with the non-linear equations, while the dark energy equations of motion are linearised, but with feedback from the non-linear dark matter through the Poisson equation.

A fully linear analysis of the equations in Fourier space shows two distinct limits: The clustering limit, $k^2 \hat{c}_{s,\text{de}}^2 / a^2 H^2 \ll 1$, and the non-clustering limit, $k^2 \hat{c}_{s,\text{de}}^2 / a^2 H^2 \gg 1$. The two limits are separated by the Jeans scale defined as $k_J \equiv aH / \hat{c}_{s,\text{de}}$. At a given time, this scale corresponds to a cluster of a particular mass,

$$M_J = \frac{4\pi}{3} \rho_m(a) \left(\frac{\pi}{k_J(a)} \right)^3. \quad (9.1)$$

To compute the cluster mass function in cosmological models with dark energy clustering, we need to compute the critical linear density contrast as described in chapter 6.

9. Spherical collapse of dark energy with an arbitrary sound speed

Our numerical analysis shows that dark energy clustering increases (decreases) the critical density contrast in models, where the dark energy equation of state is $w_{\text{de}} > -1$ ($w_{\text{de}} < -1$). In this way, δ_c becomes scale dependent and exhibits a step-like feature with two plateaus corresponding to the two clustering limits, with a transition region around M_J .

In the clustering limit, we expect to find a value of δ_c that matches equivalent models with $\hat{c}_{s,\text{de}} = 0$, where exact modeling applies. However, our "quasi-linear" approach overestimates the effect of dark energy clustering on the critical density contrast. This is because our linear treatment of dark energy underestimates the clustering of dark energy and therefore the feedback on the gravity of the system, i.e., for models with $w_{\text{de}} > -1$ a non-linear analysis would result in a slightly faster collapse and less time for the linear density contrast to evolve.

However, the general trend with the two plateaus and a transition region stands. Chapters 10 and 11 investigate how this scale dependence translates to the cluster mass function and subsequently the potential of verifying a dynamic nature of dark energy.

Spherical collapse of dark energy with an arbitrary sound speed

Tobias Basse¹, Ole Eggers Bjælde^{1,2} and Yvonne Y. Y. Wong²

¹ Department of Physics and Astronomy, Aarhus University, Ny Munkegade 120, DK-8000 Aarhus C, Denmark

² Institut für Theoretische Teilchenphysik und Kosmologie
RWTH Aachen, D-52056 Aachen, Germany

E-mail: tb06@phys.au.dk, oeb@phys.au.dk,
yvonne.wong@physik.rwth-aachen.de

Abstract. We consider a generic type of dark energy fluid, characterised by a constant equation of state parameter w and sound speed c_s , and investigate the impact of dark energy clustering on cosmic structure formation using the spherical collapse model. Along the way, we also discuss in detail the evolution of dark energy perturbations in the linear regime. We find that the introduction of a finite sound speed into the picture necessarily induces a scale-dependence in the dark energy clustering, which in turn affects the dynamics of the spherical collapse in a scale-dependent way. As with other, more conventional fluids, we can define a Jeans scale for the dark energy clustering, and hence a Jeans mass M_J for the dark matter which feels the effect of dark energy clustering via gravitational interactions. For bound objects (halos) with masses $M \gg M_J$, the effect of dark energy clustering is maximal. For those with $M \ll M_J$, the dark energy component is effectively homogeneous, and its role in the formation of these structures is reduced to its effects on the Hubble expansion rate. To compute quantitatively the virial density and the linearly extrapolated threshold density, we use a quasi-linear approach which is expected to be valid up to around the Jeans mass. We find an interesting dependence of these quantities on the halo mass M , given some w and c_s . The dependence is the strongest for masses lying in the vicinity of $M \sim M_J$. Observing this M -dependence will be a tell-tale sign that dark energy is dynamic, and a great leap towards pinning down its clustering properties.

1. Introduction

The apparent accelerating expansion of our universe is, according to the standard model of cosmology, best described by the presence of a dark energy component with a strong negative pressure, dominating the gravitational physics on large scales (see, e.g., [1–3] for reviews). However, our knowledge of the actual properties of this dark energy is very limited, and a number of open questions remain—Is dark energy dynamic or not? Does it take part in clustering? Is the dark energy’s behaviour scale-dependent?—to name but a few.

In order to distinguish between various models of dark energy, we must appeal to a variety of observational tests, each probing a different aspect of the dark energy’s dynamics. Luminosity and angular diameter distance measurements using, respectively, type Ia supernovae and the baryon acoustic oscillation scale have yielded—and will continue to yield—interesting information on the dark energy’s influence on the expansion history of the universe. The cosmic microwave background temperature anisotropies [4–8], as well as their cross-correlations with tracers of the large-scale structure distribution [9–12], provide a means to track the dark energy’s impact on the evolution of the gravitational potential via the late integrated Sachs–Wolfe effect. Weak gravitational lensing of distant objects probes the dark energy’s effect on the distance–redshift relation and the growth function [13–15]. Lastly, the formation of gravitationally bound objects such as galaxies and galaxy clusters is also sensitive to the detailed properties of the dark energy component [16–19].

Into the last category falls the so-called spherical collapse model [20], which, as the name suggests, is a model of gravitational collapse simplified by the assumption of spherical symmetry. In the model, a spherically symmetric overdense region with uniform density evolves to a configuration of infinite density under its own gravity, and a gravitationally bound object is said to be formed.

The original spherical collapse model was constructed under the assumption of an Einstein–de Sitter (EdS) universe. Already by the 1980s and the early 1990s the model had been extended to include a cosmological constant [21–23], and later for quintessence [24]. More analyses have followed since then, and all reached the conclusion that dark energy has an important impact on the formation of gravitationally bound structures [25–28]. The topic appears to have gained momentum again during the past year [29–34] mainly because of the positive expectation that these results will be testable against observations in the not-too-distant future [35].

In this paper we investigate by means of the spherical collapse model how a generic dark energy component characterised by a constant equation of state parameter $w < -1/3$ and sound speed c_s affects the formation of cosmic structures. In previous studies the dark energy component is generally allowed to take on different values of w . However, the sound speed c_s is invariably assumed to be either approaching the speed of light so that the dark energy is essentially homogeneous, or exactly vanishing so that the dark energy fluid is comoving with the matter component. These assumptions

undoubtedly simplify the calculations considerably and represent the two limiting behaviours of dark energy clustering. However, the case of a general sound speed remains interesting in that it introduces a scale-dependence into the problem. Identifying this dependence will give us yet another pointer to the true nature of dark energy. Here, we demonstrate for the first time how to incorporate a dark energy component with an arbitrary sound speed into the spherical collapse model (in an approximate way).

The paper is organised as follows. In section 2 we introduce the evolution equations for the spherical collapse and the corresponding equations of motion for the dark energy component. In section 3 we discuss dark energy clustering within the framework of linear perturbation theory. Section 4 contains our numerical results. Our conclusions are presented in section 5.

2. Spherical collapse

2.1. The spherical top hat and equations of motion for the matter component

In its most basic formulation, the spherical collapse model assumes there exists a spherically symmetric overdense region on top of an otherwise uniform background matter density field. The overdense region is characterised by a physical radius $R_i \equiv R(\tau_i)$ at the initial (conformal) time τ_i , and a uniform initial energy density

$$\rho_m^{\text{th}}(\tau_i) \equiv \bar{\rho}_m(\tau_i)(1 + \delta_{m,i}^{\text{th}}), \quad (2.1)$$

where $\bar{\rho}_m(\tau)$ denotes the energy density of the background matter field. This is our spherical “top hat” perturbation, and the mass contained within is given by

$$M = \frac{4\pi}{3}\bar{\rho}_m(\tau_i)(1 + \delta_{m,i}^{\text{th}})R_i^3 = \frac{4\pi}{3}\bar{\rho}_m(\tau_0)(1 + \delta_{m,i}^{\text{th}})X_i^3, \quad (2.2)$$

where τ_0 denotes the present time, and we have defined

$$X \equiv \frac{R}{a} \quad (2.3)$$

as the comoving radius of the top hat.

The evolution of the physical top hat radius R with respect to *cosmic time* t is described by the familiar equation of motion

$$\frac{1}{R} \frac{d^2 R}{dt^2} = -\frac{4\pi G}{3}(\rho_m^{\text{th}} + \rho_Q^{\text{th}} + 3P_Q^{\text{th}}), \quad (2.4)$$

where we have incorporated in the equation the possibility of a second energy component with a nonzero pressure denoted by the subscript Q . This second component is uniform inside the top hat region defined by the radius R , and shall be our dark energy component in this work. Equation (2.4) can be equivalently expressed as an equation of motion for the comoving top hat radius X with respect to conformal time τ ,

$$\frac{\ddot{X}}{X} + \mathcal{H} \frac{\dot{X}}{X} = -\frac{4\pi G}{3}a^2[\bar{\rho}_m\delta_m^{\text{th}} + \bar{\rho}_Q(1 + 3c_s^2)\delta_Q^{\text{th}}], \quad (2.5)$$

where $\cdot \equiv \partial/\partial\tau$, $\mathcal{H} = aH$ is the conformal Hubble parameter, and

$$c_s^2 \equiv \left. \frac{\delta P_Q}{\delta \rho_Q} \right|_{\text{rest}} \quad (2.6)$$

is the square of dark energy sound speed defined in the dark energy fluid's rest frame. Note that in identifying c_s in equations (2.5) and (2.6) as the rest frame sound speed, we have implicitly assumed that we are dealing only with length scales much smaller than the Hubble length, and that averaged over the spherical region, there is no bulk flow of dark energy relative to the dark matter fluid. We also assume c_s^2 to be constant in time and space.

Since the total mass of matter inside the top hat $M = (4\pi/3)\rho_m^{\text{th}}R^3$ is conserved, the top hat matter density contrast δ_m^{th} can be easily expressed as a function of the top hat radius,

$$\begin{aligned} \delta_m^{\text{th}}(\tau) &\equiv \frac{\rho_m^{\text{th}}(\tau)}{\bar{\rho}_m(\tau)} - 1 \\ &= (1 + \delta_{m,i}^{\text{th}}) \left[\frac{a(\tau)}{a(\tau_i)} \frac{R_i}{R(\tau)} \right]^3 - 1 = (1 + \delta_{m,i}^{\text{th}}) \left[\frac{X_i}{X(\tau)} \right]^3 - 1. \end{aligned} \quad (2.7)$$

For the dark energy density contrast δ_Q^{th} , two limiting cases have been studied in the literature. The first is the non-clustering limit, in which the dark energy sound speed c_s is taken to approach the speed of light, see e.g. [24]. In this case, δ_Q^{th} is effectively zero, so that the role of dark energy in the spherical collapse enters only through the Hubble expansion of the background.‡

The second is the “comoving” or clustering limit, in which the dark energy sound speed is exactly zero, see e.g. [31]. As we shall see in the next section, the Euler equation for the dark energy fluid in this limit is identical to its counterpart for a nonrelativistic dark matter fluid. This means that the bulk velocity fields of the two fluids are the same; the fluids are thus said to be comoving. Note that this observation does not imply the dark energy and dark matter density contrasts evolve in the same manner, since the conditions for energy conservation differ between the two fluids. It does, however, imply a conservation law for the dark energy component inside the top hat, so that the evolution of ρ_Q^{th} can be simply expressed as

$$\frac{d\rho_Q^{\text{th}}}{dt} + \frac{3}{R} \frac{dR}{dt} (\rho_Q^{\text{th}} + \bar{P}_Q) = 0, \quad (2.8)$$

or

$$\dot{\rho}_Q^{\text{th}} + 3 \left(\mathcal{H} + \frac{\dot{X}}{X} \right) (\rho_Q^{\text{th}} + \bar{P}_Q) = 0 \quad (2.9)$$

in terms of comoving quantities.

Strictly speaking, these two limiting cases are the only ones for which the top hat formulation is exact. The case of an arbitrary dark energy sound speed c_s is

‡ Note that in order to get exactly zero dark energy clustering, the sound speed would have to be infinite; See the linear solutions (3.4) and (3.6).

strictly not amenable to this simple treatment, since the existence of a finite sound speed and therefore the provision for the propagation of sound waves imply that the energy densities—both dark matter and dark energy—inside the overdense region must evolve to a nonuniform configuration, even if they are initially uniform. Having said this, however, we must also bear in mind that the spherical collapse model is itself a simplified model of structure formation, and the top hat density contrast should be interpreted as the average density contrast inside a region after a unit top hat filtering function has been applied. If we take this as our guiding principle, then the generalisation of the spherical top hat to include a dark energy component with an arbitrary sound speed simply requires that we interpret δ_Q^{th} as the spatially averaged density contrast of the dark energy field inside a region of comoving radius X . Symbolically, this spatial average can be expressed as

$$\delta_Q^{\text{th}}(\tau) \equiv \frac{3}{X^3} \int_0^X dx x^2 \delta_Q(x, \tau), \quad (2.10)$$

where $x \equiv |\mathbf{x}|$, and \mathbf{x} denotes the comoving coordinates.

2.2. Equations of motion for the dark energy component

It remains to specify an evolution equation for the dark energy density perturbation $\delta_Q(x, \tau)$. We begin by writing down the continuity and Euler equations for a relativistic fluid α in an expanding background in the pseudo-Newtonian approach [36],

$$\begin{aligned} \dot{\rho}_\alpha + 3\mathcal{H}(\rho_\alpha + P_\alpha) + \nabla \cdot [(\rho_\alpha + P_\alpha)\mathbf{u}_\alpha] &= 0, \\ \dot{\mathbf{u}}_\alpha + \mathcal{H}\mathbf{u}_\alpha + (\mathbf{u}_\alpha \cdot \nabla)\mathbf{u}_\alpha + \frac{\nabla P_\alpha + \mathbf{u}_\alpha \dot{P}_\alpha}{\rho_\alpha + P_\alpha} + \nabla\phi_N &= 0. \end{aligned} \quad (2.11)$$

Here, $\nabla \equiv \partial/\partial\mathbf{x}$, \mathbf{u}_α is the peculiar velocity of the fluid, and the potential ϕ_N can be obtained from the Poisson equation

$$\nabla^2\phi = 4\pi G a^2 \sum_\alpha \delta\rho_\alpha + 3\delta P_\alpha. \quad (2.12)$$

These equations should apply if we restrict our considerations to (i) length scales much smaller than the Hubble length, (ii) nonrelativistic peculiar velocities, and (iii) nonrelativistic sound speeds $c_s \ll 1$. We demonstrate in Appendix A that, at the linear level, these equations are indeed consistent with the Newtonian limit of a general relativistic formulation (see, e.g., [37–39]).

Defining the equation of state parameter for the dark energy component

$$w \equiv \frac{\bar{P}_Q}{\bar{\rho}_Q}, \quad (2.13)$$

and using the definitions $P_\alpha \equiv \bar{P}_\alpha + \delta P_\alpha$ and $\delta_\alpha^P \equiv \bar{\rho}_\alpha^{-1}\delta P_\alpha$, equation (2.11) can be rewritten for $\alpha = Q$ as

$$\begin{aligned} \dot{\delta}_Q + 3\mathcal{H}(\delta_Q^P - w\delta_Q) + \nabla \cdot [(\rho_Q + P_Q)\mathbf{u}_Q/\bar{\rho}_Q] &= 0, \\ \dot{\mathbf{u}}_Q + \mathcal{H}\mathbf{u}_Q + (\mathbf{u}_Q \cdot \nabla)\mathbf{u}_Q + \frac{\nabla\delta_Q^P + \mathbf{u}_Q(w\dot{\bar{\rho}}_Q/\bar{\rho}_Q + \dot{\delta}_Q^P)}{1 + w + \delta_Q + \delta_Q^P} + \nabla\phi_N &= 0. \end{aligned} \quad (2.14)$$

Since in our set-up the universe contains only dark matter and dark energy, the Poisson equation (2.12) now reads

$$\nabla^2\phi = 4\pi Ga^2[\bar{\rho}_m\delta_m + \bar{\rho}_Q(\delta_Q + 3\delta_Q^P)], \quad (2.15)$$

where, for our particular problem, the dark matter density perturbation $\delta_m(x, \tau)$ takes the form

$$\delta_m(x, \tau) = \begin{cases} \delta_m^{\text{th}}(\tau), & x \leq X(\tau), \\ 0, & x > X(\tau). \end{cases} \quad (2.16)$$

with the top hat density contrast $\delta_m^{\text{th}}(\tau)$ given by equation (2.7).

The continuity and Euler equations (2.14) are nonlinear in the quantities δ_Q and \mathbf{u}_Q , which even under the assumption of spherical symmetry are nontrivial to solve. Therefore, as a first approximation, we linearise them to obtain

$$\begin{aligned} \dot{\delta}_Q^{\text{lin}} + 3\mathcal{H}(\delta_Q^{P,\text{lin}} - w\delta_Q^{\text{lin}}) + (1+w)\theta_Q^{\text{lin}} &= 0, \\ \dot{\theta}_Q^{\text{lin}} + (1-3w)\mathcal{H}\theta_Q^{\text{lin}} + \frac{\nabla^2\delta_Q^{P,\text{lin}}}{1+w} + \nabla^2\phi_N &= 0, \end{aligned} \quad (2.17)$$

where we have defined the divergence of the dark energy velocity field to be $\theta_Q \equiv \nabla \cdot \mathbf{u}_Q$, and assumed w to be constant in time. Linearisation assumes that the perturbed quantities δ_Q and θ_Q are small. This is likely a good assumption since (i) the presence of a finite sound speed c_s naturally hinders the clustering of dark energy, keeping $\delta_Q \simeq \delta_Q^{\text{lin}}$ small relative to δ_m , and (ii) even in the limit $c_s = 0$ where the clustering of dark energy is most efficient, a fully linear analysis shows that δ_Q^{lin} is suppressed relative to δ_m^{lin} because of the dark energy's negative equation of state parameter (see section 3). Either way, the assumption of linearity in dark energy clustering can be easily checked *a posteriori* against solutions of the evolution equations for consistency. Finally, let us stress again that we are linearising *only* the dark energy equations of motion; the evolution of the dark matter component is still fully nonlinear, and described by the spherical collapse detailed in the previous section. We shall call this the ‘‘quasi-nonlinear’’ approach.

Upon linearisation, it is useful to recast the equations of motion in Fourier space. Define the Fourier transform for some field $A(x, \tau)$ as

$$\begin{aligned} A(x, \tau) &= \frac{1}{(2\pi)^3} \int d^3k \tilde{A}(k, \tau) \exp(i\mathbf{k} \cdot \mathbf{x}) \\ &= \frac{1}{2\pi^2} \int dk k^2 \tilde{A}(k, \tau) \frac{\sin(kx)}{kx}. \end{aligned} \quad (2.18)$$

Then, using the Poisson equation (2.15) and the relation $\tilde{\delta}_Q^{P,\text{lin}} = c_s^2 \tilde{\delta}_Q^{\text{lin}} + 3\mathcal{H}(1+w)(c_s^2 - w)\tilde{\theta}_Q^{\text{lin}}/k^2$ [6], equation (2.17) can be equivalently expressed as

$$\begin{aligned} \dot{\tilde{\delta}}_Q^{\text{lin}} + 3(c_s^2 - w)\mathcal{H}\tilde{\delta}_Q^{\text{lin}} + (1+w)\tilde{\theta}_Q^{\text{lin}} &= 0, \\ \dot{\tilde{\theta}}_Q^{\text{lin}} + (1-3c_s^2)\mathcal{H}\tilde{\theta}_Q^{\text{lin}} - \frac{k^2 c_s^2}{1+w} \tilde{\delta}_Q^{\text{lin}} + 4\pi Ga^2[\bar{\rho}_m \tilde{\delta}_m + \bar{\rho}_Q(1+3c_s^2)\tilde{\delta}_Q^{\text{lin}}] &= 0, \end{aligned} \quad (2.19)$$

where we have dropped subdominant terms proportional to \mathcal{H}^2/k^2 , since we are interested only in subhorizon scales $k \gg \mathcal{H}$. For the dark matter density contrast

$\delta_m(x, \tau)$ given in equation (2.16), the Fourier space equivalent is

$$\begin{aligned}\tilde{\delta}_m(k, \tau) &= 4\pi \int_0^{X(t)} dx x^2 \delta_m^{\text{th}}(\tau) \frac{\sin(kx)}{kx} \\ &= \delta_m^{\text{th}}(\tau) \frac{4\pi}{3} X^3 W(kX) = \frac{4\pi}{3} [(1 + \delta_{m,i}^{\text{th}}) X_i^3 - X^3] W(kX),\end{aligned}\quad (2.20)$$

where

$$W(kX) = \frac{3}{(kX)^3} [\sin(kX) - kX \cos(kX)] \quad (2.21)$$

by convention.

Lastly, we would like to relate $\tilde{\delta}_Q^{\text{lin}}(k, \tau)$ to the average dark energy density contrast inside the top hat, $\delta_Q^{\text{th}}(\tau)$, as defined in equation (2.10), since this is the quantity that ultimately governs the evolution of the top hat radius X via equation (2.5). This step is simple: we only need to identify $\delta_Q(x, \tau)$ with $\delta_Q^{\text{lin}}(x, \tau)$, the latter of which is obtained by Fourier transforming $\tilde{\delta}_Q^{\text{lin}}(k, \tau)$. Thus, equation (2.10) simplifies to

$$\delta_Q^{\text{th}}(\tau) = \frac{1}{2\pi^2} \int dk k^2 W(kX) \tilde{\delta}_Q^{\text{lin}}(k, \tau). \quad (2.22)$$

Our set of equations of motion is now complete.

3. Linear theory

Before we present the results of the spherical collapse model, let us first consider the evolution of dark matter and dark energy perturbations in the linear regime, i.e., where the dark matter perturbations are also tracked with linearised equations of motion. This exercise is useful for two reasons. Firstly, as we shall see, an understanding of the linear evolution can shed light on many essential features of the dependence of dark energy clustering on its equation of state parameter w and sound speed c_s . At the same time, the linear solution also sets the initial conditions for the spherical collapse model.

Secondly, some semi-analytic theories of structure formation such as the Press–Schechter formalism [40] and the excursion set theory [41–44] require as an input a linear critical density contrast $\delta_{\text{coll}}^{\text{lin}}$. In these theories a collapsed structure is assumed to have formed once the linearly evolved matter density contrast reaches the threshold value $\delta_{\text{coll}}^{\text{lin}}$ at some time τ_{coll} . The value of $\delta_{\text{coll}}^{\text{lin}}$ can be determined from the spherical collapse model by interpreting τ_{coll} as the instant at which the top hat radius vanishes. In practice, this means that in order to extract $\delta_{\text{coll}}^{\text{lin}}$ for a particular cosmological model, we need to solve *both* the nonlinear and the linear equations of motion at the same time.

We have already written down the linearised equations of motion for the dark energy perturbations in equations (2.17) and (2.19). For the dark matter component, the corresponding equations are

$$\begin{aligned}\dot{\delta}_m^{\text{lin}} + \theta_m^{\text{lin}} &= 0, \\ \dot{\theta}_m^{\text{lin}} + \mathcal{H}\theta_m^{\text{lin}} + 4\pi G a^2 [\bar{\rho}_m \delta_m^{\text{lin}} + \bar{\rho}_Q (1 + 3c_s^2) \delta_Q^{\text{lin}}] &= 0.\end{aligned}\quad (3.1)$$

These and equation (2.19) are solved simultaneously to determine the evolution of δ_Q^{lin} and δ_m^{lin} .

3.1. Dark energy evolution in the linear regime

Let us consider first the linear evolution of the dark energy perturbations. Here, it is convenient to combine the first order differential equations (2.19) for $\tilde{\delta}_Q^{\text{lin}}$ and $\tilde{\theta}_Q^{\text{lin}}$ into one second order differential equation for $\tilde{\delta}_Q^{\text{lin}}$, and also adopt a new time variable $s \equiv \ln a$. Assuming w and c_s to be constant in time, we find

$$\tilde{\delta}_Q^{\text{lin}''} + \mathcal{D}(s)\tilde{\delta}_Q^{\text{lin}'} + \left[\frac{k^2 c_s^2}{\mathcal{H}^2} \mathcal{X}(s) - \kappa(s) \right] \tilde{\delta}_Q^{\text{lin}} = \frac{3}{2}(1+w)\Omega_m(s)\tilde{\delta}_m^{\text{lin}}, \quad (3.2)$$

where $' \equiv \partial/\partial s$, and

$$\begin{aligned} \mathcal{D}(s) &\equiv 1 + \frac{\mathcal{H}'}{\mathcal{H}} - 3w, \\ \kappa(s) &\equiv 3w \left(1 + \frac{\mathcal{H}'}{\mathcal{H}} \right) + \frac{3}{2}(1+w)\Omega_Q(s), \\ \mathcal{X}(s) &\equiv 1 + 3\frac{\mathcal{H}^2}{k^2} \left[1 + \frac{\mathcal{H}'}{\mathcal{H}} - 3(c_s^2 - w) - \frac{3}{2}(1+w)\Omega_Q(s) \right]. \end{aligned} \quad (3.3)$$

For the cosmological models considered in this work, $\mathcal{D}(s)$ and $|\kappa(s)|$ are of order unity, while $\mathcal{X}(s) \approx 1$ always holds true because of our assumption of $k \gg \mathcal{H}$.

Equation (3.2) describes a damped harmonic oscillator with a driving force sourced by perturbations in the dark matter fluid. Exact analytic solutions do not exist for arbitrary cosmologies. However, approximate solutions can be constructed in certain limits:

- (i) *Clustering limit.* This is the limit in which $k^2 c_s^2 / \mathcal{H}^2 \ll |\kappa| \sim 1$. In this case, all coefficients in the differential equation are of order unity. It is therefore necessary to specify the exact time dependence of $\mathcal{D}(s)$, $\kappa(s)$ as well as $\tilde{\delta}_m^{\text{lin}}$ in order to find a solution. Formally setting $k = 0$, the solution is particularly simple during the matter domination epoch, where $\Omega_m(s) \simeq 1$, $\Omega_Q(s) \ll 1$, $\mathcal{H}'/\mathcal{H} \simeq -1/2$, $\tilde{\delta}_m^{\text{lin}} \propto a$ and $\tilde{\theta}_m^{\text{lin}} \simeq -\mathcal{H}\tilde{\delta}_m^{\text{lin}}$. At $s - s_i \gg 1$ it has the asymptotic form

$$\begin{aligned} \tilde{\delta}_Q^{\text{lin}} &\simeq \frac{1+w}{1-3w} \tilde{\delta}_m^{\text{lin}}, \\ \tilde{\theta}_Q^{\text{lin}} &\simeq -\frac{\mathcal{H}}{1+w} [3(c_s^2 - w) + 1] \tilde{\delta}_Q^{\text{lin}}, \end{aligned} \quad (3.4)$$

where we have obtained the solution for $\tilde{\theta}_Q^{\text{lin}}$ from the continuity equation by first differentiating $\tilde{\delta}_Q^{\text{lin}}$ with respect to time.

At first glance, the solution (3.4) for $\tilde{\delta}_Q^{\text{lin}}$ appears to be at odds with the solution obtained in, e.g., reference [39] in the same limit (i.e., $\mathcal{H} \ll k \ll \mathcal{H}_s$, where $\mathcal{H}_s \equiv \mathcal{H}/c_s$ is the inverse of the sound horizon, or the ‘‘Jeans wavenumber’’ k_J as we define in equation (3.5) below). In particular, the solution of [39] depends explicitly on the sound speed c_s^2 , whereas our solution does not. Part of the discrepancy can be traced to the term $\mathcal{X}(s)$ defined in equation (3.3). In our analysis we always approximate this term as $\mathcal{X}(s) = 1$, while some contributions proportional to \mathcal{H}^2/k^2 have been retained in the analysis of [39].

However, we believe that this discrepancy is of little consequence. As we demonstrate in Appendix B, the $\mathcal{H} \ll k \ll \mathcal{H}_s$ limit is well-defined only for those dark energy sound speeds satisfying $c_s^2 \lesssim 10^{-3}$. Thus, from a numerical point of view, our approximate solution and that of [39], *where they are actually applicable*, are consistent with one another to better than one part in a thousand.

- (ii) *Non-clustering limit.* This limit corresponds to $k^2 c_s^2 / \mathcal{H}^2 \gg |\kappa| \sim 1$, which is also the steady-state limit ($|\tilde{\delta}_Q^{\text{lin}''} / \tilde{\delta}_Q^{\text{lin}}|, |\tilde{\delta}_Q^{\text{lin}'} / \tilde{\delta}_Q^{\text{lin}}| \ll 1$). The solution can be obtained by formally setting $\tilde{\delta}_Q^{\text{lin}''} = \tilde{\delta}_Q^{\text{lin}'} = \kappa = 0$. Defining the ‘‘Jeans wavenumber’’

$$k_J \equiv \frac{\mathcal{H}}{c_s}, \quad (3.5)$$

the steady-state/non-clustering solution then reads

$$\begin{aligned} \tilde{\delta}_Q^{\text{lin}} &\simeq \frac{3}{2}(1+w) \Omega_m(s) \left(\frac{k_J}{k}\right)^2 \tilde{\delta}_m^{\text{lin}}, \\ \tilde{\theta}_Q^{\text{lin}} &\simeq -\frac{3\mathcal{H}}{1+w} [c_s^2 - w\Omega_m(s)] \tilde{\delta}_Q^{\text{lin}}. \end{aligned} \quad (3.6)$$

Note that, unlike the clustering solution (3.4), the non-clustering solution is not restricted to the matter domination epoch. Furthermore, the derivation of (3.6) does not in fact require the assumption of a linear $\tilde{\delta}_m$, since $\tilde{\delta}_m$ enters into the differential equation (3.2) only through the gravitational potential ϕ , and hence the Poisson equation, which is in any case linear in $\tilde{\delta}_m$. This means that the steady-state/non-clustering solution (3.6) would have been equally valid had we replaced $\tilde{\delta}_Q^{\text{lin}}$ with the Fourier transform of the top hat density contrast δ_m^{th} . We shall make use of this solution again later on in the analysis.

The form of the non-clustering solution is akin to those commonly found in hot or warm dark matter scenarios, in which k_J is associated with the free-streaming scale of the problem (see, e.g., [45]). However, since dark energy has a non-zero w while free-streaming dark matter does not, an extra prefactor $(1+w)$ is incurred in the solution (3.6).

- (iii) *Unstable limit.* So far we have implicitly assumed c_s to be a real number. Let us entertain ourselves for a moment with the possibility of an imaginary dark energy sound speed. In the limit $|k^2 c_s^2 / \mathcal{H}^2| \ll 1$, the dark energy perturbations are described by the same clustering solution as equation (3.4). Contrastingly, the $|k^2 c_s^2 / \mathcal{H}^2| \gg 1$ limit is unstable. Formally setting $\mathcal{D} = \kappa = \tilde{\delta}_m^{\text{lin}} = 0$, equation (3.2) is solved in the matter domination epoch by $\tilde{\delta}_Q^{\text{lin}} = C_1 I_0(\omega\sqrt{a}) + C_2 K_0(\omega\sqrt{a})$, where $I_0(x)$ and $K_0(x)$ are the zeroth order modified Bessel functions of the first and the second kind respectively, and $\omega \equiv 2k|c_s|/\sqrt{H_0^2 \Omega_m}$. For $x \equiv \omega\sqrt{a} \gg 1$, the modified Bessel functions have the asymptotic forms $I_0(x) \simeq \exp(x)/\sqrt{2\pi x}$ and $K_0(x) \simeq \sqrt{\pi/2x} \exp(-x)$. Thus, we find for the linear dark energy density contrast the asymptotic solution

$$\tilde{\delta}_Q^{\text{lin}} \sim a^{-1/4} \exp(\omega\sqrt{a}). \quad (3.7)$$

This exponential growth of $\tilde{\delta}_Q^{\text{lin}}$ in turn sources the evolution of the dark matter density contrast via the Poisson equation (2.15). Consequently, $\tilde{\delta}_m^{\text{lin}}$ also exhibits a similarly explosive and strongly scale-dependent growth that at first glance appears to be in conflict with our current understanding of large-scale structure formation unless $|c_s|$ is very small. We shall therefore not pursue the case of an imaginary dark energy sound speed any further in the present work.

Given the limiting solutions (3.4) and (3.6), we can try to interpolate between the clustering and non-clustering regimes using the following (rough) interpolation formulae:

$$\begin{aligned}\tilde{\delta}_Q^{\text{lin}} &= \frac{1+w}{1-3w+(2/3)(k/k_J)^2} \tilde{\delta}_m^{\text{lin}}, \\ \tilde{\theta}_Q^{\text{lin}} &= -\frac{\mathcal{H}}{1+w} \left[3(c_s^2 - w) + \frac{1-3w}{1-3w+(2/3)(k/k_J)^2} \right] \tilde{\delta}_Q^{\text{lin}}.\end{aligned}\quad (3.8)$$

The maximum error is 30% at $k \sim k_J$. These interpolation formulae are valid during the matter domination regime, and can be used to set the initial conditions for the dark energy component in the spherical collapse model.[§]

Lastly, let us define a ‘‘Jeans mass’’ scale analogous to the Jeans wavenumber k_J given in (3.5), i.e., the mass scale at which we expect the effects of the dark energy sound speed to set in. The Jeans mass is defined here as

$$M_J(a) \equiv \frac{4\pi}{3} \bar{\rho}_m(a) \left(\frac{\lambda_J(a)}{2} \right)^3, \quad (3.9)$$

where $\lambda_J \equiv 2\pi/k_J$. Evaluating the expression at $a = 1$, we find

$$M_J = 9.7 \times 10^{23} \Omega_m c_s^3 h^{-1} M_\odot. \quad (3.10)$$

For example, given $\Omega_m = 0.3$ and $h = 0.7$, we have $M_J = 1.3 \times 10^{16} M_\odot$ for $c_s^2 = 10^{-5}$, and $M_J = 4 \times 10^{14} M_\odot$ for $c_s^2 = 10^{-6}$ today. Note that the mass here refers to the mass of the dark matter component, not the dark energy!

3.2. Linear threshold density

Our second motivation for considering linear theory is the computation of the linear threshold density, defined as

$$\delta_{\text{coll}}^{\text{lin}} \equiv \delta_m^{\text{th,lin}}(\tau_{\text{coll}}), \quad (3.11)$$

where $\delta_m^{\text{th,lin}}(\tau)$ is the linearly evolved top hat matter density, and τ_{coll} is the instant at which the top hat radius goes to zero. As the name implies, $\delta_m^{\text{th,lin}}(\tau)$ is the linear version of the quantity $\delta_m^{\text{th}}(\tau)$ defined in equation (2.16), and is tracked by the equations

[§] The full equation (3.2) in fact has an exact analytic solution encompassing all three limits discussed above in terms of Bessel functions in the matter domination epoch. However, the complexity of the solution rather obscures the simple physics behind the problem. We therefore do not quote it here.

of motion (3.1) upon the replacements

$$\begin{aligned}\delta_m^{\text{lin}}(x, \tau) &\rightarrow \delta_m^{\text{th,lin}}(\tau), \\ \theta_m^{\text{lin}}(x, \tau) &\rightarrow \theta_m^{\text{th,lin}}(\tau), \\ \delta_Q^{\text{lin}}(x, \tau) &\rightarrow \delta_Q^{\text{th,lin}}(\tau),\end{aligned}\tag{3.12}$$

where

$$\delta_Q^{\text{th,lin}}(\tau) = \frac{1}{2\pi^2} \int dk k^2 W(kX) \tilde{\delta}_Q^{\text{lin}}(k, \tau)\tag{3.13}$$

is the linearly evolved dark energy density contrast averaged over the top hat volume.

4. Numerical results

In this section we proceed to solve numerically the evolution equations for the spherical collapse model presented earlier in section 2. We assume a flat spatial geometry for the universe so that the dark energy fraction today is related to the dark matter fraction by $\Omega_Q = 1 - \Omega_m$. For the choice of the parameter Ω_m and the present Hubble rate H_0 , we use the WMAP 7-year best-fit values [46]. We consider only those cases with constant w and c_s , although our formulation is applicable also to scenarios with time-dependent dark energy parameters.

We begin the evolution at a dimensionless time coordinate of

$$t_i H_0 = 2 \times 10^{-6},\tag{4.1}$$

corresponding to an initial scale factor of

$$a_i = a_0 \left(\frac{3t_i H_0 \sqrt{\Omega_m}}{2} \right)^{2/3},\tag{4.2}$$

if we assume t_i to lie well within the matter domination epoch. Taking an initial matter overdensity of $\delta_{m,i}^{\text{th}}$ the initial value of the top hat radius can then be obtained directly from equation (2.2) given some mass M . This mass, which we dub the ‘‘halo mass’’, is also the mass of dark matter contained in the final collapsed object.¶ Unless otherwise stated, the initial matter density contrast is taken to be

$$\delta_{m,i}^{\text{th}} = 3 \times 10^{-4}.\tag{4.3}$$

We have chosen the above values for the initial time and matter density contrast so that the collapse occurs at a time when the dark energy component constitutes a significant part of the universe’s energy budget.

Since the top hat evolution equation is a second order differential equation, we must also specify the time derivative of R . This can be constructed by differentiating

¶ The numerical code is written in C++ and employs GNU scientific libraries for solving the evolution equations and for interpolating the integral in equation (2.22). A verification of the convergence of equation (2.22) against the number and spacing of k -bins has been conducted.

¶ Note that the mass M here refers to the mass of the dark matter component only, although as suggested in [31], the true mass of the bound object should in principle include the contribution from the clustered dark energy component as well.

equation (2.7) with respect to time. Because the initial matter density contrast is much less than unity, we can approximate $d\delta_m^{\text{th}}/dt \simeq d\delta_m^{\text{th,lin}}/dt \simeq H\delta_m^{\text{th,lin}}$ using linear perturbation theory, and thus,

$$\left. \frac{1}{R} \frac{dR}{dt} \right|_{t_i} \simeq \frac{2}{3t_i} \left(1 - \frac{1}{3} \delta_{m,i}^{\text{th}} \right). \quad (4.4)$$

Finally the initial conditions for the dark energy evolution is given in section 3.1, particularly by the interpolation formula (3.8).

4.1. The collapse

Figures 1 to 4 shows the physical top hat radius normalised to the initial radius as a function of the dimensionless time coordinate tH_0 for several choices of w , c_s and halo masses M . The corresponding matter overdensity (2.7) and the dark energy overdensity (2.22) are also shown in juxtaposition.

In figure 1 we present the results for a dark energy component with $c_s^2 = 10^{-1}$ and a halo mass of $M = 10^{14}M_\odot$ for various equation of state parameters. These choices of c_s and M satisfy $M \ll M_J$ according to equation (3.10), and ensure that we are in the non-clustering regime. Since dark energy clustering is minimal ($< 10^{-5}$ relative to the dark matter density contrast), only the equation of state parameter w , i.e., the homogeneous part of the dark energy fluid, plays a role in the dynamics of the spherical collapse. Indeed, as we see in the figure, the less negative the equation of state parameter, the later the collapse. The reason is that for the same Ω_Q , the less negative w is, the earlier the dark energy comes to dominate the energy content of the universe, thereby inhibiting the growth of the top hat overdensity through Hubble expansion from an earlier stage. Comparing the Λ CDM case and a model with $w = -0.7$, the collapse time is delayed by some 20%. For equation of state parameters more negative than -1 , the opposite trend is seen; in the case of $w = -1.3$ the collapse occurs some 10% faster than in the Λ CDM limit.

In figure 2 we fix $M = 10^{16}M_\odot$, but vary the dark energy sound speed and equation of state. We choose $w = -0.7$ and $w = -0.8$, since, based on results from linear theory (see section 3), dark energy clustering is most enhanced by a deviation of w from -1 in the positive direction. Although the effect of dark energy clustering on the spherical collapse is quite small, the trend is clear: the smaller the sound speed, the faster the collapse. This is to be expected, since the smaller the sound speed is, the more efficiently the dark energy component clusters, and this clustering in turn contributes to sourcing the collapse of the top hat on the r.h.s. of equation (2.5). Note that although the dark energy component exhibits some degree of clustering in these cases, the density contrast for almost the entire collapse history is quite small until the last moments when $R \rightarrow 0$. This indicates that our quasi-nonlinear approach—in which the dark energy component is evolved with linearised equations—is valid for the model parameters adopted in this figure.

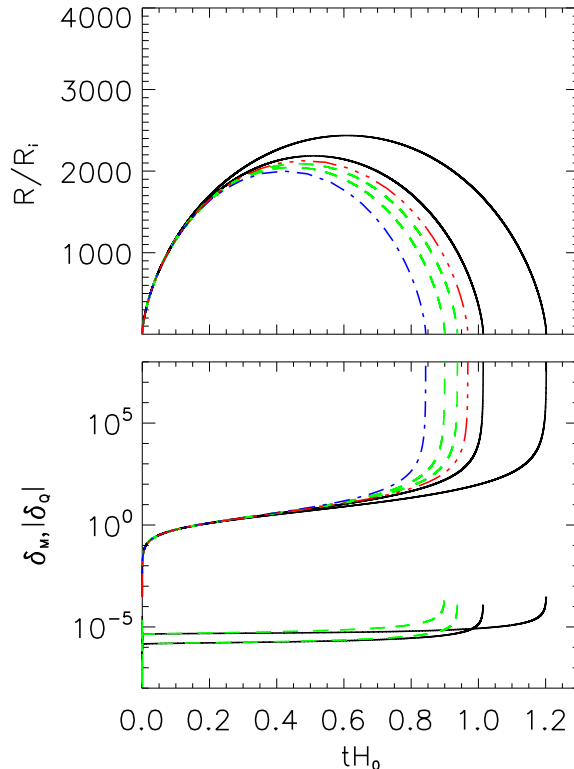


Figure 1. *Top:* Spherical top hat radius R normalised to the initial radius R_i as a function of the dimensionless time coordinate tH_0 . The reference EdS and Λ CDM models are represented by the blue dot-dash and the red dot-dot-dot-dash lines respectively. The two black solid lines denote, from right to left, the cases of $w = -0.7, -0.9$, while the two green dashed lines denote, from right to left, the cases of $w = -1.1, -1.3$. For these four cases, we have chosen the dark energy sound speed to be $c_s^2 = 10^{-1}$, and a halo mass of $M = 10^{14} M_\odot$. *Bottom:* The corresponding top hat matter and dark energy density contrasts. For the cases of $w = -1.1, -1.3$, the dark energy density contrasts are negative, i.e., they are underdensities, and the δ_Q values presented in this plot are absolute values. Note that in the reference EdS and Λ CDM models, there is no dark energy clustering. For all cases the initial matter overdensity has been chosen to be $\delta_{m,i}^{\text{th}} = 3 \times 10^{-4}$.

Figure 3 shows the cases of a fixed sound speed $c_s^2 = 10^{-4}$, equation of state parameters $w = -0.7, -0.8$, and three different halo masses. Figure 4 is similar, but with the sound speed fixed at $c_s^2 = 10^{-6}$. For these sound speeds, the corresponding Jeans masses M_J are $4 \times 10^{17} M_\odot$ and $4 \times 10^{14} M_\odot$ respectively. In both figures, we see that the larger the halo mass, the faster the collapse. This can be understood from the non-clustering solution (3.6) (valid here since (almost) all halo masses considered are less than the Jeans mass). Since the dominant Fourier mode is that corresponding to the comoving top hat radius X which is itself associated with the halo mass M , a reasonable generalisation of the non-clustering solution (3.6) for the dark energy component in

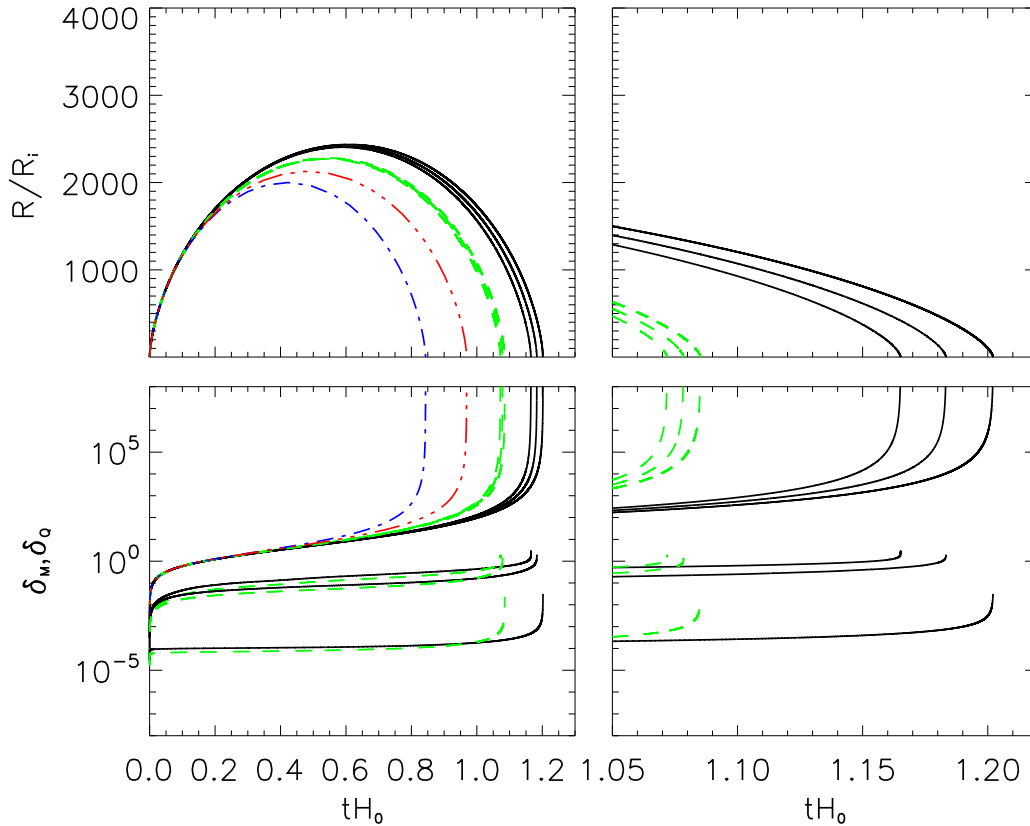


Figure 2. Same as figure 1, but for a fixed halo mass $M = 10^{16} M_{\odot}$. The black solid lines indicate $w = -0.7$ and, from right to left, a dark energy sound speed of $c_s^2 = 10^{-1}, 10^{-4}, 10^{-6}$. The green dashed lines denote $w = -0.8$ for the same set of dark energy sound speeds. The reference EdS and Λ CDM models are again represented by, respectively, the blue dot-dash and the red dot-dot-dot-dash lines. The right panels show the same results, but zoomed in on the time interval $tH_0 = 1.05 \rightarrow 1.25$.

terms of the halo mass would be

$$\delta_Q^{\text{th}}(\tau) \sim \frac{3}{2}(1+w)\Omega_m(\tau) \left(\frac{M}{M_J}\right)^{2/3} \delta_m^{\text{th}}(\tau). \quad (4.5)$$

The expression clearly shows that for a given sound speed, the absolute value of the dark energy density contrast increases with halo mass M . The enhanced dark energy density contrast in turn hastens the collapse of the dark matter top hat.

Note that for the case of $M = 10^{16} M_{\odot}$ and $c_s^2 = 10^{-6}$, the dark energy density contrast is of order 0.1 for much of the collapse history. This suggests that our approximation scheme for the dark energy evolution is approaching its limits of validity; the approximation breaks down for larger masses. Thus the rule of thumb regarding the quasi-nonlinear approach appears to be that it can be safely used for halo masses up to roughly the Jeans mass M_J , but not beyond.⁺

⁺ Obviously, we came to this conclusion based on the rather extreme cases of $w = -0.7$ and $w = -0.8$. In general, however, we expect the validity of the quasi-nonlinear approximation scheme to be dependent also on the choice of w , where the less w deviates from -1 , the higher the halo mass for which the

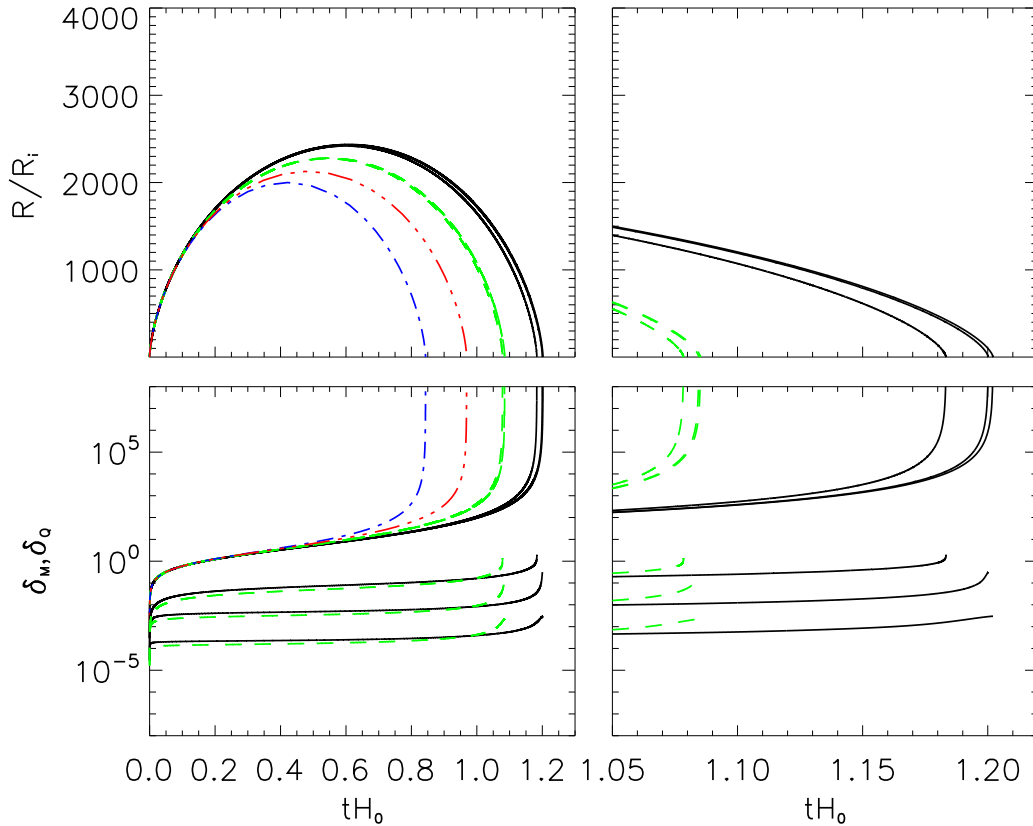


Figure 3. Same as figure 2, but for a fixed sound speed $c_s^2 = 10^{-4}$. The black solid lines denote $w = -0.7$ and, from right to left, halo masses of $M = 10^{12}, 10^{14}, 10^{16} M_\odot$. The green dashed lines denote $w = -0.8$ for the same set of halo masses. The blue dot-dash and the red dot-dot-dot-dash lines represent the reference EdS and Λ CDM models respectively. The right panels show the same results in the time interval between $tH_0 = 1.05$ and $tH_0 = 1.25$.

4.2. Linear threshold density

Next, we compute the linear critical density contrast $\delta_{\text{coll}}^{\text{lin}}$ required for use with such semi-analytic theories as the Press–Schechter formalism and the excursion set theory. This can be achieved by solving simultaneously *both* the nonlinear and the linear equations of motion for the spherical collapse, and formally identifying $\delta_{\text{coll}}^{\text{lin}}$ as the linearly evolved matter density contrast at the instant the top hat radius vanishes. Figure 5 shows $\delta_{\text{coll}}^{\text{lin}}$ as a function of the halo mass for various combinations of w and c_s . The initial matter overdensities are chosen such that all halos collapse at $z = 0$ (top panel), $z = 1$ (middle), and $z = 2$ (bottom).

Clearly, for the reference cases of an EdS and a Λ CDM universe, the linear threshold density is independent of the halo mass. However, once a finite dark energy sound speed is introduced into the picture, $\delta_{\text{coll}}^{\text{lin}}$ becomes mass-dependent, with $\delta_{\text{coll}}^{\text{lin}}(M)$ a monotonically increasing function of M when $w > -1$ and a monotonically decreasing approximation scheme remains applicable.

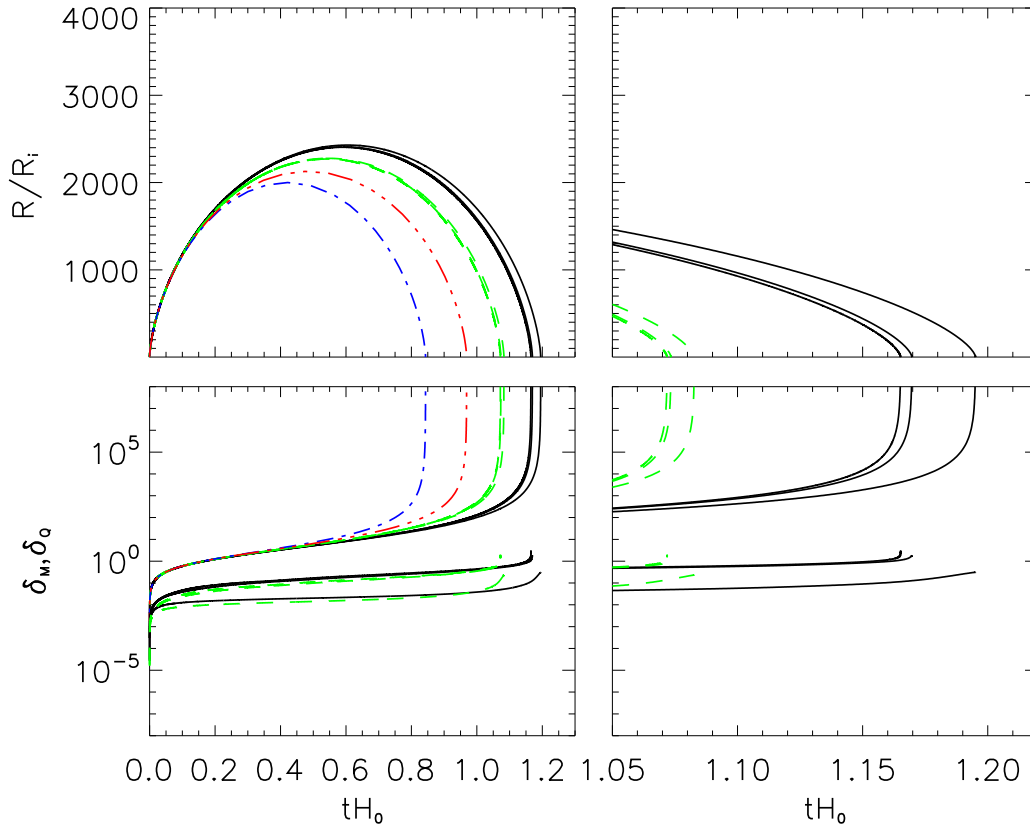


Figure 4. Same as figure 3, but with the sound speed fixed at $c_s^2 = 10^{-6}$.

function of M when $w < -1$. The M -dependence is however quite weak for those cases with w close to -1 , since dark energy clustering is generally suppressed by a factor $(1 + w)$.

The most interesting case presented here is that for $w = -0.8$, especially for $c_s^2 = 10^{-5}$ and $c_s^2 = 10^{-6}$ (corresponding Jeans masses: $1.3 \times 10^{16} M_\odot$ and $4 \times 10^{14} M_\odot$). Here, we see that at $M \ll M_J$, $\delta_{\text{coll}}^{\text{lin}}$ is at its lowest value and is essentially independent of M , indicating that we are in the fully non-clustering regime. As we move to higher values of M , we encounter a transition region where $\delta_{\text{coll}}^{\text{lin}}$ rises with M . Once $M \gg M_J$, however, $\delta_{\text{coll}}^{\text{lin}}$ reaches a plateau, where clustering is most efficient and $\delta_{\text{coll}}^{\text{lin}}$ is again independent of M . Interestingly, a similar pattern can also be seen in the $w < -1$ cases, where the dark energy density contrasts are negative, corresponding to dark energy underdensities, which have a negative effect on the clustering of matter. This negative effect is strongest for masses larger than the Jeans mass.

The dependence of $\delta_{\text{coll}}^{\text{lin}}$ on the collapse redshift is also quite clear in figure 5. The later the collapse, the larger the difference between the values of $\delta_{\text{coll}}^{\text{lin}}$ for the clustering and the non-clustering solutions. The reason is simply that the contribution of dark energy to the total energy budget in the universe increases with time. This means the effect of dark energy clustering also becomes more important at lower redshifts.

Finally, we caution the reader again that our quasi-nonlinear approximation breaks

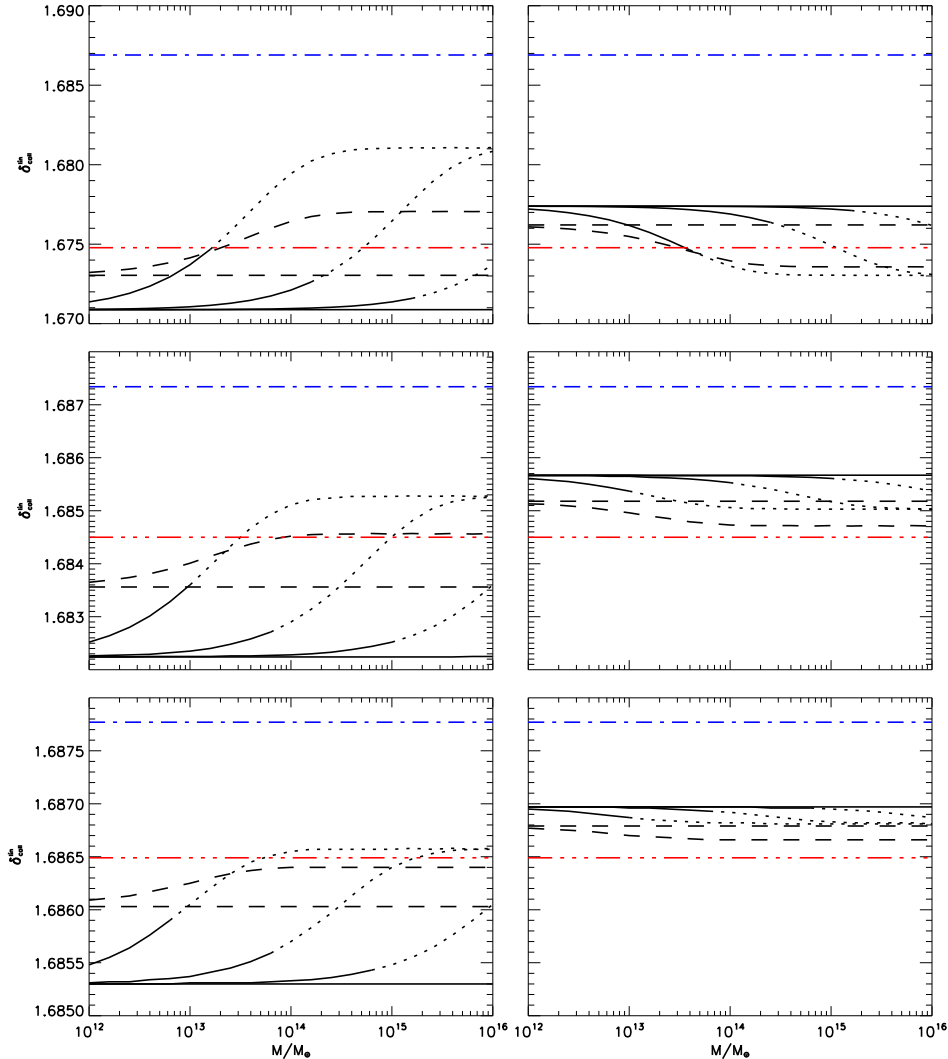


Figure 5. Linear threshold density $\delta_{\text{coll}}^{\text{lin}}$ as a function of the halo mass M at various collapse redshifts. *Top left:* Collapse redshift of $z = 0$. Solid lines denote models with $w = -0.8$ and, from top to bottom, $c_s^2 = 10^{-6}, 10^{-5}, 10^{-4}, 10^{-2}$. Dashed lines denote models with $w = -0.9$ and $c_s^2 = 10^{-6}, 10^{-2}$. For those cases in which $\delta_Q^{\text{th}} > 1$ during the collapse, we indicate the results with dotted lines. The blue dot-dash and the red dot-dot-dot-dash lines represent the reference EdS and Λ CDM models respectively. *Top right:* Same as top left, but with the solid lines denoting models with $w = -1.2$ and, from top to bottom, $c_s^2 = 10^{-2}, 10^{-4}, 10^{-5}, 10^{-6}$. Dashed lines represent models with $w = -1.1$ and $c_s^2 = 10^{-2}, 10^{-6}$. *Middle:* Same as top panel, but for a collapse redshift of $z = 1$. *Bottom:* Same as top panel, but for a collapse redshift of $z = 2$.

down if the dark energy density contrast inside the top hat becomes too large, especially when the halo mass approaches or exceeds the Jeans mass associated with a chosen sound speed. As a rule of thumb, we take the condition of breakdown to be $\delta_Q^{\text{th}} \geq 1$ at any time during the collapse process. To alert the reader to those cases where the breakdown condition is met, we indicate the resulting linear threshold densities $\delta_{\text{coll}}^{\text{lin}}$ in figure 5 with dotted lines; in these cases, the exact values of $\delta_{\text{coll}}^{\text{lin}}$ are unreliable. Clearly, for equation

of state parameters that deviate significantly from $w = -1$ (e.g., $w = -0.8, -1.2$), our approximate approach breaks down already at $M < M_J$. For $w = -0.9, -1.1$, the approach appears to remain valid for a larger mass range.

The breakdown of our approximation in the clustering limit also explains why we do not recover the exact results of reference [31] for $c_s^2 = 0$ and $w = -0.7, -1.3$. In fact, in the clustering limit, our approximation appears to overestimate the effect of dark energy clustering on the linear threshold density; had we included all nonlinear effects, nonlinear dark energy clustering would feed back on the matter clustering more effectively, thereby leading to an earlier collapse for $w > -1$ (and a later collapse for $w < -1$). An earlier collapse means that the linearly evolved matter density contrast would reach a lower value at the time of collapse, so that the real $\delta_{\text{coll}}^{\text{lin}}$ in the clustering limit would be lower than our estimate in figure 5.

4.3. Virialisation

In reality the collapse of an overdense region will never take place in the way described above, since density fluctuations inside the region will moderate the infall, and the system reaches virial equilibrium before the matter density can ever become infinite. For a single component system such as the case of a dark matter-dominated EdS universe, the process of virialisation and the radius at which virial equilibrium is attained can be obtained directly from the spherical collapse physics by assuming energy conservation between the time of turnaround—defined as the moment at which the top hat radius begins to shrink—and the time at which virial equilibrium is established. The result turns out to be rather simple,

$$R_{\text{vir}} = \frac{1}{2}R_{\text{turnaround}}, \quad (4.6)$$

i.e., virialisation is complete by the time the top hat radius decreases to half its value at turnaround.

For more complicated systems, such as the two fluid system considered in this paper, the conditions of energy conservation need to be modified. The time of virialisation can still be taken to be the instant at which the virial theorem is satisfied. However, the problem is complicated by the fact that we do not know how or if the dark energy fluid takes part in the virialisation process (see, e.g., [47, 48]). Therefore, for simplicity, we adopt equation (4.6) as the virialisation condition for this paper, and define the virial overdensity as

$$\Delta_{\text{vir}} \equiv \frac{\rho_m^{\text{th}}(\tau_{\text{vir}})}{\bar{\rho}_m(\tau_{\text{vir}})}, \quad (4.7)$$

where τ_{vir} is the time at which $R = R_{\text{vir}}$. We expect the quantitative results to be somewhat sensitive to our choice of the virialisation condition, but the qualitative features should be unaffected.

Figure 6 shows Δ_{vir} as a function of the halo mass M for various combinations of w and c_s^2 . The initial top hat matter density contrast $\delta_{m,i}^{\text{th}}$ has been fixed so that all

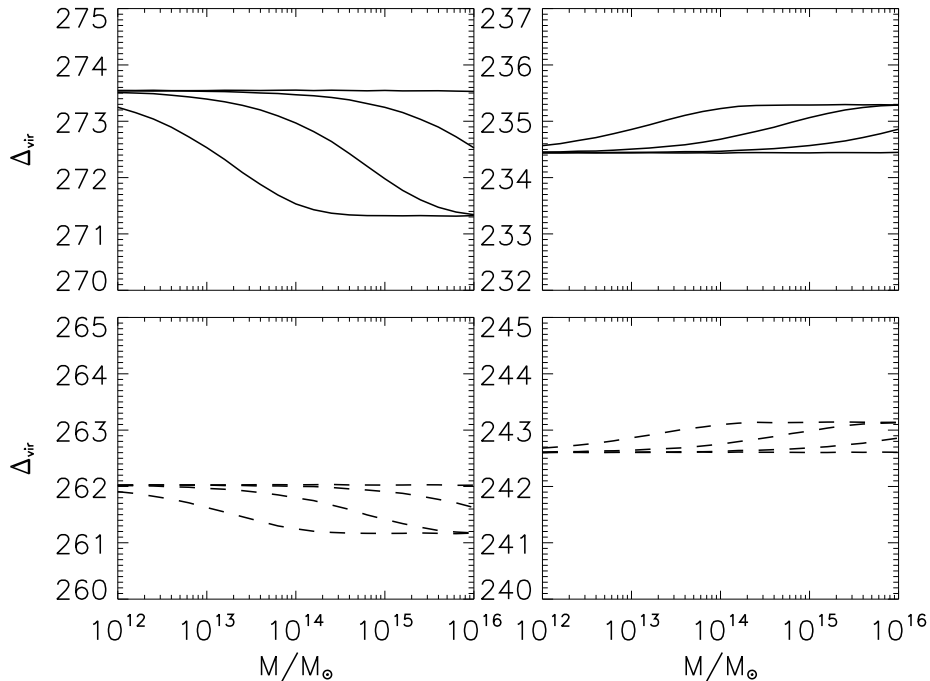


Figure 6. Virial overdensity Δ_{vir} as a function of the halo mass M for different dark energy equation of state parameters and sound speeds. In all cases $\delta_{m,i}^{\text{th}}$ has been chosen such that the collapse occurs at $z = 0$. *Top left:* $w = -0.8$ and, from top to bottom, $c_s^2 = 10^{-2}, 10^{-4}, 10^{-5}, 10^{-6}$. *Top right:* $w = -1.2$ and $c_s^2 = 10^{-6}, 10^{-5}, 10^{-4}, 10^{-2}$. *Bottom left:* $w = -0.9$ and $c_s^2 = 10^{-2}, 10^{-6}$. *Bottom right:* $w = -1.1$ and $c_s^2 = 10^{-6}, 10^{-2}$.

halos collapse at $z = 0$. As a reference point, for halos that collapse today, $\Delta_{\text{vir}} = 147$ and $\Delta_{\text{vir}} = 252$ for an EdS and a Λ CDM universe respectively (we do not plot these in figure 6 because they fall out of the plotting range).

Similar to the linear threshold density $\delta_{\text{coll}}^{\text{lin}}$, Δ_{vir} is first and foremost dependent on the choice of w . Introducing a finite dark energy sound speed into the picture induces for Δ_{vir} a dependence on the halo mass M . However, while $\delta_{\text{coll}}^{\text{lin}}$ increases with M for cosmologies with $w > -1$, Δ_{vir} decreases with it. The opposite trend is seen for cosmologies with $w < -1$. As with $\delta_{\text{coll}}^{\text{lin}}$, again we see an asymptotic non-clustering value for Δ_{vir} at $M \ll M_J$, a transition region at $M \sim M_J$ where Δ_{vir} varies strongly with M , and a second asymptotic region in the $M \gg M_J$ clustering limit.

The results in figure 6 are for a collapse redshift of $z = 0$. For halos that collapse earlier, the dependence of Δ_{vir} on the halo mass is qualitatively similar to the $z = 0$ case, but the difference in Δ_{vir} between the clustering and the non-clustering limits is smaller. This trend is reminiscent of the results in figure 5 for the linear threshold density $\delta_{\text{coll}}^{\text{th}}$ for different collapse redshifts.

Finally, note that some authors define the virial overdensity as the top hat density at the time of virialisation τ_{vir} , but normalised to the background density evaluated at the *collapse time* τ_{coll} . This means that instead of, e.g., $\Delta_{\text{vir}} = 147$ for the EdS model

according to our definition (4.7), one finds a higher value of 179 simply because between τ_{vir} and τ_{coll} the background density has become smaller due to the Hubble expansion. Since the dark energy sound speed does not play a role in the background expansion, the effect of these differing definitions is only to induce a shift in the normalisation of Δ_{vir} for a given set of w and Ω_Q . The M -dependence of Δ_{vir} is unaffected.

5. Discussions and conclusions

While a dark energy fluid with a negative equation of state parameter appears to describe the apparent accelerated expansion of our universe with reasonable success, the precise nature and properties of this dark energy remain undetermined. In this paper, we have addressed some aspects of the dark energy’s role in cosmic structure formation. Specifically, we have considered a generic dark energy fluid parameterised by a constant equation of state parameter w and sound speed c_s , and determined their impact on the formation of gravitationally bound objects.

Our main tool is the spherical collapse model, incorporating a nonrelativistic dark matter component and a generic dark energy fluid described above. Such a model has been investigated by other authors previously in the limit where the dark energy is (i) non-clustering, i.e., $c_s \rightarrow \infty$, or (ii) comoving with the dark matter, i.e., $c_s \rightarrow 0$. In this work, we have generalised the spherical collapse model to describe those intermediate cases characterised by an arbitrary c_s . Although we have focussed on scenarios with constant w and c_s , our approach is equally applicable to dark energy fluids described by time-dependent parameters. Along the way, we have also provided a detailed description of dark energy evolution in the linear regime—again for arbitrary w and c_s , and identified some salient features of dark energy clustering.

The dark energy component changes the evolution of the spherical collapse through its effect on the overall expansion of the universe as well as through its own clustering abilities. In the non-clustering limit, only the equation of state parameter w plays a role in the dynamics of the spherical collapse by altering the rate of the Hubble expansion. When the dark energy is able to cluster, however, then the dark energy density contrast also sources the evolution of the dark matter density perturbations. The amount of dark energy clustering is determined by both w and c_s .

In addition, since the introduction of a dark energy sound speed c_s necessarily brings into the picture a “Jeans scale” and hence a “Jeans mass” M_J , we find that the same sound speed can influence the spherical collapse dynamics in different ways depending on the mass of the collapsed object or the “halo mass” M . This mass dependence is especially manifest when we compute the virial overdensity Δ_{vir} and the linearly extrapolated threshold density $\delta_{\text{coll}}^{\text{lin}}$. In both cases, we find two asymptotic regions corresponding to the non-clustering $M \ll M_J$ limit and the clustering $M \gg M_J$ limit, where the value of Δ_{vir} or $\delta_{\text{coll}}^{\text{lin}}$ is practically constant with respect to M . In between these limits is a transition region, in which Δ_{vir} ($\delta_{\text{coll}}^{\text{lin}}$) declines (grows) strongly with M . Observing this transition region will be tell-tale sign that dark energy is dynamic, and

a great leap towards pinning down its clustering properties.

One possible way to discern this halo mass-dependent dark energy clustering is to measure the cluster mass function. Already it has been shown in, e.g., reference [31] that the difference between a clustering ($c_s = 0$) and a homogeneous ($c_s \rightarrow \infty$) dark energy fluid can be an order unity effect on the expected number of clusters at the high mass tail of the mass function. It remains to be seen how exactly an arbitrary dark energy sound speed would alter this conclusion, but some additional scale-dependent effects are almost guaranteed to be present.

Finally, let us remind the reader again that in our spherical collapse analysis we have simplified the equations of motion for the dark energy component so that only terms linear in the dark energy density contrast have been retained. This approach is strictly not valid for those cases in which the dark energy density contrast exceeds unity during the collapse process, and is especially prone to breakdown for cosmologies with an equation of state parameter that deviates significantly from $w = -1$. In these cases, a fully nonlinear analysis is required in order to compute accurately such quantities as Δ_{vir} and $\delta_{\text{coll}}^{\text{lin}}$ for comparison with observations. However, the qualitative features of dark energy clustering should not be affected by our simplified approach. A fully nonlinear analysis would require that we solve the equations of motion for the dark energy component—two $(1+1)$ -dimensional partial differential equations—using either a grid-based finite difference scheme or a Lagrangian method akin to a smoothed particle hydrodynamics simulation. Investigation is already underway and we hope to report the results in a future publication.

Acknowledgments

We thank Jacob Brandbyge, Jan Hamann and Cornelius Rampf for comments on the manuscript. Y³W thanks Guillermo Ballesteros for useful discussions. OEB acknowledges support from the Villum Foundation.

Appendix A. From general relativity to the pseudo-Newtonian approach

We demonstrate in this section that, at linear order, the pseudo-Newtonian approach adopted in this work is indeed consistent with the Newtonian limit of a general relativistic formulation. We work in the conformal Newtonian gauge, in which the perturbed line element is given by [49]

$$ds^2 = a^2(\tau) \{ -[1 + 2\psi(\tau, \mathbf{x})]d\tau^2 + [1 - 2\phi(\tau, \mathbf{x})](dx^2 + dy^2 + dz^2) \}, \quad (\text{A.1})$$

for a flat background spatial geometry. Assuming zero anisotropic stress so that $\psi = \phi$, the equations of motion in Fourier space for the dark matter and dark energy components [37–39] are, respectively,

$$\begin{aligned} \dot{\delta}_m + \theta_m - 3\dot{\phi} &= 0, \\ \dot{\theta}_m + \mathcal{H}\theta_m - k^2\phi &= 0, \end{aligned} \quad (\text{A.2})$$

and

$$\begin{aligned}\dot{\delta}_Q + 3(c_s^2 - w)\mathcal{H}\delta_Q + (1+w)D\theta_Q - 3(1+w)\dot{\phi} &= 0, \\ \dot{\theta}_Q + (1 - 3c_s^2)\mathcal{H}\theta_Q - \frac{k^2 c_s^2}{1+w}\delta_Q - k^2\phi &= 0,\end{aligned}\tag{A.3}$$

where $D \equiv 1 + 9(c_s^2 - w)\mathcal{H}^2/k^2$, and $\dot{D} = 18(c_s^2 - w)\dot{\mathcal{H}}\mathcal{H}/k^2$. Rearranging equations (A.2) and (A.3) respectively into second order differential equations, we find

$$\ddot{\delta}_m + \mathcal{H}\dot{\delta}_m = 3\mathcal{H}\dot{\phi} - k^2\phi + 3\ddot{\phi},\tag{A.4}$$

and

$$\begin{aligned}\ddot{\delta}_Q + [(1 - 3w)\mathcal{H} - \dot{D}/D]\dot{\delta}_Q \\ + \{Dc_s^2k^2 + 3(c_s^2 - w)[\dot{\mathcal{H}} + (1 - 3c_s^2)\mathcal{H}^2 - (\dot{D}/D)\mathcal{H}]\}\delta_Q \\ = (1+w)\{3[(1 - 3c_s^2)\mathcal{H} - \dot{D}/D]\dot{\phi} - Dk^2\phi + 3\ddot{\phi}\},\end{aligned}\tag{A.5}$$

assuming time-independent w and c_s^2 .

In order to take the subhorizon (i.e., $k \gg \mathcal{H}$) limit of equation (A.5), we note that $\dot{\mathcal{H}} \sim O(\mathcal{H}^2)$. Thus, we can replace all occurrences of D with $D = 1$ and \dot{D}/D with $\dot{D}/D = 0$. One last step concerns the coefficient of the δ_Q term on the LHS: we group all contributions proportional to c_s^2 together to get

$$\left\{ c_s^2 k^2 \left[1 + 3 \frac{\mathcal{H}^2}{k^2} \left(\frac{\dot{\mathcal{H}}}{\mathcal{H}^2} + 1 - 3(c_s^2 - w) \right) \right] - 3w(\mathcal{H}^2 + \dot{\mathcal{H}}) \right\} \delta_Q,\tag{A.6}$$

and set the $O(\mathcal{H}^2/k^2)$ terms in [...] to zero. Thus, we find

$$\begin{aligned}\ddot{\delta}_Q + (1 - 3w)\mathcal{H}\dot{\delta}_Q + [c_s^2k^2 - 3w(\dot{\mathcal{H}} + \mathcal{H}^2)]\delta_Q \\ = (1+w)[3(1 - 3c_s^2)\mathcal{H}\dot{\phi} - k^2\phi + 3\ddot{\phi}]\end{aligned}\tag{A.7}$$

for the subhorizon limit of equation (A.5).

It remains to specify the metric perturbation ϕ in terms of the density and velocity perturbations via the Einstein equation. Using the expressions given in, e.g, [49], we obtain

$$\begin{aligned}k^2\phi &= -\frac{3}{2}\mathcal{H}^2 \sum_{\alpha} \Omega_{\alpha} \left[\delta_{\alpha} + 3\frac{\mathcal{H}^2}{k^2}(1 + w_{\alpha})\frac{\theta_{\alpha}}{\mathcal{H}} \right], \\ \mathcal{H}\dot{\phi} &= \frac{3}{2}\mathcal{H}^2 \sum_{\alpha} \Omega_{\alpha} \frac{\mathcal{H}^2}{k^2} \left[\delta_{\alpha} + (1 + w_{\alpha}) \left(1 + 3\frac{\mathcal{H}^2}{k^2} \right) \frac{\theta_{\alpha}}{\mathcal{H}} \right], \\ \ddot{\phi} &= \frac{3}{2}\mathcal{H}^2 \sum_{\alpha} \Omega_{\alpha} \left\{ \left[c_{\alpha}^2 + \frac{\mathcal{H}^2}{k^2} \left(\frac{2}{\mathcal{H}^2} \frac{\ddot{a}}{a} - 4 \right) \right] \delta_{\alpha} \right. \\ &\quad \left. + 3(1 + w_{\alpha}) \frac{\mathcal{H}^2}{k^2} \left[c_{\alpha}^2 - w_{\alpha} - 1 + \left(\frac{2}{\mathcal{H}^2} \frac{\ddot{a}}{a} - 4 \right) \frac{\mathcal{H}^2}{k^2} \right] \frac{\theta_{\alpha}}{\mathcal{H}} \right\}.\end{aligned}\tag{A.8}$$

For the problem at hand, the summation is performed over $\alpha = m, Q$, and the notation should be understood to mean $\Omega_{\alpha} = \Omega_{\alpha}(\tau)$, $w_m = 0$, $w_Q = w$, $c_m^2 = 0$, and $c_Q^2 = c_s^2$. Combining these expressions to form the RHS of equation (A.4), we find the leading order contribution in the subhorizon limit to be

$$3\mathcal{H}\dot{\phi} - k^2\phi + 3\ddot{\phi} \simeq \frac{3}{2}\mathcal{H}^2 \sum_{\alpha} \Omega_{\alpha} (1 + 3c_{\alpha}^2) \delta_{\alpha}.\tag{A.9}$$

Similarly, we find for the RHS of equation (A.5),

$$3(1 - 3c_s^2)\mathcal{H}\dot{\phi} - k^2\phi + 3\ddot{\phi} \simeq \frac{3}{2}\mathcal{H}^2 \sum_{\alpha} \Omega_{\alpha}(1 + 3c_{\alpha}^2)\delta_{\alpha}, \quad (\text{A.10})$$

again to leading order in \mathcal{H}/k . Note that RHS of equations (A.9) and (A.10) are identical as a result of a \mathcal{H}^2/k^2 -suppressed $\mathcal{H}\dot{\phi}$ term relative to the $k^2\phi$ and $\ddot{\phi}$ terms, as can be seen in equation (A.8). We have *not* assumed $c_s^2 \ll 1$ to arrive at this result.

Thus, equations (A.4) and (A.5) now become, respectively,

$$\begin{aligned} \ddot{\delta}_m + \mathcal{H}\dot{\delta}_m &= \frac{3}{2}\mathcal{H}^2[\Omega_m(\tau)\delta_m + \Omega_Q(\tau)(1 + 3c_s^2)\delta_Q], \\ \ddot{\delta}_Q + (1 - 3w)\mathcal{H}\dot{\delta}_Q + [c_s^2k^2 - 3w(\dot{\mathcal{H}} + \mathcal{H}^2)]\delta_Q \\ &= (1 + w)\frac{3}{2}\mathcal{H}^2[\Omega_m(\tau)\delta_m + \Omega_Q(\tau)(1 + 3c_s^2)\delta_Q]. \end{aligned} \quad (\text{A.11})$$

These equations are consistent with the outcome of the pseudo-Newtonian approach (equations (3.1) to (3.3)).

Appendix B. Validity of the $\mathcal{H}_s^2 \gg k^2 \gg \mathcal{H}^2$ regime

A number of approximations have been made in order to arrive at the final equation of motion (A.11) for the dark energy component in the subhorizon limit. We have demanded that $(1 - 3w)\mathcal{H} \gg \dot{D}/D$ in equation (A.5), which limits the use of the approximate equation (A.11) to $\mathcal{H}^2/k^2 \ll 0.074 \rightarrow 0.15$, depending on the sound speed assumed. We have also assumed $D \approx 1$, equivalent to imposing a limit of $\mathcal{H}^2/k^2 \ll 0.055 \rightarrow 0.1$ on the validity of our approximate equations. In practice, we might want to choose a benchmark limit of

$$\max\left(\frac{\mathcal{H}^2}{k^2}\right) = 0.01, \quad (\text{B.1})$$

in order to keep all superhorizon contributions at a truly subdominant level.

Similarly, if we wish to take the super-sound-horizon limit (i.e., the clustering limit, $k \ll \mathcal{H}_s$, where $\mathcal{H}_s \equiv \mathcal{H}/c_s$), then from equation (3.2) or (A.11), we see that

$$\max\left(\frac{k^2c_s^2}{\mathcal{H}^2}\right) = 0.1 \quad (\text{B.2})$$

would work as a good benchmark limit to ensure the subdominance of sub-sound-horizon contributions. The two benchmark limits (B.1) and (B.2) together define the $\mathcal{H}_s^2 \gg k^2 \gg \mathcal{H}^2$ regime (or the ‘‘clustering regime’’ in this work).

From here, it is easy to see that the two limits (B.1) and (B.2) combine to set a constraint on the dark energy sound speed of

$$c_s^2 \lesssim 10^{-3} \quad (\text{B.3})$$

in the $\mathcal{H}_s^2 \gg k^2 \gg \mathcal{H}^2$ regime. If we were to exceed this constraint, we also run the risk of increasing the superhorizon (\mathcal{H}^2/k^2) and/or sub-sound-horizon ($k^2c_s^2/\mathcal{H}^2$) contributions to any approximate analytic solution to beyond the ‘‘negligible’’ level, in which case the $\mathcal{H}_s^2 \gg k^2 \gg \mathcal{H}^2$ regime becomes ill-defined.

References

- [1] E. J. Copeland, M. Sami and S. Tsujikawa, “Dynamics of dark energy,” *Int. J. Mod. Phys. D* **15** (2006) 1753 [arXiv:hep-th/0603057].
- [2] J. A. Frieman, “Lectures On Dark Energy And Cosmic Acceleration,” *AIP Conf. Proc.* **1057** (2008) 87 [arXiv:0904.1832 [astro-ph.CO]].
- [3] R. Bean, “TASI Lectures on Cosmic Acceleration,” arXiv:1003.4468 [astro-ph.CO].
- [4] J. Weller and A. M. Lewis, “Large Scale Cosmic Microwave Background Anisotropies and Dark Energy,” *Mon. Not. Roy. Astron. Soc.* **346** (2003) 987 [arXiv:astro-ph/0307104].
- [5] S. DeDeo, R. R. Caldwell and P. J. Steinhardt, “Effects of the sound speed of quintessence on the microwave background and large scale structure,” *Phys. Rev. D* **67** (2003) 103509 [Erratum-ibid. *D* **69** (2004) 129902] [arXiv:astro-ph/0301284].
- [6] R. Bean and O. Dore, “Probing dark energy perturbations: the dark energy equation of state and speed of sound as measured by WMAP,” *Phys. Rev. D* **69** (2004) 083503 [arXiv:astro-ph/0307100].
- [7] S. Hannestad, “Constraints on the sound speed of dark energy,” *Phys. Rev. D* **71** (2005) 103519 [arXiv:astro-ph/0504017].
- [8] R. de Putter, D. Huterer and E. V. Linder, “Measuring the Speed of Dark: Detecting Dark Energy Perturbations,” *Phys. Rev. D* **81** (2010) 103513 [arXiv:1002.1311 [astro-ph.CO]].
- [9] W. Hu and R. Scranton, “Measuring Dark Energy Clustering with CMB-Galaxy Correlations,” *Phys. Rev. D* **70** (2004) 123002 [arXiv:astro-ph/0408456].
- [10] P. S. Corasaniti, T. Giannantonio and A. Melchiorri, “Constraining dark energy with cross-correlated CMB and Large Scale Structure data,” *Phys. Rev. D* **71** (2005) 123521 [arXiv:astro-ph/0504115].
- [11] T. Giannantonio, R. Scranton, R. G. Crittenden, R. C. Nichol, S. P. Boughn, A. D. Myers and G. T. Richards, “Combined analysis of the integrated Sachs-Wolfe effect and cosmological implications,” *Phys. Rev. D* **77** (2008) 123520 [arXiv:0801.4380 [astro-ph]].
- [12] H. Li and J. Q. Xia, “Constraints on Dark Energy Parameters from Correlations of CMB with LSS,” *JCAP* **1004** (2010) 026 [arXiv:1004.2774 [astro-ph.CO]].
- [13] N. N. Weinberg and M. Kamionkowski, “Constraining dark energy from the abundance of weak gravitational lenses,” *Mon. Not. Roy. Astron. Soc.* **341** (2003) 251 [arXiv:astro-ph/0210134].
- [14] M. Jarvis, B. Jain, G. Bernstein and D. Dolney, “Dark Energy Constraints from the CTIO Lensing Survey,” *Astrophys. J.* **644** (2006) 71 [arXiv:astro-ph/0502243].
- [15] C. Schimd *et al.*, “Tracking quintessence by cosmic shear: Constraints from VIRMOS-Descart and CFHTLS and future prospects,” *Astron. Astrophys.* **463** (2007) 405 [arXiv:astro-ph/0603158].
- [16] E. Sefusatti, C. Vale, K. Kadota and J. Frieman, “Primordial non-Gaussianity and dark energy constraints from cluster surveys,” *Astrophys. J.* **658** (2007) 669 [arXiv:astro-ph/0609124].
- [17] M. Takada, “Can A Galaxy Redshift Survey Measure Dark Energy Clustering?,” *Phys. Rev. D* **74** (2006) 043505 [arXiv:astro-ph/0606533].
- [18] L. R. Abramo, R. C. Batista and R. Rosenfeld, “The signature of dark energy perturbations in galaxy cluster surveys,” *JCAP* **0907** (2009) 040 [arXiv:0902.3226 [astro-ph.CO]].
- [19] J. M. Alimi, A. Fuzfa, V. Boucher, Y. Rasera, J. Courtin and P. S. Corasaniti, “Imprints of Dark Energy on Cosmic Structure Formation I) Realistic Quintessence Models,” *Mon. Not. Roy. Astron. Soc.* **401** (2010) 775 [arXiv:0903.5490 [astro-ph.CO]].
- [20] J. E. Gunn and J. R. I. Gott, “On the infall of matter into cluster of galaxies and some effects on their evolution,” *Astrophys. J.* **176** (1972) 1.
- [21] P. J. E. Peebles, “Tests of Cosmological Models Constrained by Inflation,” *Astrophys. J.* **284** (1984) 439.
- [22] S. Weinberg, “Anthropic Bound on the Cosmological Constant,” *Phys. Rev. Lett.* **59** (1987) 2607.
- [23] O. Lahav, P. B. Lilje, J. R. Primack and M. J. Rees, “Dynamical effects of the cosmological constant,” *Mon. Not. Roy. Astron. Soc.* **251** (1991) 128.

- [24] L. M. I. Wang and P. J. Steinhardt, “Cluster Abundance Constraints on Quintessence Models,” *Astrophys. J.* **508** (1998) 483 [arXiv:astro-ph/9804015].
- [25] D. F. Mota and C. van de Bruck, “On the spherical collapse model in dark energy cosmologies,” *Astron. Astrophys.* **421** (2004) 71 [arXiv:astro-ph/0401504].
- [26] C. Horellou and J. Berge, “Dark energy and the evolution of spherical overdensities,” *Mon. Not. Roy. Astron. Soc.* **360** (2005) 1393 [arXiv:astro-ph/0504465].
- [27] M. Bartelmann, M. Doran and C. Wetterich, “Non-linear Structure Formation in Cosmologies with Early Dark Energy,” *Astron. Astrophys.* **454** (2006) 27 [arXiv:astro-ph/0507257].
- [28] L. R. Abramo, R. C. Batista, L. Liberato and R. Rosenfeld, “Structure formation in the presence of dark energy perturbations,” *JCAP* **0711** (2007) 012 [arXiv:0707.2882 [astro-ph]].
- [29] S. Basilakos, J. C. Bueno Sanchez and L. Perivolaropoulos, “The spherical collapse model and cluster formation beyond the Λ cosmology: Indications for a clustered dark energy?,” *Phys. Rev. D* **80** (2009) 043530 [arXiv:0908.1333 [astro-ph.CO]].
- [30] S. Lee and K. W. Ng, “Spherical collapse model with non-clustering dark energy,” arXiv:0910.0126 [astro-ph.CO].
- [31] P. Creminelli, G. D’Amico, J. Norena, L. Senatore and F. Vernizzi, “Spherical collapse in quintessence models with zero speed of sound,” *JCAP* **1003** (2010) 027 [arXiv:0911.2701 [astro-ph.CO]].
- [32] F. Pace, J. C. Waizmann and M. Bartelmann, “Spherical collapse model in dark energy cosmologies,” arXiv:1005.0233 [astro-ph.CO].
- [33] N. Wintergerst and V. Pettorino, “Clarifying spherical collapse in coupled dark energy cosmologies,” arXiv:1005.1278 [astro-ph.CO].
- [34] W. Valkenburg, [arXiv:1104.1082 [gr-qc]].
- [35] A. Albrecht *et al.*, “Report of the Dark Energy Task Force,” arXiv:astro-ph/0609591.
- [36] P. J. E. Peebles, “Large-scale structure of the Universe,” Princeton University Press, Princeton NJ (1980).
- [37] S. Anselmi, G. Ballesteros and M. Pietroni, “Non-linear dark energy clustering,” arXiv:1106.0834 [astro-ph.CO].
- [38] D. Sapone, M. Kunz and M. Kunz, *Phys. Rev. D* **80** (2009) 083519 [arXiv:0909.0007 [astro-ph.CO]].
- [39] G. Ballesteros and J. Lesgourgues, “Dark energy with non-adiabatic sound speed: initial conditions and detectability,” arXiv:1004.5509 [astro-ph.CO].
- [40] W. H. Press and P. Schechter, “Formation of galaxies and clusters of galaxies by selfsimilar gravitational condensation,” *Astrophys. J.* **187** (1974) 425.
- [41] J. A. Peacock and A. F. Heavens, *Mon. Not. Roy. Astron. Soc.* **243** (1990) 133.
- [42] J. R. Bond, S. Cole, G. Efstathiou and N. Kaiser, “Excursion set mass functions for hierarchical Gaussian fluctuations,” *Astrophys. J.* **379** (1991) 440.
- [43] M. Maggiore and A. Riotto, “The Halo Mass Function from the Excursion Set Method. I. First principle derivation for the non-markovian case of gaussian fluctuations and generic filter,” *Astrophys. J.* **711** (2010) 907 [arXiv:0903.1249 [astro-ph.CO]].
- [44] M. Maggiore and A. Riotto, “The halo mass function from the excursion set method. II. The diffusing barrier,” *Astrophys. J.* **717** (2010) 515 [arXiv:0903.1250 [astro-ph.CO]].
- [45] A. Ringwald and Y. Y. Y. Wong, “Gravitational clustering of relic neutrinos and implications for their detection,” *JCAP* **0412** (2004) 005 [arXiv:hep-ph/0408241].
- [46] E. Komatsu *et al.*, “Seven-Year Wilkinson Microwave Anisotropy Probe (WMAP) Observations: Cosmological Interpretation,” arXiv:1001.4538 [astro-ph.CO].
- [47] I. Maor and O. Lahav, “On virialization with dark energy,” *JCAP* **0507** (2005) 003 [arXiv:astro-ph/0505308].
- [48] P. Wang, “Virialization in Dark Energy Cosmology,” *Astrophys. J.* **640** (2006) 18 [arXiv:astro-ph/0507195].
- [49] C. P. Ma and E. Bertschinger, “Cosmological perturbation theory in the synchronous and conformal Newtonian gauges,” *Astrophys. J.* **455** (1995) 7 [arXiv:astro-ph/9506072].

10

CONFRONTING THE SOUND SPEED OF DARK ENERGY WITH FUTURE CLUSTER SURVEYS

This was the natural continuation of Basse et al. (2011) and I was fully involved in every aspect of the process. The paper³ (Basse et al. (2012)) investigates how the findings of chapter 9 affect the observables, namely the cluster mass function. We model the cluster mass function using the excursion set result of equation (6.13).

Along the way, we develop a novel treatment of the virialization process in the spherical collapse when including dark energy. Here, we use the tools of section 6.3.1. The mass of the system, however, is no longer constant, since the dark energy mass contribution varies in time. We find that the ratio of the virial radius and the radius at turnaround exhibits a trend similar to that of the critical density contrast as a function of cluster mass. The effect of the homogeneous dark energy in the background is to lower the value of $R_{\text{vir}}/R_{\text{ta}}$ compared to the Einstein-de Sitter universe with $R_{\text{vir}} = R_{\text{ta}}/2$. The value of the dark energy equation of state determines the magnitude and redshift dependence of this effect. For models with $w_{\text{de}} > -1$, the effect of dark energy clustering is to increase the ratio due to extra gravity from the dark energy. In addition, we find that the dark energy contribution to the mass is less than one percent of the dark matter mass of the system. See Maor & Lahav (2005) and Wang (2006) for alternative discussions of virialization with dark energy.

As mentioned, we model the cluster mass function using the excursion set, i.e., we compute the cluster mass function as

$$\frac{dn}{dM_{\text{vir}}} dM_{\text{vir}} = \sqrt{\frac{2}{\pi}} \frac{\bar{\rho}_m}{M_{\text{vir}}^2} \nu \left| \frac{d \ln \nu}{d \ln M_{\text{vir}}} \right| e^{-\frac{\nu^2}{2}} dM_{\text{vir}}, \quad (10.1)$$

where $\nu \equiv \delta_c(M_{\text{vir}})/\sigma(R_{\text{vir}})$ and M_{vir} is the total mass of the system at the time of virialization. Here, $\sigma(R_{\text{vir}})$ is the variance of the linear matter power spectrum smoothed on the scale of R_{vir} . This modeling of the mass function encodes the effect of dark energy clustering in three ways: Through the mass of the system, the smoothing scale of the power spectrum, and the critical density contrast. Whether this is the correct modeling for inhomogeneous dark energy models like this, remains to be verified by N-body simulations. This matter is discussed further in chapter 11.

³This paper has not been published in a peer reviewed journal, but is available on arXiv.

10. Confronting the sound speed of dark energy with future cluster surveys

We find that dark energy clustering affects the mass function in a scale dependent way, leading to an excess of clusters with masses above the Jeans mass when compared to a similar model with effectively homogeneous dark energy, i.e., $\hat{c}_{s,\text{de}}^2 = 1$. In addition, the transition region around the Jeans scale leaves a distinct signature.

Finally, we investigate the potential of future weak lensing cluster surveys to constrain the sound speed of dark energy. Using the ESA Euclid mission Laureijs et al. (2011) as an example, we apply a Fisher matrix analysis with redshift bins of constant width. Our results show that future cluster surveys are highly complementary to CMB surveys such as Planck. The combination increases the sensitivity toward the cosmological parameters by breaking some of the degeneracies in the parameters space. In optimistic scenarios, where the dark energy equation of state deviates sufficiently from $w_{\text{de}} = -1$, a combination of cluster and CMB surveys hold the potential to pin down the order of magnitude of the dark energy sound speed.

It must be mentioned that the analysis in this paper has a few drawbacks. First, our parameter settings for the Euclid mission are on the optimistic side. Second, the Fisher matrix tends to underestimate the uncertainty on the parameters if the posterior deviates from a Gaussian. Third, we use the "quasi-linear" treatment of chapter 9, which suffers drawbacks previously discussed. In chapter 11, we remedy the above by adjusting the survey parameters, applying an MCMC analysis of the parameter space, and a scheme that interpolates between two limits of dark energy clustering. Chapter 12 describes our attempt at a non-linear treatment of dark energy fluid in the spherical collapse.

Confronting the sound speed of dark energy with future cluster surveys

Tobias Basse¹, Ole Eggers Bjælde¹, Steen Hannestad¹ and Yvonne Y. Y. Wong²

¹ Department of Physics and Astronomy, Aarhus University, Ny Munkegade 120, DK-8000 Aarhus C, Denmark

² Institut für Theoretische Teilchenphysik und Kosmologie RWTH Aachen, D-52056 Aachen, Germany

E-mail: basse@phys.au.dk, oeb@phys.au.dk, sth@phys.au.dk, yvonne.wong@physik.rwth-aachen.de

Abstract.

Future cluster surveys will observe galaxy clusters numbering in the hundred thousands. We consider how these surveys can be used to constrain dark energy parameters: in particular, the equation of state parameter w and the non-adiabatic sound speed c_s^2 . We demonstrate that, in combination with Cosmic Microwave Background (CMB) observations from Planck, cluster surveys such as that in the ESA Euclid project will be able to determine a time-independent w with sub-percent precision. Likewise, if the dark energy sound horizon falls within the length scales probed by the cluster survey, then c_s^2 can be pinned down to within an order of magnitude. In the course of this work, we also investigate the process of dark energy virialisation in the presence of an arbitrary sound speed. We find that dark energy clustering and virialisation can lead to dark energy contributing to the total cluster mass at approximately the 0.1% level at maximum.

1. Introduction

Current observational evidence for the accelerated expansion of the universe is compelling [1–3]. This accelerated expansion is generally attributed to the presence of a “dark energy” component in the universe’s energy budget, a component with a strong negative pressure which dominates gravitational physics on large scales. The nature of this dark energy is, however, still a secret the universe keeps to itself—at least for now—and much effort is being invested to measure the properties of this dark energy in order that we may reveal its secret one day.

Because of its unknown nature, there is no shortage of explanations for what this dark energy may be [4]. Therefore, in order to distinguish between the various explanations, we must appeal to a range of observational tests, each probing a different aspect of dark energy dynamics. The distribution of galaxy clusters in the universe, as quantified by the cluster mass function, is one such observational test [5–8].

The cluster mass function (or halo mass function) is sensitive to dark energy properties primarily through their effects on the growth function. Firstly, the dark energy equation of state $w \equiv \bar{P}_Q/\bar{\rho}_Q$, where \bar{P}_Q and $\bar{\rho}_Q$ denote respectively the mean pressure and the mean energy density, affects the universal expansion rate. This in turn alters the overall growth rate of structures, and can be probed by way of the cluster abundance as a function of redshift. Secondly, if the dark energy is associated with a characteristic scale (such as a sound horizon), then the growth function will also inherit this scale-dependence. Indeed, as demonstrated in [8–11], a non-adiabatic dark energy sound speed c_s^2 differing from unity leads to the clustering of dark energy on scales larger than the sound horizon. This in turn introduces a scale-dependence in the clustering of matter, which, as we shall show, ultimately translates into a distinctive mass-dependence in the cluster abundance. Note that in the case of a vanishing sound speed, dark energy is comoving with dark matter and clusters on all scales, a case that has been studied in e.g., [12, 13].

The purpose of this work is therefore two-fold. Firstly, we wish to estimate as best we can the dependence of the cluster mass function on the dark energy equation of state and non-adiabatic sound speed. To this end, we make use of the Press-Schechter formalism [14], which takes as an input the linear matter power spectrum and the linear threshold density from the spherical collapse model. Linear power spectra for nonstandard values of w and c_s^2 are readily calculable using a Boltzmann code such as CLASS [15]. Likewise, a method for estimating the (cluster-mass dependent) linear threshold density in the case of $c_s^2 \neq 0, 1$ was previously established in [9]. What remains to be determined is the fractional contribution of clustering dark energy to the total halo mass, and for this purpose we must address the issue of virialisation in the presence of clustering dark energy. Virialisation of a combined matter and dark energy system has been studied in, e.g., [16], in the limit $c_s^2 = 0$ in the context of the spherical collapse model. In this work, we propose a simple method to track the virialisation process in a spherical collapse for an arbitrary dark energy sound speed.

Secondly, having computed the cluster abundance as a function of w and c_s^2 , we wish to investigate the sensitivities of future cluster surveys to these parameters. In particular, the Euclid project expects to observe some half a million clusters through weak gravitational lensing [17]. Using the appropriate survey specifications, we perform a parameter sensitivity forecast for Euclid based on the Fisher matrix approach.

The paper is organised as follows. In section 2 we review the spherical collapse model and the issue of virialisation in dark energy cosmologies. In section 3 we present the cluster mass function as functions of the dark energy parameters w and c_s^2 . The sensitivities of Euclid to these parameters are investigated in section 4. Section 5 contains our conclusions.

2. Virialisation in the spherical collapse model

2.1. The spherical top hat and equations of motion for the matter component

In the spherical collapse model, a spherically symmetric overdense region is assumed to sit on top of an otherwise uniform background matter density field. The overdense region has a physical radius $R_i \equiv R(\tau_i)$ at the initial (conformal) time τ_i , and a uniform initial energy density

$$\rho_m^{\text{th}}(\tau_i) \equiv \bar{\rho}_m(\tau_i)(1 + \delta_{m,i}^{\text{th}}), \quad (2.1)$$

where $\bar{\rho}_m(\tau)$ denotes the energy density of the background matter field. This is our spherical “top-hat” perturbation, and the mass contained within the top-hat region is given by

$$M_{\text{halo}} = \frac{4\pi}{3} \bar{\rho}_m(\tau_i)(1 + \delta_{m,i}^{\text{th}})R_i^3 = \frac{4\pi}{3} \bar{\rho}_m(\tau_0)(1 + \delta_{m,i}^{\text{th}})X_i^3, \quad (2.2)$$

where τ_0 denotes the present time, and we have defined $X \equiv R/a$ as the comoving radius of the top hat.

The evolution of the physical top-hat radius R with respect to *cosmic time* t is described by the familiar equation of motion

$$\frac{1}{R} \frac{d^2 R}{dt^2} = -\frac{4\pi G}{3}(\rho_m^{\text{th}} + \rho_Q^{\text{th}} + 3P_Q^{\text{th}}), \quad (2.3)$$

where we have incorporated in the equation a dark energy component denoted by the subscript Q . Like the matter component, the dark energy component is taken to be uniform inside the top hat region defined by the radius R . Equation (2.3) can be equivalently expressed as an equation of motion for the comoving top-hat radius X with respect to conformal time τ ,

$$\frac{\ddot{X}}{X} + \mathcal{H} \frac{\dot{X}}{X} = -\frac{4\pi G}{3} a^2 [\bar{\rho}_m \delta_m^{\text{th}} + \bar{\rho}_Q (1 + 3c_s^2) \delta_Q^{\text{th}}], \quad (2.4)$$

where $\cdot \equiv \partial/\partial\tau$, $\mathcal{H} = aH$ is the conformal Hubble parameter, and

$$c_s^2 \equiv \frac{\delta P_Q}{\delta \rho_Q} \quad (2.5)$$

is the square of dark energy sound speed defined in the rest frame of the dark energy fluid. Note that in identifying c_s in equations (2.4) and (2.5) as the rest frame sound speed, we have implicitly assumed that we are dealing only with length scales much smaller than the Hubble length, and that the relative velocity between the dark energy and the dark matter fluids is much smaller than the speed of light. We also assume c_s^2 to be constant in time and space.

Since the total mass of matter inside the top hat $M_{\text{halo}} = (4\pi/3)\rho_m^{\text{th}}R^3$ is conserved, the top-hat matter density contrast δ_m^{th} can be easily expressed as a function of the top-hat radius,

$$\begin{aligned}\delta_m^{\text{th}}(\tau) &\equiv \frac{\rho_m^{\text{th}}(\tau)}{\bar{\rho}_m(\tau)} - 1 \\ &= (1 + \delta_{m,i}^{\text{th}}) \left[\frac{a(\tau)}{a(\tau_i)} \frac{R_i}{R(\tau)} \right]^3 - 1 = (1 + \delta_{m,i}^{\text{th}}) \left[\frac{X_i}{X(\tau)} \right]^3 - 1.\end{aligned}\quad (2.6)$$

In the absence of dark energy perturbations, equations (2.4) and (2.6) form a closed system for the matter component.

2.2. Equations of motion for the dark energy component

On sub-horizon scales, the pseudo-Newtonian approach [18] applies, so that the (Fourier space) equations of motion for the dark energy density perturbations read [9]

$$\begin{aligned}\dot{\tilde{\delta}}_Q + 3\mathcal{H}(c_s^2 - w)\tilde{\delta}_Q + (1 + w)\tilde{\theta}_Q &= 0, \\ \dot{\tilde{\theta}}_Q + (1 - 3c_s^2)\mathcal{H}\tilde{\theta}_Q - \frac{k^2 c_s^2}{1 + w}\tilde{\delta}_Q + 4\pi G a^2 [\bar{\rho}_m \tilde{\delta}_m + \bar{\rho}_Q \tilde{\delta}_Q] &= 0,\end{aligned}\quad (2.7)$$

where the top-hat matter density contrast is given in Fourier space by

$$\tilde{\delta}_m(k, \tau) = \frac{4\pi}{3} [(1 + \delta_{m,i}^{\text{th}}) X_i^3 - X^3] W(kX), \quad (2.8)$$

with the filter function

$$W(kX) = \frac{3}{(kX)^3} [\sin(kX) - kX \cos(kX)]. \quad (2.9)$$

The dark energy density contrast $\tilde{\delta}_Q^{\text{lin}}(k, \tau)$ is then related to its top-hat average $\delta_Q^{\text{th}}(\tau)$, as appearing in equation (2.4), via

$$\delta_Q^{\text{th}}(\tau) = \frac{1}{2\pi^2} \int dk k^2 W(kX) \tilde{\delta}_Q^{\text{lin}}(k, \tau). \quad (2.10)$$

We refer the reader to reference [9] for a more detailed discussion of this formulation, but note that in equation (2.7) we have only kept terms up to linear order in the perturbed quantities $\tilde{\delta}_Q$ and $\tilde{\theta}_Q$. This is a reasonable approximation for $\tilde{\delta}_Q$ not exceeding unity, a condition that is generally satisfied during most of the spherical collapse process except the final moment of collapse [9].

Equations (2.4) and (2.7) have been solved in [9] for a range of top-hat masses to determine the linear threshold density δ_c as a function of the halo mass. In particular,

figure 5 in the said paper shows a distinct step-like feature in $\delta_c(M)$, with the step occurring in the vicinity of the “Jeans mass”

$$M_J(a) \equiv \frac{4\pi}{3} \bar{\rho}_m(a) \left(\frac{\lambda_J(a)}{2} \right)^3, \quad (2.11)$$

where $\lambda_J \equiv 2\pi/k_J$ and $k_J \equiv \mathcal{H}/c_s$ are the Jeans’ length and wavenumber respectively associated with dark energy clustering.

2.3. Dark energy contribution to the cluster mass

So far we have not considered the possibility that clustering dark energy might also contribute to the mass of the collapsed object. Following [12], we define the dark energy contribution to the total mass as

$$M_Q \equiv \frac{4\pi}{3} R(\tau)^3 \delta\rho_Q^{\text{th}}(\tau), \quad (2.12)$$

with

$$\delta\rho_Q^{\text{th}}(\tau) = \bar{\rho}_Q(\tau) \delta_Q^{\text{th}}(\tau) \equiv \bar{\rho}_Q(\tau) \frac{3}{X^3} \int_0^X dx x^2 \delta_Q(x, \tau), \quad (2.13)$$

where we have smoothed the dark energy density contrast over the spherical top hat. In defining M_Q in this manner, we have implicitly assumed that only the dark energy perturbations contribute to the total mass of the bound object, and that once gravitationally bound, the dark energy perturbations behave like non-relativistic matter. It then follows that

$$M_{\text{tot}} \equiv M_{\text{halo}} + M_Q \quad (2.14)$$

gives the total mass of the system.

2.4. Virialisation

In the spherical collapse model, a gravitationally-bound halo is said to have formed in the top-hat region at the instant at which the virial theorem is first satisfied. After this time, the spherical region is taken to remain in a fixed configuration, with a constant radius R_{vir} and mass M_{vir} (even though formally the equations of motion dictate that the region should eventually collapse to a point of infinite density).

When only dark matter clusters and virialises, mass is conserved in the collapsing spherical region, and the virial radius R_{vir} can be computed relatively simply by following the kinetic and potential energies of the collapsing matter and the potential energy of the dark energy contained in the spherical region. This case of dark energy not participating in the virialisation process was examined in e.g. [16, 19]. However, when clustering dark energy also partakes in the virialisation process, the condition for virialisation changes from these simple prescriptions, because unless $c_s^2 = 0$, dark energy is not conserved in the spherical region. This necessitates a reexamination of the virialisation conditions in clustering dark energy cosmologies. Such an analysis has been carried out in [16], where both the homogeneous background as well as the clustered part of dark energy

take part in virialisation. See also [20–23] for other studies of dark energy virialisation. Based on our definition of M_Q in equation (2.12), however, we will assume that only the clustered part of dark energy virialises.

Our starting point is the tensor virial theorem for a system of point particles [24],

$$\frac{1}{2} \frac{d^2 I_{jk}}{dt^2} = 2K_{jk} + W_{jk}, \quad (2.15)$$

where K_{jk} and W_{jk} are the kinetic-energy and potential-energy tensor respectively, and I_{jk} is defined as

$$I_{jk} \equiv \sum_{\alpha} m_{\alpha} x_{\alpha j} x_{\alpha k}, \quad (2.16)$$

with α running over the particles, and \mathbf{x}_{α} denoting their positions. Taking the trace of the equation (2.15) and assuming that the system is in a steady state, we find the well-known scalar virial theorem,

$$\frac{d^2 I}{dt^2} = 0, \quad (2.17)$$

where $I \equiv \text{trace}(\mathbf{I})$. Since the trace I is precisely the moment of inertia of the system, the condition for virialisation can also be paraphrased as the vanishing of its second time-derivative.

For a spherical system, the moment of inertia for a set of non-relativistic particles is

$$I = 2M_{\text{tot}}R^2/5, \quad (2.18)$$

where M_{tot} denotes the mass that takes part in virialisation. Thus, in the case that mass is conserved in the spherical region (i.e., $dM_{\text{tot}}/dt = 0$), equation (2.17) together with equation (2.18) provide a simple relation between the radius of the system and the first and second derivatives of the radius with respect to time at the time of virialisation:

$$\frac{1}{R^2} \left(\frac{dR}{dt} \right)^2 + \frac{1}{R} \frac{d^2 R}{dt^2} = 0. \quad (2.19)$$

In an Einstein-de Sitter universe ($\Omega_m = 1$) where only dark matter clusters and virialises, mass is conserved in the collapsing region, and equation (2.19) dictates that virialisation happens when the radius of the system reaches half the radius at turn-around, i.e., $R_{\text{vir}} = (1/2)R_{\text{ta}}$, where turn-around refers to the instant at which the expansion of the spherical object stalls and the region starts to collapse (i.e., $dR/dt|_{\text{ta}} = 0$).

Generalising to the case of mass non-conservation (such as when dark energy also clusters and virialises), we find from equations (2.17) and (2.18) the virialisation condition

$$\frac{1}{2M_{\text{tot}}} \frac{d^2 M_{\text{tot}}}{dt^2} + \frac{2}{M_{\text{tot}}R} \frac{dM_{\text{tot}}}{dt} \frac{dR}{dt} + \frac{1}{R^2} \left(\frac{dR}{dt} \right)^2 + \frac{1}{R} \frac{d^2 R}{dt^2} = 0, \quad (2.20)$$

where M_{tot} is the total mass of the system given by equation (2.14). In practice, after solving the spherical collapse, we locate the time at which equation (2.20) is satisfied. The total mass of the system at that time is then taken to be the virial mass M_{vir} of the collapsed object.

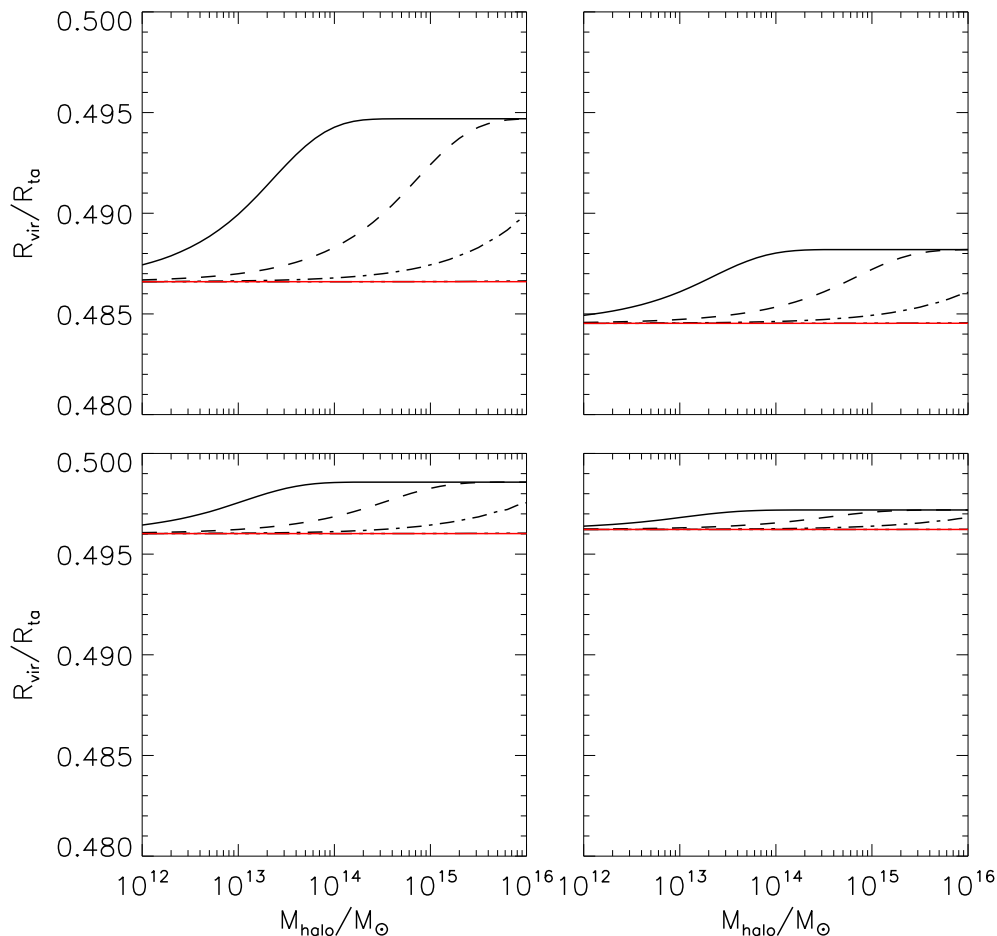


Figure 1. The virial radius R_{vir} , normalised to the radius at turnaround R_{ta} , as a function of the dark matter halo mass M_{halo} . The left and right panels correspond to $w = -0.8$ and $w = -0.9$ respectively, while the upper and lower panels correspond to collapse at $z = 0$ and at $z = 1$. The solid black lines correspond to $c_s^2 = 10^{-6}$, dashed lines to 10^{-5} , dash-dot to 10^{-4} , and dash-dot-dot-dot to 10^{-2} . The solid red line corresponds to $c_s^2 = 1$.

2.5. Results

Figure 1 shows the radius of the spherical halo at the time of virialisation as a function of the halo’s dark matter mass for several clustering dark energy cosmologies. For clarity we have normalised the results to the radius at turn-around (i.e., the time at which $dR/dt = 0$). As with the linear threshold density δ_c in figure 5 of [9], a distinct step-like feature at the Jeans mass can be seen in the mass-dependence of the virial radius R_{vir} . The case of $c_s^2 = 10^{-6}$, for example, has $M_J \sim 10^{14} M_\odot$, as is evident in figure 1.

The results presented in figure 1 can be understood in terms of a combination of several different effects: (i) the overall effect of the background homogeneous dark energy, (ii) the evolution of the ratio of the dark energy to dark matter densities, and (iii) the effect of the dark energy clustering.

Firstly, adding a homogeneous dark energy to the universe adds a negative pressure and hence a negative contribution to the spherical system's potential energy, making it more difficult for the system to virialise. The equation of state of dark energy tells us how strong this pressure is. Thus, the overall effect of the background dark energy is that $R_{\text{vir}}/R_{\text{ta}}$ becomes smaller compared to the Einstein-de Sitter case, in which $R_{\text{vir}}/R_{\text{ta}} = 0.5$ as discussed in the previous section.

Secondly, the more w deviates from -1 (in the positive direction), the less rapidly the ratio ρ_Q/ρ_m evolves with time. Fixing the ratio at $z = 0$, this means that at high redshifts dark energy is present in smaller amounts in models with $w = -0.9$ than in models with $w = -0.8$. The net effect is that $R_{\text{vir}}/R_{\text{ta}}$ changes more dramatically as a function of time for $w = -0.9$ than for $w = -0.8$. (Note that the redshift at which dark energy starts to dominate over dark matter is $z \sim 0.45$ and $z \sim 0.52$ for $w = -0.9$ and $w = -0.8$ respectively.)

The final effect of dark energy clustering draws $R_{\text{vir}}/R_{\text{ta}}$ more closely to the value for an Einstein-de Sitter universe, because a larger portion of the spherical object now participate in virialisation, and the virialisation of dark energy has been assumed in our work to proceed like non-relativistic matter. As previously explained, the dark energy sound speed sets the scale at which dark energy clustering becomes relevant, and the transition from weak to strong clustering is clearly evident in figure 1 in the case of $c_s^2 = 10^{-6}$. The accompanying figure 2 shows the contribution of dark energy to the total halo mass relative to the dark matter contribution at the time of virialisation. Clearly, dark energy clustering becomes more efficient with increasing halo mass, in the sense that the dark energy contribution to the total mass of the halo becomes increasingly important. However, this relative contribution does not increase indefinitely: M_Q/M_{halo} saturates at just above the Jeans mass, reaching a value of order 10^{-3} . Comparing the M_Q/M_{halo} ratio at different redshifts, we see that the contribution of dark energy to the mass of the system is larger at $z = 0$ than at $z = 1$. This follows simply from the fact that dark energy dominates the energy budget more at later times.

3. The cluster mass function

The cluster mass function is a power probe of dark energy properties. Firstly, its redshift dependence can be used to pin down the time evolution of the linear growth function, and hence the also the dark energy density as a function of time. Secondly, because the cluster mass function counts the comoving number density of virialised objects per mass interval, it can also be used to probe scale-dependent effects, such as the presence of a sound horizon due to a sound speed in the dark energy fluid.

A fully accurate cluster mass function can in principle only be computed by way of numerical simulations (e.g., N -body methods). However, for the purpose of a parameter error forecast, it suffices to estimate of the generic effects of dark energy using semi-analytical methods. To this end, we adopt the Press-Schechter formalism [14], which prescribes a cluster mass function in the mass interval $[M_{\text{vir}}, M_{\text{vir}} + dM_{\text{vir}}]$ and at redshift

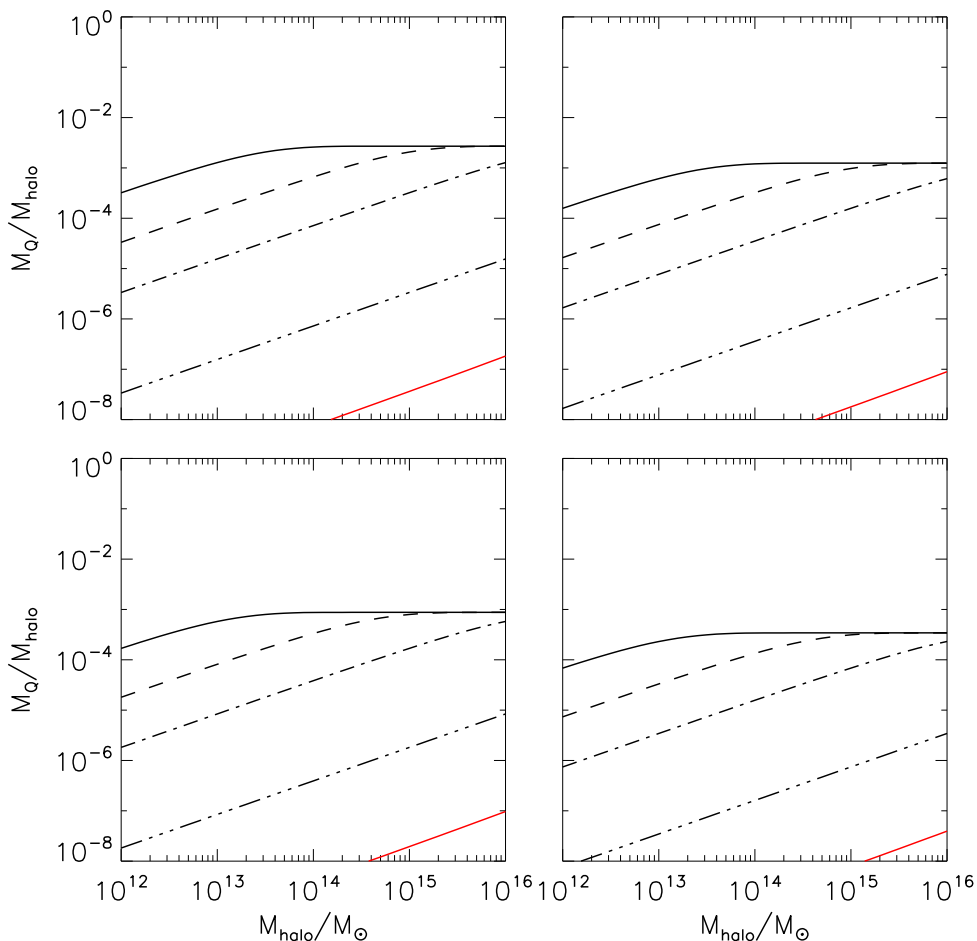


Figure 2. Dark energy contribution to the total mass at virialisation relative to the dark matter mass. The left and right panels correspond to $w = -0.8$ and $w = -0.9$ respectively, while the upper and lower panels correspond to collapse at $z = 0$ and $z = 1$. The solid black lines correspond to $c_s^2 = 10^{-6}$, dashed lines to 10^{-5} , dash-dot to 10^{-4} , and dash-dot-dot-dot to 10^{-2} . The solid red line corresponds to $c_s^2 = 1$.

z of the form

$$\frac{dn}{dM_{\text{vir}}}(M_{\text{vir}}, z)dM_{\text{vir}} = \sqrt{\frac{2}{\pi}} \frac{\bar{\rho}_{m,0}}{M_{\text{vir}}^2} \nu \frac{d \ln \nu}{d \ln M_{\text{vir}}} \exp\left[-\frac{\nu^2}{2}\right] dM_{\text{vir}}. \quad (3.1)$$

Here, $\bar{\rho}_{m,0}$ is the present-day matter density, and $\nu \equiv \delta_c(z)/\sigma_m(M_{\text{vir}}, z)$, with $\delta_c(z)$ the linear threshold density (for matter) at collapse and $\sigma_m(M_{\text{vir}}, z)$ the variance of the linear matter density field. The latter can be computed from linear matter power spectrum $P_m^{\text{lin}}(k, z)$ via

$$\sigma_m^2(M_{\text{vir}}, z) \equiv \frac{1}{2\pi^2} \int_0^\infty dk k^2 |W(kR)|^2 P_m^{\text{lin}}(k, z), \quad (3.2)$$

where $|W(kR)|$ is the Fourier space representation of a spherical top-hat filter of radius R , and $M_{\text{vir}} = \frac{4\pi}{3} \bar{\rho}_m(z) R^3$ relates R to the virial mass of the collapsed object via the

mean matter density $\bar{\rho}_m(z)$ at redshift z .[‡] The linear power spectrum $P_m^{\text{lin}}(k, z)$ can be obtained from a Boltzmann code such as CLASS [15]; the publicly available version already incorporates an option for constant adiabatic dark energy sound speeds.

Apart from its effect on the linear power spectrum, a dark energy sound speed also gives rise to a mass-dependence in the linear threshold density δ_c [9]. This can be incorporated into the Press-Schechter mass function (3.1) simply by promoting

$$\nu \equiv \frac{\delta_c(z)}{\sigma_m(M_{\text{vir}}, z)} \rightarrow \frac{\delta_c(M_{\text{vir}}, z)}{\sigma_m(M_{\text{vir}}, z)}, \quad (3.3)$$

where $\delta_c(M_{\text{vir}}, z)$ is computed from following a spherical collapse as discussed in section 2. See [9] for details. Note that the definition of M_{vir} here includes the contribution from clustered dark energy M_Q .

3.1. Results

Figure 3 shows the cluster mass functions at redshifts $z = 0$ and $z = 1$, for two cosmologies with $w = -0.9$ and $w = -0.8$ respectively, and a common sound speed $c_s^2 = 1$. Other cosmological parameters have been fixed at the WMAP7 Λ CDM best-fit values [1]. The corresponding linear matter power spectrum are also shown in the same figure. Dark energy dominates earlier in the case of $w = -0.8$ compared to $w = -0.9$, leading to a slightly scale-dependent suppression in the matter power spectrum of order 8% at $z = 0$ and 5% at $z = 1$. This suppression of power due to a larger w is also reflected in the cluster mass function in the form of a decrease in the number of massive objects. At $10^{16}M_\odot$, the $w = -0.9$ cosmology has four times more objects than the $w = -0.8$ case at $z = 0$, and two times at $z = 1$.

Compared with the effect of w , changing the dark energy sound speed from $c_s^2 = 1$ to a smaller value has a considerably smaller effect on both the linear matter power spectrum and the cluster mass function. Figure 4 shows the linear matter power spectra for fixed $w = -0.9$ and $w = -0.8$, while varying the dark energy sound speed between $c_s^2 = 10^{-2}$ and 10^{-6} . The normalised (to the $c_s^2 = 1$ case) spectra show that changing the dark energy sound speed induces an additional scale dependence the matter power spectrum. In particular, on scales above the sound horizon and below the Hubble horizon, the amplitude of the matter power spectrum is enhanced. In the $w = -0.8$ case, the enhancement is only 2% at $z = 0$, and less than 1% at $z = 1$. The $w = -0.9$ case sees even less enhancement. Note that on scales close to the Hubble horizon (i.e., at very small values of k), a $c_s^2 \ll 1$ in fact causes the matter density contrast to decrease. This is an artifact of the synchronous gauge used in the computation of the matter power spectrum (see, e.g., [10]), and has no consequence on the observable scales.

Interestingly, the effect of a dark energy sound speed appears to be somewhat more sizable on the cluster mass function. Figure 5 shows the cluster mass functions for a range of dark energy sound speeds, all of which have been normalised to the $c_s^2 = 1$

[‡] On average, the dark energy does not contribute to the mass, since only the perturbations have been included in the definition M_Q in equation (2.12).

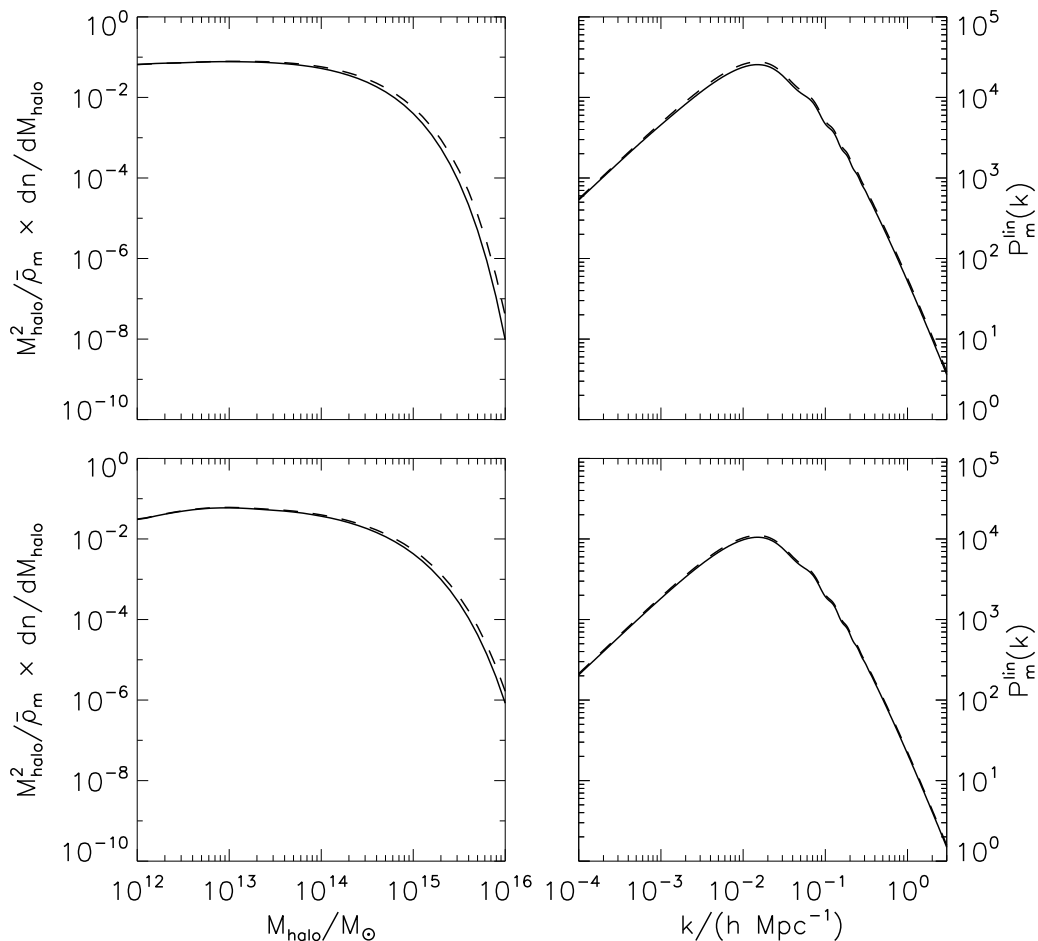


Figure 3. Cluster mass functions (left) and linear matter power spectra (right) for the case of $c_s^2 = 1$. Solid lines represent a cosmology with $w = -0.8$, and dashed lines to $w = -0.9$. The upper and lower panels correspond to collapse at $z = 0$ and $z = 1$ respectively.

case. Evidently, clustering dark energy with sound speeds in the range $c_s^2 = 10^{-6} \rightarrow 10^{-4}$ increases the number of massive objects ($\sim 10^{16} M_\odot$) at $z = 0$ by as much as 15% in the $w = -0.8$ case, and 5% in the $w = -0.9$ case.

The astute reader will have noticed by now that some of the cluster mass functions presented in figure 5 have rather peculiar shapes. This calls for an explanation. Firstly, it is clear from equation (3.1) that the Press-Schechter mass function represents an interplay between the linear threshold density at collapse δ_c and the variance of the matter density field σ_m , with the relevant measure being the ratio $\nu = \delta_c/\sigma_m$ which generally increases with M_{vir} . The shape of the cluster mass function for large masses is dominated by the exponential factor $\exp(-\nu^2/2)$ in equation (3.1), as can be discerned from figure 3. Here, for a fixed value of M_{vir} , the role of dark energy clustering is to subtly increase $\sigma_m(M_{\text{vir}})$ via its effect on the linear matter power spectrum as per equation (3.2), especially for cluster masses exceeding the Jeans mass M_J . This leads to

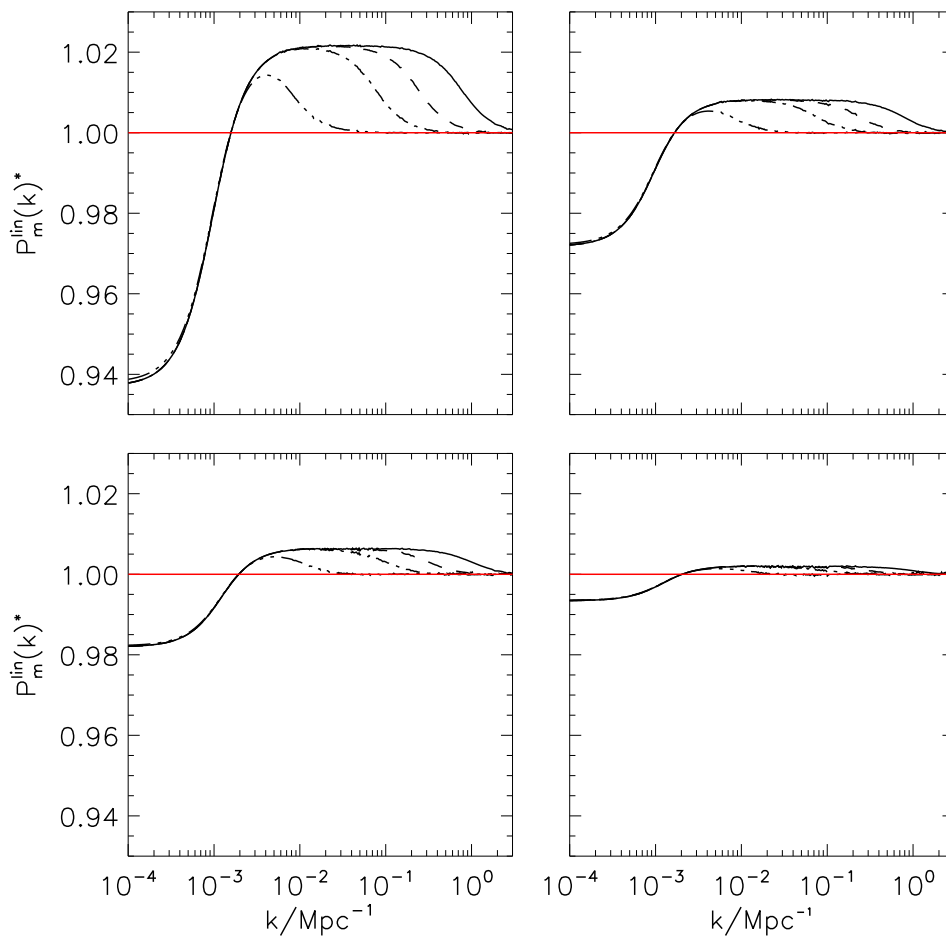


Figure 4. Linear matter power spectra for various values of c_s^2 normalised to the $c_s^2 = 1$ case. The left and right panels correspond to $w = -0.8$ and $w = -0.9$ respectively, while the upper panels show $z = 0$ and the lower ones $z = 1$. The solid black lines correspond to $c_s^2 = 10^{-6}$, dashed lines to 10^{-5} , dash-dot to 10^{-4} , and dash-dot-dot-dot to 10^{-2} .

a lower ν , and hence an increased number of halos on large scales. This is the primary cause of the shapes of the cluster mass functions in figure 5.

Secondly, when the dark energy sound speed deviates from $c_s^2 = 1$, the linear threshold density δ_c is a function of the cluster mass M_{vir} . This dependence on M_{vir} is most pronounced at masses around the Jeans mass M_J ; away from M_J , δ_c asymptotes to δ_c^{min} at $M_{\text{vir}} \ll M_J$, and to δ_c^{max} at $M_{\text{vir}} \gg M_J$ [9]. For the case of $c_s^2 = 10^{-6}$ (solid line in figure 5), for instance, the sudden increase in δ_c occurs at around $M_J = 4 \times 10^{14} M_\odot$. This increase in δ_c compensates the growth of σ_m with respect to M_{vir} , thereby causing a plateau in the cluster mass function. At $M_{\text{vir}} \gg M_J$, δ_c asymptotes to δ_c^{max} , and the cluster mass function recovers its exponential behaviour.

To clarify this interplay between $\delta_c(M_{\text{vir}})$ and $\sigma_m(M_{\text{vir}})$, we show in figure 6 the cluster mass functions that would have arisen had the linear threshold density δ_c been fixed at δ_c^{vir} (i.e., the value of δ_c at in the case of no dark energy clustering). Observe

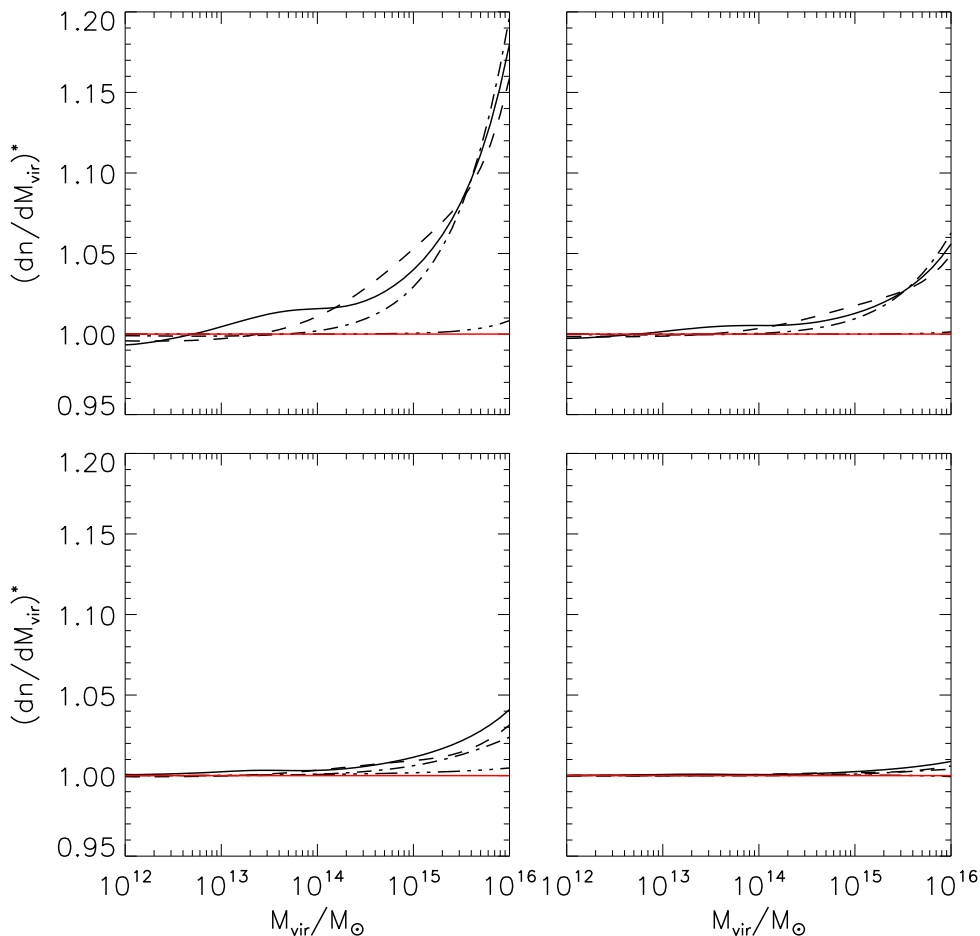


Figure 5. Cluster mass functions for various values of c_s^2 normalised to the $c_s^2 = 1$ case. The left and right panels correspond to $w = -0.8$ and $w = -0.9$ respectively, while the upper panels show $z = 0$ and the lower ones $z = 1$. The solid black lines correspond to $c_s^2 = 10^{-6}$, dashed lines to 10^{-5} , dash-dot to 10^{-4} , and dash-dot-dot-dot to 10^{-2} .

the absence of the aforementioned plateau. Note also that the number of very massive clusters is a little higher here than in the figure 5. This is because the higher δ_c at large M_{vir} in figure 5 leads to a stronger exponential suppression.

Finally, we note that the mass-dependence of the linear threshold density $\delta_c(M_{\text{vir}})$ has been computed in this work using a linear treatment of the dark energy perturbations adopted from [9]. While this approximation works well up to the Jeans scale, it breaks down at $M > M_J$ because the dark energy density contrast inevitably exceeds unity at the time of collapse. This break-down leads to an overestimation of the exact value of δ_c at $M > M_J$, because nonlinear dark energy clustering is expected to feed back on the matter clustering more efficiently, thereby leading to an earlier collapse for $w > -1$ than is implied by our linear treatment. An earlier collapse in turn leads to less evolution for the linear matter density contrast, and hence a δ_c at $M > M_J$ that is lower than that computed using our linear approximation.

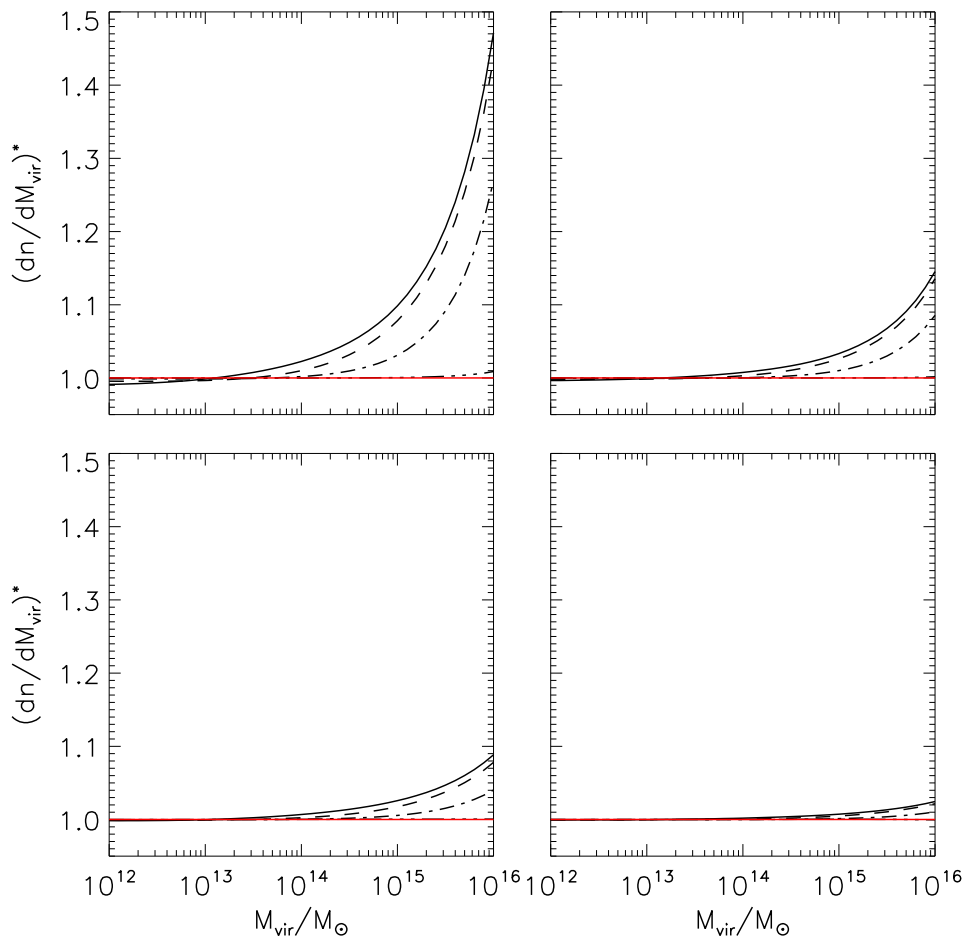


Figure 6. Same as figure 5, but for a linear threshold density δ_c fixed at a mass-independent $\delta_c(z) = \delta_c(z, c_s^2 = 1)$.

Fortunately, however, the mass-dependence of δ_c works to counter the effect of dark energy clustering on σ_m , so that, as shown in figures 5 and 6, the contrasts between the cluster mass functions for different values of c_s^2 are smaller when δ_c has been allowed to vary with M_{vir} than when it has not. (Compare figures 5 and 6 also to figure 7 of [12].) In other words, our overestimation of δ_c at $M > M_J$ leads to an *underestimation* of the effect of c_s^2 on the cluster mass function. Thus, when we confront our semi-analytical cluster mass functions with future observations in the next section, the sensitivities to c_s^2 that will be derived will be conservative.

4. Constraining dark energy with future cluster surveys

In this section we perform a forecast for the sensitivity of the Euclid cluster survey to the dark energy equation of state parameter w and non-adiabatic sound speed c_s^2 using the Fisher matrix formalism. As we expect data of the cosmic microwave background anisotropies from Planck to be available long before Euclid is launched, we combine the

constraints from the Euclid cluster survey with those from Planck.

4.1. Fisher matrix formalism

The Fisher matrix formalism provides a quick way to compute the expected sensitivity of an experiment to cosmological parameters. Although Monte Carlo methods are arguably a more robust forecast tool [25], we opt not to use it here because of the time consuming real-time evaluation of the spherical collapse. Furthermore, the Fisher matrix has the advantage that, once computed, individual Fisher matrices for different observational probes can be combined together by simple addition. Priors on specific parameters can likewise be incorporated into the Fisher matrix by adding $\sigma^{-2}(p_i)$ to the ii entry. We shall make use of these properties when assessing the constraining power of Euclid and Planck, both separately and in combination.

The Fisher matrix is defined as

$$F_{ij} \equiv \left\langle -\frac{\partial^2 (\ln \mathcal{L})}{\partial p_i \partial p_j} \right\rangle, \quad (4.1)$$

where \mathcal{L} is the likelihood function, and p_i is the i th parameter of the model. The inverse Fisher matrix, $(F^{-1})_{ij}$, provides the best attainable covariance matrix, regardless of the specific method used to estimate the parameters from the data [26]. As a consequence, $(F^{-1})_{ii}^{1/2}$ is the optimal statistical uncertainty attainable on parameter p_i after marginalisation over all other model parameters.

Assuming a Gaussian likelihood function, the Fisher matrix for the Euclid cluster survey can be constructed as [27, 28]

$$F_{ij} = \sum_{\alpha} \frac{\partial N_{\alpha}}{\partial p_i} \frac{\partial N_{\alpha}}{\partial p_j} \frac{1}{N_{\alpha}}, \quad (4.2)$$

where

$$N_{\alpha} = \Delta\Omega\Delta z \frac{d^2V}{d\Omega dz}(z_{\alpha}) \int_{M_{\min}(z_{\alpha})}^{\infty} \frac{dn(M, z_{\alpha})}{dM} dM \quad (4.3)$$

is the number of clusters with masses above the detection threshold $M_{\min}(z_{\alpha})$ in a redshift bin centered on z_{α} . In our analysis we consider 13 redshift bins from $z = 0.1$ to $z = 1.4$ with bin width $\Delta z = 0.1$, chosen so that Δz is twice the expected uncertainty in the determination of the cluster redshifts in the survey [17]. We assume the redshift bins to be top-hat functions, effectively ignoring small leakages that may arise as a result of a cluster being assigned to the wrong redshift bin. Note that a cluster survey such as Euclid extends to $z \sim 2$. However, our analysis shows that the number of detectable clusters is negligible already at $z \sim 1.4$ since M_{\min} at this redshift is of order $10^{16} M_{\odot}$. The remaining quantities in the expression (4.3) are $\Delta\Omega$ the solid angle covered by the survey, $d^2V/(d\Omega dz)(z_{\alpha})$ the comoving volume element at redshift z_{α} , and $dn/dM(M, z_{\alpha})$ is the cluster mass function discussed in section 3.

Table 1. Euclid survey parameters. See section 4.2 for an explanation.

Parameter	Value	Parameter	Value
$\Delta\Omega$	20000 deg ²	c_{nfw}	5
θ_G	1 arcmin	α	2
n_{bg}	30 arcmin ⁻²	β	2
σ_ϵ	0.1	z_0	1
Δz	0.1		

4.2. Euclid survey parameters

In order to determine the detection threshold of the weak lensing survey, i.e., $M_{\text{min}}(z_\alpha)$ in equation (4.3), we adopt the approach of [27] and [29]. The average shear within a Gaussian filter of angular size θ_G , κ_G , is related to the mass of the cluster M_{vir} by [27],

$$\kappa_G = \alpha(\theta_G) \frac{M_{\text{vir}} / (\pi R_s^2)}{\Sigma_{\text{cr}}}. \quad (4.4)$$

Assuming the mass distribution in each cluster obeys a Navarro-Frenk-White density profile with a scale radius $R_s = R_{\text{vir}}(M_{\text{vir}}) / c_{\text{nfw}}$, where $R_{\text{vir}}(M_{\text{vir}})$ is determined in this work via the spherical collapse, the coefficient $\alpha(\theta_G)$ is given by

$$\alpha(\theta_G) = \frac{\int_0^\infty dx (x/x_G^2) \exp(-x^2/x_G^2) f(x)}{\ln(1+c_{\text{nfw}}) - c_{\text{nfw}}/(1+c_{\text{nfw}})}. \quad (4.5)$$

Here, $x = \theta/\theta_s$ is an angular coordinate scaled with the angular scale radius $\theta_s = R_s/d_A(z_l)$, $d_A(z_l)$ the angular diameter distance to the cluster at redshift z_l , $x_G \equiv \theta_G/\theta_s$ the smoothing scale, and the dimensionless surface density profile $f(x)$ is given by equation (7) of [29].

In a geometrically flat universe, the mean inverse critical surface mass density is

$$\Sigma_{\text{cr}}^{-1} = \frac{4\pi G}{c^2(1+z_l)} \chi(z_l) \frac{\int_{z_l}^\infty dz dn/dz (1 - \chi(z_l)/\chi(z))}{n_{\text{bg}}}, \quad (4.6)$$

where χ denotes the comoving radial distance to the cluster, and dn/dz is the number density of source galaxies per steradian at redshift z , normalised such that $n_{\text{bg}} = \int_0^\infty dz dn/dz$. We assume that dn/dz takes the form [30]

$$\frac{dn}{dz} dz = n_{\text{bg}} \frac{\beta}{z_0 \Gamma\left(\frac{1+\gamma}{\beta}\right)} \left(\frac{z}{z_0}\right)^\gamma \exp\left[-\left(\frac{z}{z_0}\right)^\beta\right] dz, \quad (4.7)$$

where γ , β , and z_0 are chosen to fit the observed galaxy redshift distribution. In our analysis, we fix the parameters at $\gamma = 2$, $\beta = 2$, and $z_0 = 1$.

In order for Euclid to detect a lensing signal, the shear κ_G must be larger than the noise. Here we adopt a detection threshold of $\kappa_G = 4.5\sigma_{\text{noise}}$, where the noise term σ_{noise} is modeled as a ratio of the mean ellipticity dispersion of galaxies σ_ϵ and the number of background galaxies within the smoothing aperture $N_{\text{bg}} = 4\pi n_{\text{bg}} \theta_G^2$ [31], i.e.,

$$\sigma_{\text{noise}}^2 = \frac{\sigma_\epsilon^2}{4\pi \theta_G^2 n_{\text{bg}}}. \quad (4.8)$$

Table 2. Fiducial parameter values of the two models analysed in this work.

Parameter		Model 1	Model 2
w	Dark energy equation of state	-0.9	-0.8
$\log c_s^2$	Dark energy sound speed	-6	-6
h	Hubble parameter		0.710
$100\Omega_b h^2$	Physical baryon density		2.26
$10\Omega_{cdm}$	CDM density		2.22
$\log 10^{10} \Delta_{\mathcal{R}}^2$	Primordial fluctuation amplitude		1.39
n_s	Scalar spectral index		0.963

All parameters relevant for the Euclid analysis are listed in table 1. Parameter values are sourced from primarily from [17]; parameter values missing in [17] are taken to match those for the LSST [27].

The detection threshold $M_{\min}(z)$ at a given redshift z can now be computed from equation (4.4) simply by finding the lowest value of M_{vir} at z that satisfies the condition $\kappa_G > 4.5\sigma_{\text{noise}}$. For cosmologies in the vicinity of Λ CDM, the detection threshold is $M_{\min} \sim 10^{13} M_{\odot}$ at $z = 0.15$, and $M_{\min} \sim 9 \times 10^{15} M_{\odot}$ at $z = 1.15$.

4.3. Fiducial Cosmologies

We consider a 7-parameter cosmological model defined by the free parameters

$$\theta = \{w, \log c_s^2, h, \Omega_b h^2, \Omega_{cdm}, \log 10^{10} \Delta_{\mathcal{R}}^2, n_s\}, \quad (4.9)$$

denoting, respectively, the dark energy equation of state, its sound speed, the Hubble parameter, the physical baryon density, the CDM density, the scalar fluctuation amplitude, and scalar spectral index. A flat spatial geometry, i.e., $\Omega_Q = 1 - \Omega_{cdm} - \Omega_b$, has been assumed. We examine two different fiducial cosmologies in our analysis:

- (i) model 1: $w = -0.9$ and $c_s^2 = 10^{-6}$,
- (ii) model 2: $w = -0.8$, and $c_s^2 = 10^{-6}$,

where the remaining model parameters have fiducial values set by the Λ CDM best-fit of the WMAP 7-year observations [1]. See table 2 for details. The value of $c_s^2 = 10^{-6}$ has been chosen such that the characteristic sound horizon scale falls squarely within the length scales resolved by the Euclid cluster survey (recall that the Jeans mass for $c_s^2 = 10^{-6}$ is $\sim 10^{14} M_{\odot}$), while $w = -0.9, -0.8$ correspond approximately to the 1σ and 2σ lower limits inferred from the WMAP7+BAO+ H_0 observations [1].

Ideally, we would also like to examine Euclid's sensitivity to dark energy models with sound speeds close to unity. However, we find that this exercise is not feasible within the Fisher matrix framework. This is because, as shown in figures 5 and 6, a sound speed c_s^2 larger than $\sim 10^{-2}$ has essentially no observable effect on the cluster mass function on the mass scales probed by the Euclid cluster survey ($10^{13} M_{\odot} < M < 10^{16} M_{\odot}$). The corresponding likelihood function is virtually flat in the c_s^2 direction in the neighbourhood of the fiducial model, which is ultimately translated by the Fisher

Table 3. 1σ sensitivities of the Euclid cluster survey to various cosmological parameters in the two fiducial models considered in this work. Note that the uncertainties in $100\Omega_b h^2$ and n_s are identically the priors we set on these parameters using the WMAP 7-year data.

Parameter	Model 1	Model 2
w	0.054	0.065
$\log c_s^2$	1.19	0.46
h	0.074	0.089
$100\Omega_b h^2$	0.10	0.10
$10\Omega_{cdm}$	0.039	0.038
$\log 10^{10} \Delta_{\mathcal{R}}^2$	0.12	0.14
n_s	0.020	0.020

matrix into unbounded or unrealistically lax constraints on c_s^2 (recall that a Fisher matrix forecast is based upon evaluating the curvature of the likelihood function locally at the fiducial model). The failure of the formalism to take into account the full extent of the likelihood function is a severe drawback of the Fisher matrix approach, § which can be remedied only with a full Monte Carlo simulation [25]. We defer this exercise to a later study.

4.4. Constraints from Euclid alone

Table 3 shows the 1σ sensitivities to various cosmological parameters attainable by the Euclid cluster survey alone. Note that when deriving these numbers, we have included the priors $\sigma(\Omega_b h^2) = 0.001$ and $\sigma(n_s) = 0.02$ on $\Omega_b h^2$ and n_s respectively, because the Euclid cluster survey has no particular constraining power for these parameters. These prior ranges correspond approximately to twice the 1σ uncertainties inferred from the WMAP 7-year data [1].

The Euclid cluster survey alone is already fairly sensitive to the dark energy equation of state and hence the evolution of the dark energy density, with a 1σ sensitivity to w of better than 10% in both models 1 and 2. These sensitivities should be compared with the uncertainties on w from the current generation of measurements: for a flat model with $c_s^2 = 1$, a constant w parameter can be constrained to the same level of uncertainty ($\sigma(w) \sim 0.05$) only with a combination of the WMAP 7-year data, measurements of the baryon acoustic oscillations, and type Ia supernovae; dropping the supernova measurements immediately enlarges the uncertainty by at least a factor of two [1].

Our results also show that, if the fiducial dark energy sound speed falls well within the observable range of the cluster survey, then the model can be distinguished from $c_s^2 = 0, 1$ with a good degree of certainty. In our example of $\log c_s^2 = -6$, the 1σ

§ Although the Fisher matrix approach is local in nature, it does return reasonable estimates if the likelihood function does not deviate too much from a (multivariate) Gaussian distribution, for which the curvature in a chosen direction is constant no matter the distance from the best-fit.

Table 4. Survey specifications of Planck in three frequency channels [35].

	100 GHz	143 GHz	217 GHz
θ_c (arcmin)	10.7	8.0	5.5
$\sigma_{T,c}$ (μK)	5.4	6.0	13.1
$\sigma_{E,c}$ (μK)	–	11.4	26.7
ℓ_c	757	1012	1472

sensitivity of Euclid to $\log c_s^2$ is 1.19 and 0.46 for fiducial w values of -0.9 and -0.8 respectively: the sensitivity to $\log c_s^2$ is better in the latter model because dark energy clustering is generally suppressed by a factor $(1+w)$ relative to dark matter clustering.

4.5. Constraints from Planck+Euclid

Planck measures the temperature and polarisation anisotropies of the Cosmic Microwave Background (CMB). These measurements are quantified at the simplest level in terms of auto- and cross-correlations of the temperature T and E -/ B -type polarisation fluctuations. Neglecting B -mode polarisation, the CMB Fisher matrix is given by [32]

$$F_{ij} = \sum_{\ell} \sum_{X,Y} \frac{\partial C_{X,\ell}}{\partial p_i} \text{Cov}^{-1}(C_{X,\ell}, C_{Y,\ell}) \frac{\partial C_{Y,\ell}}{\partial p_j}, \quad (4.10)$$

where X and Y runs over TT , EE and TE , and the entries in the symmetric covariance matrix are given by

$$\begin{aligned} \text{Cov}(C_{TT,\ell}, C_{TT,\ell}) &= \frac{2}{(2\ell+1) f_{\text{sky}}} (C_{TT,\ell} + B_{T,\ell}^{-2})^2, \\ \text{Cov}(C_{EE,\ell}, C_{EE,\ell}) &= \frac{2}{(2\ell+1) f_{\text{sky}}} (C_{EE,\ell} + B_{E,\ell}^{-2})^2, \\ \text{Cov}(C_{TE,\ell}, C_{TE,\ell}) &= \frac{1}{(2\ell+1) f_{\text{sky}}} [C_{TE,\ell}^2 + (C_{TT,\ell} + B_{T,\ell}^{-2})(C_{EE,\ell} + B_{E,\ell}^{-2})], \\ \text{Cov}(C_{TT,\ell}, C_{EE,\ell}) &= \frac{2}{(2\ell+1) f_{\text{sky}}} C_{TE,\ell}^2, \\ \text{Cov}(C_{TT,\ell}, C_{TE,\ell}) &= \frac{2}{(2\ell+1) f_{\text{sky}}} C_{TE,\ell} (C_{TT,\ell} + B_{T,\ell}^{-2}), \\ \text{Cov}(C_{EE,\ell}, C_{TE,\ell}) &= \frac{2}{(2\ell+1) f_{\text{sky}}} C_{TE,\ell} (C_{EE,\ell} + B_{E,\ell}^{-2}). \end{aligned} \quad (4.11)$$

Here, f_{sky} is the fraction of the sky remaining after removal of foregrounds and galactic plane contaminations, etc., and $B_{X,\ell}$ denotes the expected error of the experimental apparatus [33, 34],

$$B_{X,\ell}^2 = \sum_c (\sigma_{X,c} \theta_c)^{-2} e^{-\ell(\ell+1)/\ell_c^2}, \quad (4.12)$$

where the index c labels the different frequency channels, $\sigma_{X,c}^2$ is the variance of the instrumental noise in the temperature/polarisation measurement, θ_c is the width of the beam assuming a Gaussian profile, and $\ell_c \equiv 2\sqrt{2\ln 2}/\theta_c$ is the corresponding cut-off multipole. Table 4 lists the values of these quantities specific to Planck's observations.

Table 5. 1σ sensitivities to various cosmological parameters from the Planck temperature and polarisation measurements (TT , EE and TE).

Parameter	Model 1	Model 2
$\sigma(w)$	0.21	0.21
$\sigma(\log c_s^2)$	5340.77	948.04
$\sigma(h)$	0.082	0.090
$\sigma(100\Omega_b h^2)$	0.026	0.025
$\sigma(10\Omega_{cdm})$	0.52	0.57
$\sigma(\log 10^{10}\Delta_{\mathcal{R}}^2)$	0.010	0.010
$\sigma(n_s)$	0.0067	0.0063

Table 6. 1σ sensitivities to various cosmological parameters from combining the Euclid cluster survey and the Planck temperature and polarisation measurements (TT , EE and TE).

Parameter	Model 1	Model 2
w	0.0060	0.0046
$\log c_s^2$	0.58	0.22
h	0.0025	0.0022
$100\Omega_b h^2$	0.017	0.017
$10\Omega_{cdm}$	0.016	0.014
$\log 10^{10}\Delta_{\mathcal{R}}^2$	0.0047	0.0047
n_s	0.0032	0.0032

Table 5 shows the 1σ sensitivities of Planck to the parameters of our two fiducial models. Compared with the Euclid-only results in table 3, it is immediately clear that Planck has very little sensitivity to dark energy parameters compared with cluster surveys; the 1σ sensitivity to w is only about 20%, while $\log c_s^2$ is completely unconstrained, consistent with previous expectations (e.g., [36–38]). Planck’s sensitivity to h is comparable to that of the Euclid cluster survey ($\sim 10\%$), but the latter performs ten times better for the Ω_{cdm} measurement.

What is more interesting is when observations from Planck and the Euclid cluster survey are used in combination. The combined 1σ sensitivities of Planck and the Euclid cluster survey are displayed in table 6. Compared with the expectations from Planck or Euclid alone, we see that Planck+Euclid improves the sensitivities to some parameters, especially h and w , by more than tenfold; the 1σ sensitivities to w and h from the combined analysis are both now better than 1%. Such a significant improvement shows that Planck and the Euclid cluster survey are individually sensitive to different degenerate combinations of these parameters. However, once these observations are used in combination, the degeneracies are completely broken. Figure 7 illustrates how the degeneracies in h and w inherent in the Planck and in the Euclid observations can be broken by a combined analysis.

Importantly, while Planck alone has no constraining power whatsoever on the dark energy sound speed, because of the breaking of parameter degeneracies discussed above, the combination of Planck and Euclid turns out to improve the Euclid-alone sensitivity

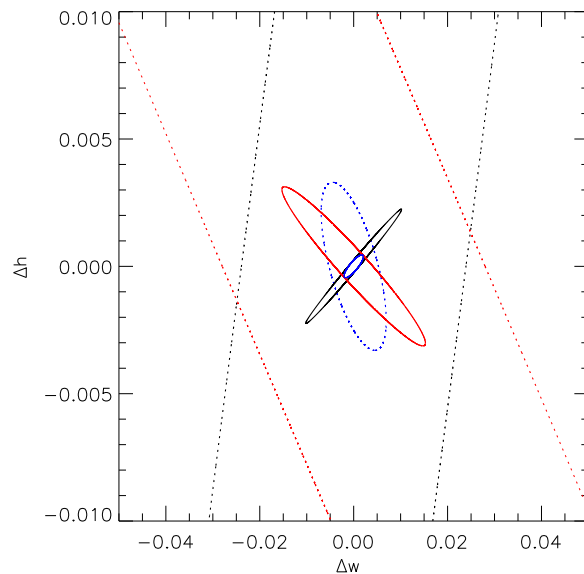


Figure 7. 1σ sensitivities in the (h, w) -parameter space for the Euclid cluster survey (black lines), Planck (red), and combined Planck+Euclid (blue), assuming fiducial model 2. The dotted lines represent sensitivities after marginalising over all other cosmological parameters, while the solid lines correspond to no marginalisation (i.e., parameters not shown in this plot are kept fixed at their fiducial values).

to $\log c_s^2$ by about a factor of two. Parameters such as the physical baryon density $\Omega_b h^2$ and the scalar spectral index n_s , to which Planck is most sensitive, also benefit somewhat from a combined analysis with Euclid: the sensitivity to n_s from the combined improves on the Planck-alone result by about a factor two, while for $\Omega_b h^2$ we find a $\sim 30\%$ improvement.

5. Discussions and conclusions

Current observation of an accelerated universal expansion is commonly attributed to the presence of a dark energy component in universe’s total energy budget. However, apart from that it should have some negative pressure, our understanding of the details of this dark energy component is quite limited. In this work, we have investigated how future cluster surveys can help to shed light on this dark energy through their potential to observe galaxy clusters numbering in the hundred thousands. We have considered in particular how the cluster survey of the ESA Euclid project will allow us to determine the equation of state and the sound speed of a generic dark energy fluid.

The main role of a dark energy sound speed is that it enables the clustering of dark energy on length scales above the sound horizon, thereby allowing the dark energy component to participate actively in the formation of structure in the universe. This means that, if the sound horizon is comparable to or smaller than the typical length scales of a galaxy or galaxy cluster, one should expect to find dark energy

bound gravitationally in the collapsed objects and contribute to their mass. We have demonstrated in this work, using the spherical collapse model, that the maximum dark energy contribution to the total cluster mass is of order a few tenths of a per cent at the time of virialisation.

Secondly, because dark energy clustering feeds back on the evolution of the dark matter density perturbations, it leads to a scale-dependence in the dark matter clustering that turns out to be more significant than is suggested by the mere $\sim 0.1\%$ infall discussed immediately above. For dark energy sound speeds approximately in the range $c_s^2 = 10^{-6} \rightarrow 10^{-4}$, the effect of dark energy clustering is directly visible in the cluster mass function in the mass range $10^{12} \rightarrow 10^{16} M_\odot$; for dark energy models consistent with present observations, the number massive clusters ($\sim 10^{16} M_\odot$) can potentially change by as much as 15% when compared with the no clustering case.

Using our predictions for the cluster mass functions, we have performed a Fisher matrix forecast in order to assess the potential of the Euclid cluster survey to constrain dark energy parameters. We find that a 1σ sensitivity to the (time-independent) dark energy equation of state parameter w at the sub-percent level is possible, especially when the the Euclid cluster survey is complemented by CMB observations from Planck. Furthermore, if the dark energy has a sound speed that deviates appreciably from unity, we will be able to pin it down with future cluster surveys to roughly within an order of magnitude.

The results presented in this work are well in line with those from previous studies, where observational probes other than cluster surveys had been considered [7, 8, 10, 39, 40]. We therefore conclude that future cluster surveys will be competitive with other probes in their constraining power on dark energy parameters, and that the optimal strategy is a combination of different observations.

Acknowledgments

OEB thanks the Villum Foundation for support. TB thanks Thomas Tram for assistance with CLASS.

References

- [1] E. Komatsu et al. Seven-Year Wilkinson Microwave Anisotropy Probe (WMAP) Observations: Cosmological Interpretation. *Astrophys.J.Suppl.*, 192:18, 2011. 57 pages, 20 figures. Accepted for publication in ApJS. (v2) References added. The SZ section expanded with more analysis. The discrepancy between the KS and X-ray derived profiles has been resolved. (v3) New analysis of the SZ effect on individual clusters added (Section 7.3). The LCDM parameters have been updated using the latest recombination history code (RECFAST version 1.5).
- [2] M. Kowalski et al. Improved Cosmological Constraints from New, Old and Combined Supernova Datasets. *Astrophys.J.*, 686:749–778, 2008.
- [3] W. Michael Wood-Vasey et al. Observational Constraints on the Nature of the Dark Energy: First Cosmological Results from the ESSENCE Supernova Survey. *Astrophys.J.*, 666:694–715, 2007.

- [4] Edmund J. Copeland, M. Sami, and Shinji Tsujikawa. Dynamics of dark energy. *Int.J.Mod.Phys.*, D15:1753–1936, 2006.
- [5] Emiliano Sefusatti, Chris Vale, Kenji Kadota, and Joshua Frieman. Primordial non-Gaussianity and Dark Energy constraints from Cluster Surveys. *Astrophys.J.*, 658:669–679, 2007.
- [6] Masahiro Takada and Sarah Bridle. Probing dark energy with cluster counts and cosmic shear power spectra: including the full covariance. *New J.Phys.*, 9:446, 2007.
- [7] L.Raul Abramo, Ronaldo C. Batista, and Rogerio Rosenfeld. The signature of dark energy perturbations in galaxy cluster surveys. *JCAP*, 0907:040, 2009.
- [8] Masahiro Takada. Can A Galaxy Redshift Survey Measure Dark Energy Clustering? *Phys.Rev.*, D74:043505, 2006.
- [9] Tobias Basse, Ole Eggers Bjaelde, and Yvonne Y.Y. Wong. Spherical collapse of dark energy with an arbitrary sound speed. *JCAP*, 1110:038, 2011.
- [10] Guillermo Ballesteros and Julien Lesgourgues. Dark energy with non-adiabatic sound speed: initial conditions and detectability. *JCAP*, 1010:014, 2010.
- [11] Qiao Wang and Zuhui Fan. Simulation studies of dark energy clustering induced by the formation of dark matter halos. *Phys.Rev.*, D85:023002, 2012. 11 pages, 8 figures, Physical Review D. (accepted).
- [12] Paolo Creminelli, Guido D’Amico, Jorge Norena, Leonardo Senatore, and Filippo Vernizzi. Spherical collapse in quintessence models with zero speed of sound. *JCAP*, 1003:027, 2010.
- [13] Emiliano Sefusatti and Filippo Vernizzi. Cosmological structure formation with clustering quintessence. *JCAP*, 1103:047, 2011.
- [14] William H. Press and Paul Schechter. Formation of galaxies and clusters of galaxies by selfsimilar gravitational condensation. *Astrophys.J.*, 187:425–438, 1974.
- [15] Diego Blas, Julien Lesgourgues, and Thomas Tram. The Cosmic Linear Anisotropy Solving System (CLASS) II: Approximation schemes. *JCAP*, 1107:034, 2011.
- [16] Irit Maor and Ofer Lahav. On virialization with dark energy. *JCAP*, 0507:003, 2005. 15 pages, 5 figures. Accepted for publication in JCAP.
- [17] R. Laureijs, J. Amiaux, S. Arduini, J.-L. Augeres, J. Brinchmann, et al. Euclid Definition Study Report. 2011.
- [18] P. J. E. Peebles. *Large-scale structure of the Universe*. Princeton University Press, Princeton NJ, 1980.
- [19] Peng Wang. Virialization in dark energy cosmology. *Astrophys.J.*, 640:18–21, 2006.
- [20] D.F. Mota and C. van de Bruck. On the Spherical collapse model in dark energy cosmologies. *Astron.Astrophys.*, 421:71–81, 2004.
- [21] Cathy Horellou and Joel Berge. Dark energy and the evolution of spherical overdensities. *Mon.Not.Roy.Astron.Soc.*, 360:1393–1400, 2005.
- [22] Will J. Percival. Cosmological structure formation in a homogeneous dark energy background. *Astron.Astrophys.*, 443:819, 2005.
- [23] David F. Mota, Douglas J. Shaw, and Joseph Silk. On the Magnitude of Dark Energy Voids and Overdensities. *Astrophys.J.*, 675:29–48, 2008.
- [24] J. Binney and S. Tremaine. *Galactic Dynamics*. Princeton University Press, Princeton NJ, 2008.
- [25] Laurence Perotto, Julien Lesgourgues, Steen Hannestad, Huitzu Tu, and Yvonne Y.Y. Wong. Probing cosmological parameters with the CMB: Forecasts from full Monte Carlo simulations. *JCAP*, 0610:013, 2006.
- [26] Max Tegmark, Andy Taylor, and Alan Heavens. Karhunen-Loeve eigenvalue problems in cosmology: How should we tackle large data sets? *Astrophys.J.*, 480:22, 1997.
- [27] Sheng Wang, Justin Khoury, Zoltan Haiman, and Morgan May. Constraining the evolution of dark energy with a combination of galaxy cluster observables. *Phys.Rev.*, D70:123008, 2004.
- [28] Gilbert Holder, Zoltan Haiman, and Joseph Mohr. Constraints on ω_m , ω_Λ , and σ_8 , from galaxy cluster redshift distributions. *Astrophys.J.*, 560:L111–L114, 2001.
- [29] Takashi Hamana, Masahiro Takada, and Naoki Yoshida. Searching for massive clusters in weak

- lensing surveys. *Mon.Not.Roy.Astron.Soc.*, 350:893, 2004.
- [30] Steen Hannestad, Huitzu Tu, and Yvonne Y.Y. Wong. Measuring neutrino masses and dark energy with weak lensing tomography. *JCAP*, 0606:025, 2006.
- [31] Ludovic Van Waerbeke. Noise properties of gravitational lens mass reconstruction. *Mon.Not.Roy.Astron.Soc.*, 313:524–532, 2000.
- [32] Matias Zaldarriaga and Uros Seljak. An all sky analysis of polarization in the microwave background. *Phys.Rev.*, D55:1830–1840, 1997.
- [33] G. Efstathiou and J.R. Bond. Cosmic confusion: Degeneracies among cosmological parameters derived from measurements of microwave background anisotropies. *Mon.Not.Roy.Astron.Soc.*, 304:75–97, 1999.
- [34] LLoyd Knox. Determination of inflationary observables by cosmic microwave background anisotropy experiments. *Phys.Rev.*, D52:4307–4318, 1995. 28 pages of uuencoded postscript with 8 included figures. A postscript version is also available by anonymous ftp at <ftp://astro.uchicago.edu/pub/astro/knox/fullsim.ps> Report-no: FERMILAB-Pub-95/008-A.
- [35] G. Rocha, R. Trotta, C.J.A.P. Martins, A. Melchiorri, P.P. Avelino, et al. Measuring alpha in the early universe: cmb polarization, reionization and the fisher matrix analysis. *Mon.Not.Roy.Astron.Soc.*, 352:20, 2004.
- [36] Simon DeDeo, R.R. Caldwell, and Paul J. Steinhardt. Effects of the sound speed of quintessence on the microwave background and large scale structure. *Phys.Rev.*, D67:103509, 2003.
- [37] Rachel Bean and Olivier Dore. Probing dark energy perturbations: The Dark energy equation of state and speed of sound as measured by WMAP. *Phys.Rev.*, D69:083503, 2004.
- [38] Steen Hannestad. Constraints on the sound speed of dark energy. *Phys.Rev.*, D71:103519, 2005.
- [39] Wayne Hu and Ryan Scranton. Measuring dark energy clustering with CMB-galaxy correlations. *Phys.Rev.*, D70:123002, 2004.
- [40] Jun-Qing Xia, Yi-Fu Cai, Tao-Tao Qiu, Gong-Bo Zhao, and Xinmin Zhang. Constraints on the Sound Speed of Dynamical Dark Energy. *Int.J.Mod.Phys.*, D17:1229–1243, 2008.

11

DARK ENERGY PROPERTIES FROM LARGE FUTURE GALAXY SURVEYS

After finishing Basse et al. (2012), our work branched of in two directions: Spherical collapse with non-linear dark energy and improving the forecast of dark energy sensitivities in the future. Our efforts in the first direction are discussed in chapter 12, while the second direction is the topic of this chapter. During the process I was involved in all aspects from writing the code that computes the observed number of clusters to analyzing the results.

As mentioned, the aim here is to rectify the drawbacks of the analysis of the previous chapter by, e.g., an MCMC estimation of parameter uncertainties. In recap, the shortcomings are the Fisher matrix approach, the survey parameters, and mainly the inability of the quasi-linear approach to reproduce the clustering limit accurately. The robustness of the analysis is increased by accounting for scatter in the weak lensing determination of the mass of the observed cluster, as well as completeness and efficiency different from unity. In addition, we investigate binning strategies and the complementarity of cluster surveys to other data from galaxy surveys. The parameter space of our analysis is quite extensive, including neutrino parameters, $\sum m_\nu$ and N_{eff} , and dark energy parameters, w_0 , w_a , and $\hat{c}_{s,\text{de}}^2$, where the equation of state is a linear function of the scale factor, $w_{\text{de}}(a) = w_0 + (1 - a)w_a$.

We use the knowledge obtained in chapters 9 and 10 to construct interpolation functions between the sound speed limits of the spherical collapse. This allows us to construct cluster mass functions and weak lensing detection mass thresholds in our models of inhomogeneous dark energy. We bin the observable clusters after mass and redshift according to a scheme ensuring that each bin contains approximately the same number of clusters.

For the MCMC analysis, we compute the binning and observed number of clusters in each bin for our fiducial values of the cosmological parameters of interest. This result is used as our mock data to be compared with theoretical predictions of the expected number of clusters in the bins constructed for the fiducial model. The effect of an incomplete survey with an efficiency different from unity is folded in at the level of the likelihood. We opt to always combine the cluster data with synthetic CMB data from a Planck-like experiment. With regard to the binning strategy, we find that more bins result in better sensitivity. Some parameters gain sensitivity from binning in redshift while others gain from binning in mass. The maximal and optimal number of bins is

essentially determined by the uncertainties on redshift and mass measurements.

In addition to CMB data, we also combine cluster data with angular power spectra of the galaxy distribution and the cosmic shear. These data are constructed in accordance with Hamann et al. (2012) and described in some detail in the next section.

11.1 Angular power spectra

We are interested in a measure of the distribution of galaxies across the sky and the shear of their images as seen from a photometric survey. Making three dimensional power spectra require high resolution along the line of sight, i.e., in redshift. This high resolution can be achieved with spectroscopic measurements, but not photometric. Therefore, we restrict ourselves to angular power spectra with the option of coarse redshift binning. From the data, we can construct a number of different power spectra, $\mathcal{C}_{\ell,ij}^{XY}$. Here X and Y refer to the type of data, i.e., shear (s) or galaxy (g) power spectra, with both auto-spectra ($X = Y$) and cross-spectra ($X \neq Y$). The subscripts i and j refer to the different redshift bins, again with auto- and cross-spectra.

From theory, the angular power spectra are computed as,

$$\mathcal{C}_{\ell,ij}^{XY} = 4\pi \int d \ln k \mathcal{S}_{\ell,i}^X(k) \mathcal{S}_{\ell,j}^Y(k) \Delta^2(k), \quad (11.1)$$

where $\Delta^2(k)$ is the dimensionless power spectrum of the primordial perturbations and the source functions, \mathcal{S}_ℓ , can be found in Hamann et al. (2012). The panels of figure 11.1 show theoretical angular power spectra for different combinations of data types and redshift bins.

The angular power spectra are first and foremost subject to the inherent statistical uncertainty cosmic variance, see section 5.3. This is folded into the analysis at the likelihood level. Furthermore, a finite surface density of source galaxies introduces a shot noise term,

$$\delta \mathcal{C}_{\text{noise},ij}^{XY} = \delta_{ij} \delta_{XY} \left(\Xi_i^X \right)^2 n_i^{-2}, \quad (11.2)$$

contributing to the observed angular power spectra. The Kronecker deltas δ_{ij} and δ_{XY} ensure that the shot noise only applies to the auto-correlations. For galaxy power spectra, we have $\Xi_i^g = 1$, and for shear power spectra, we have $\Xi_i^s = \sigma_\epsilon$, where σ_ϵ is the mean ellipticity dispersion of the source galaxies, which is modeled as redshift independent. Finally, n_i is the source galaxy surface density in redshift bin i . We include the photometric redshift uncertainty of $\sigma(z) \sim 0.03(1+z)$ into the source functions.

For the Bayesian exercise of estimating the parameter sensitivities of a survey, it suffices to set the mock angular power spectra, $\hat{\mathcal{C}}_{\ell,ij}^{XY}$, equal to the total angular power spectra of the fiducial model, $\bar{\mathcal{C}}_{\ell,ij}^{XY}$, where

$$\bar{\mathcal{C}}_{\ell,ij}^{XY} = \mathcal{C}_{\ell,ij}^{XY} + \delta \mathcal{C}_{\text{noise},ij}^{XY}, \quad (11.3)$$

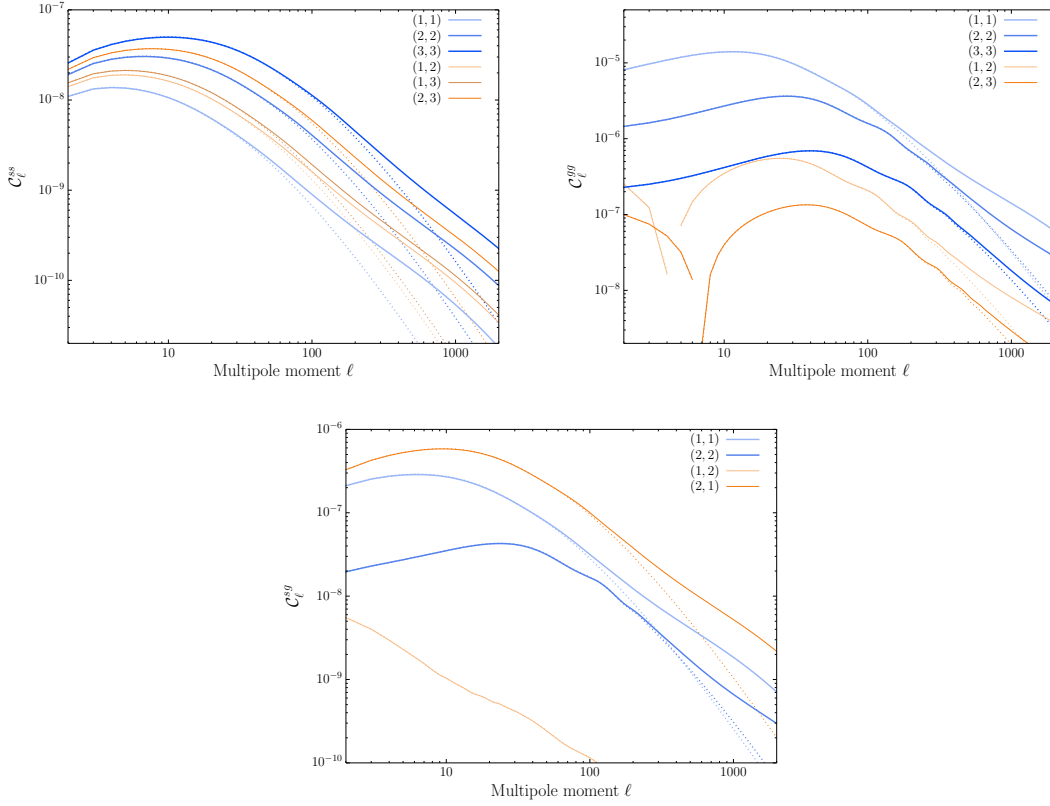


Figure 11.1: Angular power spectra for three redshift bins (bin 1: $z \in [0, 0.61]$, bin 2: $z \in [0.61, 1.03]$, bin 3: $z \in [1.03, 3]$). The legends show the redshift bin combinations for the shear-galaxy cross-spectra (not symmetric in redshift bins) the first bin is shear and the second galaxy. The solid lines include HaloFit non-linear corrections, while the dotted lines are based on linear theory.

includes all error contributions discussed, except cosmic variance. The likelihood in terms of an effective chi-squared is given by

$$\chi_{\text{eff}}^2 = \sum_{\ell} (2\ell + 1) f_{\text{sky}} \left[\text{Tr} \left(\bar{\mathcal{C}}_{\ell}^{-1} \hat{\mathcal{C}}_{\ell} \right) + \ln \frac{\text{Det} \left(\bar{\mathcal{C}}_{\ell} \right)}{\text{Det} \left(\hat{\mathcal{C}}_{\ell} \right)} - N \right] \quad (11.4)$$

where $\bar{\mathcal{C}}_{\ell} \equiv \bar{\mathcal{C}}_{\ell,ij}^{XY}$, $\hat{\mathcal{C}}_{\ell} \equiv \hat{\mathcal{C}}_{\ell,ij}^{XY}$, and N is the dimension of the covariance matrix, i.e., the total number of redshift bins. With no cross-spectra, the shear and galaxy spectra can be treated independently with $\chi_{\text{eff}}^2 = \chi_{\text{eff},s}^2 + \chi_{\text{eff},g}^2$. The factor $(2\ell + 1) f_{\text{sky}}$ encodes the cosmic variance accounting for partial sky coverage.

11.2 Results

We have build an extension to the public Boltzmann code, CAMB Lewis et al. (2000), that computes the desired observables, and the Bayesian inference is made with the public code CosmoMC⁴ Lewis & Bridle (2002). Preliminary investigations across Hamann et al. (2012) and Basse et al. (2014a) show that the optimal binning strategy is two and eleven redshift bins for shear and galaxy power spectra, respectively. For the cluster survey having ten mass and redshift bins yields good results, while keeping the redshift bins wide enough that we need not worry about redshift uncertainties. Spectroscopic follow-up is expected for the clusters. In general, we show that cluster data are complementary to the shear and galaxy power spectra – on a few parameters, the constraints from clusters even exceed those from the angular power spectra. The combination of all data leads to significant sensitivity gains as some of the parameter degeneracies are lifted.

The following summarizes our findings for non-standard cosmological parameters. In the neutrino sector, we find that the sum of neutrinos masses can be measured to deviate from zero with about 4σ with fiducial model, where $\sum m_\nu = 0.06$ eV – the smallest value allowed by oscillation experiments. Regarding extra radiation, we find that the deviation of 0.046 from 3 in the standard scenario can be measured at a 1σ level for the first time. This is with a highly complex parameter space including parameters known to be degenerate with neutrino parameters in a CMB analysis, e.g., the dark energy equation of state.

For the time dependent dark energy equation of state, we compute the dark energy figure of merit proportional to the one defined by the Dark Energy Task Force Albrecht et al. (2006),

$$\text{FoM} \equiv (\sigma(w_p) \sigma(w_a))^{-1}. \quad (11.5)$$

Here, $w_p = w_0 + (1 - a_p) w_a$, where a_p is chosen such that the w_p and w_a are uncorrelated. We find that a large next-generation galaxy survey holds the potential to improve the dark energy figure of merit by two to three orders of magnitude compared to present constraints.

Finally, we show that in optimistic scenarios, where the (time independent) equation of state of dark energy deviates significantly from $w_{\text{de}} = -1$, some signature of inhomogeneous dark energy might be detected by a large cluster survey. We find that low sound speeds, $\hat{c}_{s,\text{de}} \sim 10^{-3}$, can be constrained from above while high sound speeds, $\hat{c}_{s,\text{de}} \sim 1$, can be constrained from below. The physics behind these conclusions is that for low sound speeds, the Jeans mass for dark energy clustering lies close to or below the detection threshold of the cluster survey, i.e., all clusters contain dark energy in the fiducial model. As the sound speed is increased, so is the Jeans mass and eventually no

⁴<http://cosmologist.info/cosmomc>

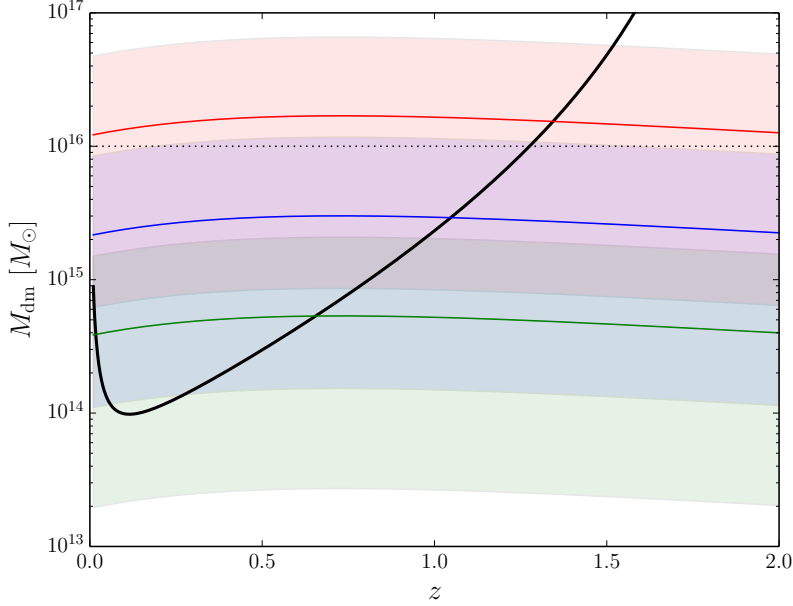


Figure 11.2: Evolution of the Jeans mass for dark energy clustering with redshift for three different sound speeds. $\hat{c}_{s,\text{de}}^2 = 10^{-5}$ (red), $\hat{c}_{s,\text{de}}^2 = 10^{-5.5}$ (blue), $\hat{c}_{s,\text{de}}^2 = 10^{-6}$ (green). The equation of state of dark energy is $w_{\text{de}} = -0.83$. The black solid line shows the detection threshold of the cluster survey, which is essentially the same in the models. The shaded regions show the transition from no dark energy clustering to to the limit where the non-relativistic matter and dark energy fluids are comoving. The boundaries of the region corresponds to deviating by one percent of the splitting from either limit.

cluster contain significant amounts of dark energy. This argument can be reversed for fiducial models with high sound speeds.

We wish to know whether some values of the dark energy sound speed can be constrained from both sides. This would require the Jeans mass to fall well within both mass limits of the cluster survey. The upper limit that we adopt is $M_{\text{dm}} = 10^{16} M_{\odot}$, above which essentially no cluster exists. Figure 11.2 shows the Jeans mass as a function of redshift with three different sound speeds along with the detection threshold. The latter is essentially the same in the different models. The shaded regions show the transition region between the two plateaus of the spherical collapse model as the transition is modeled in our interpolation scheme. The boundaries of the region correspond to deviating by one percent of the total difference from either plateau. The figure clearly illustrates why the sound speed in a fiducial model with $w_{\text{de}} = -0.83$ and $\hat{c}_{s,\text{de}}^2 = 10^{-6}$ cannot be

constrained from below. The model with $\hat{c}_{s,\text{de}}^2 = 10^{-5.5}$ could hold the potential to be constrained from both sides. Alternatively a better survey would have a lower detection threshold, and some of our early runs showed that the sound speed can be constrained from sides, see the first version of Basse et al. (2014a) on arXiv.

Dark energy properties from large future galaxy surveys

Tobias Basse^a Ole Eggers Bjælde^a Jan Hamann^b Steen Hannestad^{a,c} Yvonne Y.Y. Wong^d

^aDepartment of Physics and Astronomy
Aarhus University, DK-8000 Aarhus C, Denmark

^bTheory Division, Physics Department
CERN, CH-1211 Geneva 23, Switzerland

^cAarhus Institute of Advanced Studies,
Aarhus University, DK-8000 Aarhus C, Denmark

^dSchool of Physics
The University of New South Wales, Sydney NSW 2052, Australia

E-mail: basse@phys.au.dk, oeb@phys.au.dk, jan.hamann@cern.ch,
sth@phys.au.dk, yvonne.y.wong@unsw.edu.au

Abstract. We perform a detailed forecast on how well a EUCLID-like survey will be able to constrain dark energy and neutrino parameters from a combination of its cosmic shear power spectrum, galaxy power spectrum, and cluster mass function measurements. We find that the combination of these three probes vastly improves the survey's potential to measure the time evolution of dark energy. In terms of a dark energy figure-of-merit defined as $(\sigma(w_p)\sigma(w_a))^{-1}$, we find a value of 690 for EUCLID-like data combined with PLANCK-like measurements of the cosmic microwave background (CMB) anisotropies in a 10-dimensional cosmological parameter space, assuming a Λ CDM fiducial cosmology. For the more commonly used 7-parameter model, we find a figure-of-merit of 1900 for the same data combination. We consider also the survey's potential to measure dark energy perturbations in models wherein the dark energy is parameterised as a fluid with a nonstandard non-adiabatic sound speed, and find that in an *optimistic* scenario in which w_0 deviates by as much as is currently observationally allowed from -1 , models with $\hat{c}_s^2 = 10^{-6}$ and $\hat{c}_s^2 = 1$ can be distinguished at more than 2σ significance. We emphasise that constraints on the dark energy sound speed from cluster measurements are strongly dependent on the modelling of the cluster mass function; significantly weaker sensitivities ensue if we modify our model to include fewer features of nonlinear dark energy clustering. Finally, we find that the sum of neutrino masses can be measured with a 1σ precision of 0.015 eV, even in complex cosmological models in which the dark energy equation of state varies with time. The 1σ sensitivity to the effective number of relativistic species $N_{\text{eff}}^{\text{ml}}$ is approximately 0.03, meaning that the small deviation of 0.046 from 3 in the standard value of $N_{\text{eff}}^{\text{ml}}$ due to non-instantaneous decoupling and finite temperature effects can be probed with 1σ precision for the first time.

Contents

1	Introduction	1
2	Dark energy parameterisation	2
3	The cluster mass function as a EUCLID observable	3
3.1	Cluster mass function from theory	3
3.2	The observable	5
4	Measurement errors	5
4.1	Redshift uncertainty	5
4.2	Uncertainty in the weak lensing mass determination	5
5	Mock data generation	6
5.1	Mass detection threshold	6
5.2	Redshift and mass binning	8
5.3	Completeness and efficiency	8
5.4	Synthetic data sets	9
6	Forecasting	10
6.1	Model parameter space	10
6.2	Likelihood function	11
7	Results	11
7.1	Impact of the number of bins	11
7.2	Probes of the expansion history versus probes of the power spectrum	12
7.3	Combining all data sets: constraints on neutrino parameters	14
7.4	The dark energy figure-of-merit	15
7.5	Dark energy sound speed and perturbations	16
7.5.1	Modelling of the cluster mass function	18
8	Conclusions	19
A	Interpolating the spherical collapse between the two limits of \hat{c}_s^2	21

1 Introduction

The coming decade will see spectacular advances in the measurement of the large-scale structure distribution in the universe. Perhaps the most interesting of these measurements are the large-scale photometric surveys to be conducted by the Large Synoptic Survey Telescope (LSST) [1] and the ESA EUCLID mission [2]. Both projects will map the positions and measure the shapes of order a billion galaxies in a significant fraction of the current Hubble volume. This will in turn allow for a precision measurement of both the galaxy clustering and the cosmic shear power spectra, and likewise an impressively precise determination of the cosmological parameter values. As an example, assuming a vanilla Λ CDM model extended with nonzero neutrino masses, a EUCLID-like survey will be able to measure the neutrino mass

sum $\sum m_\nu$ at a precision of at least 0.03 eV [3, 4] (most optimistically up to 0.01 eV [5]) when combined with measurements of the cosmic microwave background (CMB) anisotropies from the Planck mission [6]. Such a precision will see the absolute neutrino mass scale detected at high confidence even if the true value of $\sum m_\nu$ should be the minimum compatible with current neutrino oscillation data, i.e., $\sum m_\nu \simeq 0.06$ eV [5].

As yet unexplored in reference [5] is the role played by the cluster mass function in cosmological parameter inference. Weak gravitational lensing measurements available to both the LSST and EUCLID will allow for the efficient detection and mass determination of galaxy clusters; EUCLID, for example, is expected to detect and accurately measure the masses of close to 100,000 clusters [2]. In this work, we continue the cosmological parameter sensitivity forecast begun in [5] by adding the cluster mass function inferred from a EUCLID-like cluster survey to the galaxy and the shear power spectra measurements already considered in reference [5]. We also extend the study to dark energy models with a time-dependent equation of state and/or a nonstandard non-adiabatic sound speed. As in [5] we shall adopt the survey specifications of the EUCLID mission in terms of the number of objects observed, the redshift range, and the sky coverage. However, the analysis procedure can be easily adapted to other similar redshift surveys such as the LSST.

The paper is structured as follows. We discuss first our dark energy parameterisation in section 2, before introducing in section 3 the cluster mass function as a cosmological observable. In section 4 we examine some uncertainties likely to be encountered in a EUCLID-like measurement of the cluster mass function, and discuss how we model and propagate these uncertainties in our forecast analysis. Sections 5 and 6 outline respectively our mock data generation and forecast procedures, while section 7 contains our results. We conclude in section 8.

2 Dark energy parameterisation

Although dark energy is the most popular explanation for the apparent accelerated expansion of the universe, there is as yet no consensus on its actual physical properties. For this reason, and for reasons of simplicity, dark energy is usually described as a fluid obeying the laws of general relativity. The homogeneous part of this fluid is responsible for driving the expansion of the universe, and can be represented by an equation of state $w(\tau) = \bar{P}_Q(\tau)/\bar{\rho}_Q(\tau)$, where $\bar{P}_Q(\tau)$ and $\bar{\rho}_Q(\tau)$ denote the unperturbed dark energy pressure and energy density respectively, and τ is conformal time. Except in the case of a cosmological constant, for which $w(\tau)$ is precisely the constant -1 , dynamical dark energy models have in general equations of state that are functions of time. For this reason, we model dark energy equation of state using the popular parameterisation [7, 8]

$$w(\tau) = w_0 + w_a[1 - a(\tau)], \quad (2.1)$$

where w_0 and w_a are constants, and $a(\tau)$ denotes the scale factor. Note that this parameterisation should be regarded simply as a toy model that facilitates comparisons across different observational probes. We make no pretence here that it actually captures the behaviour of any realistic dynamic dark energy model. For an example of a forecast tailored specifically to scalar-field models of dark energy, see, e.g., [9].

A general relativistic fluid evolving in an inhomogeneous spacetime will in general develop inhomogeneities of its own. We express inhomogeneities in the dark energy density in

terms of a density contrast $\delta_Q(\tau, \mathbf{x})$ satisfying $\rho_Q(\tau, \mathbf{x}) = \bar{\rho}_Q(\tau)[1 + \delta_Q(\tau, \mathbf{x})]$, where $\rho_Q(\tau, \mathbf{x})$ is the fully time- and space-dependent dark energy density.

The evolution of the density contrast $\delta_Q(\tau, \mathbf{x})$ can be described by a set of (nonlinear) fluid equations coupled to the (nonlinear) Einstein equation. For the nonlinear aspects of the formation of clusters we refer to section 3.1 and appendix A. For the purpose of calculating the linear matter power spectrum we implement the linear evolution for the dark energy density contrast, described in the synchronous gauge and in Fourier space by the equations of motion (see, e.g., [10–13])

$$\begin{aligned} \dot{\delta}_Q + (1+w) \left(\theta_Q + \frac{\dot{h}}{2} \right) + 3(\hat{c}_s^2 - w)\mathcal{H}\delta_Q + 9(1+w)(\hat{c}_s^2 - c_a^2)\mathcal{H}^2 \frac{\theta_Q}{k^2} &= 0, \\ \dot{\theta}_Q + (1 - 3\hat{c}_s^2)\mathcal{H}\theta_Q - \frac{\hat{c}_s^2 k^2}{1+w} \delta_Q + k^2 \sigma_Q &= 0, \end{aligned} \quad (2.2)$$

where $\delta_Q(\tau, k)$ now denotes the dark energy density contrast in Fourier k -space, $\theta_Q(\tau, k)$ is the divergence of the dark energy velocity field, h the metric perturbation, $\mathcal{H} \equiv \dot{a}/a$ the conformal Hubble parameter, σ_Q is the shear stress which we assume to be vanishing in this work, and $\hat{c}_s^2 \equiv \delta P_Q / \delta \rho_Q|_{\text{rest}}$ and $c_a^2 \equiv \dot{P}_Q / \dot{\rho}_Q$ are the non-adiabatic and adiabatic dark energy sound speeds respectively. Note that the non-adiabatic sound speed \hat{c}_s^2 is defined as the ratio of the pressure perturbation δP_Q to the energy density perturbation $\delta \rho_Q$ in the rest-frame of the dark energy fluid, while the adiabatic sound speed c_a^2 is related to the homogeneous fluid equation of state via $\dot{w} = 3(1+w)(w - c_a^2)\mathcal{H}$. We employ natural units throughout this work, i.e., $c = 1$ denotes the speed of light.

3 The cluster mass function as a EUCLID observable

Cluster surveys can be an excellent probe of dynamical dark energy because the abundance of the most massive gravitationally bound objects at any one time depends strongly on both the growth function of the matter perturbations and the late-time expansion history of the universe (see, e.g., [14–19]). The EUCLID mission will identify clusters in the photometric redshift survey accompanied by a spectroscopic follow-up. The same survey will also determine the masses of the detected clusters by way of weak gravitational lensing.

3.1 Cluster mass function from theory

A simple quantification of the cluster distribution is the cluster mass function. Denoted $dn/dM(M, z)$, the cluster mass function counts the number of clusters per comoving volume in a given mass interval $[M, M + dM]$ as a function of redshift z .

For any given cosmological model, an accurate prediction of the corresponding cluster mass function necessitates the use of N -body/hydrodynamics simulations. However, a number of fitting functions, calibrated against simulation results in the vanilla Λ CDM model framework, have been proposed in the literature (e.g., [20–22]). In this work, we model the cluster mass function after the Sheth-Tormen fitting function [20]

$$\frac{dn_{\text{ST}}}{dM}(M, z) = -\sqrt{\frac{2a}{\pi}} A \left[1 + \left(\frac{a\delta_c^2}{\sigma_m^2} \right)^{-p} \right] \frac{\bar{\rho}_m}{M^2} \frac{\delta_c}{\sigma_m} \left(\frac{d \log \sigma_m}{d \log M} - \frac{d \log \delta_c}{d \log M} \right) \exp \left[-a \frac{\delta_c^2}{2\sigma_m^2} \right], \quad (3.1)$$

where the fitting parameters are $a = 0.707$, $A = 0.322184$, and $p = 0.3$, and $\bar{\rho}_m(z)$ is the mean matter density (it was shown in [23] that this function provides a very good fit also in models with non-zero neutrino mass). The quantity $\sigma_m^2(M, z)$ denotes the variance of the linear matter density field smoothed on a comoving length scale $X_{\text{sm}} \equiv a^{-1}[3M/(4\pi\bar{\rho}_m)]^{1/3}$, and is computed from the linear matter power spectrum $P_m^{\text{lin}}(k, z)$ via

$$\sigma_m^2(M, z) \equiv \frac{1}{2\pi^2} \int_0^\infty dk k^2 |W(kX_{\text{sm}})|^2 P_m^{\text{lin}}(k, z), \quad (3.2)$$

where $W(x) = 3(\sin x - x \cos x)/x^3$ is the Fourier transform of the spherical (spatial) top-hat filter function. The linear power spectrum $P_m^{\text{lin}}(k, z)$ can be obtained from a Boltzmann code such as CAMB [24].

The quantity $\delta_c(M, z)$ is known as the linear threshold density of matter at the time of collapse. Its value is established by tracking the full nonlinear collapse of a spherical top-hat over-density, noting the time τ_{coll} the region collapses to an infinitely dense point, and then computing from *linear* perturbation theory the *linear* density contrast at $\tau = \tau_{\text{coll}}$. In many applications it suffices to take the constant value $\delta_c = 1.68$. In dark energy cosmologies, however, this may not be a very good approximation (see, e.g., [25, 26]). Here, we estimate $\delta_c(M, z)$ as described immediately above, and track the spherical collapse of a top-hat overdensity by solving the equations

$$\frac{\ddot{X}}{X} + \mathcal{H} \frac{\dot{X}}{X} = -\frac{4\pi G}{3} a^2 [\bar{\rho}_m \delta_m + \bar{\rho}_Q (1 + 3\hat{c}_s^2) \delta_Q], \quad (3.3)$$

$$\delta_m(\tau) = [1 + \delta_m(\tau_i)] \left[\frac{X(\tau_i)}{X(\tau)} \right]^3 - 1, \quad (3.4)$$

where $X(\tau)$ is the comoving radius of the top-hat, $\delta_m(\tau)$ and $\delta_Q(\tau)$ the matter and the dark energy density contrasts respectively in the top-hat region, and τ_i is a reference initial time. Note that equation (3.4) follows from conservation of the total mass of nonrelativistic matter M_m in the top-hat region. For more detailed discussions of the spherical collapse model, we direct the reader to references [27–29].

The presence of the $\bar{\rho}_Q(1 + 3\hat{c}_s^2)\delta_Q$ term on the right hand side of equation (3.3) indicates that the dark energy component also participates in the collapse, especially when the initial dimension $X(\tau_i)$ of the top-hat matter overdensity exceeds the comoving Jeans length associated with the fluid’s non-adiabatic sound speed [26, 30–32]. The resulting linear threshold density δ_c therefore exhibits generically a dependence on the mass of the collapsing region, in addition to the usual z -dependence. However, tracking the nonlinear evolution of the dark energy density contrast δ_Q is in general nontrivial because the spherical top-hat region is well-defined strictly only in the $\hat{c}_s^2 = 0$ and the $\hat{c}_s^2 \rightarrow \infty$ limits, where, supplemented with [26, 31]

$$\bar{\rho}_Q(1 + 3\hat{c}_s^2)\delta_Q \rightarrow 0, \quad \hat{c}_s^2 \rightarrow \infty, \quad (3.5)$$

$$\dot{\rho}_Q + 3 \left(\mathcal{H} + \frac{\dot{X}}{X} \right) (\rho_Q + \bar{P}_Q) = 0, \quad \hat{c}_s^2 = 0, \quad (3.6)$$

the collapse equation (3.3) can be solved exactly. Extending the application of equation (3.3) to the intermediate regime necessitates additional assumptions, which do not however render the system any less intractable [26, 32]. For this reason, we shall resort to modelling the mass-dependence of $\delta_c(M, z)$ by interpolating between the two known limits using a hyperbolic

tangent function, where the location of the kink at each redshift is adjusted to reflect the Jeans mass corresponding to the given \hat{c}_s^2 . See appendix A for details.

Finally, the virial radius R_{vir} and the virial mass M_{vir} can likewise be computed from equations (3.3) to (3.6) in the two limits of \hat{c}_s^2 . Here, $R_{\text{vir}} \equiv aX(\tau_{\text{vir}})$ is defined as the physical radius of the top-hat region and M_{vir} the total mass contained therein at virialisation, where virialisation is taken to mean the moment at which the virial theorem is satisfied by the collapsing region, τ_{vir} . The virial mass $M_{\text{vir}} = M_{\text{m}} + M_Q(\tau_{\text{vir}})$ counts both contributions from nonrelativistic matter M_{m} and from the clustered dark energy $M_Q \equiv (4\pi/3)\bar{\rho}_Q\delta_Q(aX)^3$, and it is M_{vir} , not M_{m} , that we identify with the cluster mass M throughout this work. Further details can be found in appendix A. The virial radius will be used in section 5.1 to determine the cluster mass detection threshold.

3.2 The observable

The actual observable quantity is the number of clusters $N_{i,j(i)}$ in the redshift bin i and the (redshift-dependent) mass bin $j(i)$, defined as

$$N_{i,j(i)} = \Delta\Omega \int_0^\infty dz \int_0^\infty dM \frac{d^2V}{d\Omega dz}(z) W_{i,j(i)}(M, z) \frac{dn_{\text{ST}}}{dM}(M, z), \quad (3.7)$$

where $\Delta\Omega$ is the solid angle covered by the survey (taken to be $15,000 \text{ deg}^2$ following [2]), $d^2V/(d\Omega dz)(z)$ the comoving volume element at redshift z , and $W_{i,j(i)}(M, z)$ is the window function defining the redshift and mass bin. Note that the window functions are in general not sharp in z - and M -space because of uncertainties in the redshift and the mass determinations (see sections 4.1 and 4.2). We defer the discussion of our binning scheme to section 5.2.

4 Measurement errors

4.1 Redshift uncertainty

The photometric survey will measure redshifts with an estimated scatter of $\sigma(z) \sim 0.03(1+z)$ and almost no bias [2]. Nonetheless, because the detected clusters will be subject to a follow-up spectroscopic study, the effective uncertainty in the redshift determination *per se* can be taken as negligible. Additional redshift errors may arise from the peculiar velocities of the clusters, where velocities up to $\sim 1000 \text{ km s}^{-1}$ may lead to an error of $\delta z \sim 0.003$. However, as we shall see in section 5.2, even the narrowest redshift bins adopted in our analysis typically have widths of order $\Delta z \sim 0.03$, i.e., a factor of ten larger than the peculiar velocity uncertainty. We therefore treat the cluster redshift as infinitely well-determined, and approximate the window function of the redshift bin i as

$$\theta(z - z_{\text{min},i})\theta(z_{\text{max},i} - z), \quad (4.1)$$

where $z_{\text{min},i}$ and $z_{\text{max},i}$ denote, respectively, the lower and upper boundaries of the bin, and θ is the Heaviside step function.

4.2 Uncertainty in the weak lensing mass determination

The mass of a cluster determined through weak lensing, M_{obs} , is subject to scatter and bias with respect to the true mass of the cluster M [33, 34]. For a mass determination algorithm that treats clusters as spherical objects, the triaxiality of realistic cluster density profiles,

for example, could cause the cluster mass to be over- or underestimated depending on the orientation of the major axis in relation to the line-of-sight. Additional biases are incurred if the true density profile deviates from the assumed one.

In this work, we assume that the bias can be controlled to the required level of accuracy, and model only the scatter in the mass determination using a log-normal distribution [33, 34],

$$P(M_{\text{obs}}|M) = \frac{1}{M_{\text{obs}}\sqrt{2\pi\sigma^2}} \exp\left[-\frac{(\ln M_{\text{obs}} - \mu)^2}{2\sigma^2}\right], \quad (4.2)$$

whose mean is given by $\exp(\mu + \sigma^2/2)$. Here, $P(M_{\text{obs}}|M)$ denotes the probability that a cluster with true mass M is mistakenly determined to have a mass M_{obs} by the survey. Since we assume an unbiased mass determination, it follows that the mean of the distribution must match the true mass M and subsequently $\mu = \ln M - \sigma^2/2$. We use $\sigma = 0.6$ to model the mass scatter [33].

The distribution (4.2) can be integrated over M_{obs} in the interval $[M_{\text{min},j(i)}, M_{\text{max},j(i)}]$ in order to determine the probability that a cluster of true mass M in the redshift bin i will be determined to lie in the mass bin $j(i)$. Combing the resulting integral with the redshift window function $V_i(z)$ from equation (4.1), we obtain the window function for the redshift and mass bin $\{i, j(i)\}$,

$$W_{i,j(i)}(M, z) = \theta(z - z_{\text{min},i})\theta(z_{\text{max},i} - z) \int_{M_{\text{min},j(i)}}^{M_{\text{max},j(i)}} dM_{\text{obs}} P(M_{\text{obs}}|M) \theta(M_{\text{obs}} - M_{\text{thr}}(z)), \quad (4.3)$$

where $M_{\text{thr}}(z)$ is the mass detection threshold, to be discussed in section 5.1.

5 Mock data generation

The observable quantity in a cluster survey is the number of clusters $N_{i,j(i)}$ in the redshift bin i and mass bin $j(i)$. Thus for any given fiducial cosmology and survey specifications, one may compute the fiducial cluster numbers $N_{i,j(i)}^{\text{fid}}$ as per equation (3.7), and then create a mock data set $\hat{N}_{i,j(i)}$ by assuming $\hat{N}_{i,j(i)}$ to be a stochastic variable that follows a Poisson distribution with parameter $N_{i,j(i)}^{\text{fid}}$. An ensemble of realisations may be generated by repeating the procedure multiple times, and parameter inference performed on each mock realisation in order to assess the performance of a survey.

This is clearly a very lengthy process. However, as shown in reference [35], for the sole purpose of establishing a survey's sensitivity to cosmological parameters, it suffices to use only one mock data set in which the data points are set to be equal to the predictions of the fiducial model, i.e., $\hat{N}_{i,j(i)} = N_{i,j(i)}^{\text{fid}}$. This much simplified procedure correctly reproduces the survey sensitivities in the limit of infinitely many random realisations, and is the procedure we adopt in our analysis.

In the following we describe in some detail the survey specifications that go into the computation of the fiducial $N_{i,j(i)}^{\text{fid}}$: the mass detection threshold, our redshift and mass binning scheme, and the survey completeness and efficiency. In section 5.4 we summarise the mock data sets to be used in our parameter sensitivity forecast.

5.1 Mass detection threshold

We model the redshift-dependent mass detection threshold $M_{\text{thr}}(z)$ following the approach of references [14, 36]. A cluster of mass M at redshift z produces a shear signal $\kappa_G(M, z)$,

where

$$\kappa_G(M, z) = \alpha(M, z) \frac{M/[\pi R_s^2(M, z)]}{\Sigma_{\text{cr}}(z)}. \quad (5.1)$$

Here, assuming a truncated Navarro-Frenk-White (NFW) density profile [37], $R_s(M, z) = R_{\text{vir}}(M, z)/c_{\text{nfw}}$, where R_{vir} is the cluster's virial radius computed according to the spherical collapse model outlined in section 3.1 and appendix A, and c_{nfw} is the halo concentration parameter determined from N -body simulations. We use $c_{\text{nfw}} = 5$ following [33]. The factor $\alpha(M, z)$ is computed from smoothing the (projected) NFW profile using a Gaussian filter of angular smoothing scale θ_G , i.e.,

$$\alpha(M, z) = \frac{\int_0^\infty dx (x/x_G^2) \exp(-x^2/x_G^2) f_{\text{nfw}}(x)}{\ln(1 + c_{\text{nfw}}) - c_{\text{nfw}}/(1 + c_{\text{nfw}})}, \quad (5.2)$$

where $x \equiv \theta/\theta_s$ and $x_G \equiv \theta_G/\theta_s$, with $\theta_s(M, z) = R_s(M, z)/d_A(z)$ and $d_A(z)$ the angular diameter distance to the cluster. The projected NFW profile is encoded in the dimensionless surface density profile $f_{\text{nfw}}(x)$, which can be found in equation (7) of reference [36]. In our analysis we use an angular smoothing scale of $\theta_G = 1$ arcmin.

The mean critical surface mass density $\Sigma_{\text{cr}}(z)$ is, assuming a flat spatial geometry, given by the expression

$$\Sigma_{\text{cr}}^{-1}(z) = \frac{4\pi G}{(1+z)} n_{\text{bg}}^{-1} \int_z^\infty dz' \, dn/dz' \chi(z) [1 - \chi(z)/\chi(z')], \quad (5.3)$$

where $\chi(z')$ denotes the comoving radial distance to the redshift z' , and $(dn/dz')dz'$ is the number density of source galaxies per steradian at redshift $(z', z' + dz')$, normalised such that $n_{\text{bg}} = \int_0^\infty dz' \, dn/dz'$ gives the source galaxy surface density. As in [5], we assume a galaxy redshift distribution of the form

$$\frac{dn}{dz} \propto \left(\frac{z}{z_0}\right)^2 \exp\left[-\left(\frac{z}{z_0}\right)^\beta\right], \quad (5.4)$$

where for a EUCLID-like survey we choose $\beta = 1$, $z_0 = 0.3$, and a source galaxy surface density of $n_{\text{bg}} = 30 \text{ arcmin}^{-2}$ [2].

In order for a cluster to be considered detected, its shear signal κ_G must exceed the ‘‘noise’’ of the survey σ_{noise} by a predetermined amount. Shear detection is limited firstly by the intrinsic ellipticity of the background galaxies, and secondly by the number of galaxy images lensed by the cluster that fall within the smoothing aperture. Thus, the noise term may be estimated as [38]

$$\sigma_{\text{noise}}^2 = \frac{\sigma_\epsilon^2}{4\pi\theta_G^2 n_{\text{bg}}}, \quad (5.5)$$

where σ_ϵ denotes the total mean dispersion of the galaxy intrinsic ellipticity, and we use $\sigma_\epsilon = 0.35$ in our analysis.

Defining a signal-to-noise ratio of $S/N = 3$ to be our detection threshold [2], the expression

$$S/N = \frac{\kappa_G(M_{\text{thr}}(z), z)}{\sigma_{\text{noise}}} \quad (5.6)$$

can now be solved for the mass detection threshold $M_{\text{thr}}(z)$. This sets a lower limit on the cluster mass detectable by lensing at a given redshift z .

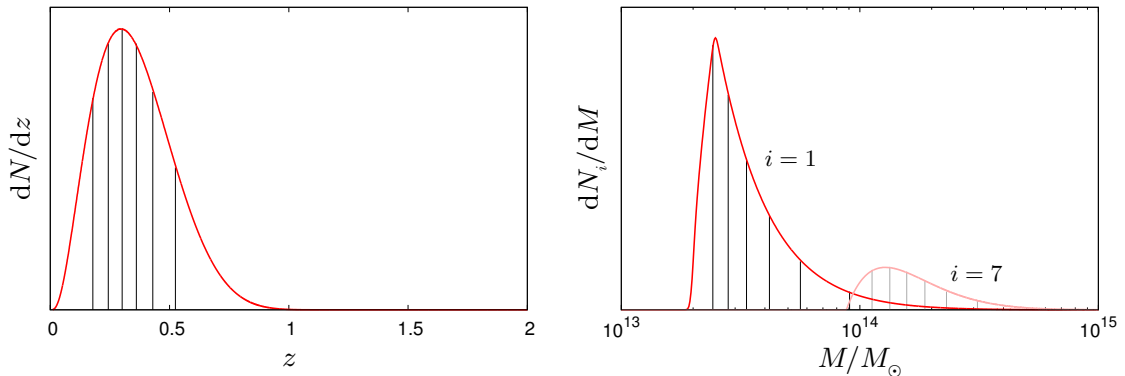


Figure 1. The left panel shows the division into of the observed number of clusters into 7 redshift bins while keeping the cluster count common for all bins. The right panel shows the subsequent division of redshift bins $i = 1, 7$ into 7 mass bins, again with the stipulation that all mass bins contain the same number of clusters.

5.2 Redshift and mass binning

We consider a survey that observes clusters in the redshift range $[z_{\text{low}}, z_{\text{high}}]$. We subdivide this range into N_z bins in such a way so as to maintain the same number of clusters in all bins i in the fiducial cosmology. The resulting bin boundaries $z_{\text{min},i}$ and $z_{\text{max},i}$ then define the redshift window functions (4.1). Clusters in each redshift bin are further subdivided according to their observed masses into N_m mass bins labelled by $j(i)$, again with the enforcement that the number of clusters $N_{i,j(i)}$ should be similar in all bins.

An immediate consequence of such a binning scheme is a variation of the mass bin boundaries $M_{\text{min},j(i)}$ and $M_{\text{max},j(i)}$ with redshift because of (i) the z -dependence of the mass detection threshold $M_{\text{thr}}(z)$, and (ii) the rarity of high-mass clusters at high redshifts. For the latter point, we impose in practice an absolute high-mass cut-off of $M_{\text{high}} = 10^{16} M_{\odot}$, i.e., the upper limit of the last mass bin, $M_{\text{max},N_m(i)}$, is always equal to M_{high} at all redshifts. This number also sets the high-redshift cut-off z_{high} , which is defined to be the redshift at which the mass detection threshold $M_{\text{thr}}(z)$ exceeds M_{high} . The lower cut-off is set at $z_{\text{low}} = 0.01$, since the survey contains a negligible number of clusters below this redshift because of the small volume and a large detection threshold.

Figure 1 illustrates the division of the observed number of clusters into redshift and mass bins in the case $N_z = N_m = 7$. The left panel shows the first division in redshift, while the right panel shows the subsequent division of redshift bins $i = 1, 7$ into mass bins.

5.3 Completeness and efficiency

The completeness f_c of a cluster survey is defined as the fraction of clusters actually detected as peaks by the cluster finding algorithm, while the efficiency f_e is the fraction of detected peaks that correspond to real clusters. In general these quantities can be established precisely only with the help of mock cluster catalogues generated from N -body simulations (see, e.g., [18, 36, 39–42]). Here, we adopt the same simplistic approach taken in reference [17], and assume both f_c and f_e to be mass- and redshift-independent.

The effect of a survey completeness and efficiency not equal to unity can be estimated from simple considerations. The observable N computed from theory as introduced in equation (3.7) is the number of *detectable* clusters in a survey. However, the cluster

finding algorithm will typically detect only a fraction of these, say, N_{peak} peaks, of which $N_{\text{false}} = (1 - f_e)N_{\text{peak}}$ do not correspond to real clusters at all. Thus, the number of *detected* clusters to the *detectable* clusters are related by

$$N = \frac{1}{f_c} (N_{\text{peak}} - N_{\text{false}}), \quad (5.7)$$

where $N_{\text{peak}} = f_c N / f_e$, and $N_{\text{false}} = (1/f_e - 1) f_c N$. Since both N_{peak} and N_{false} follow Poisson statistics, i.e., with variances $\sigma^2(N_{\text{peak}}) \sim N_{\text{peak}}$ and $\sigma^2(N_{\text{false}}) \sim N_{\text{false}}$, the variance of N in a realistic survey can be estimated to be

$$\begin{aligned} \sigma^2(N) &= \frac{1}{f_c^2} [\sigma^2(N_{\text{peak}}) + \sigma^2(N_{\text{false}})] \\ &= N [1/f_e + (1/f_e - 1)] / f_c. \end{aligned} \quad (5.8)$$

From the second equality we see that $f_c \neq f_e \neq 1$ simply amounts to increasing the uncertainty on each individual data point by a factor $\sqrt{[1/f_e + (1/f_e - 1)]/f_c}$, which can be incorporated into the forecast analysis at the level of the likelihood function. We shall return to this point in section 6.2 where we discuss explicitly the construction of the likelihood function. Suffice it to say for now that we adopt the values $f_c = 0.70$ and $f_e = 0.75$, which may be reasonably expected for the LSST [17], and which are likely very conservative when applied to EUCLID because of its much narrower point spread function.

5.4 Synthetic data sets

We summarise here the mock EUCLID-like data sets we generate and use in our parameter sensitivity forecast.

- A cluster data set in the redshift range $z \in [0.01, z_{\text{high}}]$, and the mass range $M \in [M_{\text{thr}}(z), 10^{16} M_{\odot}]$, where $M_{\text{thr}}(z)$ denotes the redshift-dependent mass detection threshold as described in section 5.1, and z_{high} is defined as the redshift at which $M_{\text{thr}}(z)$ exceeds $10^{16} M_{\odot}$ as discussed in section 5.2. We slice the redshift- and the mass-space into N_z and N_m bins respectively according to the scheme detailed in section 5.2.
- Mock data from a PLANCK-like CMB measurement, generated according to the procedure of [35]. Note that although we do not use real PLANCK data [43], only synthetic CMB data of comparable constraining power, we shall continue to refer to this synthetic data set as “PLANCK data” when discussing parameter constraints.
- We use also the cosmic shear auto-correlation power spectrum, the galaxy clustering auto-spectrum, and the shear-galaxy cross-correlation power spectrum that will be derived from a EUCLID-like photometric survey. The procedure for generating these mock data sets has already been described detail in [5], and is recapitulated here for completeness.
 - The cosmic shear auto-spectrum is $C_{\ell,ij}^{\text{ss}}$, where the multipole ℓ runs from 2 to $\ell_{\text{max}}^s = 2000$ independently of redshift. The indices $i, j \in [1, N_s]$ label the redshift bin, where the redshift slicing is such that all bins contain similar numbers of source galaxies and so suffer the same amount of shot noise. We use $N_s = 2$; introducing more redshift bins does not significantly improve the parameter sensitivities [5].

- The galaxy auto-spectrum $C_{\ell,ij}^{\text{gg}}$ comprises multipole moments running from $\ell = 2$ to $\ell_{\text{max}}^{\text{g},i}$ in redshift bins $i, j \in [1, N_{\text{g}}]$, where the choice of $N_{\text{g}} = 11$ exhausts to a large extent the information extractable from $C_{\ell,ij}^{\text{gg}}$ [5]. The redshift slicing is again designed to maintain the same number of source galaxies across all redshift bins. In contrast to the cosmic shear auto-spectrum, we implement here also a redshift-bin-dependent maximum multipole $\ell_{\text{max}}^{\text{g},i}$ so as to eliminate those (redshift-dependent) scales on which nonlinear scale-dependent galaxy bias becomes important. The linear galaxy bias is however always assumed to be exactly known.
- Finally, the shear-galaxy cross-spectrum $C_{\ell,ij}^{\text{sg}}$ in the shear redshift bin $i \in [1, N_{\text{s}}]$ and galaxy redshift bin $j \in [1, N_{\text{g}}]$ runs from $\ell = 2$ to $\ell_{\text{max}}^{\text{g},j}$ determined by the galaxy redshift binning.

6 Forecasting

We now describe our parameter sensitivity forecast for a EUCLID-like photometric survey including a measurement of the cluster mass function. The forecast is based on the construction of a likelihood function for the mock data, whereby the survey’s sensitivities to cosmological parameters can be explored using Bayesian inference techniques.

6.1 Model parameter space

Reference [5] considered a 7-parameter space spanned by the physical baryon density ω_{b} , the physical dark matter (cold dark matter and massive neutrinos) density ω_{dm} , the dimensionless Hubble parameter h , the amplitude and spectral index of the primordial scalar fluctuations A_{s} and n_{s} , the reionisation redshift z_{re} , and the neutrino density fraction $f_{\nu} = \omega_{\nu}/\omega_{\text{dm}}$, with $\omega_{\nu} = \sum m_{\nu}/(94.1 \text{ eV})$. In the present analysis we extend this model parameter space to include also the possibility of a non-standard radiation content, quantified by the effective number of massless neutrinos $N_{\text{eff}}^{\text{ml}}$, as well as three dynamical dark energy parameters $\Theta^{\text{Q}} \equiv (w_0, w_a, \hat{c}_{\text{s}}^2)$, taking the total number of free parameters to eleven:

$$\Theta^{(11)} \equiv (\Theta^{(8)}, \Theta^{\text{Q}}) \equiv \left((\omega_{\text{b}}, \omega_{\text{dm}}, h, A_{\text{s}}, n_{\text{s}}, z_{\text{re}}, f_{\nu}, N_{\text{eff}}^{\text{ml}}), (w_0, w_a, \hat{c}_{\text{s}}^2) \right). \quad (6.1)$$

As in [5] we assume only one massive neutrino state, so that $N_{\text{eff}}^{\text{ml}} = 2.046 + \Delta N$, where ΔN parameterises any non-standard physics that may induce a non-standard radiation content. Note that the 0.046 contribution in $N_{\text{eff}}^{\text{ml}}$ comes from non-instantaneous neutrino decoupling and finite temperature QED effects, and should in principle be shared between *both* the massless and the massive neutrino states. However, in practice, the precise treatment of this small correction has no measurable effect on our parameter forecast. Lastly, we remark that, parameterised as such, ΔN can run from the lowest value of -2.046 to anything positive. Many popular models with non-standard radiation contents associate a positive ΔN with additional relativistic particle species such as, e.g., sterile neutrinos [44, 45]. A negative ΔN can however arise in, e.g., models with extremely low reheating temperatures [46, 47].

For the non-dark energy part of the parameter space, our fiducial model is defined by the parameter values

$$\Theta_{\text{fid}}^{(8)} = (0.022, 0.1126228, 0.7, 2.1 \times 10^{-9}, 0.96, 11, 0.00553, 2.046). \quad (6.2)$$

For the dark energy sector, we begin with the fiducial values $\Theta_{\text{fid}}^{\text{Q}} = (-1, 0, \infty)$ corresponding to dark energy in the form of a cosmological constant. The first part of our analysis (up to

and including section 7.4) will also be performed with the dark energy sound speed fixed at $c_s^2 = \infty$, i.e., homogeneous dark energy. We shall return to dark energy density perturbations in section 7.5, and study the constraints on the dark energy sound speed under a variety of assumptions for the fiducial dark energy parameter values Θ_{fid}^Q .

6.2 Likelihood function

Given a theoretical prediction N_{th} for the observable number of clusters in a specific redshift and mass bin, the probability of actually observing N_{obs} clusters follows a Poisson distribution of N_{obs} degrees of freedom. However, the imperfect completeness and efficiency of the survey necessitate that we rescale uncertainty on each data point by an amount $f^{-1} \equiv \sqrt{[1/f_e + (1/f_e - 1)]/f_c}$ (see section 5.3). We accomplish this by defining an effective number of observed clusters $\tilde{N}_{\text{obs}} \equiv f^2 N_{\text{obs}}$, and likewise an effective theoretical prediction $\tilde{N}_{\text{th}} \equiv f^2 N_{\text{th}}$. The effective probability distribution is then

$$\mathcal{L}_{\text{P}} \left(\tilde{N}_{\text{obs}} | \tilde{N}_{\text{th}} \right) = \frac{\tilde{N}_{\text{th}}^{\tilde{N}_{\text{obs}}}}{\tilde{N}_{\text{obs}}!} \exp \left[-\tilde{N}_{\text{th}} \right]. \quad (6.3)$$

In a real survey, the effective observed number of clusters \tilde{N}_{obs} in any one bin is necessarily an integer so that equation (6.3) applies directly. In our forecast, however, \tilde{N}_{obs} corresponds to the theoretical expectation value of the fiducial model which generally does not evaluate to an integer. To circumvent this inconvenience, we generalise the likelihood function (6.3) by linearly interpolating the logarithm of the discrete distribution \mathcal{L}_{P} in the interval $[\text{floor}(\tilde{N}_{\text{obs}}), \text{ceiling}(\tilde{N}_{\text{obs}})]$, i.e.,

$$\begin{aligned} \ln \mathcal{L}(\tilde{N}_{\text{obs}} | \tilde{N}_{\text{th}}) \equiv & \left(1 + \text{floor}(\tilde{N}_{\text{obs}}) - \tilde{N}_{\text{obs}} \right) \ln \mathcal{L}_{\text{P}} \left(\text{floor}(\tilde{N}_{\text{obs}}) | \tilde{N}_{\text{th}} \right) \\ & + \left(\tilde{N}_{\text{obs}} - \text{floor}(\tilde{N}_{\text{obs}}) \right) \ln \mathcal{L}_{\text{P}} \left(\text{ceiling}(\tilde{N}_{\text{obs}}) | \tilde{N}_{\text{th}} \right). \end{aligned} \quad (6.4)$$

The total cluster log-likelihood function is then obtained straightforwardly by summing $\ln \mathcal{L}$ over all redshift and mass bins.

7 Results

7.1 Impact of the number of bins

We examine first how the parameter sensitivities of the cluster survey depend on the number of redshift and mass bins used. Figure 2 shows the posterior standard deviations for a range of cosmological parameters derived from a combination of synthetic PLANCK and cluster data as functions of N_z and N_m , normalised to the corresponding $N_z = N_m = 1$ result.

A general trend is immediately clear: for the parameters w_0 and h , while increasing the number of mass bins results in moderate gain, it is the number of redshift bins used that contributes mostly to improving the parameter sensitivities. For example, in the case of a fixed $N_m = 1$, the number of redshift bins needs to be increased to two or three in order for the sensitivities to improve as much or more than what can be gained for a fixed $N_z = 1$ by splitting the data into ten or more redshift bins. For $N_{\text{eff}}^{\text{ml}}$ and ω_m improvements in sensitivity are absent when no mass binning is used. From $N_m = 2$ and beyond decent improvements are found in both directions. This can be traced to the fact that these parameters are primarily responsible for the shape and the overall normalisation of the cluster mass function, less so

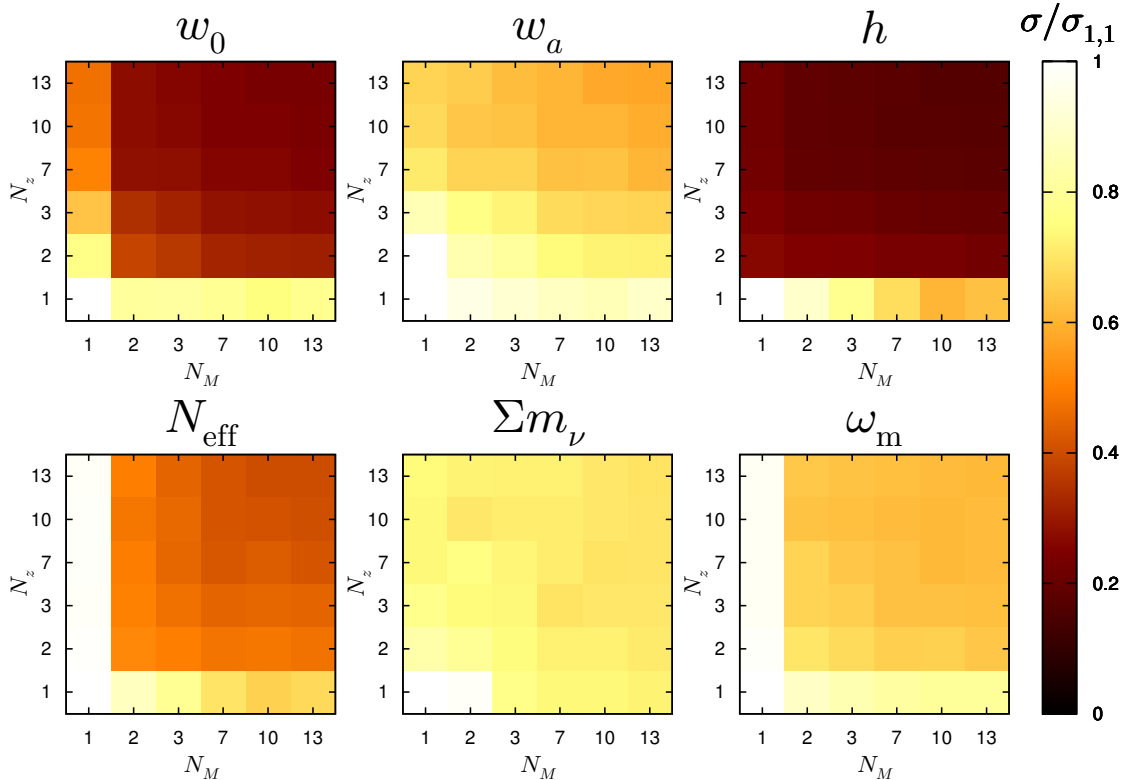


Figure 2. Dependence of the posterior standard deviations, σ , for selected cosmological parameters for CMB+clusters on the number of redshift bins N_z and mass bins N_m . All numbers have been normalised to the corresponding $N_z = N_m = 1$ result.

the redshift dependence. See section 7.2. For w_a and Σm_ν the sensitivity increases roughly equally with increasing N_z and N_m .

Some parameter sensitivities continue to improve beyond $N_z = 10$ and one might therefore argue for using a very large number of redshift bins. However, for $N_z = 10$, the narrowest bin typically has a width of order $\Delta z = 0.03$; pushing much beyond $N_z = 10$ may cause our results to lose their robustness against redshift uncertainty (see section 4.1). Furthermore, when cluster data are used in conjunction with angular power spectra from cosmic shear and/or galaxy clustering, the gain in going beyond $N_z = 10$ is substantially reduced. Henceforth, we shall adopt $N_z = N_m \equiv N_{\text{bin}} = 10$. Figure 3 shows the marginalised joint two-dimensional posteriors in the (w_0, w_a) - and the $(N_{\text{eff}}^{\text{ml}}, \omega_m)$ -subspace from CMB+clusters for this configuration, as well as for $N_{\text{bin}} = 1, 2$.

7.2 Probes of the expansion history versus probes of the power spectrum

One of the advantages of the cluster mass function (with redshift binning) is that it is highly sensitive to those parameters that govern the linear growth function and hence (in the case of standard gravity) the expansion history of the universe. This makes redshift-binned cluster measurements powerful for constraining dark energy parameters, as well as for establishing the reduced matter density $\Omega_m \equiv \omega_m/h^2$. Furthermore, because the normalisation of the cluster abundance is directly sensitive to the physical matter density ω_m , the Hubble parameter h can also be very effectively constrained.

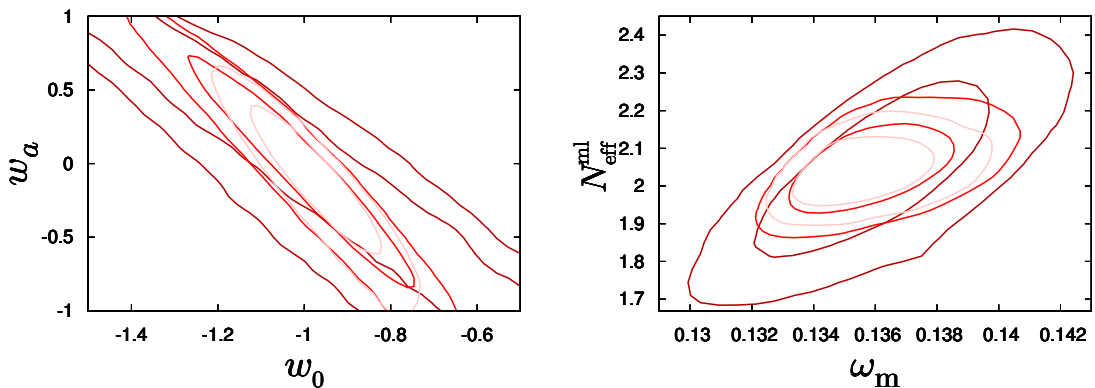


Figure 3. Marginalised joint two-dimensional 68% and 95% credible contours from the CMB+clusters data set. The default redshift and mass binning configuration for the cluster data is $N_{\text{bin}} = 10$ (light red), but we also show the results for $N_{\text{bin}} = 1$ bin (dark red) and 2 (red).

Table 1. Posterior standard deviations for the parameters ω_m , h , $\sum m_\nu$, $N_{\text{eff}}^{\text{ml}}$, w_0 , and w_a derived from various combinations of data sets. Here, “c” denotes PLANCK CMB data, “g” galaxy auto-spectrum (11 redshift bins), “s” shear auto-spectrum (2 bins), “x” shear-galaxy cross-correlation, and “cl” the cluster data (10 redshift bins, 10 mass bins). The table also shows the posterior standard deviation of w_p defined in section 7.4 and the w_p - w_a figure-of-merit (FoM), defined in equation (7.1) as $(\sigma(w_p)\sigma(w_a))^{-1}$.

Data	$10^3 \times \sigma(\omega_m)$	$100 \times \sigma(h)$	$\sigma(\sum m_\nu)/\text{eV}$	$\sigma(N_{\text{eff}}^{\text{ml}})$	$\sigma(w_0)$	$\sigma(w_p)$	$\sigma(w_a)$	FoM/ 10^3
csgx	1.3	0.69	0.023	0.074	0.13	0.011	0.19	0.48
ccl	1.6	0.80	0.050	0.061	0.24	0.036	0.33	0.084
csgxcl	0.50	0.46	0.015	0.033	0.11	0.0096	0.15	0.69
cscl	0.67	0.70	0.020	0.043	0.17	0.015	0.24	0.28

The sum of neutrino masses $\sum m_\nu$ is significantly less well measured by clusters than by the shear and the galaxy power spectra. This is because firstly, $\sum m_\nu$ plays a negligible role (compared with, e.g., dark energy parameters) in the redshift dependence of the late-time linear growth function. Secondly, although the shape of the cluster mass function is in principle also subject to a mass-dependent suppression due to neutrino free-streaming (e.g., [23, 48]), the actual range of cluster masses probed by a realistic cluster survey is very narrow (see figure 1), so that the suppression can be easily be mimicked by other effects such as an excess of relativistic energy density or simply a smaller initial fluctuation amplitude.

Interestingly, a non-standard radiation content as parameterised by $N_{\text{eff}}^{\text{ml}}$, although has no direct effect on the late-time expansion or growth history, is quite well constrained by CMB+clusters. This can be understood as follows: using CMB data alone, $N_{\text{eff}}^{\text{ml}}$ is strongly degenerate with ω_m and h . However, because the cluster mass function is directly sensitive to ω_m and h , it very effectively lifts any degeneracy of these parameters with $N_{\text{eff}}^{\text{ml}}$ when used in combination with CMB data. As shown in the lower right panel of figure 4, very little degeneracy remains between $N_{\text{eff}}^{\text{ml}}$ and ω_m for the CMB+clusters data set. A more telling illustration of how the binned cluster data removes the $(N_{\text{eff}}, \omega_m)$ -degeneracy can be found in the right panel of figure 3: Here, when only one redshift and mass bin is used, the cluster mass function is primarily sensitive to the fluctuation amplitude on small scales so that the

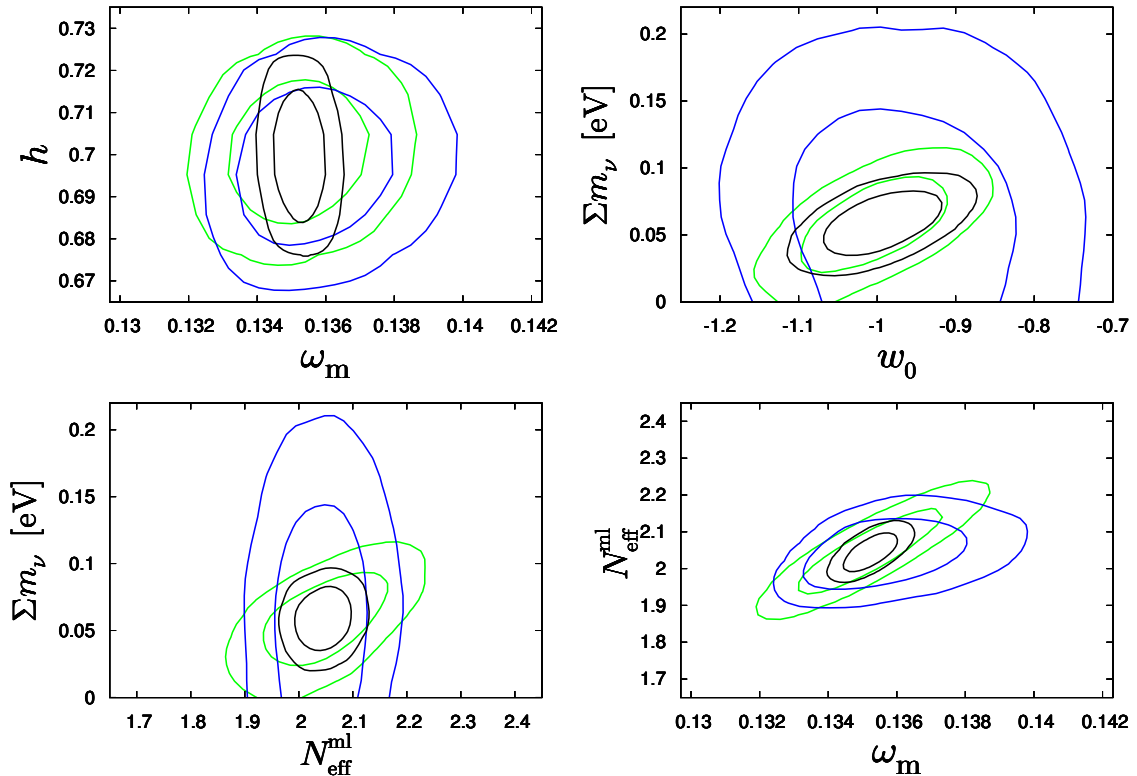


Figure 4. Marginalised joint two-dimensional 68% and 95% credible contours from the CMB+clusters data set (“ccl”, blue), CMB+shear+galaxies (“csgx”, green), and all data sets (“csgxcl”, black) for various parameters, using the default binning configuration of $N_{\text{bin}} = 10$ for the cluster data.

$(N_{\text{eff}}, \omega_m)$ -degeneracy persists in the CMB+clusters fit. However, as soon as access to the linear growth function and some shape information become available through as little as $N_z = N_m = 2$ bins, the degeneracy is partly broken because of the growth function’s direct dependence on Ω_m and of the normalisation’s dependence on ω_m .

7.3 Combining all data sets: constraints on neutrino parameters

Perhaps the most noteworthy result of table 1 is that, while CMB+shear+galaxies (“csgx”) and CMB+clusters (“ccl”) are well-suited to measuring different parameters and are hence in a sense complementary to each other, the combined usage of *all* data sets, i.e., the “csgxcl” combination, always leads to fairly significant enhancements in *all* parameter sensitivities. This result can be understood from figure 4, where it is clear that the ‘csgx” and ‘ccl” datasets give rise to almost orthogonal parameter degeneracy directions. In combination these data sets conspire to lift each other’s degeneracies.

For neutrino parameters, it is interesting to note that while “csgx” and “ccl” return $\sigma(\sum m_\nu) = 0.023$ eV and 0.050 eV respectively, in combination the sensitivity improves to $\sigma(\sum m_\nu) = 0.015$ eV. This is nearly as good a sensitivity as was found earlier in [5] from the “csgx” data set, but for a much simpler 7-parameter cosmological model. This extraordinary sensitivity to $\sum m_\nu$ does not deteriorate much even if we exclude galaxy clustering from the analysis; as shown in table 1, the “cscl” combination yields a similar $\sigma(\sum m_\nu) = 0.020$ eV. This is an especially reassuring result in view of the assumption of an exactly known linear

galaxy bias we have adopted for the galaxy power spectrum, which some may deem unrealistic. Thus, we again conclude that EUCLID, in combination with PLANCK CMB data, will be able to probe neutrino masses at 3σ precision or better. Likewise, the “csgxcl” data set is now sensitive to $N_{\text{eff}}^{\text{ml}}$ at $\sigma(N_{\text{eff}}^{\text{ml}}) = 0.033$ (0.043 for “cscl”), meaning that for the first time the small deviation of 0.046 from 3 in the fiducial $N_{\text{eff}}^{\text{ml}}$ can be probed with 1σ precision.

7.4 The dark energy figure-of-merit

It is useful to quantify the constraining power of an observation (or a combination thereof) over a particular set of cosmological parameters in terms of a figure-of-merit (FoM). For the dark energy equation of state $w(a)$, one could define the FoM to be the inverse of the N -volume spanned by the error ellipsoid in the N -dimensional parameter space describing $w(a)$, such that the larger the volume the smaller the constraining power. A naïve volume (or area) estimator in the 2-dimensional space of our parameterisation might be the product $\sigma(w_0)\sigma(w_a)$. However, because w_0 and w_a are strongly correlated, as is evident in figure 3, and the degree of correlation is *a priori* unknown, the product $\sigma(w_0)\sigma(w_a)$ will not only always overestimate the area of the ellipse, but do so also in a way that is strongly dependent on the degree of correlation between the two parameters. For this reason, a more commonly adopted definition, used also in, e.g., the EUCLID Red Book [2], is

$$\text{FoM} \equiv (\sigma(w_p)\sigma(w_a))^{-1}, \quad (7.1)$$

following from a parameterisation of the dark energy equation of state of the form $w(a) = w_p + w_a(a_p - a)$. Here, the “pivot” scale factor a_p is chosen such that w_p and w_a are uncorrelated, i.e., the parameter directions are defined to align with the axes of the error ellipse. Note that this parameterisation of $w(a)$ is entirely equivalent to the conventional (w_0, w_a) -parameterisation; the parameter spaces are related by a linear rotation, thus preserving the area of the error ellipse [49].

Table 2 contrasts the FoM computed as per definition (7.1) and the naïve estimate $(\sigma(w_0)\sigma(w_a))^{-1}$. For our default 10-parameter model, the FoM of the “csgxcl” data combination is approximately 690, while the naïve approach underestimates the figure by about a factor of ten. To facilitate comparison with other estimates in the literature, we also perform the same calculation for a reduced 7-parameter model,

$$\Theta^{\text{reduced}} \equiv (\omega_b, \omega_{\text{dm}}, h, A_s, n_s, w_0, w_a), \quad (7.2)$$

motivated in part by the model used in EUCLID Red Book [2].¹ As expected, the smaller parameter space yields a significantly better FoM, about 1900, than our default 10-parameter model. This figure is about 50% lower than the official value of 4020 from the EUCLID Red Book [2], however, it climbs up to a higher value of about 5200 if we switch from MCMC to a Fisher matrix forecast such as that in [2].² Many factors could have contributed to the difference between our and the Euclid official FoM, from the assumed parameter space (see footnote 1) to the survey parameters actually used in the analysis. As the discrepancy is

¹The model adopted in reference [2] has spatial curvature Ω_k also as a free parameter. However, the degree of correlation between Ω_k and the dark energy parameters w_0 and w_a is expected to be quite small for a EUCLID-like survey [50]. We therefore adhere to our original assumption of spatial flatness, but simply note that the FoM obtained in this work for the reduced parameter space (7.2) will in general be more optimistic than the value quoted in [2].

²Fisher matrix forecasts have a tendency to overestimate parameter sensitivities compared with MCMC analyses, a point also discussed in, e.g., [35, 51, 52].

Table 2. The dark energy figure-of-merit (FoM/ 10^3) computed using an MCMC forecast [MCMC(w_p, w_a)] and a Fisher matrix forecast [Fisher(w_p, w_a)] for the two parameter spaces of equations (6.1) and (7.2). For comparison, we also show the corresponding values obtained from a naïve estimate [MCMC(w_0, w_a)] as discussed in the main text. See legend in table 1.

Data	Parameter space	MCMC (w_0, w_a)	MCMC (w_p, w_a)	Fisher (w_p, w_a)
csgxcl	equation (6.1) ($\hat{c}_s^2 = \infty$)	0.060	0.69	
csgxcl	equation (7.2)	0.30	1.9	5.2

Table 3. Posterior standard deviations for the parameters w_0 , w_p , and w_a derived from the “ccl” and “csgxcl” data combinations (see legend in table 1) assuming different fiducial values for the parameters. Also shown are the corresponding FoMs as per definition (7.1).

Data	w_0^{fid}	w_a^{fid}	$\sigma(w_0)$	$\sigma(w_p)$	$\sigma(w_a)$	FoM/ 10^3
ccl	-1.00	0.00	0.24	0.036	0.33	0.084
ccl	-0.83	0.00	0.18	0.027	0.26	0.14
ccl	-1.17	0.00	0.31	0.044	0.39	0.058
ccl	-1.00	0.35	0.17	0.029	0.25	0.14
ccl	-1.00	-0.35	0.28	0.041	0.38	0.064
csgxcl	-1.00	0.00	0.11	0.0096	0.15	0.69
csgxcl	-0.83	0.00	0.082	0.0087	0.12	0.96
csgxcl	-1.17	0.00	0.13	0.011	0.18	0.51
csgxcl	-1.00	0.35	0.075	0.0088	0.11	1.0
csgxcl	-1.00	-0.35	0.11	0.010	0.16	0.63

no more than 50%, which could be interpreted as a reasonable compatibility, we shall not investigate its origin any further. However, we stress that any FoM quoted for an observation or a set of observations is strongly dependent on the assumptions about the underlying cosmological parameter space, and therefore should always be taken *cum grano salis*.

Lastly, we present in table 3 the FoMs for various fiducial models and data combinations. Clearly, the FoM depends crucially on the data combination used to derive it; between the combinations “ccl” and “csgxcl”, the difference in the FoMs is typically a factor of five to ten. When changing the fiducial cosmology, the trend is that a less negative equation of state at the present or in the past leads to a higher figure of merit. The dependence on the choice of fiducial values for the model parameters is however fairly weak; moving away from a Λ CDM fiducial cosmology ($w_0^{\text{fid}} = -1, w_a^{\text{fid}} = 0$) induces no more than a 50% variation in the FoM (provided the same number of parameters is varied). We may therefore consider the FoM computed for $w_0^{\text{fid}} = -1$ and $w_a^{\text{fid}} = 0$ as representative.

7.5 Dark energy sound speed and perturbations

In the analysis so far we have neglected the effect of dark energy perturbations. We now introduce dark energy perturbations into the analysis as per the discussion in section 2, and investigate the constraining power of a EUCLID-like survey on this aspect of dark energy.

We consider four fiducial models differing in their fiducial values of (w_0, w_a, \hat{c}_s^2):

- Model 1: (w_0, w_a) = (-1, 0) and $\hat{c}_s^2 = 1^3$ (i.e., Λ CDM)

³The choice of \hat{c}_s^2 for the Λ CDM model is immaterial, since by definition dark energy does not cluster in

Table 4. Posterior 68% (95%) credible limits $\log \hat{c}_s^2$ in various fiducial models derived from the combined “csgxcl” data set. See legend in table 1.

Data	w_0	w_a (fixed)	\hat{c}_s^2	$\log \hat{c}_s^2$	$\log \hat{c}_s^2$ 68%(95%) C.I.
csgxcl	-1.00	0.00	1	0	unconstrained
csgxcl	-1.17	0.00	1	0	> -3.0(-4.1)
csgxcl	-0.83	0.00	1	0	> -5.8(-)
csgxcl	-0.83	0.00	10^{-6}	-6	< -5.9(-3.5)

- Model 2: $(w_0, w_a) = (-1.17, 0)$ and $\hat{c}_s^2 = 1$
- Model 3: $(w_0, w_a) = (-0.83, 0)$ and $\hat{c}_s^2 = 1$
- Model 4: $(w_0, w_a) = (-0.83, 0)$ and $\hat{c}_s^2 = 10^{-6}$

In all models, we fix $w_a = 0$ because of the pathological behaviour of dark energy perturbations when crossing the phantom divide $w = -1$ [53, 54]. We present only results obtained from the “csgxcl” data sets, shown in table 4 and figure 5. All results have been obtained assuming a top-hat prior on $\log \hat{c}_s^2$ of $\log \hat{c}_s^2 \in [-10, 2]$. Note that the posteriors for $\log \hat{c}_s^2$ in all models show no clear peak structure so that $\log \hat{c}_s^2$ can only be constrained from one side. Instead of the posterior standard deviation, we therefore quote in table 4 the appropriate one-sided limits.

For the three models with $\hat{c}_s^2 = 1$, the Jeans mass M_J , defined in equation (A.6), is of order $10^{23} M_\odot$ at $z = 0$ and lies well above the maximum observed cluster mass M_{high} . This tells us immediately that these models are undetectable by a EUCLID-like cluster survey. However, as \hat{c}_s^2 drops below $\sim 10^{-3}$ ($M_J \sim 10^{17} M_\odot$), the additional mass-dependence it produces on the cluster mass function begins to be visible to EUCLID, and we see a sharp decrease in the posterior probability for $\log \hat{c}_s^2$ in figure 5. In the case of model 2, the corresponding posterior probabilities eventually drop to zero, **thereby (was originally “thus”)** allowing us to place a lower limit on \hat{c}_s^2 . The same trend can be seen also for model 3, although in this case the posterior probability does not drop all the way to zero. A likely reason for this is that the main constraining power towards \hat{c}_s^2 comes from the cluster survey and $w_0 > -1$ leads to fewer clusters compared to $w_0 < -1$, e.g., model 3 has about two thirds of the number clusters in model 2. This makes the effect of the dark energy perturbations less significant compared to the Poisson noise. No constraints on \hat{c}_s^2 are available for model 1 (the Λ CDM model), because dark energy perturbations are generally suppressed by a factor of $1 + w_0$ relative to dark matter perturbations and are hence practically nonexistent in the vicinity of $w_0 = -1$.

In the remaining model 4 with $\hat{c}_s^2 = 10^{-6}$ the dark energy sound speed can be constrained from above. This is a consequence of $M_J (\simeq 4 \times 10^{14} M_\odot$ at $z = 0$) lying close to the detection threshold of the EUCLID cluster survey, i.e., the effect of the dark energy perturbations disappears when the sound speed is increased. Our studies show that with a lower detection threshold, so that the Jeans mass falls well within the cluster mass range probed by EUCLID, the transition from minimal dark energy clustering to full dark energy clustering can be very effectively observed with the help of cluster mass binning. This would allow the dark energy sound speed to be constrained from both sides. We emphasise however that our choice of

this model and $\delta_Q = 0$ is automatically implemented in CAMB.

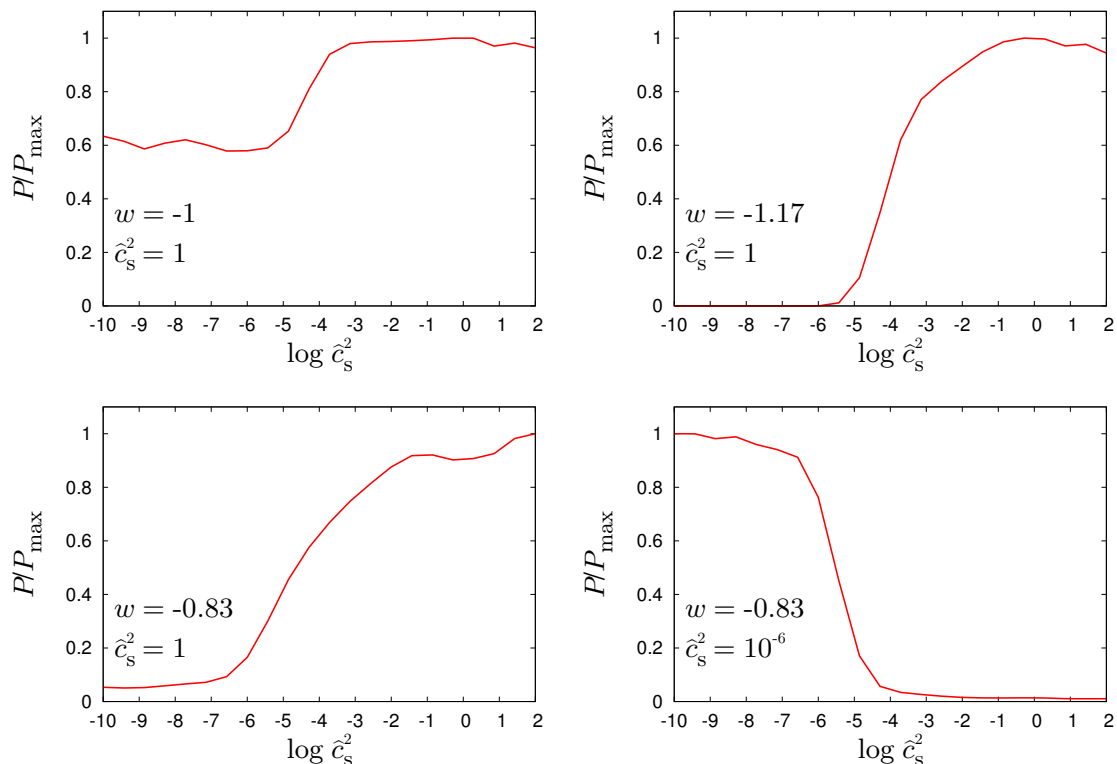


Figure 5. Marginalised one-dimensional posterior probability density for $\log \hat{c}_s^2$ for four different fiducial models (see labels in plots) from a “csgxcl” fit.

the fiducial value of w_0 also plays a crucial role towards establishing the quoted limits, again because of the $1 + w_0$ suppression suffered by the dark energy perturbations relative to the dark matter perturbations. When comparing the constraints obtained on model 3 and 4, one should remember that the mass and redshift bins are assigned according to the fiducial model, so the signature of dark energy clustering at some value of \hat{c}_s^2 appears different in the two models. The quantitative constraints on $\log \hat{c}_s^2$ obtained here should be taken *cum gran salis* as discussed in the next section.

7.5.1 Modelling of the cluster mass function

The constraints obtained thus far on the dark energy sound speed are based on our particular modelling of the cluster mass function, namely, equation (3.1) and the prescriptions of appendix A. In this model, the cluster mass function is assumed to take the Sheth-Tormen form as a function of the *total cluster mass* $M = M_m + M_Q$, i.e., including both masses of the nonrelativistic matter and the virialised dark energy. Thus there are three ways in which the dark energy sound speed is propagated into the observable: (i) via the linear power spectrum into $\sigma_m(M)$, (ii) the mass-dependent linear threshold density $\delta_c(M, z)$, and (iii) the virial mass of the cluster.

However, our model is by no means unique. Other models exist and differ from ours essentially in the implementation of the above three points. We emphasise that until full-scale numerical simulations including clustering dark energy become available, it is not clear which of these models is the most correct. For this reason, it is useful to test how strongly

Table 5. Posterior 68% (95%) credible limits $\log \hat{c}_s^2$ for various definitions of the cluster mass function (CMF) derived from the “csgxcl” data combination. See legend in table 1.

Data	CMF	w_0	w_a (fixed)	\hat{c}_s^2	$\log \hat{c}_s^2$	$\log \hat{c}_s^2$ 68%(95%) C.I.
csgxcl	equation (3.1)	-0.83	0.00	10^{-6}	-6	$< -5.9(-3.5)$
csgxcl	equation (7.3)	-0.83	0.00	10^{-6}	-6	$< -1.4(1.4)$
csgxcl	$P_m^{\text{lin}}(k, z)$ only	-0.83	0.00	10^{-6}	-6	$< -2.5(0.12)$

the constraints on \hat{c}_s^2 depend on the modelling of the cluster mass function. Here, we consider two variations:

1. The model of, e.g., [31, 55] assumes the cluster mass function to follow the Sheth-Tormen form as a function of the *nonrelativistic matter mass*, i.e.,

$$\frac{dn_{\text{ST}}}{dM_m}(M, z) = -\sqrt{\frac{2a}{\pi}} A \left[1 + \left(\frac{a\delta_c^2}{\sigma_m^2} \right)^{-p} \right] \frac{\bar{\rho}_m}{M_m^2} \frac{\delta_c}{\sigma_m} \left(\frac{d \log \sigma_m}{d \log M_m} - \frac{d \log \delta_c}{d \log M_m} \right) \exp \left[-a \frac{\delta_c^2}{2\sigma_m^2} \right], \quad (7.3)$$

where $\sigma_m^2(M_m, z)$ is the variance of the linear matter density field smoothed on a comoving length scale $X_{\text{sm}} \equiv a^{-1}[3M_m/(4\pi\bar{\rho}_m)]^{1/3}$. The observed cluster mass M is identified with the total virial mass of the cluster $M_{\text{vir}} = M_m + M_Q(\tau_{\text{vir}})$, which in the arbitrary \hat{c}_s^2 case can be established using our interpolation method described in appendix A.

This definition of the cluster mass function will in general result in weaker constraints on the dark energy sound speed compared with our default model, because the effect of the virialised dark energy M_Q on the observable is factored in only through the selection function of the survey. We explicitly test this definition for the fiducial model 4 ($w_0 = -0.83, w_a = 0, \hat{c}_s^2 = 10^{-6}$), and find that the sensitivity to $\log \hat{c}_s^2$ degrades significantly (see table 5).

2. Another possibility is to completely ignore dark energy perturbations in the nonlinear modelling of the collapse (i.e., the spherical collapse) of the cluster. In this case dark energy perturbations affect the observable quantity only through their effects on the linear matter power spectrum. This leads to even fewer features in the cluster distribution and hence even weaker constraints on the dark energy sound speed. Again, table 5 shows that, assuming the fiducial model 4, the constraints on $\log \hat{c}_s^2$ degrade.

In summary, any constraint on the dark energy sound speed derived from cluster measurements is strongly dependent on the modelling of the cluster mass function. To this end, a full-scale numerical simulation is mandatory to establish the definitive model, in order for any quoted constraint on \hat{c}_s^2 to be meaningful.

8 Conclusions

In this paper we have considered the constraining power of a EUCLID-like galaxy survey on cosmological parameters in conjunction with PLANCK CMB data. This study is an extension of our previous investigation in [5], in that we have included in the present analysis mock data from the EUCLID cluster survey in addition to the angular cosmic shear and galaxy power

spectra expected from the photometric redshift survey, and we have expanded the parameter space to encompass also dynamical dark energy as well as the possibility of (small-scale) dark energy perturbations.

We find that the different combinations of data sets, CMB+clusters and CMB+shear+galaxies, give comparable sensitivities for parameters that affect only the late-time growth and expansion history of the universe, i.e., those parameters that determine the dynamical dark energy equation of state and the Hubble parameter. The constraints for CMB+clusters depend chiefly on our adoption of redshift binning for the observed clusters, which allows us in particular to probe the transition from matter to dark energy domination. Neutrino masses, on the other hand, are not particularly well-constrained by CMB+clusters ($\sigma(\sum m_\nu) = 0.050$ eV in a 10-parameter model), clearly because they do not play a major role in the overall linear growth of matter density perturbations. Importantly, however, the degeneracy directions of CMB+clusters and CMB+shear+galaxies are largely orthogonal. This means that even though neither data set performs particularly impressively for any one cosmological parameter, in combination they help to lift each other's degeneracies. The sensitivities to $\sum m_\nu$ from CMB+shear+galaxies+clusters is, for example, $\sigma(\sum m_\nu) = 0.015$ eV in a 10-parameter model, which is almost as good as that obtained previously in [5] from CMB+shear+galaxies for a much simpler 7-parameter Λ CDM model. Thus, we can conclude again that a EUCLID-like survey has the potential to measure neutrino masses at 4σ precision or more.

For the dark energy parameters, we find that the combination of CMB+shear+galaxies+clusters results in a dark energy figure-of-merit (FoM), defined in this work as $(\sigma(w_p)\sigma(w_a))^{-1}$, of 690 for a Λ CDM fiducial cosmology, with variations of up to 50% for fiducial cosmologies in which $w_0 \neq -1$ and $w_a \neq 0$. We emphasise that this number has been derived for a 10-parameter cosmological model. Were we to adopt instead a simpler 7-parameter model in which $\sum m_\nu$, N_{eff} and z_{re} are fixed, then the FoM would climb up to 1900 (and to 5200 if a Fisher matrix analysis, instead of MCMC, was used), a value that is comparable to the official estimate of 4020 from the EUCLID Red Book [2].

Finally, we investigate the detectability of dark energy perturbations, parameterised in terms of a non-adiabatic fluid sound speed \hat{c}_s^2 . Along the way we also introduce a model of the cluster mass function that incorporates the effects of \hat{c}_s^2 based on solving and interpolating the spherical top-hat collapse in the known limits of $\hat{c}_s^2 \rightarrow \infty$ (homogeneous dark energy) and $\hat{c}_s^2 = 0$ (dark energy comoving with nonrelativistic matter). We find that for values of the dark energy sound speed whereby the associated Jeans mass lies within the mass detection range of the cluster survey, dark energy perturbations imprint a distinct step-like signature in the observed cluster mass function. With the help of cluster mass binning, this signature makes these models distinguishable from those in which the Jeans mass lies well outside (both below and above) the detection range. The models tested in this paper have associated Jeans masses either well above the mass range probed or close to the detection threshold, and we show that these can be distinguished at 2σ , as long as the fiducial value of w_0 deviates from -1 by as much as is presently allowed by observations.

We emphasise however that constraints on the dark energy sound speed from cluster measurements depend strongly on the modelling of the cluster mass function, with our default model being a very optimistic one. The very large sensitivity range clearly illustrates the enormous uncertainties in the current state of cluster mass function modelling for clustering dark energy cosmologies. The need for full-scale numerical simulations including dark energy perturbations cannot be overstated if future observations are to be interpretable in these contexts.

Note added: As this work was in its final stage of completion, we learnt of the investigation of [56] which considered the EUCLID cluster survey’s sensitivities to neutrino parameters. While a full comparison is difficult because of the generally different assumptions about the survey parameters and the model parameter space, where the assumptions do to some extent coincide the two analyses appear to be compatible.

Acknowledgements

We acknowledge computing resources from the Danish Center for Scientific Computing (DCSC). OEB acknowledges support from the Stellar Astrophysics Centre at Aarhus University. We thank Ronaldo Batista for discussions on the modelling of the cluster mass function in the context of clustering dark energy.

A Interpolating the spherical collapse between the two limits of \hat{c}_s^2

The spherical top-hat collapse model is exactly defined only in the limits $\hat{c}_s^2 \rightarrow \infty$ and $\hat{c}_s^2 = 0$. In the first case, the dark energy component is non-clustering. The dark matter and baryon components alone suffer gravitational collapse, so that the overdense region preserves its top-hat density profile throughout the collapse, with a comoving radius X given by

$$\frac{\ddot{X}}{X} + \mathcal{H}\frac{\dot{X}}{X} = -4\pi G a^2 \bar{\rho}_m \delta_m, \quad (\text{A.1})$$

where

$$\delta_m(\tau) = [1 + \delta_m(\tau_i)] \left[\frac{X(\tau_i)}{X(\tau)} \right]^3 - 1 \quad (\text{A.2})$$

follows from conservation of the total mass of nonrelativistic matter M_m in the top-hat region. The virial radius R_{vir} , defined as the physical radius of the top-hat at the moment the collapsing region fulfils the virial theorem, is as usual one half of physical radius at turn-around, and the virial mass M_{vir} is identical to M_m , which we also equate with the mass of the cluster M .

In the second case, an exactly vanishing non-adiabatic dark energy sound speed means that, like nonrelativistic matter, dark energy density perturbations also evolve identically on all scales. This again leads to the preservation of the top-hat density profile and hence the conservation of M_m in the region defined by the comoving radius X , now determined by

$$\frac{\ddot{X}}{X} + \mathcal{H}\frac{\dot{X}}{X} = -4\pi G a^2 [\bar{\rho}_m \delta_m + \bar{\rho}_Q \delta_Q]. \quad (\text{A.3})$$

A conservation law can likewise be written down for the clustered dark energy component

$$\dot{\rho}_Q + 3 \left(\mathcal{H} + \frac{\dot{X}}{X} \right) (\rho_Q + \bar{P}_Q) = 0, \quad (\text{A.4})$$

where ρ_Q denotes the dark energy density in the top-hat region. We assume that at any one time the clustered dark energy contributes a mass [31]

$$M_Q(\tau) \equiv \frac{4\pi}{3} \bar{\rho}_Q(\tau) \delta_Q(\tau) [a(\tau) X(\tau)]^3 \quad (\text{A.5})$$

to the total mass of the system. This clustered dark energy takes part in virialisation, defined here as the instant the system satisfies the condition $d^2I/dt^2 = 0$, where $I \equiv (2/5)(M_m + M_Q)(aX)^2$ is the top-hat's moment of inertia, and t is the cosmic time ($dt = a d\tau$). The physical radius of the top-hat at this instant is the virial radius $R_{\text{vir}} \equiv aX(\tau_{\text{vir}})$, and the total mass the virial mass $M_{\text{vir}} \equiv M_m + M_Q(\tau_{\text{vir}})$. Linearised forms of equations (A.1) to (A.4) can be found in references [26, 31].

Between the two limits, any finite nonvanishing \hat{c}_s^2 necessarily causes the overdense region to evolve away from the top-hat configuration and to become ill-defined. The absence of strict conservation laws in this intermediate regime also renders the system not readily soluble. Nonetheless, the transition between the two known limits have been investigated using a quasi-linear approach in [26, 32], where it was found that, for a fixed \hat{c}_s^2 and at a given collapse redshift z , the transition generically results in a step-like feature in the linear threshold density δ_c , as well as in the quantities $\Delta_{\text{vir}} \equiv 3M_m/4\pi\bar{\rho}_m(\tau_{\text{vir}})R_{\text{vir}}^3$ and $\eta_{\text{vir}} \equiv M_Q(\tau_{\text{vir}})/M_m$, as M_m is varied from $M_m \ll M_J$ to $M_m \gg M_J$, with

$$\begin{aligned} M_J(a) &\equiv \frac{4\pi}{3}\bar{\rho}_m(a) \left[\frac{a\lambda_J(a)}{2} \right]^3 \\ &= 9.7 \times 10^{23} c_s^3 \Omega_m a^{-3} \left(\Omega_m a^{-3} + \Omega_Q e^{-3 \int_0^a da' [1+w(a')]/a'} \right)^{-3/2} h^{-1} M_\odot \quad (\text{A.6}) \end{aligned}$$

denoting the Jeans mass, and $\lambda_J \equiv 2\pi\hat{c}_s/\mathcal{H}$ the corresponding comoving Jeans length.

To incorporate this feature in the cluster mass function for our MCMC analysis, our strategy is as follows.

1. For each given set of cosmological parameters, we solve the spherical collapse model for δ_c , Δ_{vir} , and η_{vir} in the two limits of \hat{c}_s^2 using equations (A.1) to (A.4) as functions of the collapse redshift z .
2. At each redshift, we interpolate the two limits using the formulae

$$\delta_c(M_m) = \Delta(\delta_c^\infty, \delta_c^0) \tanh \left[A_1 \left(\log M_m - \log \frac{M_J}{B_1} \right) \right] + \Sigma(\delta_c^\infty, \delta_c^0), \quad (\text{A.7})$$

$$\Delta_{\text{vir}}(M_m) = \Delta(\Delta_{\text{vir}}^\infty, \Delta_{\text{vir}}^0) \tanh \left[A_2 \left(\log M_m - \log \frac{M_J}{B_2} \right) \right] + \Sigma(\Delta_{\text{vir}}^\infty, \Delta_{\text{vir}}^0), \quad (\text{A.8})$$

$$\eta_{\text{vir}}(M_m) = \Delta(\eta_{\text{vir}}^\infty, \eta_{\text{vir}}^0) \tanh \left[A_3 \left(\log M_m - \log \frac{M_J}{B_3} \right) \right] + \Sigma(\eta_{\text{vir}}^\infty, \eta_{\text{vir}}^0), \quad (\text{A.9})$$

where x^∞ denotes the value of $x = \delta_c, \Delta_{\text{vir}}, \eta_{\text{vir}}$ in the $\hat{c}_s^2 \rightarrow \infty$ limit, x^0 the $\hat{c}_s^2 = 0$ limit, and $\Delta(x^\infty, x^0) \equiv (x^\infty - x^0)/2$ and $\Sigma(x^\infty, x^0) \equiv (x^\infty + x^0)/2$ represent their difference and sum respectively. The parameters $A_{1,2,3}$ and $B_{1,2,3}$ are fitting coefficients, adjusted to fit respectively the sharpness and location of the transition. At $z = 0$ and for $(w_0, w_a) = (-0.8, 0)$, we find that $A_{1,2,3} \simeq 1.4$, and $B_{1,2,3} \simeq 20$ reproduce the quasi-linear results of [26, 32] in the region immediately below the Jeans mass quite well. For simplicity, we adopt these parameter values for all redshifts and cosmological models.

3. Lastly, we identify the virial mass with the cluster mass, i.e., $M_{\text{vir}} \equiv M$, and construct the functions $\delta_c(M, z)$ and $R_{\text{vir}}(M, z)$ according to

$$\delta_c(M, z) \equiv \delta_c(M_{\text{vir}}(M_m), z) \equiv \delta_c(M_m, z), \quad (\text{A.10})$$

$$R_{\text{vir}}(M, z) \equiv R_{\text{vir}}(M_{\text{vir}}(M_m), z) \equiv R_{\text{vir}}(M_m, z), \quad (\text{A.11})$$

which are used in sections 3.1 and 5.1 determine the cluster mass function and the mass detection threshold, respectively.

References

- [1] **LSST Science Collaborations, LSST Project** Collaboration, P. A. Abell *et al.*, “LSST Science Book, Version 2.0,” [arXiv:0912.0201](#) [[astro-ph.IM](#)].
- [2] R. Laureijs, J. Amiaux, S. Arduini, J.-L. Augueres, J. Brinchmann, *et al.*, “Euclid Definition Study Report,” [arXiv:1110.3193](#) [[astro-ph.CO](#)].
- [3] C. Carbone, C. Fedeli, L. Moscardini, and A. Cimatti, “Measuring the neutrino mass from future wide galaxy cluster catalogues,” *JCAP* **1203** (2012) 023, [arXiv:1112.4810](#) [[astro-ph.CO](#)].
- [4] B. Audren, J. Lesgourgues, S. Bird, M. G. Haehnelt, and M. Viel, “Neutrino masses and cosmological parameters from a Euclid-like survey: Markov Chain Monte Carlo forecasts including theoretical errors,” *JCAP* **1301** (2013) 026, [arXiv:1210.2194](#) [[astro-ph.CO](#)].
- [5] J. Hamann, S. Hannestad, and Y. Y. Y. Wong, “Measuring neutrino masses with a future galaxy survey,” *JCAP* **1211** (2012) 052, [arXiv:1209.1043](#) [[astro-ph.CO](#)].
- [6] **Planck** Collaboration, “The scientific programme of Planck,” [arXiv:astro-ph/0604069](#) [[astro-ph](#)].
- [7] M. Chevallier and D. Polarski, “Accelerating universes with scaling dark matter,” *Int.J.Mod.Phys. D* **10** (2001) 213–224, [arXiv:gr-qc/0009008](#) [[gr-qc](#)].
- [8] E. V. Linder, “Exploring the expansion history of the universe,” *Phys.Rev.Lett.* **90** (2003) 091301, [arXiv:astro-ph/0208512](#) [[astro-ph](#)].
- [9] A. Pavlov, L. Samushia, and B. Ratra, “Forecasting cosmological parameter constraints from near-future space-based galaxy surveys,” *Astrophys.J.* **760** (2012) 19, [arXiv:1206.3123](#) [[astro-ph.CO](#)].
- [10] S. DeDeo, R. Caldwell, and P. J. Steinhardt, “Effects of the sound speed of quintessence on the microwave background and large scale structure,” *Phys.Rev.* **D67** (2003) 103509, [arXiv:astro-ph/0301284](#) [[astro-ph](#)].
- [11] R. Bean and O. Doré, “Probing dark energy perturbations: The Dark energy equation of state and speed of sound as measured by WMAP,” *Phys.Rev.* **D69** (2004) 083503, [arXiv:astro-ph/0307100](#) [[astro-ph](#)].
- [12] J. Weller and A. Lewis, “Large scale cosmic microwave background anisotropies and dark energy,” *Mon.Not.Roy.Astron.Soc.* **346** (2003) 987–993, [arXiv:astro-ph/0307104](#) [[astro-ph](#)].
- [13] G. Ballesteros and J. Lesgourgues, “Dark energy with non-adiabatic sound speed: initial conditions and detectability,” *JCAP* **1010** (2010) 014, [arXiv:1004.5509](#) [[astro-ph.CO](#)].
- [14] S. Wang, J. Khoury, Z. Haiman, and M. May, “Constraining the evolution of dark energy with a combination of galaxy cluster observables,” *Phys.Rev.* **D70** (2004) 123008, [arXiv:astro-ph/0406331](#) [[astro-ph](#)].
- [15] M. Takada and S. Bridle, “Probing dark energy with cluster counts and cosmic shear power spectra: including the full covariance,” *New J.Phys.* **9** (2007) 446, [arXiv:0705.0163](#) [[astro-ph](#)].
- [16] E. Sefusatti, C. Vale, K. Kadota, and J. Frieman, “Primordial non-Gaussianity and Dark Energy constraints from Cluster Surveys,” *Astrophys.J.* **658** (2007) 669–679, [arXiv:astro-ph/0609124](#) [[astro-ph](#)].

- [17] S. Wang, Z. Haiman, W. Hu, J. Khoury, and M. May, “Weighing neutrinos with galaxy cluster surveys,” *Phys.Rev.Lett.* **95** (2005) 011302, [arXiv:astro-ph/0505390](#) [[astro-ph](#)].
- [18] M. Lima and W. Hu, “Self-calibration of cluster dark energy studies: Observable-mass distribution,” *Phys.Rev.* **D72** (2005) 043006, [arXiv:astro-ph/0503363](#) [[astro-ph](#)].
- [19] L. R. Abramo, R. C. Batista, and R. Rosenfeld, “The signature of dark energy perturbations in galaxy cluster surveys,” *JCAP* **0907** (2009) 040, [arXiv:0902.3226](#) [[astro-ph.CO](#)].
- [20] R. K. Sheth and G. Tormen, “Large scale bias and the peak background split,” *Mon.Not.Roy.Astron.Soc.* **308** (1999) 119, [arXiv:astro-ph/9901122](#) [[astro-ph](#)].
- [21] A. Jenkins, C. Frenk, S. D. White, J. Colberg, S. Cole, *et al.*, “The Mass function of dark matter halos,” *Mon.Not.Roy.Astron.Soc.* **321** (2001) 372, [arXiv:astro-ph/0005260](#) [[astro-ph](#)].
- [22] J. L. Tinker, A. V. Kravtsov, A. Klypin, K. Abazajian, M. S. Warren, *et al.*, “Toward a halo mass function for precision cosmology: The Limits of universality,” *Astrophys.J.* **688** (2008) 709–728, [arXiv:0803.2706](#) [[astro-ph](#)].
- [23] J. Brandbyge, S. Hannestad, T. Haugbølle, and Y. Y. Y. Wong, “Neutrinos in Non-linear Structure Formation - The Effect on Halo Properties,” *JCAP* **1009** (2010) 014, [arXiv:1004.4105](#) [[astro-ph.CO](#)].
- [24] A. Lewis, A. Challinor, and A. Lasenby, “Efficient computation of CMB anisotropies in closed FRW models,” *Astrophys.J.* **538** (2000) 473–476, [arXiv:astro-ph/9911177](#) [[astro-ph](#)].
- [25] D. Mota and C. van de Bruck, “On the Spherical collapse model in dark energy cosmologies,” *Astron.Astrophys.* **421** (2004) 71–81, [arXiv:astro-ph/0401504](#) [[astro-ph](#)].
- [26] T. Basse, O. E. Bjælde, and Y. Y. Y. Wong, “Spherical collapse of dark energy with an arbitrary sound speed,” *JCAP* **1110** (2011) 038, [arXiv:1009.0010](#) [[astro-ph.CO](#)].
- [27] J. E. Gunn and I. Gott, J. Richard, “On the Infall of Matter into Clusters of Galaxies and Some Effects on Their Evolution,” *Astrophys.J.* **176** (1972) 1–19.
- [28] L.-M. Wang and P. J. Steinhardt, “Cluster abundance constraints on quintessence models,” *Astrophys.J.* **508** (1998) 483–490, [arXiv:astro-ph/9804015](#) [[astro-ph](#)].
- [29] A. Cooray and R. K. Sheth, “Halo models of large scale structure,” *Phys.Rept.* **372** (2002) 1–129, [arXiv:astro-ph/0206508](#) [[astro-ph](#)].
- [30] L. Abramo, R. Batista, L. Liberato, and R. Rosenfeld, “Structure formation in the presence of dark energy perturbations,” *JCAP* **0711** (2007) 012, [arXiv:0707.2882](#) [[astro-ph](#)].
- [31] P. Creminelli, G. D’Amico, J. Norena, L. Senatore, and F. Vernizzi, “Spherical collapse in quintessence models with zero speed of sound,” *JCAP* **1003** (2010) 027, [arXiv:0911.2701](#) [[astro-ph.CO](#)].
- [32] T. Basse, O. E. Bjælde, S. Hannestad, and Y. Y. Y. Wong, “Confronting the sound speed of dark energy with future cluster surveys,” [arXiv:1205.0548](#) [[astro-ph.CO](#)].
- [33] Y. M. Bahe, I. G. McCarthy, and L. J. King, “Mock weak lensing analysis of simulated galaxy clusters: bias and scatter in mass and concentration,” *Mon.Not.Roy.Astron.Soc.* **421** (2012) 1073–1088, [arXiv:1106.2046](#) [[astro-ph.CO](#)].
- [34] M. R. Becker and A. V. Kravtsov, “On the Accuracy of Weak Lensing Cluster Mass Reconstructions,” *Astrophys.J.* **740** (2011) 25, [arXiv:1011.1681](#) [[astro-ph.CO](#)].
- [35] L. Perotto, J. Lesgourgues, S. Hannestad, H. Tu, and Y. Y. Y. Wong, “Probing cosmological parameters with the CMB: Forecasts from full Monte Carlo simulations,” *JCAP* **0610** (2006) 013, [arXiv:astro-ph/0606227](#) [[astro-ph](#)].
- [36] T. Hamana, M. Takada, and N. Yoshida, “Searching for massive clusters in weak lensing

- surveys,” *Mon.Not.Roy.Astron.Soc.* **350** (2004) 893, [arXiv:astro-ph/0310607](#) [[astro-ph](#)].
- [37] J. F. Navarro, C. S. Frenk, and S. D. White, “The Structure of cold dark matter halos,” *Astrophys.J.* **462** (1996) 563–575, [arXiv:astro-ph/9508025](#) [[astro-ph](#)].
- [38] L. Van Waerbeke, “Noise properties of gravitational lens mass reconstruction,” *Mon.Not.Roy.Astron.Soc.* **313** (2000) 524–532, [arXiv:astro-ph/9909160](#) [[astro-ph](#)].
- [39] M. J. White, L. van Waerbeke, and J. Mackey, “Completeness in weak lensing searches for clusters,” *Astrophys.J.* **575** (2002) 640–649, [arXiv:astro-ph/0111490](#) [[astro-ph](#)].
- [40] F. Feroz, P. Marshall, and M. Hobson, “Cluster detection in weak lensing surveys,” [arXiv:0810.0781](#) [[astro-ph](#)].
- [41] F. Pace, M. Maturi, M. Meneghetti, M. Bartelmann, L. Moscardini, *et al.*, “Testing the reliability of weak lensing cluster detections,” [arXiv:astro-ph/0702031](#) [[ASTRO-PH](#)].
- [42] J. F. Hennawi and D. N. Spergel, “Mass selected cluster cosmology. 1: Tomography and optimal filtering,” *Astrophys.J.* (2004) , [arXiv:astro-ph/0404349](#) [[astro-ph](#)].
- [43] **Planck Collaboration** Collaboration, P. Ade *et al.*, “Planck 2013 results. I. Overview of products and scientific results,” [arXiv:1303.5062](#) [[astro-ph.CO](#)].
- [44] R. Barbieri and A. Dolgov, “Neutrino oscillations in the early universe,” *Nucl.Phys.* **B349** (1991) 743–753.
- [45] K. Kainulainen, “Light singlet neutrinos and the primordial nucleosynthesis,” *Phys.Lett.* **B244** (1990) 191–195.
- [46] M. Kawasaki, K. Kohri, and N. Sugiyama, “MeV scale reheating temperature and thermalization of neutrino background,” *Phys.Rev.* **D62** (2000) 023506, [arXiv:astro-ph/0002127](#) [[astro-ph](#)].
- [47] S. Hannestad, “What is the lowest possible reheating temperature?,” *Phys.Rev.* **D70** (2004) 043506, [arXiv:astro-ph/0403291](#) [[astro-ph](#)].
- [48] F. Marulli, C. Carbone, M. Viel, L. Moscardini, and A. Cimatti, “Effects of Massive Neutrinos on the Large-Scale Structure of the Universe,” *Mon.Not.Roy.Astron.Soc.* **418** (2011) 346, [arXiv:1103.0278](#) [[astro-ph.CO](#)].
- [49] A. Albrecht, G. Bernstein, R. Cahn, W. L. Freedman, J. Hewitt, *et al.*, “Report of the Dark Energy Task Force,” [arXiv:astro-ph/0609591](#) [[astro-ph](#)].
- [50] G. Barenboim, E. Fernandez-Martinez, O. Mena, and L. Verde, “The dark side of curvature,” *JCAP* **1003** (2010) 008, [arXiv:0910.0252](#) [[astro-ph.CO](#)].
- [51] S. Khedekar and S. Majumdar, “Cosmology with the largest galaxy cluster surveys: Going beyond Fisher matrix forecasts,” *JCAP* **1302** (2013) 030, [arXiv:1210.5586](#) [[astro-ph.CO](#)].
- [52] L. Wolz, M. Kilbinger, J. Weller, and T. Giannantonio, “On the Validity of Cosmological Fisher Matrix Forecasts,” *JCAP* **1209** (2012) 009, [arXiv:1205.3984](#) [[astro-ph.CO](#)].
- [53] A. Vikman, “Can dark energy evolve to the phantom?,” *Phys.Rev.* **D71** (2005) 023515, [arXiv:astro-ph/0407107](#) [[astro-ph](#)].
- [54] W. Hu, “Crossing the phantom divide: Dark energy internal degrees of freedom,” *Phys.Rev.* **D71** (2005) 047301, [arXiv:astro-ph/0410680](#) [[astro-ph](#)].
- [55] R. Batista and F. Pace, “Structure formation in inhomogeneous Early Dark Energy models,” [arXiv:1303.0414](#) [[astro-ph.CO](#)].
- [56] M. C. A. Cerbolini, B. Sartoris, J.-Q. Xia, A. Biviano, S. Borgani, *et al.*, “Constraining neutrino properties with a Euclid-like galaxy cluster survey,” [arXiv:1303.4550](#) [[astro-ph.CO](#)].

12

NON-LINEAR APPROACHES

The aim of this chapter is to outline the progress made on non-linear dark energy implementations. We work on two different implementations: Non-linear spherical collapse and dark energy in N-body simulations. With the non-linear spherical collapse, we aim to properly model the transition between the non-clustering and clustering limits and to construct fitting functions for the parameters that effect the cluster mass function, similar to the interpolation scheme applied in chapter 11, but tested for a larger range of models. Regarding N-body simulations, the ultimate goal is a completely non-linear simulation with a dark energy fluid leading to non-linear matter power spectra and reliable N-body cluster mass functions. Currently, the state of both projects is partial completion.

In both implementations the equations governing the evolution of the system are the familiar fluid equations, i.e., the continuity and Euler equations, for a relativistic fluid α in an expanding background. Here the pseudo-Newtonian approach is adopted and the equation take the form

$$\begin{aligned}\dot{\rho}_\alpha + 3\mathcal{H}(\rho_\alpha + P_\alpha) + \nabla \cdot [(\rho_\alpha + P_\alpha) \mathbf{u}_\alpha] &= 0 \\ \dot{\mathbf{u}}_\alpha + \mathcal{H}\mathbf{u}_\alpha + (\mathbf{u}_\alpha \cdot \nabla) \mathbf{u}_\alpha + \frac{\nabla P_\alpha + \mathbf{u}_\alpha \dot{P}_\alpha}{\rho_\alpha + P_\alpha} + \nabla \phi &= 0\end{aligned}\quad (12.1)$$

where $\mathbf{u}_\alpha = d\mathbf{x}_\alpha/d\tau$ is the peculiar velocity of the fluid and ϕ is the gravitational potential obtained from the Poisson equation as in chapters 9 to 11.

12.1 Non-linear dark energy and spherical collapse

The non-linear treatment of dark energy removes the benefits of switching the Fourier space by leading to mixing of different k -values. We therefore opt to solve the equations of motion on a comoving radial grid in real space. We thereby utilizing the spherical symmetry, which is preserved during the collapse. Under spherical symmetry the equations of motion for the perturbed quantities reduce to

$$\begin{aligned}0 &= \dot{\delta}_\alpha(x) + 3\mathcal{H}(\delta_\alpha^P(x) - \delta_\alpha(x)w_\alpha) \\ &+ (1 + w_\alpha + \delta_\alpha(x) + \delta_\alpha^P(x)) \nabla_x \cdot u_\alpha(x) + u_\alpha(x) \nabla_x (\delta_\alpha(x) + \delta_\alpha^P(x)),\end{aligned}\quad (12.2)$$

for the continuity equation and

$$0 = \dot{u}_\alpha(x) + \mathcal{H}u_\alpha(x) + u_\alpha(x) \nabla_x u_\alpha(x) + \frac{\nabla_x \delta_\alpha^P(x) + u_\alpha(x) \left(\dot{\delta}_\alpha^P(x) - 3\mathcal{H}(1+w_\alpha) \left(c_{a\alpha}^2 + \delta_\alpha^P(x) \right) \right)}{1+w_\alpha + \delta_\alpha(x) + \delta_\alpha^P(x)} + \nabla_x \phi(x), \quad (12.3)$$

for the Euler equation. In the equations above x is the comoving radial coordinate, u_α is the radial component of \mathbf{u}_α , $\delta_\alpha^P \equiv \delta P_\alpha / \bar{\rho}_\alpha$, and $c_{a\alpha}^2 \equiv \dot{P}_\alpha / \dot{\bar{\rho}}_\alpha$ is the adiabatic sound speed. For the dark matter fluid these equations reduce even further, since the dark matter component has no pressure at any level of perturbations.

The dark energy component on the other hand has pressure perturbations and the task is now to calculate these. The sound speed of dark energy defined as $c_{s\alpha}^2 = \delta P_\alpha / \delta \rho_\alpha$ is gauge dependent, so as previously we use the gauge transformation of Bean & Dore (2004) to relate δP_α to the sound speed in the rest frame of dark energy, $\hat{c}_{s\alpha}^2$, and $\delta \rho_\alpha$. Note this transformation is only valid to linear order in perturbed quantities. In Fourier space the transformation has the form

$$\tilde{\delta}_\alpha^P(k) = \hat{c}_{s\alpha}^2 \tilde{\delta}_\alpha(k) + 3\mathcal{H}(1+w_\alpha) \left(\hat{c}_{s\alpha}^2 - c_{a\alpha}^2 \right) \bar{\rho}_\alpha \frac{\tilde{\theta}_\alpha(k)}{k^2}, \quad (12.4)$$

where θ_α is the divergence of \mathbf{u}_α . Taking the inverse Fourier transform, utilizing the spherical symmetry of the system, and imposing the boundary conditions $\delta P_\alpha = \delta \rho_\alpha = 0$ at infinity, we find the real-space relation for δ_α^P ,

$$\delta_\alpha^P(x) = \hat{c}_{s\alpha}^2 \delta_\alpha(x) + 3\mathcal{H}(1+w_\alpha) \left(\hat{c}_{s\alpha}^2 - c_{a\alpha}^2 \right) \int_x^\infty u_\alpha(\xi) d\xi, \quad (12.5)$$

where the integral is over the radial coordinate. We can take the gradient and time derivative of this expression to obtain the quantities needed in the equations of motion. Note, taking the time derivative of equation (12.5) results in a radial integral over \dot{u}_α , which goes into the Euler equation. In the numerical implementation, we therefore calculate this integral with a trapezoidal rule, which results in an equation for \dot{u}_α on each grid point depending on \dot{u}_α of all grid point larger radial coordinate.

All that remains is to calculate the gravitational potential from the Poisson equation. Writing the Poisson equation on the form

$$\Delta_x^2 \phi(x) = f(x), \quad (12.6)$$

the spherical symmetry allows an exact solution,

$$\phi(x) = -x^{-1} \int_0^x f(\xi) \xi^2 d\xi - \int_x^\infty f(\xi) \xi d\xi. \quad (12.7)$$

We now have all the elements needed for the implementation, where the idea is to solve the non-linear collapse to obtain the redshift of collapse and the virial over-density, and then subsequently run CAMB with the appropriate initial conditions to compute the linear critical density contrast, δ_c .

12.1.1 State of the project

As mention in the introduction to this chapter, work still needs to be done on this project. So far, the code works in the clustering limit of dark energy, i.e., on scales well above the sound horizon. This has been tested in the limit of zero speed of sound, where the regular spherical collapse is exact, and the code reproduces radial evolution of this solution and the redshift of collapse. This is the limit where the quasi-linear approach of Basse et al. (2011) fails because the dark energy perturbations grow to $\delta_{\text{de}} \gtrsim 1$ toward the end of the collapse. In the most interesting region of intermediate scales, i.e., the transition region between non-clustering and clustering dark energy (where the validity of the quasi-linear approach is questionable), the code has numerical instabilities that are blown up by the acoustic oscillations relevant on these scales. Although, we are interested in solving these problems, more effort has been invested into N-body simulations with dark energy fluids, since, ultimately, we need N-body results to test the validity and reliability of the cluster mass functions obtained from the spherical collapse.

12.2 Dark energy N-body simulations

Our attempt to include dynamical dark energy in an N-body simulation is not the first, many authors have done so with success for a variety of specific models, see Baldi (2012) for a relatively recent review. However, we are not aware of any simulations treating dark energy as an inhomogeneous fluid.

A thorough discussion of N-body simulations is beyond the scope of this dissertation as the actual implementation has been done by collaborators. Our implementation is based on the publicly available N-body code GADGET-2⁵ described in Springel (2005). GADGET-2 is a TreePM code, utilizing a Tree algorithm for calculation of the short-range gravitational force and for the long-range gravitational force, the particles are interpolated onto a particle mesh grid for a Fourier calculation. Although being a rather old code, the gravity solver of GADGET-2 is not outdated, since the main developments of N-body codes have focused on improving the treatment of baryonic physics or dark energy.

Ideally, we would include the dark energy fluid on the grid of the simulation and solve the non-linear equations of motion, i.e., the continuity equation and the three dimensional Euler equation, in real space. The structures for this have already been included in the code. However, a fluid with arbitrary equation of state, w_α , and rest frame sound speed, $\hat{c}_{s\alpha}^2$, can break the weak energy condition of general relativity, $\rho_\alpha + P_\alpha > 0$, if care is not taken. In addition, the crossing of $\rho_\alpha + P_\alpha = 0$ causes severe numerical instability as our version of the Euler equation is singular at that point, see Kunz & Sapone (2006) for a discussion of models crossing $\rho_\alpha + P_\alpha = 0$. To avoid this, we need a

⁵<http://www.mpa-garching.mpg.de/gadget/>

barotropic model with a full equation of state, $P_\alpha(\rho_\alpha)$. These barotropic models must conform to the constraints of Linder & Scherrer (2009). The implementation of a non-linear barotropic fluid still needs some modifications and rigorous testing.

Brandbyge & Hannestad (2009) showed that a grid based linear implementation of neutrinos is successful at reproducing the non-linear matter power spectrum with high precision. Inspired by this, we have made a linear implementation of the dark energy fluid on the grid of GADGET-2 – the linear Euler equation does not suffer from the singularity at $\rho_\alpha + P_\alpha = 0$. The singularity is now at $\bar{\rho}_\alpha + \bar{P}_\alpha = 0$ or $w_\alpha = -1$, and in this case the effect of dark energy is only through the background. With a linear implementation, we regain the advantages of working in Fourier space. The dark energy perturbations are therefore kept in Fourier space, interacting with matter only through the particle mesh gravitational force. The initial conditions for the simulations are random realizations of the statistics of the linear power spectra of both matter and dark energy. These linear power spectra are obtained from the transfer functions computed by CAMB. The initial velocity divergence is set to $\theta_\alpha = \mathcal{H}\delta_\alpha$ – choosing $\theta_\alpha = \mathcal{H}\delta_\alpha$ or $\theta_\alpha = 0$ makes a negligible difference on the power spectrum at low redshift. We aim now to compute the non-linear power spectrum for a range of models and analyze it within the framework of Halofit.

12.2.1 Halofit

Halofit maps the total linear power spectrum to the total non-linear power spectrum through a fitting form originally proposed by Smith et al. (2003). The form is based on a decomposition of the density field into a distribution of isolated halo, see Smith et al. (2003) and references therein. Recently, the fit has adjusted to include neutrinos by Bird et al. (2012) and homogeneous dynamical dark energy with $w \neq -1$ by Takahashi et al. (2012).

Using the Halofit, the total non-linear dimensionless power spectrum can be written on the form,

$$\Delta_{\text{NL}}^2(k) = \Delta_{\text{Q}}^2(k) + \Delta_{\text{H}}^2(k), \quad (12.8)$$

where the term $\Delta_{\text{Q}}^2(k)$ accounts for the power on quasi-linear scales generated by the large-scale correlations between halos and $\Delta_{\text{H}}^2(k)$ is the power that results from correlation of the distribution of matter inside individual halos. The transition scale, k_σ , between the two contributions is defined by

$$\sigma^2(k_\sigma) \equiv \int \Delta_{\text{L}}^2(k) e^{-(k/k_\sigma)^2} d \ln k = 1, \quad (12.9)$$

where we use the notation $\Delta_{\text{L}}^2(k)$ for the total linear power spectrum to avoid confusion. The forms of the two terms in equation (12.8) are complicated, albeit justified, see Smith

et al. (2003).

$$\Delta_{\text{Q}}^2(k) = \Delta_{\text{L}}^2(k) \frac{[1 + \Delta_{\text{L}}^2(k)]^{\beta_n}}{1 + \alpha_n \Delta_{\text{L}}^2(k)} e^{-y/4 - y^2/8}, \quad (12.10)$$

$$\Delta_{\text{H}}^2(k) = \frac{a_n y^{3f_1(\Omega_m)}}{(1 + \mu_n y^{-1} + \nu_n y^{-2}) (1 + b_n y^{f_2(\Omega_m)} + [c_n f_3(\Omega_m) y]^{3-\gamma_n})}, \quad (12.11)$$

where $y \equiv k/k_\sigma$ and the parameters a_n , b_n , c_n , α_n , β_n , γ_n , μ_n , ν_n , f_1 , f_2 , and f_3 depend on relevant cosmological parameters and properties of the linear power spectrum. The parameters f_1 , f_2 , and f_3 are powers of Ω_m , while the remaining parameters or their logarithms are polynomials in the quantities n_{eff} and C defined by

$$n_{\text{eff}} + 3 \equiv \left. \frac{d \ln \sigma^2(R)}{d \ln R} \right|_{R=k_\sigma^{-1}}, \quad C \equiv - \left. \frac{d^2 \ln \sigma^2(R)}{d \ln R^2} \right|_{R=k_\sigma^{-1}}. \quad (12.12)$$

Takahashi et al. (2012) added a weak dependence on the dark energy density parameter and equation of state, $(1 + w_{\text{de}}) \Omega_{\text{de}}(z)$, to some of the parameters. Our goal is to investigate the need for a dependence on the sound speed for dark energy in the Halofit, based on our N-body simulations.

12.2.2 State of the project

The current state of the code is that we find a discrepancy between the results of the power spectra from simulation and the power spectra from CAMB in the fully linear regime. This is illustrated on figure 12.1, which shows the ratio of power between models with $\hat{c}_s^2 = 0$ and $\hat{c}_s^2 = 1$ – we plot this ratio to minimize the effects of sample variance due to the actual realization chosen for the initial conditions of the simulations. The problem is present in simulations both with a comoving volume of $(256 \text{ Mpc}/h)^3$ and $(1024 \text{ Mpc}/h)^3$. The larger volume has a better resolution of the Fourier modes in the linear regime, since both simulations have a particle mesh grid of 512^3 points. Before fully understanding or resolving this discrepancy, we are hesitant to trust to the results in the non-linear regime. Our investigations into this matter will continue. To achieve higher flexibility, it might be worth switching from GADGET-2 to code with an adaptive grid.

Figure 12.1 shows that, in linear theory for $w = -0.8$, the effect of dark energy clustering on the power spectrum is a two percent effect. Figure 4 in Basse et al. (2012) (chapter 10) shows the same with more sound speeds included. The current precision of Halofit is five to ten percent, so it is not clear whether Halofit will be able to pick up the effect of dark energy clustering. The effect on smaller and non-linear scales might of course be larger, which could warrant an update of Halofit.

To conclude this chapter, N-body simulations are important theoretical tools in the endeavors toward understanding the full nature of dark energy. We need as large a

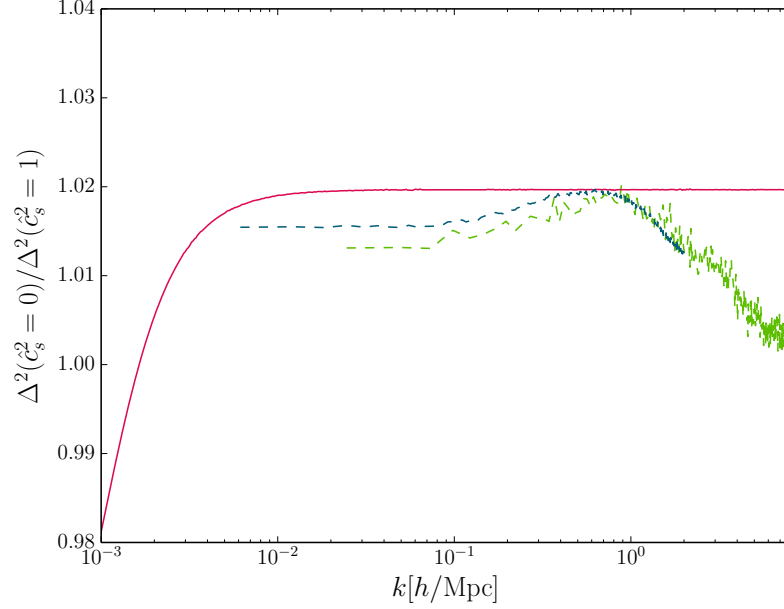


Figure 12.1: Ratio of power spectra of models with inhomogeneous ($\hat{c}_s^2 = 0$) and effectively homogeneous ($\hat{c}_s^2 = 1$) dark energy at $z = 0$. The solid red line shows the ratio in linear theory calculated in CAMB (the relative decrease of power on the largest scales is an artifact of the synchronous gauge). The dashed lines show the ratio of power spectra obtained from simulations on a particle mesh grid with 512^3 points. The green and blue lines have co-moving volumes of $(256 \text{ Mpc}/h)^3$ and $(1024 \text{ Mpc}/h)^3$, respectively. The power spectra from simulations have been cut before shot noise sets in.

variety of simulations including dark energy as possible, and although our code is not fully functional, we have taken the first steps and intend to continue.

Part IV

OUTLOOK

CONCLUSIONS AND PERSPECTIVES

This dissertation has presented some of the observational basis that has led to our current understanding of the universe. A universe about which we know much, but have even more yet to learn. Phenomena such as dark matter and dark energy are still elusive. After an introduction to the theoretical framework, the dissertation investigates the formation of structures with a generic model for dark energy.

In Basse et al. (2011), we study fluid dark energy within the framework of the spherical collapse model. We find that treating dark energy as a fluid with perturbations, naturally introduces a Jeans scale, above and below which the behavior of dark energy is fundamentally different. On scales below the Jeans scale, dark energy is essentially homogeneous and affects the structure formation through the background only. On scales above the Jeans scale, however, pressure perturbations in dark energy cannot keep the fluid from clustering under the gravitational potential.

In Basse et al. (2012), we proceed to investigate how this scale dependence in the nature of dark energy affects the formation of structures in terms of quantities that we can observe. We find that the cluster mass function inherits a similar scale dependence. This is most prominent when comparing models with and without dark energy clustering. Along the way, we develop a novel approach to the virialization of clusters in dark energy models. We conclude with a Fisher matrix analysis of a future cluster survey. This shows that clusters are an excellent probe of dark energy.

The studies of Basse et al. (2012) are extended in Basse et al. (2014a). We opt for a more robust MCMC approach and analyze the complementarity of clusters to the angular power spectra that, along with the clusters, can be obtained from large future galaxy surveys. Across Hamann et al. (2012) and Basse et al. (2014a), we study these probes individually and in various combinations. For dark energy parameters, we find that the constraints on the equation of state will improve drastically, while the sound speed of dark energy is a different matter. We show that the constraints on the sound speed are highly dependent on the exact modeling of the cluster mass function in these cosmologies. A better understanding of this requires a suite of N-body simulations – our efforts pursuing this have been outlined in chapter 12.

We do not restrict ourselves to studying dark energy parameters. In Basse et al. (2014a), we find that the sum of neutrino masses can be constrained with unprecedented

13. Conclusions and perspectives

accuracy, allowing the first cosmological confirmation of neutrino masses different from zero. Also, the effective number of relativistic species is well constrained by large galaxy surveys in combination with current measurements of the cosmic microwave background. The numerical tools developed for computing the observables can easily be applied in studies of other models, such as hot dark matter axions in Archidiacono et al. (2014) and inflation in Basse et al. (2014b).

Toward the end of my Ph.D., we started a project looking into the effect of dark energy clustering on the most extreme or rare clusters in terms of mass and redshift. Our approach combines the work of Harrison & Hotchkiss (2013) and Waizmann et al. (2012). Extreme clusters could hold the potential of telling models with and without dark energy perturbations apart, since dark energy clustering affects the high-mass end of the cluster mass function while hardly changing σ_8 . We already have the numerical tools for this project, but need to analyze the output.

The field of cosmology is definitely worth following over the next decade, since everything points toward significant advances. To ensure maximum benefit from future surveys, we still need to improve our theoretical understanding of dark energy models, and this dissertation is one of many steps toward achieving this.

Part V

BACK MATTER

APPENDIX

A Details of excursion set theory

The solution to the diffusion equation in (6.8) is the main focus of this appendix. First, a new parameter, $\gamma = \delta_c - \delta$, is introduced to measure the distance to the barrier. The boundary conditions now become $\Pi(\gamma = 0, S) = 0$ and $\Pi(\gamma, S_0) = \delta_D(\gamma - \gamma_0)$, where $\gamma_0 = \delta_c - \delta_0$. Taking the Fourier transform of $\Pi(\gamma, S)$ with respect to γ , i.e.,

$$\tilde{\Pi}(\xi, S) = \int_{-\infty}^{\infty} \Pi(\gamma, S) e^{i\xi\gamma} d\gamma, \quad (\text{A.1})$$

turns equation (6.8) into,

$$\frac{\partial \tilde{\Pi}(\xi, S)}{\partial S} = -\frac{\xi^2}{2} \tilde{\Pi}(\xi, S). \quad (\text{A.2})$$

This differential equation is solved by,

$$\tilde{\Pi}(\xi, S) = g(\xi) e^{-\frac{\xi^2}{2} S}, \quad (\text{A.3})$$

where $g(\xi)$ is determined by the boundary conditions. With the inverse Fourier transform, the first boundary condition states that,

$$\Pi(0, S) = \frac{1}{2\pi} \int_{-\infty}^{\infty} g(\xi) e^{-\frac{\xi^2}{2} S} d\xi = 0, \quad (\text{A.4})$$

indicating that $g(\xi)$ must be odd. The odd property of $\tilde{\Pi}(\xi, S)$ ensures that only the odd part of $e^{-i\gamma\xi}$, i.e., $-i \sin(\gamma\xi)$, in the inverse Fourier transform survives. The inverse Fourier transform now reads,

$$\Pi(\gamma, S) = \frac{-i}{2\pi} \int_{-\infty}^{\infty} g(\xi) \sin(\gamma\xi) e^{-\frac{\xi^2}{2} S} d\xi. \quad (\text{A.5})$$

We can impose two conditions on $g(\xi)$: First, $\Pi(\gamma, S)$ must be real, making $g(\xi)$ purely imaginary, and second, the boundary conditions dictate $\Pi(\gamma, S_0) = \delta_D(\gamma - \gamma_0)$. To ensure the latter, we utilize the orthogonality of $\sin(px)$ when integrated over x from $-\infty$ to ∞ , with p being a real number. Thus,

$$g(\xi) \propto \sin(\gamma_0\xi) e^{\frac{\xi^2}{2} S_0}, \quad (\text{A.6})$$

where the constant of proportionality is determined such that $\Pi(\gamma, S_0)$ integrates to unity over γ . This can be computed using integration in the complex plane with the result,

$$g(\xi) = 2i \sin(\gamma_0 \xi) e^{\frac{\xi^2}{2} S_0}. \quad (\text{A.7})$$

Remembering that the integrand is even in ξ , the solution can now be calculated.

$$\begin{aligned} \Pi(\gamma, S) &= \frac{1}{\pi} \int_{-\infty}^{\infty} \sin(\gamma_0 \xi) \sin(\gamma \xi) e^{-\frac{\xi^2}{2}(S-S_0)} d\xi \\ &= \frac{2}{\pi} \int_0^{\infty} \sin(\gamma_0 \xi) \sin(\gamma \xi) e^{-\frac{\xi^2}{2}(S-S_0)} d\xi. \end{aligned} \quad (\text{A.8})$$

Employing trigonometric relations gives

$$\Pi(\gamma, S) = \frac{1}{\pi} \int_0^{\infty} [\cos(\xi(\gamma_0 - \gamma)) - \cos(\xi(\gamma_0 + \gamma))] e^{-\frac{\xi^2}{2}(S-S_0)} d\xi. \quad (\text{A.9})$$

The remaining integrals are standard integrals, so one finds

$$\Pi(\gamma, S) = \frac{1}{\sqrt{2\pi(S-S_0)}} \left[e^{-\frac{(\gamma_0 - \gamma)^2}{2(S-S_0)}} - e^{-\frac{(\gamma_0 + \gamma)^2}{2(S-S_0)}} \right]. \quad (\text{A.10})$$

Re-inserting the smoothed density contrast, $\gamma_0 - \gamma = \delta - \delta_0$ and $\gamma_0 + \gamma = 2\delta_c - \delta_0 - \delta$, yields the result of equation (6.9),

$$\Pi(\delta, S) = \frac{1}{\sqrt{2\pi(S-S_0)}} \left(e^{-\frac{(\delta - \delta_0)^2}{2(S-S_0)}} - e^{-\frac{(2\delta_c - \delta_0 - \delta)^2}{2(S-S_0)}} \right). \quad (\text{A.11})$$

Now, the details of equation (6.10) are presented. First, the probability distribution of equation (6.9) is inserted and the integral is split into two,

$$\begin{aligned} F(S) &= 1 - \int_{-\infty}^{\delta_c} \Pi(\delta, S) d\delta \\ &= 1 - \frac{1}{\sqrt{2\pi S}} \int_{-\infty}^{\delta_c} e^{-\frac{\delta^2}{2S}} d\delta + \frac{1}{\sqrt{2\pi S}} \int_{-\infty}^{\delta_c} e^{-\frac{(2\delta_c - \delta)^2}{2S}} d\delta. \end{aligned} \quad (\text{A.12})$$

To proceed, a substitution is made in each integral. For the first integral, the substitution is $\mathcal{U} = \delta/\sqrt{2S}$, and for the second integral, the substitution is $\mathcal{T} = (2\delta_c - \delta)/\sqrt{2S}$.

$$F(S) = 1 - \frac{1}{\sqrt{\pi}} \int_{-\infty}^{\delta_c/\sqrt{2S}} e^{-\mathcal{U}^2} d\mathcal{U} - \frac{1}{\sqrt{\pi}} \int_{\infty}^{\delta_c/\sqrt{2S}} e^{-\mathcal{T}^2} d\mathcal{T}. \quad (\text{A.13})$$

Regarding the first integral, the integrand is a normalised Gaussian distribution, i.e., the integral from $-\infty$ to ∞ equals unity, so the first integral can be expressed in terms of

the integral from the upper limit, $\delta_c/\sqrt{2S}$, and to ∞ . For the second integral, a switch of the limits, and thus the sign in front of the integral, does the job.

$$\begin{aligned} F(S) &= 1 - \left(1 - \frac{1}{\sqrt{\pi}} \int_{\delta_c/\sqrt{2S}}^{\infty} e^{-U^2} dU \right) + \frac{1}{\sqrt{\pi}} \int_{\delta_c/\sqrt{2S}}^{\infty} e^{-\mathcal{T}^2} d\mathcal{T} \\ &= \frac{2}{\sqrt{\pi}} \int_{\delta_c/\sqrt{2S}}^{\infty} e^{-\mathcal{T}^2} d\mathcal{T} = \operatorname{erfc} \left(\frac{\delta_c}{\sqrt{2S}} \right). \end{aligned} \quad (\text{A.14})$$

The probability for the first crossing of δ_c to occur within the interval from S to $S + dS$ is given by

$$\begin{aligned} \frac{dF}{dS} dS &= - \left[\int_{-\infty}^{\delta_c} \frac{\partial \Pi(\delta, S)}{\partial S} d\delta \right] dS = - \left[\int_{-\infty}^{\delta_c} \frac{1}{2} \frac{\partial^2 \Pi(\delta, S)}{\partial \delta^2} d\delta \right] dS \\ &= -\frac{1}{2} \left[\frac{\partial \Pi(\delta, S)}{\partial \delta} \right]_{-\infty}^{\delta_c} dS = \frac{1}{\sqrt{8\pi S}} \left[\frac{\delta}{S} e^{-\frac{\delta^2}{2S}} + \frac{2\delta_c - \delta}{S} e^{-\frac{(2\delta_c - \delta)^2}{2S}} \right]_{-\infty}^{\delta_c} dS \\ &= \frac{\delta_c}{\sqrt{2\pi S}} e^{-\frac{\delta_c^2}{2S}} dS. \end{aligned} \quad (\text{A.15})$$

BIBLIOGRAPHY

- Ade, P., et al. (2013). Planck 2013 results. XVI. Cosmological parameters.
- Ade, P., et al. (2014). Detection of B-Mode Polarization at Degree Angular Scales by BICEP2. Phys.Rev.Lett., 112, 241101.
- Albrecht, A., Bernstein, G., Cahn, R., Freedman, W. L., Hewitt, J., et al. (2006). Report of the Dark Energy Task Force.
- Anselmi, S., Ballesteros, G., & Pietroni, M. (2011). Non-linear dark energy clustering. JCAP, 1111, 014.
- Archidiacono, M., Basse, T., Hamann, J., Hannestad, S., Raffelt, G., & Wong, Y. Y. (2014). Future cosmological sensitivity for hot dark matter axions. In preparation.
- Baldi, M. (2012). Dark Energy Simulations. Phys.Dark Univ., 1, 162–193.
- Ballesteros, G., & Lesgourgues, J. (2010). Dark energy with non-adiabatic sound speed: initial conditions and detectability. JCAP, 1010, 014.
- Basse, T., Bjaelde, O. E., Hamann, J., Hannestad, S., & Wong, Y. Y. (2014a). Dark energy properties from large future galaxy surveys. JCAP, 1405, 021.
- Basse, T., Bjaelde, O. E., Hannestad, S., & Wong, Y. Y. (2012). Confronting the sound speed of dark energy with future cluster surveys. arXiv:1205.0548.
- Basse, T., Bjaelde, O. E., & Wong, Y. Y. (2011). Spherical collapse of dark energy with an arbitrary sound speed. JCAP, 1110, 038.
- Basse, T., Hamann, J., Hannestad, S., & Wong, Y. Y. (2014b). Getting leverage on inflation. In preparation.
- Bean, R. (2010). TASI Lectures on Cosmic Acceleration.
- Bean, R., & Dore, O. (2004). Probing dark energy perturbations: The Dark energy equation of state and speed of sound as measured by WMAP. Phys.Rev., D69, 083503.

Bibliography

- Bird, S., Viel, M., & Haehnelt, M. G. (2012). Massive Neutrinos and the Non-linear Matter Power Spectrum. Mon.Not.Roy.Astron.Soc., 420, 2551–2561.
- Blas, D., Lesgourgues, J., & Tram, T. (2011). The Cosmic Linear Anisotropy Solving System (CLASS) II: Approximation schemes. JCAP, 1107, 034.
- Bond, J., Cole, S., Efstathiou, G., & Kaiser, N. (1991). Excursion set mass functions for hierarchical Gaussian fluctuations. Astrophys.J., 379, 440.
- Brandbyge, J., & Hannestad, S. (2009). Grid Based Linear Neutrino Perturbations in Cosmological N-body Simulations. JCAP, 0905, 002.
- Brandbyge, J., Hannestad, S., Haugboelle, T., & Wong, Y. Y. (2010). Neutrinos in Non-linear Structure Formation - The Effect on Halo Properties. JCAP, 1009, 014.
- Brooks, S. P., & Gelman, A. (1998). General methods for monitoring convergence of iterative simulations. Journal of Computational and Graphical Statistics, 7(4), 434–455.
- Carroll, S. M. (2001). The Cosmological constant. Living Rev.Rel., 4, 1.
- Carroll, S. M., Duvvuri, V., Trodden, M., & Turner, M. S. (2004). Is cosmic speed-up due to new gravitational physics? Phys.Rev., D70, 043528.
- Copeland, E. J., Sami, M., & Tsujikawa, S. (2006). Dynamics of dark energy. Int.J.Mod.Phys., D15, 1753–1936.
- Cowles, M. K., & Carlin, B. P. (1996). Markov chain monte carlo convergence diagnostics: A comparative review. Journal of the American Statistical Association, 91(434), pp. 883–904.
- Creminelli, P., D’Amico, G., Norena, J., Senatore, L., & Vernizzi, F. (2010). Spherical collapse in quintessence models with zero speed of sound. JCAP, 1003, 027.
- Davis, T. M. (2014). Cosmological constraints on dark energy.
- Frieman, J., Turner, M., & Huterer, D. (2008). Dark Energy and the Accelerating Universe. Ann.Rev.Astron.Astrophys., 46, 385–432.
- Frieman, J. A. (2008). Lectures on dark energy and cosmic acceleration. AIP Conf.Proc., 1057, 87–124.
- Frieman, J. A., Hill, C. T., Stebbins, A., & Waga, I. (1995). Cosmology with ultralight pseudo Nambu-Goldstone bosons. Phys.Rev.Lett., 75, 2077–2080.
- Gelman, A., & Rubin, D. B. (1992). Inference from iterative simulation using multiple sequences. Statistical Science, 7(4), pp. 457–472.

Bibliography

- Hamann, J., Hannestad, S., & Wong, Y. Y. (2012). Measuring neutrino masses with a future galaxy survey. *JCAP*, 1211, 052.
- Harrison, I., & Hotchkiss, S. (2013). A Consistent Approach to Falsifying Lambda-CDM with Rare Galaxy Clusters. *JCAP*, 1307, 022.
- Hu, W., & Sawicki, I. (2007). Models of $f(R)$ Cosmic Acceleration that Evade Solar-System Tests. *Phys.Rev.*, D76, 064004.
- Jenkins, A., Frenk, C., White, S. D., Colberg, J., Cole, S., et al. (2001). The Mass function of dark matter halos. *Mon.Not.Roy.Astron.Soc.*, 321, 372.
- Kaloper, N., & Sorbo, L. (2006). Of pngb quintessence. *JCAP*, 0604, 007.
- Komatsu, E., et al. (2011). Seven-Year Wilkinson Microwave Anisotropy Probe (WMAP) Observations: Cosmological Interpretation. *Astrophys.J.Suppl.*, 192, 18.
- Kowalski, M., et al. (2008). Improved Cosmological Constraints from New, Old and Combined Supernova Datasets. *Astrophys.J.*, 686, 749–778.
- Kunz, M., & Sapone, D. (2006). Crossing the Phantom Divide. *Phys.Rev.*, D74, 123503.
- Laureijs, R., Amiaux, J., Arduini, S., Augueres, J.-L., Brinchmann, J., et al. (2011). Euclid Definition Study Report.
- Lewis, A., & Bridle, S. (2002). Cosmological parameters from CMB and other data: a Monte- Carlo approach. *Phys. Rev.*, D66, 103511.
- Lewis, A., Challinor, A., & Lasenby, A. (2000). Efficient computation of CMB anisotropies in closed FRW models. *Astrophys.J.*, 538, 473–476.
- Liddle, A. R. (2009). Statistical methods for cosmological parameter selection and estimation. *Ann.Rev.Nucl.Part.Sci.*, 59, 95–114.
- Linder, E. V., & Scherrer, R. J. (2009). Aetherizing Lambda: Barotropic Fluids as Dark Energy. *Phys.Rev.*, D80, 023008.
- Ma, C.-P., & Bertschinger, E. (1995). Cosmological perturbation theory in the synchronous and conformal Newtonian gauges. *Astrophys.J.*, 455, 7–25.
- Maggiore, M., & Riotto, A. (2010). The Halo Mass Function from Excursion Set Theory. I. Gaussian fluctuations with non-Markovian dependence on the smoothing scale. *Astrophys.J.*, 711, 907–927.
- Maor, I., & Lahav, O. (2005). On virialization with dark energy. *JCAP*, 0507, 003.

Bibliography

- Martin, J. (2012). Everything You Always Wanted To Know About The Cosmological Constant Problem (But Were Afraid To Ask). Comptes Rendus Physique, 13, 566–665.
- Padmanabhan, T. (2003). Cosmological constant: The Weight of the vacuum. Phys.Rept., 380, 235–320.
- Peacock, J., & Heavens, A. (1990). Alternatives to the Press-Schechter cosmological mass function. Mon.Not.Roy.Astron.Soc., 243, 133–143.
- Peccei, R. D., & Quinn, H. R. (1977). Cp conservation in the presence of pseudoparticles. Phys. Rev. Lett., 38, 1440–1443.
- Peebles, P., & Ratra, B. (2003). The Cosmological constant and dark energy. Rev.Mod.Phys., 75, 559–606.
- Peebles, P. J. E. (1980). Large-scale structure of the Universe. Princeton University Press, Princeton NJ.
- Perotto, L., Lesgourgues, J., Hannestad, S., Tu, H., & Wong, Y. Y. (2006). Probing cosmological parameters with the CMB: Forecasts from full Monte Carlo simulations. JCAP, 0610, 013.
- Press, W. H., & Schechter, P. (1974). Formation of galaxies and clusters of galaxies by selfsimilar gravitational condensation. Astrophys.J., 187, 425–438.
- Ryden, B. (2003). Introduction to Cosmology. Addison Wesley.
- Sheth, R. K., & Tormen, G. (1999). Large scale bias and the peak background split. Mon.Not.Roy.Astron.Soc., 308, 119.
- Sikivie, P. (2008). Axion Cosmology. Lect.Notes Phys., 741, 19–50.
- Silvestri, A., & Trodden, M. (2009). Approaches to Understanding Cosmic Acceleration. Rept.Prog.Phys., 72, 096901.
- Smith, R., et al. (2003). Stable clustering, the halo model and nonlinear cosmological power spectra. Mon.Not.Roy.Astron.Soc., 341, 1311.
- Springel, V. (2005). The Cosmological simulation code GADGET-2. Mon.Not.Roy.Astron.Soc., 364, 1105–1134.
- Takahashi, R., Sato, M., Nishimichi, T., Taruya, A., & Oguri, M. (2012). Revising the Halofit Model for the Nonlinear Matter Power Spectrum. Astrophys.J., 761, 152.
- Tegmark, M., Taylor, A., & Heavens, A. (1997). Karhunen-Loeve eigenvalue problems in cosmology: How should we tackle large data sets? Astrophys.J., 480, 22.

Bibliography

- Tinker, J. L., Kravtsov, A. V., Klypin, A., Abazajian, K., Warren, M. S., et al. (2008). Toward a halo mass function for precision cosmology: The Limits of universality. *Astrophys.J.*, 688, 709–728.
- Trotta, R. (2008). Bayes in the sky: Bayesian inference and model selection in cosmology. *Contemp.Phys.*, 49, 71–104.
- Visinelli, L., & Gondolo, P. (2014). Axion cold dark matter in view of BICEP2 results. *Phys.Rev.Lett.*, 113, 011802.
- Waizmann, J.-C., Ettori, S., & Bartelmann, M. (2012). Order statistics applied to the most massive and most distant galaxy clusters.
- Wang, P. (2006). Virialization in dark energy cosmology. *Astrophys.J.*, 640, 18–21.
- Weinberg, S. (2008). *Cosmology*. Oxford University Press, Oxford.
- Wood-Vasey, W. M., et al. (2007). Observational Constraints on the Nature of the Dark Energy: First Cosmological Results from the ESSENCE Supernova Survey. *Astrophys.J.*, 666, 694–715.
- Zentner, A. R. (2007). The Excursion Set Theory of Halo Mass Functions, Halo Clustering, and Halo Growth. *Int.J.Mod.Phys.*, D16, 763–816.